UNIVERSIDADE DE LISBOA

FACULDADE DE CIÊNCIAS

DEPARTAMENTO DE FÍSICA

Modeling and design of an electromagnetic actuation system for the manipulation of microrobots in blood vessels

Patrícia Alexandra Afonso Zoio

Dissertação
Mestrado Integrado em Engenharia Biomédica e Biofísica
Perfil em Engenharia Clínica e Instrumentação Médica

2015

UNIVERSIDADE DE LISBOA

FACULDADE DE CIÊNCIAS

DEPARTAMENTO DE FÍSICA

Modeling and design of an electromagnetic actuation system for the manipulation of microrobots in blood vessels

Patrícia Alexandra Afonso Zoio

Dissertação orientada por:
Professora Doutora Rita G. Nunes
Professor Doutor Hugo A. Ferreira

Mestrado Integrado em Engenharia Biomédica e Biofísica
Perfil em Engenharia Clínica e Instrumentação Médica

2015

Abstract

Navigation of nano/microdevices has great potential for biomedical applications, offering a means for diagnosis and therapeutic procedures inside the human body. Due to their ability to penetrate most materials, magnetic fields are naturally suited to control magnetic nano/microdevices in inaccessible spaces. One recent approach is the use of custom-built apparatus capable of controlling magnetic devices. This is a promising area of research, but further simulation studies and experiments are needed to estimate the feasibility of these systems in clinical applications.

The goal of this project was the simulation and design of an electromagnetic actuation system to study the two dimensional locomotion of microdevices. The first step was to identify, through finite element analysis using software COMSOL, different coil configurations that would allow the control of magnetic devices at different scales. Based on the simulation results, a prototype of a magnetic actuation system to control devices with more than 100 μm was designed and built from the ground up, taking into account cost constraints. The system comprised one pair of rotational Helmholtz coils and one pair of rotational Maxwell coils placed along the same axis. Furthermore, additional components had to be designed or selected to fulfil the requirements of the system. For the evaluation of the fabricated system, preliminary tests were carried out. The locomotion of a microdevice was tested along different directions in the x-y plane.

The simulations and experiments confirmed that it is possible to control the magnetic force and torque acting on a microdevice through the fields produced by Maxwell and Helmholtz coils, respectively. Thus, this type of magnetic actuation seems to provide a suitable means of energy transfer for future biomedical microdevices.

Keywords: Magnetic navigation, microrobotics, biomedicine, simulations.

Resumo

A navegação de nano/microdispositivos apresenta um grande potencial para aplicações biomédicas, oferecendo meios de diagnóstico e procedimentos terapêuticos no interior do corpo humano. Dada a sua capacidade de penetrar quase todos os materiais, os campos magnéticos são naturalmente adequados para controlar nano/microdispositivos magnéticos em espaços inacessíveis. Uma abordagem recente é o uso de um aparelho personalizado, capaz de controlar campos magnéticos. Esta é uma área de pesquisa prometedora, mas mais simulações e experiências são necessárias para avaliar a viabilidade destes sistemas em aplicações clínicas.

O objectivo deste projecto foi a simulação e desenho de um sistema de atuação eletromagnética para estudar a locomoção bidimensional de microdispositivos. O primeiro passo foi identificar, através da análise de elementos finitos, usando o software COMSOL, diferentes configurações de bobines que permitiriam o controlo de dispositivos magnéticos em diferentes escalas. Baseado nos resultados das simulações, um protótipo de um sistema de atuação magnética para controlar dispositivos com mais de 100 μm foi desenhado e construído de raiz, tendo em conta restrições de custos. O sistema consistiu num par de bobines de Helmholtz e rotacionais e um par de bobines de Maxwell dispostas no mesmo eixo. Além disso, componentes adicionais tiveram de ser desenhados ou selecionados para preencher os requisitos do sistema. Para a avaliação do sistema fabricado, testes preliminares foram realizados. A locomoção do microrobot foi testada em diferentes direções no plano x-y.

As simulações e experiências confirmaram que é possível controlar a força magnética e o momento da força que atuam num microdispositivo através do campos produzidos pelas bobines de Maxwell e Helmholtz, respectivamente. Assim, este tipo de atuação magnética parece ser uma forma adequada de transferência de energia para futuros microdispositivos biomédicos.

Palavras-chave: Navegação magnética, microrobótica, biomedicina, simulações.

Acknowledgements

"If I have seen further it is by standing on the shoulders of Giants."

Isaac Newton

I would like to thank my supervisors Professor Rita Nunes and Professor Hugo Ferreira, for their helpful guidance during this work and for all the valuable advices. Both of them were a source of encouragement.

I would also like to thank Professor Maria Margarida Cruz for the gaussmeter.

A very special thanks goes to my friend Mariana for all the support since the beginning and for helping me reviewing this dissertation.

Finally, I would like to express my gratitude to my parents for encouraging me every step of the way. This thesis is dedicated to them.

Contents

1. Introduction 1

1.1 Motivation 1

1.2 Dissertation Objectives 3

1.3 Thesis Outline 4

2. Principles of Magnetism 7

2.1 Brief history of magnetism 7

2.2 Maxwell's Equations 8

2.3 Magnetic materials 9

2.3.1 Diamagnetic materials 12

2.3.2 Paramagnetic materials 13

2.3.3 Ferromagnetic materials 13

2.3.3.1 Soft and hard magnetic materials 14

2.3.3.1.1 Permanent magnets 15

2.4 Electromagnetic coils 17

2.4.1 Helmholtz and Maxwell Coils 18

3. Microrobotics for biomedical applications 23

3.1 Introduction 24

3.2 Potential applications of medical microrobots 25

3.2.1 Basic functions 26

3.2.1.1 Targeted therapy 26

3.2.1.2 Material removal 27

3.2.1.3 Controllable structures 28

3.2.1.4 Telemetry 28

3.2.2 Application Areas 29

3.2.2.1 Circulatory system 29

3.2.2.2 Central nervous system 30

3.2.2.3 Urinary system and prostate 31

3.2.2.4 The eye 31
3.3 Power and Actuation methods 32
3.4 Wireless Magnetic actuation 33
3.4.1 State-of-the-art 33
3.4.1.1 MRI systems for propulsion 34
3.4.1.2 Custom built apparatus 36
3.4.1.3 Modeling and Computational Tools 38
3.4.2 Forces acting on a microdevice 40
3.4.2.1 Magnetic Force and Torque 40
3.4.2.1.1 Magnetic dipole moment 41
3.4.2.1.2 Magnetically linear particle 42
3.4.2.1.3 Nonlinear magnetic media 43
3.4.2.1.4 Magnetic Torque 44
3.4.2.2 Hydrodynamic drag force 44
3.4.2.3 Apparent weight 46
3.5 Microrobots localization 46

4. Modeling 49
4.1 Problem description 50
4.1.1 Magnetic actuation of a permanently magnetized microdevice 54
4.1.2 Magnetic actuation of small microparticles 58
4.2 COMSOL Modeling 63
4.2.1 Magnetic actuation of microdevices 64
4.2.1.1 Geometry 64
4.2.1.2 Magnetic Fields Mode 65
4.2.1.3 Coefficient Form PDE 67
4.2.1.5 Results 69
4.2.1.5.1 x-axis Helmholtz coils 70
4.2.1.5.2 x-axis Maxwell coils 73
4.2.1.5.3 x-axis Helmholtz and Maxwell coils 77
4.2.1.5.4 y-axis Helmholtz and Maxwell coils 79
4.2.1.5.5 x-axis and y-axis Helmholtz and Maxwell coils 81
4.2.1.6 Particle Tracing 83
4.2.2 Magnetic actuation of small microparticles 90

4.2.2.1 Geometry 90
4.2.2.2 Helmholtz coils 91
4.2.2.3 Maxwell coils 93
4.2.2.4 Helmholtz and Maxwell coils 96
4.2.2.5 Particle Tracing 98
4.2.5.5.1 Results 101

5. Experimental Work 111
5.1 Problem Description 112
5.2 Setup Overview 114
5.2.1 Coils 115
5.2.2. Coil support 122
5.2.3. Wiring and microscope support 124
5.2.4 Electronic system 125
5.2.4.1 Stepper motor 126
5.2.4.2 Arduino and driver 127
5.2.4.3 Switch for current inversion 130
5.3 Experiments 131
5.3.1 Experimental setup 131
5.3.2 Experimental Results and Discussion 132

6. Conclusion and Future Work 139
6.1 Conclusion 139
6.2 Future Work 143

References 149

Appendix A 157
Appendix B 158
Appendix C 160
Appendix D 161

Nomenclature

Abbreviations and Acronyms

MIT	Minimally invasive therapy
MEMS	Micro-electro-mechanical-systems
MRI	Magnetic resonance imaging
EMA	Electromagnetic actuation system
DOF	Degree of freedom
FEM	Finite element modeling
FEA	Finite element analysis
GI	Gastrointestinal
CT	Computer tomography
IR	Infrared
PET	Positron emission tomography
ROI	Region of interest
USB	Universal Serial Bus
GND	Ground
DIY	*Do-it-yourself*
CAD	Computer-aided design

Symbols

$\vec{H}$	Magnetic field	[A/m]
$\vec{B}$	Magnetic flux density	[T]
$\vec{E}$	Electric field	[V/m]
ρ	Free electrical charge	[C/m^3]
$\vec{J}$	Free current density	[A/m^2]
μ	Magnetic permeability	[N/A^2]
μ_0	Magnetic permeability of free space: $4\pi \times 10^{-7}$ N.A^{-2}	[N/A^2]
μ_r	Relative permeability of the medium	
χ	Magnetic susceptibility	
$\vec{m}$	Magnetic moment	[A.m^2]
$\vec{M}$	Magnetization	[A/m]
I	Current	[A]
N	Number of wire turns of a coil	
r,R	Radius	[m]
d	Diameter	[m]
D	Distance	[m]
$\vec{F}$	Force	[N]
V	Volume	[m^3]
$\overrightarrow{F_m}$	Magnetic force	[N]
$\overrightarrow{F_d}$	Drag froce	[N]
$\overrightarrow{W_a}$	Apparent weight	[N]
φ	Magnetic scalar potential	[(V.s)/m]
A	Magnetic vector potential	[(V.s)/m]
$\vec{\tau}_m$	Torque	[N.m]
ρ_f	Density of a fluid	[kg/m^3]
A	Area	[m^2]

$\vec{v}$	Velocity	[m/s]
C_d	Drag coefficient	
Re	Reynolds number	
μ_f	Viscosity of a fluid	[kg/(s.m)]
λ	Ratio of particle to vessel diameter	
m_p	Mass of a particle	[kg]
C_{MD}	Ratio of magnetic forces over drag forces	
w	Width	[m]
h	Height	[m]
D_c	Diameter of the copper wire	[m]
θ	Angle	[º]
R	Resistance	[Ω]
t	Time	[s]
x	First world coordinate frame direction or distance	[m]
y	Second world coordinate frame direction	[m]
z	Third world coordinate frame direction	[m]

"In the beginning there was nothing, which exploded"

-Terry Pratchett

Chapter 1

Introduction

The goal of this dissertation was to study the feasibility of a magnetic actuation system to control microrobots in blood vessels. In this chapter, the motivation behind this goal will be discussed. Also, the different objectives will be defined and the outline of the thesis will be presented.

1.1 Motivation

Cancer is a class of diseases involving unregulated cell growth. These cells can invade adjoining parts of the body and spread to other organs in a process referred to as metastasis which is one of the major causes of death. Surgery is the primary method of treatment of most isolated solid cancers. However, depending on the tumor location and the damaged caused to surrounding tissues, surgery is not always possible. Other options for cancer treatment include chemotherapy and radiotherapy. However, these treatments have many drawbacks mainly because of the difficulty in differentiating healthy and diseased tissue.

Approximately twenty years ago, there was a paradigm shift in medicine with the advent of minimally invasive therapies (MIT) [1]. Nowadays, this is an active area of research since related techniques can reach remote places without the need of open surgery, achieving better results. Some of the patient related benefits of MIT are reduced trauma, reduced infection risk, reduced postoperative pain and a faster recoveries [2].

The ability to localize, target and have a protected, prolonged and controlled interaction with the diseased tissue in the body, would allow better treatment not only for

cancer but many other diseases. This would allow reducing the drug or radiation dosages taken by the patient, reducing the possible side-effects.

One of the most used minimally invasive techniques is catheter embolization. It is used to treat a wide variety of conditions affecting different organs in the human body. However, it has several limitations since it is unable to reach remote areas within the cardiovascular system [3].

The use of robots in minimally invasive treatments aims to benefit medicine by further reducing treatment invasiveness in a way that until now was not possible to conceive, enabling the treatment of previously inoperable patients.

In the human body there is a large number of cavities/ canals filled with fluids (circulatory system, urinary system, central nervous system, eyes) which can be accessed through open orifices or a needle injection. It is conceivable that, in the future, robots could use this natural pathways within the body to reach its target and perform a new set of minimally invasive diagnostic, therapeutic, and surgical procedures. As technology advances, allowing further reduction in the size of these robots, their potential could increase allowing them to have a better penetration depth inside the body.

This dissertation focuses on the manipulation of microrobots. This is a very challenging area and several problems and limitations have to be studied and discussed. Specifically, power and actuation are generally some of the most challenging problems in the field of microrobotics. At this moment, due to fabrication limitations, a microrobot that it is entirely autonomous, including actuators, power source and integrated sensors is unrealistic. An alternative is to develop actuation systems capable of controlling the microrobots from a distance. One approach to the wireless control of untethered microrobots is through externally applied magnetic fields.

The design of an effective magnetic actuation system requires research in three main areas:

- The development of the magnetic robot taking into account its material, geometry, and capabilities;
- Real-time imaging of the magnetic devices as they move through the blood vessels;
- The development of technology to propel/steer the microrobot through the circulatory system.

This dissertation focuses on the third area of research, studying the feasibility of a magnetic actuation system for microrobots control.

1.2 Dissertation Objectives

This dissertation had two major goals. One was to simulate, using the finite element method, different magnetic actuation systems and test the effect of their produced magnetic force on the locomotion of microdevices. The second goal was to fabricate, from the ground up, one of the simulated magnetic actuation systems. With these theoretical and experimental studies the objective was to evaluate the technical feasibility of magnetic actuation of microrobots in blood vessels, for future medical interventions.

Overall, the different sub-goals defined during this work were:

- Study in detail the main forces acting on a magnetic device traveling in the blood vessels, when subjected to a magnetic force;
- Perform preliminary numerical simulations using MATLAB in order to define the general requirements for the control of magnetic devices in blood vessels, at different scales;
- Simulate different coil configurations that would allow the control of microrobots, through finite element analysis, using the software COMSOL and test the efficiency of these proposed systems using the Particle Tracing Module. Since the control of magnetic devices in blood vessels is very dependent on the scale of the problem, the goal was to explore two special cases, separately:
    - Perform finite element simulations for designed electromagnetic actuation systems with the purpose of controlling devices that are permanently magnetized and bigger than 100 μm;
    - Perform finite element simulations for electromagnetic actuation systems with the purpose of controlling particles with diameters ranging from 1 μm to 100 μm and considering different values of saturation magnetization.
- Taking into account the results from the finite element simulations, one important goal was to design and fabricate a system, from the ground up, capable of controlling permanently magnetized devices bigger than 100 μm in the vessels, considering cost constraints and using a *do-it-yourself* approach. Next, the goal was to test the fabricated system using the available material;
- Based on the results from the fabricated device and on the knowledge acquired through the simulations, the final goal was to discuss the potential and limitations of magnetic actuation and to propose a system capable of controlling particles at a smaller scale.

1.3 Thesis Outline

This dissertation work is presented in 6 chapters. The overall view of the dissertation is depicted in Figure 1.1.

After discussing the motivations and the objectives of this work in chapter 1, in chapter 2, the basic magnetic principles are reviewed with focus on the most relevant aspects for this work such as the study of different coil configurations.

In chapter 3, after an overview of the theoretical background of microrobotics and its potential applications in medicine, a review of the previous work related to wireless magnetic actuation is presented. Also in this chapter, the forces acting on a magnetic device in the blood vessels when subjected to magnetic field are discussed in some detail. Finally, the different possibilities for localization *in vivo* of microrobots are presented and discussed.

Chapter 4 starts with numerical simulations using MATLAB, to define the general requirements for the control of magnetic devices in blood vessels, at different scales. Based on these requirements, this chapter follows with the finite element analysis using the software COMSOL, showing the results of different coil configurations that would allow this control. Through the Particle Tracing Module the efficiency of these proposed systems is evaluated.

In chapter 5, the experimental work is described. First, the different components of the system, with its characteristics, functionality and constraints are discussed in some detail. Also, the magnetic field was measured to investigate the linearity and magnitude of the magnetic fields produced by the coil configuration and the results are presented and compared to the finite element model. Also in this chapter, the results from the 2-dimensional control of a millimeter-sized permanent magnet using the fabricated electromagnetic actuation system are shown and discussed.

Finally, chapter 6 summarizes the main results and findings from this dissertation and presents ideas for future projects.

Chapter 2 and 3

Literature Review

Forces acting on a microdevice

$\vec{F}_m = \mu_0 V(\vec{M} \cdot \nabla)\vec{H}$ $\quad \vec{\tau}_m = V_m \vec{M} \times \vec{B}$ $\quad \overrightarrow{F_d} = -\frac{1}{2}\rho_f(\vec{v} - \overrightarrow{v_f})^2_\infty A C_d$ $\quad m\ddot{x} = \vec{F}_{d_x} + \vec{F}_{m_x}$

Chapter 4

Comsol Simulations

Different Designs

Particle Tracing Module

Chapter 5

Experimental Work

Chapter 6

Conclusions

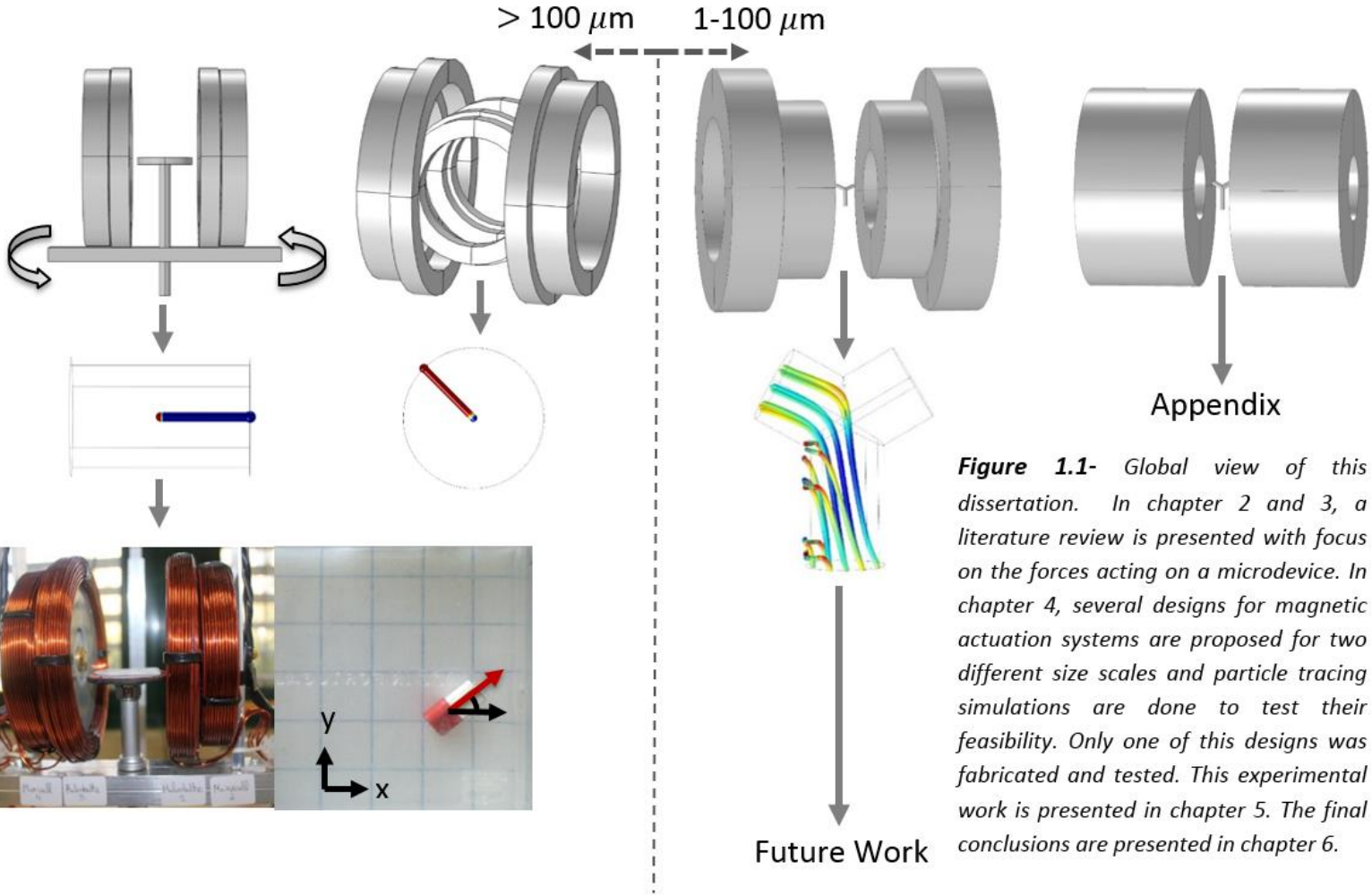

Figure 1.1- *Global view of this dissertation. In chapter 2 and 3, a literature review is presented with focus on the forces acting on a microdevice. In chapter 4, several designs for magnetic actuation systems are proposed for two different size scales and particle tracing simulations are done to test their feasibility. Only one of this designs was fabricated and tested. This experimental work is presented in chapter 5. The final conclusions are presented in chapter 6.*

"The magnetic force is animate, or imitates soul; in many respects it surpasses the human soul while it is united to an organic body."

-William Gilbert in De Magnet, 1600

Chapter 2

Principles of Magnetism

In this work, the forces used to propel the biomedical microdevices are generated by a coil system capable of producing the desired magnetic fields. Nowadays, this and many other applications are possible due to the work of many researchers throughout history. This chapter will start with a brief history of magnetism, followed by a brief explanation of the fundamentals of magnetism, highlighting the most relevant aspects to this project.

2.1 Brief history of magnetism*

The history of the study of magnetic and electric effects is an old one, originated in Greek culture as an offspring of philosophy in 6th century B.C. Aristotle attributed the first of what could be called a scientific discussion on magnetism to the Greek philosopher Thales of Miletus, who discovered the interesting properties of Iodestone, capable of attracting iron or assuming north-south orientation. Around the same time, in ancient India, the surgeon Sushruta was the first to make use of a magnet for surgical purposes.

The first systematic experiments on magnetism did not occur until 1600 A.D. with the publication of *De magnete* by W. Gilbert where he concluded that the earth is magnetic. In the 18^{th} century there were numerous and ordered observations of magnetic and electric phenomena mainly by D. Bernoulli, H. Cavendish, Ch. A. Coulomb, B. Franklin, A. Galvani and A. Volta. Also, the refinement of mathematical analysis introduced by I. Newton and G.W. Leibniz in 1670-75, and extended by L. Euler and J. L. Lagrange in 1744-55 contributed to the progress in the study of electromagnetic phenomena.

*This chapter follows loosely the book from J.M.D.Coey [4]

In 1820, the physicist Oersted discovered the connection between electrical current and magnetic field when a current-carrying conductor near a compass caused the compass needle to deflect. The mathematician A.M. Ampère was stimulated by Oersted's discovery and, within a few months, he extended both experimentally and theoretically the understanding of magnetic effects related to electric currents. For this work Ampère is considered by many to be the "father" of electromagnetism. In 1826, G.S. Ohm finally established the relation between electric field and current.

In 1831, M.Faraday described the law of induction and introduced the concept of magnetic lines of force. Throughout the following decades, several scientists and mathematicians contributed to the electromagnetism theory. In particular, electromagnetic phenomena were gradually formulated in more exact mathematical terms through the contribution of C.F. Gauss, W.E. Weber, W. Thomson, R. Kohlraush, and H. Helmholtz.

In 1855, the Scottish mathematician and physicist J.C Maxwell further extended the ideas about field lines and in 1873 his *Treatise on Electricity and Magnetism* was published. The contributions in 1885-85 by H. Hertz and O. Heaviside gave Maxwell's equations their final form. In the next section (2.2) these equations will be briefly discussed in the context of this thesis.

In the first half of the 20th century, with the advent of quantum mechanics, magnetic effects were explained considering the atomic structure of material. Classical electromagnetic theory was coupled with quantum mechanics into quantum electrodynamics.

2.2 Maxwell's Equations

Maxwell's equations represent the concluding highlight of centuries of discoveries and studies in electromagnetism and set the comprehensive foundation of classical electromagnetic theory. In differential form, the equations can be written as:

Gauss's Law	$\nabla \cdot \vec{D} = \rho$	2.1
Gauss's Law for Magnetism	$\nabla \cdot \vec{B} = 0$	2.2
Faraday's Law of Induction	$\nabla \times \vec{E} = -\frac{\partial \vec{B}}{\partial t}$	2.3
Ampère's Law	$\nabla \times \vec{H} = \vec{J} + \frac{\partial \vec{D}}{\partial t}$	2.4

In the above equations, $\vec{H}$ (in A/m) and $\vec{E}$ (in V/m) are the magnetic and electric field respectively, $\vec{D}$ (in C/m^2) and $\vec{B}$ (in T) are the electric and magnetic flux density (or electric and magnetic induction), ρ (in C/m^3) and $\vec{J}$ (in A/m^2) are, respectively, the free electric charge and free current density. The nabla operator, ∇, in Cartesian coordinates is defined as:

$$\nabla = \left[\frac{\partial}{\partial x}, \frac{\partial}{\partial y}, \frac{\partial}{\partial z}\right]^T$$

Gauss's Law is the first of Maxwell's Equations which dictates how the electric field behaves around electric charges. This law states that a charge density is the source of the electric flux density. Gauss's law for magnetism means that there are no "magnetic charges" analogous to electric charges. Instead, the magnetic fields due to materials are generated by a configuration called a dipole. The Maxwell-Faraday's equation version of Faraday's law describes how a time varying magnetic field induces an electric field. The Ampère's law with Maxwell's equation states that magnetic fields can be generated in two ways: by electric current and by changing electric fields. More specifically, a current density and a time-varying electric flux density cause a curl of the electric field.

In this dissertation, the special case of magnetostatics is considered. Under static conditions, there are no electric charges ($\rho = 0$), no electric fields ($\vec{E} = 0$) and the condition of static fields ($\frac{d}{dt}(\cdot) = 0$) it is considered. Thus, it is possible to reduce Maxwell's equations to equations 2.5 and 2.6.

$$\nabla \cdot \vec{B} = 0 \qquad 2.5$$

$$\nabla \times \vec{H} = \vec{J} \qquad 2.6$$

Also, if there are no currents in the region of interest $\vec{J}$=0.

Equation 2.5 states that the number of field lines entering any given volume in space is equal to the number of field lines leaving that volume (the net flux of $\vec{B}$ through surface *S* is zero).

To make a general solution possible (of a system defined by 2.5 and 2.6) the constitutive relationship between $\vec{B}$ and $\vec{H}$, i.e, $\vec{B}(\vec{H})$ of a material is required. This relationship defines the classification of magnetic materials as discussed in section 2.3.

2.3 Magnetic materials

The magnetic flux density, $\vec{B}$ is the response of a material when applying an external magnetic field, $\vec{H}$ [5]. The relationship between these vectors depends on the material itself and it is given by the constitutive law:

$$\vec{B} = \mu(\vec{H})\vec{H} \quad 2.7$$

where $\mu(\vec{H})$ is the magnetic permeability tensor, which is generally anisotropic (directionally dependent) and nonlinear. In this dissertation, linear and isotropic materials are considered. In this case, $\mu(\vec{H})$ reduces to a scalar:

$$\vec{B} = \mu \cdot \vec{H} \quad 2.8$$

$$\mu = \mu_0 \mu_R \quad 2.9$$

where the magnetic permeability of free space μ_0 is, by definition, $4\pi \times 10^{-7}$Tm/A and μ_r (dimensionless) is the relative permeability of the media. The relative permeability can be used to classify materials into three categories: diamagnetic ($\mu_r < 1$), paramagnetic ($\mu_r = 1$ to 10) and ferromagnetic ($\mu_r \gg 10$). This parameter can be seen as a measure of how well a material concentrates the flux lines. The higher the relative permeability, the more flux lines go through the material for the same magnetic field $\vec{H}$. The relative permeability for several materials can be seen in Table 2.1.

Material	μ_r
Iron	4,000
Permalloy	70,000
Supermalloy	1,000,000
Permendur	5,000
Cobalt	600
Manganese-Zinc Ferrite	750
Nickel-Zinc Ferrite	650
Bismuth	0.9998
Mercury	0.9999
Copper	0.9999
Water	0.9999
Air	1.0000
Tungsten	1.0000
Manganese	1.0010

Table 2.1 *Relative permeability of several materials* [6].

In general, it is only possible to see an effect on materials with a large relative permeability (ferromagnetic materials) and this is the reason why they are usually referred to as "magnetic materials". In vacuum or air, $\mu_r = 1$. In this case, $\vec{H}$ and $\vec{B}$ are simply related by the magnetic constant μ_0:

$$\vec{B} = \mu_0 \vec{H} \quad 2.10$$

The properties of a magnetic material are dependent on the net magnetic moment $\vec{m}$ (A.m^2), which results from the presence of an external magnetic field. In magnetic materials, the cause of the magnetic moment are the spin and orbital angular momentum states of the electrons. The magnetic susceptibility χ quantifies the tendency of a material to form magnetic dipoles. It is a dimensionless scalar related to the relative permeability μ_r by equation 2.11.

$$\chi = \mu_r - 1 \tag{2.11}$$

The magnetic susceptibility of various materials can be seen in Table 2.2.

Material	Magnetic Susceptibility χ
Bismuth	-17.6×10^{-5}
Silver	-2.4×10^{-5}
Copper	-0.88×10^{-5}
Water	-0.90×10^{-5}
Cabon Dioxide	-1.2×10^{-5}
Oxygen	0.19×10^{-5}
Sodium	0.85×10^{-5}
Aluminum	2.3×10^{-5}
Tungsten	7.8×10^{-5}
Gadolinium	48000×10^{-5}
Iron	30×10^{3}
Iron-Nickel	$80 - 300 \times 10^{3}$

Table 2.2 *Magnetic susceptibility of several materials* [6].

Using equations 2.9 and 2.11, Equation 2.8 can be expressed as:

$$\vec{B} = \mu_0(1 + \chi)\vec{H} \tag{2.12}$$

It is an experimental fact that in most materials, when subjected to a magnetic field $\vec{H}$, an additional magnetic field component $\vec{M}$ (A/m) is generated locally. This component is called magnetization vector and it is defined as the net magnetic moment per unit of volume. This vector is related to the magnetization current $\overrightarrow{J_m}$ or movement of bound charges through equation 2.13.

$$\overrightarrow{J_m} = \nabla \times \vec{M} \tag{2.13}$$

Using equations 2.6 and 2.11, the total current density $\vec{J}$ can be expressed as:

$$\vec{J} = \overrightarrow{J_m} + \overrightarrow{J_f} \tag{2.14}$$

where $\overrightarrow{J_f}$ is the current density in free space. Thus, equation 2.4 becomes:

$$\nabla \times \vec{B} = \mu_0(\overrightarrow{J_m} + \overrightarrow{J_f}) \tag{2.15}$$

Substituting equation 2.13 into equation 2.15:

$$\nabla \times \frac{\vec{B}}{\mu_0} - \vec{M} = \overrightarrow{J_f} \quad 2.16$$

In the case of linear and isotropic materials, the relative permeability is dependent on the magnetic field intensity $\vec{H}$, with $\vec{B}$ and $\vec{H}$ parallel to each other and in the same direction. As a result, magnetization can be defined as:

$$\vec{M} = \chi \vec{H} \quad 2.17$$

Using the equations here described it is possible to define $\vec{H}$ as:

$$\vec{H} = \frac{\vec{B}}{\mu_0} - \vec{M} \quad 2.18$$

It is important to note that the linear relationship between $\vec{H}$ and $\vec{B}$ is a simplification and only holds for sufficiently small magnetic fields. Nonlinear magnetic materials vary from equation 2.20. In these case, the relationship expressed in equations 2.11 and 2.19 implies that the magnetization vector $\vec{M}$ also depends on $\vec{H}$. Thus:

$$\vec{B} = \mu \vec{H} + \overrightarrow{B_{rem}} \quad 2.19$$

Where $\overrightarrow{B_{rem}} = \mu \vec{M}$ (in T) is the residual magnetic flux density (remanence).

The magnetic properties of materials, expressed by the magnetization $\vec{M}$ depend on two main atomic effects, which can give rise to large local magnetic fields: the orbital motion of electrons around the nucleus, which can be seen as current loops of atomic dimensions or as small magnetic dipole moments; the intrinsic spin of electrons (or nuclei) with the related magnetic dipole moment. The relative permeability or the magnetic susceptibility, which define $\vec{M}$, varies widely, as shown in the previous tables. In the next sections the different types of magnetic materials will be described.

2.3.1 Diamagnetic materials

Diamagnetic substances are materials where, in the absence of an external magnetic field, orbit and pin magnetic moments cancel resulting in no net magnetic moment in the material. The response to an applied magnetic field is the creation of circulating atomic currents that produce a very small bulk magnetization antiparallel to the magnetic field, causing the field $\vec{B}$ within the material to reduce slightly. The susceptibility, which is a measure of how effective an applied field is for inducing a magnetic dipole, for a diamagnetic material is negative, as can be seen in equation 2.20.

$$\chi = -\frac{N}{V}\frac{\mu_0 e^2}{6m}\sum_i \langle r^2 \rangle \quad 2.20$$

where *N* is the number of atoms, *e* is the charge of an electron, *V* is the volume, *m* is the mass of the electron, and $\langle r \rangle$ is the average orbital radius. With a μ_R value less than one, diamagnetic materials experience a slight repulsive force from permanent magnets and are thus repelled. Examples of diamagnetic materials from tables 2.1 and 2.2 include: bismuth, mercury, copper, water, silver, and carbon dioxide.

2.3.2 Paramagnetic materials

Paramagnetic materials have a net angular momentum arising from unpaired electrons. In bulk material the random orientation of atoms may result in almost no net magnetic moment. In the presence of an external magnetic field, the atomic dipoles in a material will experience a torque which tends to align the magnetic moment to the applied field, producing a small increase in the field $\vec{B}$ inside the material. Upon removal of the applied magnetic fields, these materials return to their initial state. Paramagnetic materials have a value of μ_R slightly greater than one and a positive magnetic susceptibility. Air, tungsten, manganese, oxygen, sodium, and aluminum are examples of paramagnetic materials presented in tables 2.1 and 2.2.

2.3.3 Ferromagnetic materials

Ferromagnetic materials are the ones with the largest relative permeability ($10^3 - 10^5$), exhibiting strong magnetic effects. In order to characterize the properties of a given ferromagnetic material, it is necessary to measure the magnetic induction $\vec{B}$ as a function of $\vec{H}$ over a continuous range of $\vec{H}$ to obtain the hysteresis curve. The term hysteresis, introduced by Ewing, means to lag behind and it is the most common way to represent the bulk magnetic properties of a ferromagnetic material. Alternatively, plots of magnetization $\vec{M}$ against $\vec{H}$ are used, however this contain the same information since $\vec{B} = \mu_0(\vec{H} + \vec{M})$. Figure 2.1 shows the dependence of magnetization on external fields for a ferromagnetic material. With these types of materials, when an external magnetic field is applied, the atomic dipoles align themselves with it. If the field $\vec{H}$ is increased indefinitely the magnetization eventually reaches the saturation magnetization, M_s, a condition where all the magnetic dipoles within the material

are aligned in the direction of the magnetic field $\vec{H}$. The saturation magnetization is dependent on the magnitude of the atomic magnetic moments and the number of atoms per unit of volume. Upon removal of the field, a considerable fraction of the moments are still left aligned, resulting in a remanent magnetization, M_r [7].

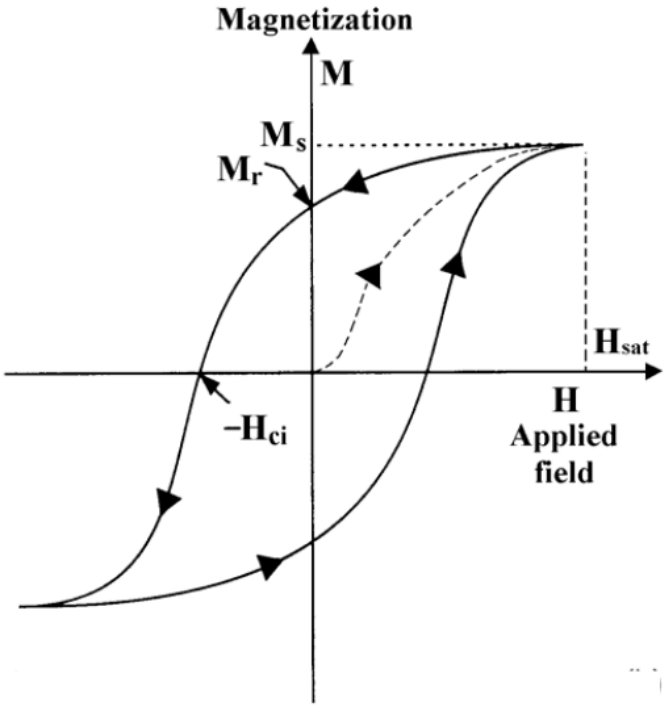

Figure 2.1. *Hysteresis curve for a ferromagnetic material (M vs H)* [8].

This is used to describe the remaining magnetization when the field has been removed after magnetizing to an arbitrary level. Therefore, when a magnetic field is applied to a material that displays ferromagnetic behavior and then removed, the magnetization does not follow the initial magnetization curve and this gives rise to the hysteresis loop of the material. To demagnetize the material it is necessary to apply a magnetic field H_{ci} (intrinsic coercivity) in the opposite direction of magnetization. Ferromagnetic materials are classified as either soft or hard depending on their coercivity which is a structure-sensitive magnetic property.

2.3.3.1 Soft and hard magnetic materials

Soft magnetic materials, for example iron, are characterized by their high permeability and low coercivity (H_c < 1 kA/m), thus these materials can be easily magnetized and demagnetized by external fields. On the other hand, hard magnetic materials, for example permanent magnets, have lower permeability but high coercivity (H_c > 10 kA/m) and large

remanent magnetization. Thus, once magnetized, they retain their magnetization against external fields. The difference between these two materials is illustrated in Figure 2.2.

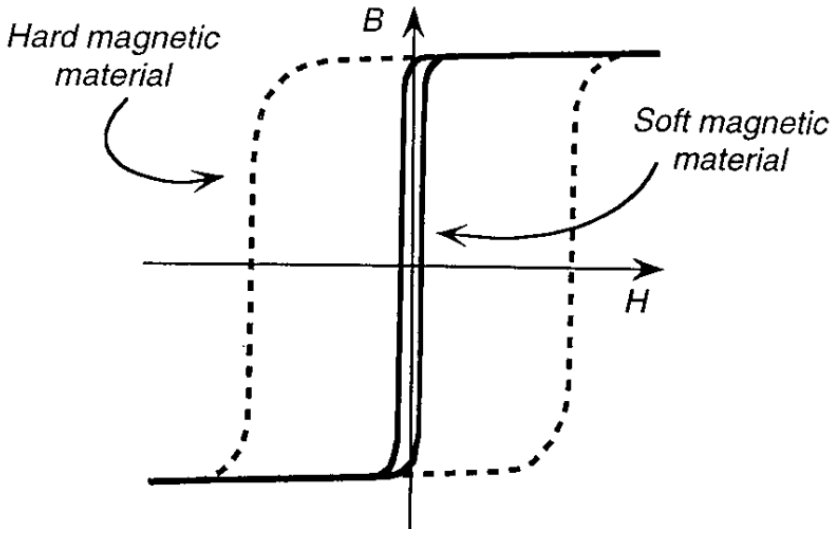

Figure 2.2. *Hysteresis loops for soft and hard magnetic materials* [9].

There are several applications for soft ferromagnetic materials as a result of their ability to enhance the flux produced by an electric current. Their uses are closely connected with electrical applications such as electrical power generation and transmission, receipt of radio signals, microwaves, inductors, relays and electromagnets. The most commonly used soft magnets are soft iron (widely used as a core material for electromagnets), alloys of iron-silicon, nickel-iron, and soft ferrites. When selecting a soft material, the most important properties are its permeability, saturation magnetization, resistance and coercivity.

Hard magnetic materials, due to its characteristics, are suitable for applications such as permanent magnets and magnetic recording media.

2.3.3.1.1 Permanent magnets

A permanent magnet is a passive device used for generating a magnetic field. It is obtained by applying to a hard ferromagnetic material a field pulse that runs from zero up to when saturation induction is obtained, and back to zero. Permanent magnets deliver magnetic flux into a region of space called the *air gap*, with no expenditure of energy.

In recent years, a permanent magnet material based on neodymium-iron-boron has been discovered. This has superior magnetic properties for many applications when compared

with its predecessor samarium-cobalt. As can be seen in table 2.3, its coercivity can be as high as 1120 kA/m compared with 696 kA/m for samarium-cobalt.

In addition to the coercivity another parameter of prime importance to permanent magnet users is the maximum energy product $(BH)_{max}$. This is obtained by finding the maximum value of the product |BH| in the second, or demagnetizing, quadrant of the hysteresis loop. It represents the magnetic energy stored in a permanent magnet material.

The great advantage of permanent magnets is that they maintain a magnetic field without any power input, as it happens with electromagnets. For practical reasons, the field must remain as much as possible unaffected by time, temperature, and imposed outer field variations. These properties can be obtained with the correct choice of ferromagnetic material, which must possess, among other properties: a) A large energy product defined in the upper left quadrant of the hysteresis curve; b) a large value of magnetization M or remnant induction Br; c) a large value of the coercive field H_c (to avoid canceling the remaining induction. Typical parameters of some hard ferromagnetic materials suitable for the construction of permanent magnets are given in Table 2.3. The most important uses of permanent magnets are in electric motors, generators and actuators. In this dissertation, a permanent magnet made of this material was used as the microdevice to be controlled.

Material	*Composition*	*Remanence* (T)	*Coercivity* (kA/m)	$(BH)_{max}$ (kJ/m^3)
Steel	99% Fe, 1% C	0.9	4	1.59
36Co Steel	36% Co, 3.75% W, 5.75% Cr, 0.8% C	0.96	18.25	7.42
Alnico 2	12% Al, 26% Ni, 3% Cu, 63% Fe	0.7	52	13.5
Alnico 5	8% Al, 15% Ni, 24% Co, 3% Cu, 50% Fe	1.2	57.6	40
Alnico DG	8% Al, 15% Ni, 24% Co, 3% Cu, 50% Fe	1.31	56	52
Ba Ferrite	$BaO{\cdot}6Fe_2O_3$	0.395	192	28
PtCo	77% Pt, 23% Co	0.645	344	76
Remalloy	12% Co, 17% Mo, 71% Fe	1.0	18.4	9
Vicalloy	13% V, 52% Co, 35% Fe	1.0	36	24
Samarium–cobalt	$SmCO_5$	0.9	696	160
Neodymium–iron–boron	$Nd_2Fe_{14}B$	1.3	1120	320

Table 2.3 *Important magnetic properties of selected permanent magnet materials* [10].

2.4 Electromagnetic coils

The Bio-Savart Law is an equation used for computing the magnetic field generated at an arbitrary point by a steady current. It states that the magnetic field $\vec{B}$ from a wire length $d\vec{s}$, carrying a steady current I, is given by equation 2.21.

$$\vec{B} = \frac{\mu_0}{4\pi}\int \frac{Id\vec{s}\times\hat{r}}{r^3} \qquad 2.21$$

where μ_0 is the permeability of free space, $\hat{r}$ is the displacement unit vector in the direction pointing from the wire element towards the point at which the field is being calculated and r is the radius. This equation allows the calculation of the magnetic fields for arbitrary current distributions such as circular or rectangular loops.

The magnitude of the magnetic field $\vec{B}$ along an axis through the center of a circular loop as shown in Figure 2.3, carrying steady current I can be expressed as:

$$B(z) = \frac{\mu_0 I R^2 N}{2(r^2+z^2)^{3/2}} \qquad 2.22$$

Where r is the radius of the loop and N is the number of turns in the current loop.

The direction of the magnetic field at the center is perpendicular to the plane of the loop, and the direction is given by the right hand rule for a current loop: fingers curls around the loop in the direction of the current, the thumb points in the direction of the magnetic field at the center of the loop. At the center of the loop (N=1), when *z=0*, the magnetic field is given by equation 2.23.

$$B = \frac{\mu_0 I}{2r} \qquad 2.23$$

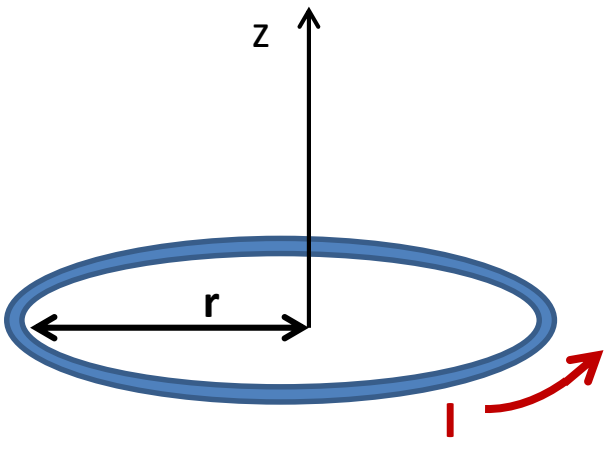

Figure 2.3. *Single circular coil with radius r, carrying an electrical current I.*

2.4.1 Helmholtz and Maxwell Coils

Considering two identical circular loops of radius *r*, separated by a distance *D*, and carrying the same current in the same direction as can be seen in Figure 2.4. The magnetic field produced by these two loops is the sum of the fields produced by the individual loops.

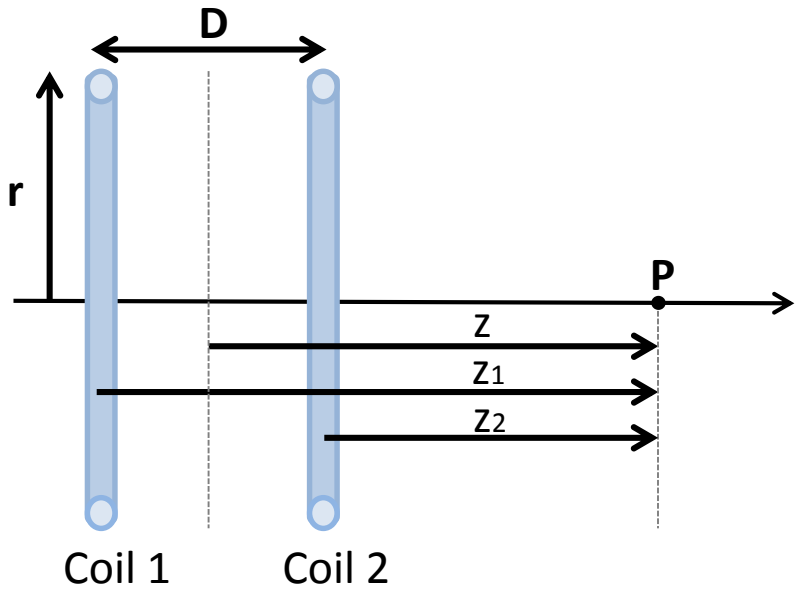

Figure 2.4. *Two identical circular loops with radius r, separated by a distance D, carrying the same current in the same direction. P is an arbitrary point at a distance z from their center, and at distance z1 from coil 1 and distance z2 from coil 2.*

The magnetic field along their axis of symmetry at point *P* at a distance *z* from their center can be determined for each coil and the fields can be added together for the final result. If the currents in each coil are in the same direction, then the fields will complement each other to produce a strengthened magnetic field at each point.

Equation 2.24 can be used to determine the magnetic field of a pair of Helmholtz coils. Applying this equation, the magnetic fields at point *P* will be given by equations 2.24 and 2.25 for coil 1 and coil 2, respectively.

$$B_1 = \frac{\mu_0 NI}{2} \frac{r^2}{(r^2 + z_1^2)^{3/2}} \qquad 2.24$$

$$B_2 = \frac{\mu_0 NI}{2} \frac{r^2}{(r^2 + z_2^2)^{3/2}} \qquad 2.25$$

The total magnetic field at point *P* will be the sum of the fields B_1 and B_2 and with the necessary coordinate transformations the longitudinal component of the magnetic field created by the coil pair at a distance z from the origin is obtained.

$$B_z = \frac{\mu_0 N I r^2}{2}\left(\frac{1}{\left[r^2+\left(\frac{D}{2}-z\right)^2\right]^{3/2}}+\frac{1}{\left[r^2+\left(\frac{D}{2}+z\right)^2\right]^{3/2}}\right) \qquad 2.26$$

Where *r* is the coil radius and D is the distance between the coils. It is possible to find a maximal field at the center *z=0* between the coils. For that it is useful to expand B_z as a Taylor series around this point. For an arbitrary function f(z):

$$f(z_0+h) \approx f(z_0)+hf'(z_0)+\frac{h^2}{2!}f''(z_0)+\cdots+\frac{h^n}{n!}f^{(n)}(z_0) \qquad 2.27$$

It is possible to take the first derivative of Equation 2.26 to find:

$$\frac{dB_z}{dz} = \frac{3\mu_0 N I r^2}{2}\left(\frac{(D/2-z)}{\left[r^2+\left(\frac{D}{2}-z\right)^2\right]^{5/2}}-\frac{(D/2+z)}{\left[r^2+\left(\frac{D}{2}+z\right)^2\right]^{5/2}}\right) \qquad 2.28$$

Which vanishes at z=0 for any *D*. Taking the second derivative:

$$\frac{d^2B_z}{dz^2} = \frac{3\mu_0 N I r^2}{2}\left(\frac{4(d/2-z)^2-r^2}{\left[r^2+\left(\frac{d}{2}-z\right)^2\right]^{7/2}}+\frac{4(d/2+z)^2-r^2}{\left[r^2+\left(\frac{d}{2}+z\right)^2\right]^{7/2}}\right) \qquad 2.29$$

which vanishes at z=0 for D=r. Since the third derivative, like all other odd derivatives, vanished for any *d*, B_z is uniform around *z=0* up to a term of order z^4

$$B_z(z) = B_z(0) + O[(z/d)^4] \qquad 2.30$$

when the distance is chosen to be the same as the radius of the loops. This special configuration is called a Helmholtz coil, invented by Hermann von Helmholtz in the middle of the 19th century. This device, consisting of two identical circular magnetic coils placed symmetrically along a common axis, and separated by a distance equal to the radius of the coil as can be seen in Figure 2.5, generate a uniform constant field of magnitude $B_0 = \frac{\mu_0 I}{r}$, around

the origin. The Helmholtz coil configuration has found applications in MRI as RF coils because of its ability to generate a uniform field in the vicinity of their midpoint. Figure 2.5b shows the magnetic field (B_z) of the Helmholtz coil pair along the axis with coils of radius 5 cm and a current of 1 A.

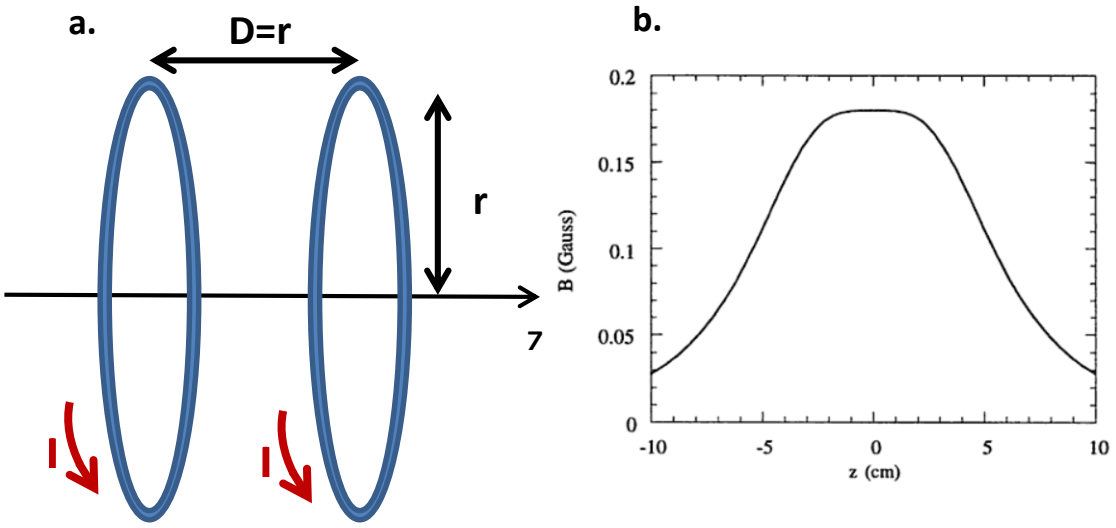

Figure 2.5. *Helmholtz coil pair a) Schematics, b) The magnetic field of the Helmholtz coil pair along the axis with r=5 cm and I=1A (1 Gauss=1*$\times 10^{-4} Tesla$*)* [11].

If the currents in the two loops are in opposite directions, with origin at the center, it is possible to calculate from the Biot-Savart law that the axial field B_z is given by equation 2.31.

$$B_z = \frac{\mu_0 N I r^2}{2}\left(\frac{1}{\left[r^2+\left(\frac{D}{2}-z\right)^2\right]^{3/2}} - \frac{1}{\left[r^2+\left(\frac{D}{2}+z\right)^2\right]^{3/2}}\right) \qquad 2.31$$

From which it is possible to find that B_z, as well as all the even derivatives, vanish at z=0. Its third derivative is found to be:

$$\frac{d^3 B_z}{dz^3} = \frac{15\mu_0 I r^2}{2}\left(\frac{4(\frac{D}{2}-z)^3 - 3\left(\frac{D}{2}-z\right)r^2}{\left[r^2+\left(\frac{D}{2}-z\right)^2\right]^{9/2}} - \frac{4(\frac{D}{2}+z)^3 - 3\left(\frac{D}{2}+z\right)r^2}{\left[r^2+\left(\frac{D}{2}+z\right)^2\right]^{9/2}}\right) \qquad 2.32$$

which vanishes at z=0 for $D = \sqrt{3}a$. At this distance, the first derivative is nonzero, therefore, B_z around z=0 is linear along z up through the fourth power of z, that is:

$$B_z(z) = B_z'(0) + O[(z/d)^5] \qquad 2.33$$

when the distance is chosen to be $\sqrt{3}$ times the radius of the loops. This configuration is called the Maxwell coil configuration, named in honor of the Scottish physicist James Clerk Maxwell. It is a device for producing uniform gradient magnetic flux intensity along its axis and has found applications in MRI as a gradient coil. Figure shows the configuration for a Maxwell coil pair and the resultant magnetic field (B_z) along the axis with coils of radius 5 cm and a current of 1 A.

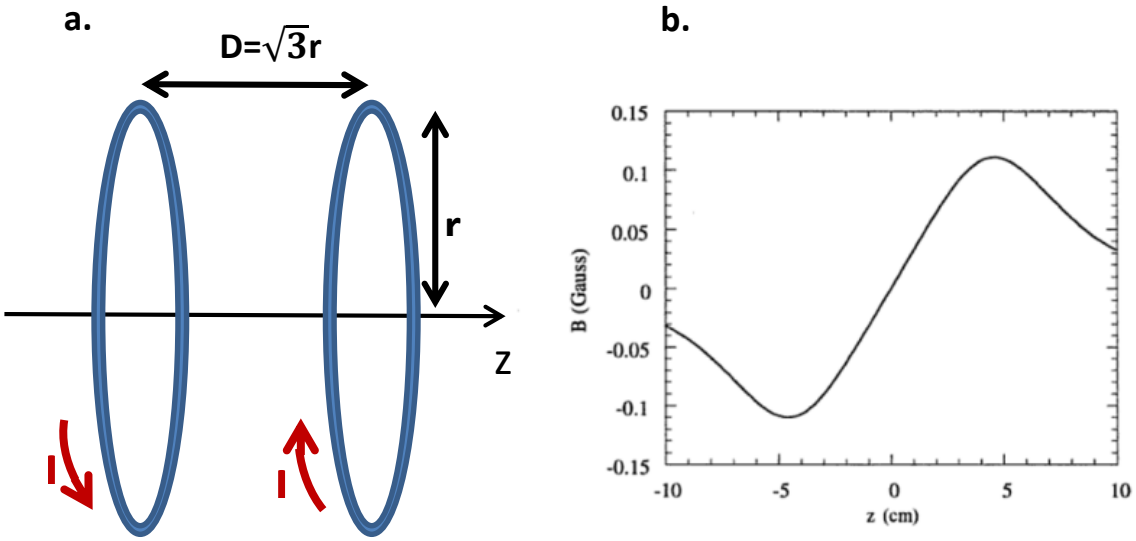

Figure 2.6. *Maxwell coil pair a) Schematics, b) The magnetic field of the Maxwell coil pair along the axis with r=5 cm and I=1A (1 Gauss=1×* $10^{-4}Tesla$*)* [11].

The analysis from this chapter is important for the project since the proposed magnetic actuation systems are based on the Helmholtz and Maxwell coil configurations due to their ability to produce static magnetic fields and constant magnetic gradients, respectively. In the next chapters it will be explained how this can be used to control microrobots.

"Man is the center of the universe. We stand in the middle of infinity between outer and inner space, and there's no limit to either."

-Fantastic Voyage, 1966

Chapter 3

Microrobotics for biomedical applications

In recent years, there have been tremendous advances in the field of microrobotics. Potential applications in this field include minimally invasive diagnosis and treatment inside the human body. In this chapter, a brief review about microrobotics for biomedical applications will be presented.

It is important to start this study with some definitions. First, regarding the term robot. Although literature defines this concept in many ways, in this work it will be defined as a moving device that can make decisions by processing incoming information [12]. Thus, in the future, an untethered robot must not only have the capability to move or travel in blood vessels, but also to obtain and process information, being able to operate within specific constraints. Also, in this work, the field of microrobotics will be considered to include the design and fabrication of robots with characteristic dimensions from 1 micrometer to 1 millimeter (1000 μm) [13].

This chapter will start off with a brief introduction about the field of microrobotics with focus on the potential applications of microrobots in biomedicine. Afterwards, a review of the previous work related to wireless magnetic actuation will be presented. The principles governing the actuation of these devices rely on an understating of microscale physics. In this chapter, the forces acting on a microdevice navigating in the blood vessels, when subjected to a magnetic field will be presented in detail. Finally, localization *in vivo* of microrobots, required for feedback control and safety, will be discussed.

3.1 Introduction

It can be predicted that Micro-Electro-Mechanical-Systems (MEMS) technology will have an important impact in minimally invasive surgical techniques by providing untethered biomedical microrobots capable of performing new medical procedures in the human body. This idea was first presented by the physicist Richard Feynman, in 1959, in his famous lectures [14], wherein he introduced the world to the concept of "swallowing the doctor" which involved building small, swallowable surgical robots*. In 1966, the sci-fi movie *Fantastic Voyage* was released. In the movie, a team of scientists and their submarine are miniaturized and injected into the blood vessels of a dying man with the intention of treating a blood clot. Since its release almost 50 years ago, countless references to this film have been made in literature.

Interest in microrobotics grew rapidly in recent decades, parallel with advances in MEMS, and the results of several research groups suggest that microrobots for biomedical applications will not remain in the realm of science fiction much longer. The first studies in untethered robots were made in the 90's, such as a swimming mechanism composed of a small magnet attached to a spiral wire [15]. In recent years, there has been significant progress especially in miniature robots (usually with a few centimeters) for use in the gastrointestinal (GI) tract [16]. Motivated by the capsule endoscopes already in clinical use, several researchers started exploring ways of expanding the capabilities of these devices, ranging from lab-on-a-chip applications equipped with several sensors (for pressure, pH, temperature) to new possible ways of locomotion. Other groups have started exploring the possibility of using smaller devices, at the microscale, in other locations in the human body. Microrobots, because of their dimensions can navigate in very narrow spaces such as blood vessels. This gives rise to a vast array of potential applications, mainly related to *in vivo* biomedical applications and therapy.

As the devices are scaled down to the microscale, one important concept is related to the types of physical interactions which dominate the motion and interaction of the robot. Briefly, in the case of centi/milli-scale robots the main forces are inertial and other bulk forces, while the motion of micro-scale robots is dominated by surface area-related forces (friction, adhesion, drag and viscous forces).

*According to Feynman, it was his friend and graduate student Albert Hibbs who originally suggested to him the idea of a medical use for his theoretical micromachines.

At sizes below tens of micrometers, effects such as Brownian motion and chemical interactions have to be considered. This is the case of nanorobots, which will not be discussed in this thesis. Nanorobots are generally envisioned as devices to target individual cells and most proposed nanosized devices are more like pharmaceuticals and less like machines, using concepts from synthetic biology and requiring large numbers to complete a task [17].

In this work, microrobots are defined as being in the size range of single to a thousand of micrometers. Thus, it is considered that they are being dominated by micro-scale physical forces and effects (this analysis will be made in detail in chapter 3.4.2). This size range presents several challenges, not only in fabrication but also in actuation and power supply. Miniature on-board power sources are one of the main problems of miniature robots, since at present there are no feasible on-board power sources for millimeter-scale robots. Also, although miniaturized actuators have been proposed, their employment for actuation of microrobots is still a problem. In chapter 3.3 this problematic will be discussed in more detail and some solutions will be explored.

In general, there is a need to take a different perspective on microrobot design and control when comparing to traditional macroscopic robots. However, even with this difficulties, this is an exciting new field and preliminary experimental results are demonstrating their feasibility for several applications. These potential applications include mobile sensor networks, micro-factories, microfluidics, bioengineering and healthcare. In this thesis, we are interested in exploring the latter.

3.2 Potential applications of medical microrobots*

According to Nelson *et al.* in [17], the trend in medicine is towards smaller devices and components to reduce recovery times and risks for the patients. Remote microrobots can offer a means for advanced diagnostics and therapeutic procedures inside the human body. Some of the potential application areas for medical microrobots are shown in figure 3.1. Progress in other potential medical application areas will come with the refinement of microrobot motion strategies in 3-dimensional liquid environments and with the development of relevant integrated microtools.

*This chapter follows loosely the paper [17] from Nelson *et al.*

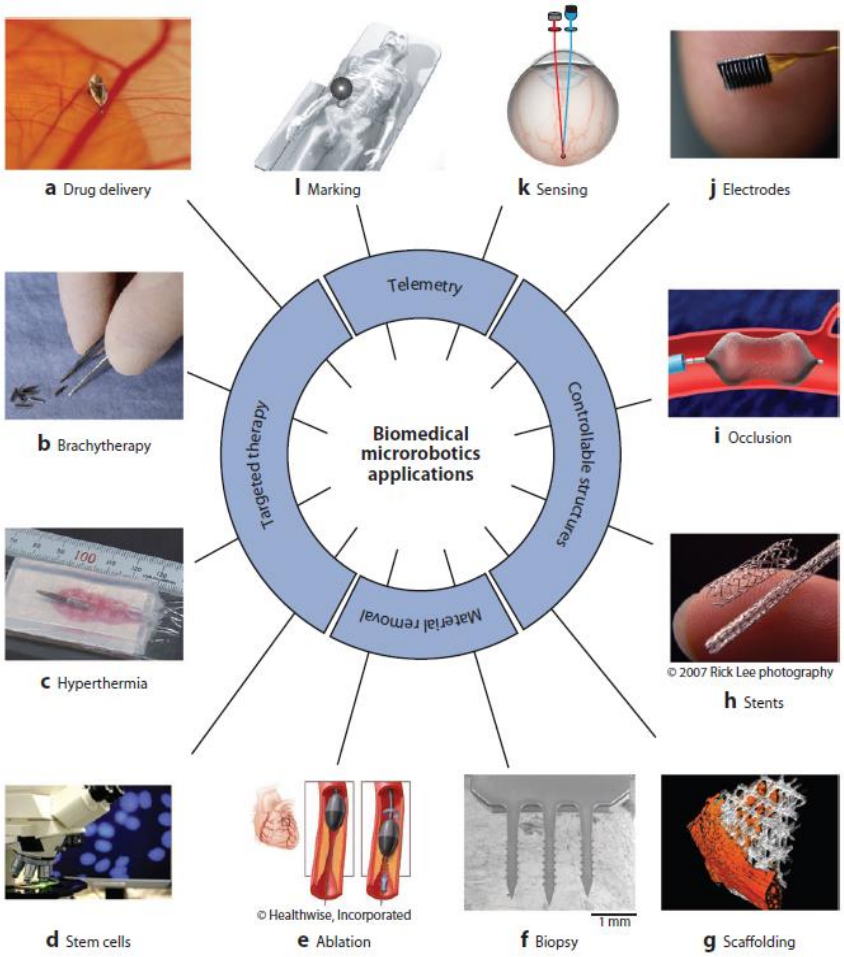

Figure 3.1 *Examples of possible biomedical microrobotics applications, including targeted therapy, telemetry, controllable structures and material removal* [17].

3.2.1 Basic functions

Some simple tasks could be achieved with the use of biomedical microrobots. In the following sections possible tasks for medical microrobots are presented.

3.2.1.1 Targeted therapy

One of the main potential applications for microrobots is targeted therapy allowing the localized delivery of chemical and biological substances or other forms of energy. Possible therapeutic uses for microrobots include:

- Drug delivery. With this approach a pharmaceutical compound is transported in the blood vessels to safely achieve its target and performing the desired therapeutic effect, thus reducing the side effects in the rest of the body.
- Brachytherapy (internal radiotherapy). This is a form of radiotherapy where a radioactive source is placed inside or next to the area needing treatment. The radiated energy results in the destruction of the cells surrounding the radioactive source.
- Hyperthermia. This is a technique involving the selective deactivation of cancer cells by heating the damaged areas in the temperature range of 42- 45 ºC. The adverse side effects from conventional therapies and the resulting patient discomfort have encouraged researchers to explore these site-specific therapies using magnetic nanoparticles.
- Stem cell therapies. Stem cells are undifferentiated biological cells that can differentiate into specialized cells or divide to produce more stem cells. They hold enormous potential for future therapies and there's a possibility that microrobotic assistance will be needed.

3.2.1.2 Material removal

Another potential application of microrobots is to remove biological material by mechanical means. Possible methods of material removal using microrobots include:

- Ablation. This process consists on the removal of material from the surface of an object by erosive processes. This can be achieved using the rotary motion of microrobots, which could be useful, for example, in the treatment for atherosclerosis through the removal of fatty deposits from the internal walls of blood vessels. It could also be possible to use ultrasound ablation, in which the microrobot uses a resonating mechanical structure to emit ultrasonic pressure waves to destroy an object such as a kidney stone.
- Biopsy. This is an intervention involving sampling of cells or tissues for examination. This intervention could be performed by microrobots. Also, in the future, it could also be possible to combine the excision with remote-sensing technology. Thus, the sample could be analyzed *in situ*.

3.2.1.3 Controllable structures

It could also be possible to use microrobots as simple structures whose positions are controllable. Some examples of this type of applications include:

- Tissue scaffolds, which act as cell support frames. The microrobot itself can act as a scaffold, or the microrobots can deploy the building blocks which will act as a scaffold.
- Stents. These are mesh tubes inserted into a natural passage in the body to prevent or counteract a disease-induced, localized flow constriction. A stent can be used, for example, to keep blood flowing through a clogged vessel. The microrobot could serve as a stent and would navigate and deploy in the targeted location.
- Occlusions. This can be introduced to intentionally block a passageway. A potential future application could be to use microrobots which could function as occlusions, for example, to clog a blood vessel that nourishes a tumor.
- Electrodes for medical purposes. These electrical conductors can be introduced by microrobots, which could operate wirelessly. The microrobot could act as a permanent or temporary implant which could be useful for many purposes, for example, for brain stimulation.

3.2.1.4 Telemetry

Telemetry is the communication process in which measurements are made and other data collected at remote or inaccessible points and transmitted to receiving equipment for monitoring. Microrobots can be used to transmit information that otherwise would be difficult (or impossible) to obtain. Some of the applications of microrobots in the area of telemetry include:

- Remote sensing. Microrobots could transmit the time history of a physical signal of interest or transmit a simple binary signal upon detecting the presence of an analyte of interest.
- Marking a specific location. This could be useful specially when combined with remote sensing to localize unknown internal phenomena (for example, bleeding). To perform this task, the microrobots must be able not only to sense and transmit information but also to maintain its location at the site.

3.2.2 Application Areas

Some of the targeted areas of the body could include the circulatory system, central nervous system, urinary tract, and the eye.

3.2.2.1 Circulatory system

The essential components of the human circulatory system are the heart, blood, and blood vessels. The blood vessels are the conduits responsible for the transport of the blood throughout the body. The three major types of blood vessels are: the arteries, which carry the blood away from the heart, the capillaries, which enable the exchanges of substances between the blood and the tissues, and the veins, which carry blood from the capillaries back toward the heart. Figure 3.2 shows a schematic representation of various types of blood vessels, with the inner diameter, average blood-flow speed and Reynolds number. The Reynolds number is a dimensionless number that relates the effects of inertial forces to those of viscous forces on a fluid and it is used to determine the flow regime of the flow (laminar or turbulent). Generally, in the body, blood flow is laminar; however, under conditions of high flow, laminar flow can be disrupted and become turbulent. When this happens, blood does not flow linearly and smoothly in adjacent layers, but instead the flow can be described as being chaotic [18].

The circulatory system could be the most important application area for wireless microrobots since nearly every site of the body can be accessed by the blood vessels. Some possible applications are target drug delivery, lysis of blood clots (thrombolysis) and the use of microrobots acting as stents to maintain blood flow.

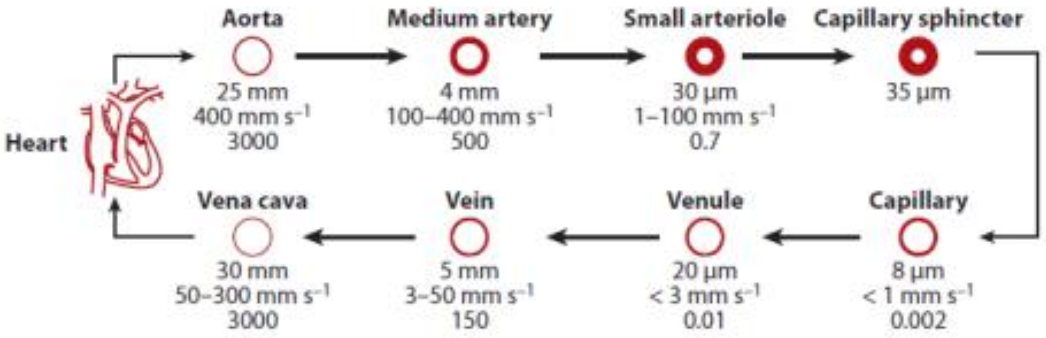

Figure 3.2 *Schematic representation of the vessels of the cardiovascular system, with the inner diameter, average blow-flow speed, and Reynolds number from Berger et al* [19].

3.2.2.2 Central nervous system

The central nervous system consists of two major structures: the brain and the spinal cord. These structures are bathed in the cerebrospinal fluid, a colorless body fluid with properties similar to water. It acts as a cushion or buffer for the brain's cortex, providing a mechanical and immunological protection to the brain. The cerebrospinal fluid occupies the subarachnoid space and the ventricular system around and inside the brain and spinal cord. It constitutes the content of ventricles, cisterns, and sulci of the brain, as well as the central canal of the spinal cord. These structures can be seen in figure 3.3.

Craniotomy is a surgical operation in which a bone flap is temporarily removed from the skull to access the brain. This type of procedure is highly invasive, usually performed on patients who are suffering from brain lesions. This procedure can also allow doctors to surgically implant deep brain stimulators for the treatment of epilepsy and Parkinson's disease. Untethered microrobots have the potential to dramatically affect central nervous system interventions. For example, it could be possible to insert a microrobot in the subarachnoid space, in a similar process to the lumbar puncture and navigate the device to the brain for intervention. This procedure would be much less invasive. Recently, in [20], this concept of using percutaneous intraspinal navigation was applied to brain surgery, using catheters.

Research has been made to develop wireless manipulation of magnetic seeds in the brain for the purpose of hyperthermia [21]. Also, in [22], Kósa *et al.* proposed a swimming microrobot for endoscopic procedures in the subarachnoid space of the spine. In [23], the use of several MEMS devices for neurosurgery which could be incorporated into a wireless microrobot was proposed.

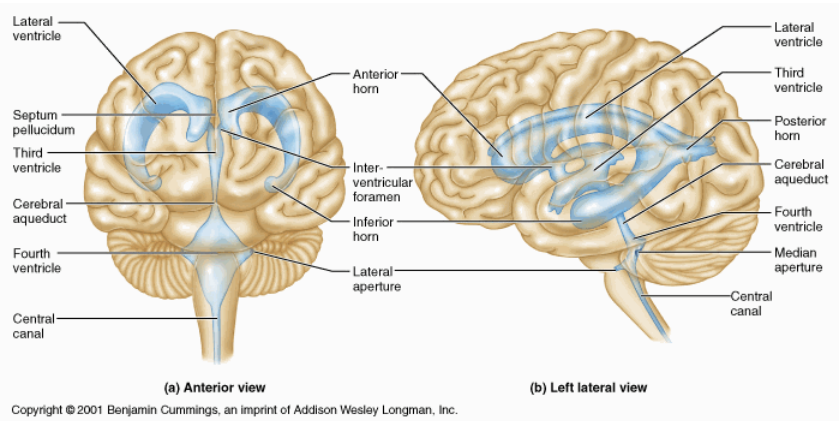

Figure 3.3 *Schematic representation of the ventricle system, a set of cavities in the brain where the cerebrospinal fluid is produced* [24].

3.2.2.3 Urinary system and prostate

The urinary system consists of the two kidneys, ureters, the bladder, and the urethra. In [25], Edd *et al.* proposed a microrobot that could swim up the ureter and destroy kidney stones. This process could have several potential benefits and would result in less harm to the kidneys. Also, MEMS devices designed for use in urology could be incorporated in the microdevices [26].

Another potential application for biomedical microrobots is in the treatment of prostate cancer. The current treatments may involve surgery (radical prostatectomy) and radiation therapy including brachytherapy. This involves the insertion of a needle through the perineum which is a difficult process in part due to the fact that the prostate deforms and moves due to the force of the needle. As a result, the radioactive seed may be released in a location different than planned. Also, during the insertion of the needle there is a risk of damaging to the surrounding nerves. An untethered microrobot could offer a minimally invasive access to the prostate though the urethra and carry a radioactive seed to the tumor site, improving the effectiveness and reducing the chances of nerve damage.

3.2.2.4 The eye

The human eye is made of three layers. The outermost layer is composed of the cornea and sclera, the middle layer consists of the choroid, ciliary body and iris and the innermost layer is the retina. It is in the latter structure that the microrobots could be more promising since retina health is critical for vision and current retinal microsurgery is both difficult and risky.

Some of the possible applications of intraocular microrobots are therapies for retinal vein occlusions, detached retinas, and epiretinal membranes, as well as diagnosis.

In [27], Yesin *et al.* proposed a microrobot for intraocular procedures, controlled wireless with magnetic fields and visually tracked through the pupil. In [28], Dogangil *et al.* proposed a method of targeted drug delivery based on diffusion from a surface-coated microrobot. In [29], Hollingan *et al.* proposed magnetic particles in the form of ferrofluid to act as a tamponading agent in magnetic fluid therapies designed to alleviate retinal detachments and other types of retinopathy.

3.3 Power and Actuation methods

Power supply for microrobots is a challenging research topic. Powering techniques can be classified into three main categories: on-board, scavenged, and transmitted [30]. On-board power supplies consist on the miniaturization of existing macro scaled generators (for example, batteries). Batteries offer an inexpensive power source, however, the integration and use of these sources smaller than 1 mm in size for untethered microrobots have yet to be done [31]. The total deliverable energy provided by on-board power sources typically scale with the volume of the power source which is an obstacle to achieving functional microrobots.

MEMS-based power generators can be an interesting approach since they provide higher energy densities than traditional generators and batteries [32]. Several research groups have developed transducers to convert various types of energy into electrical energy. There are also designs that harvest thermal energy from the environment as well as designs that scavenge mechanical energy through the form of vibrations from the environment. Other interesting option could be the use of a microrobot to harvest chemical energy directly from the biochemical environment using a similar approach to bacteria. For example, a microrobot inside the human body could use the glucose in the blood to power simple circuits using a biofuel cell [33].

In contrast to carrying or producing energy on-board, it is possible to wirelessly transmit power to the device. Using inductive coupling, it is possible to convert the energy of an alternating magnetic field into electrical power, based on Faraday's Law of induction (equation 2.3). With this method, when current flows in a primary circuit, a magnetic field is generated in its surroundings and an effective voltage source develops in the nearby secondary circuits. The challenge with this approach it is the design of the receiver coil at the microscale since it is constrained by planar microfabrication processes.

Rather than converting an external magnetic field into electricity, the field can be used directly to actuate a microrobot. By fabricating parts of the microrobot out of a ferromagnetic material, it will experience torques related to the field strength and its own magnetization and magnetic forces related to the magnetic field gradient, the body magnetization and its volume. This approach will be discussed in detail in the next chapters.

3.4 Wireless Magnetic actuation

Magnetic actuation is widely used for remote microrobot power and control. Due to their ability to penetrate most materials, magnetic fields are naturally suited to control microscale objects in remote, inaccessible spaces.

Magnetizable particles experience a force in a nonuniform magnetic field, a process called magnetophoresis, which has been exploited in a variety of industrial and commercial processes for separation and beneficiation of solids suspended in liquids. The next section will start with the state-of-art in wireless magnetic actuation followed by an analysis of the physics behind this phenomenon. To finish, some other aspects including approaches for microrobot localization will be discussed.

3.4.1 State-of-the-art

The concept of magnetic guidance for biomedical applications is not a new area of research. Actually, it has been studied for more than fifty years. In these early studies, aneurysm embolization was based on powders formed by iron microparticles confined within magnetic-tipped catheters [34]. In the eighties, a project named Video Tumor Fighter (VTF) aimed at controlling a ferromagnetic cylinder through brain tissue, using an external electromagnet, so that it could reach a brain tumor [21], [35]. The propulsion of the cylinder was achieved using induction coils and, once penetrated in the tumor, eddy currents heated it in a process called hyperthermia. Since then, many other applications have been investigated, including magnetic drug delivery with carriers that evolved into state-of-the-art nanoparticles [36]–[38]. Indeed, over the years, most of the research seemed to have been placed on the development of these particles while the targeting and tracking methods remained almost unchanged. More recently, state-of-the-art methods for targeting the magnetic particles have been developed.

At present, the most common magnetic targeting strategy relies on attracting circulating magnetic particles to a selected region of the body, using external permanent magnets placed next to the tissue to be targeted. This approach as several advantages since permanent magnets are cheap, portable, widely available and produce high static magnetic fields and high magnetic field gradients. However, although state-of-the-art magnetic carriers are available, this classical magnetic targeting approach has several limitations. The main

drawback of this technique is that it is limited to organs that are close to the surface of the skin, as demonstrated by Grief and Richardson in [39]. Another problem with permanent magnets is their inflexible fields. Unlike electromagnets where it is possible to change the field by changing the currents, a permanent magnet has to be physically moved to alter the field in a specific point. Also, the use of external magnets does not allow precise control over the trajectory of the magnetic particles. Some improvements over classical magnetic targeting include the use of magnetic needles, wires or stents to reach internal organs [40]–[42]. However, with these methods the distribution of the particles is not fully controlled. To overcome these problems and achieve a more precise magnetic targeting, in recent years, two main approaches for the control magnetic devices have been proposed: one approach is the use of an MRI system and other is the use of custom-built apparatus.

3.4.1.1 MRI systems for propulsion

The use of MRI gradient coils for magnetic actuation has been pioneered since 2003 by Sylvain Martel at École Polytechnique of Montréal, Canada. This approach has several advantages since it provides the imaging modality, making the observation of the device position possible and, at the same time, the actuation of the particles by generating magnetic gradients. Also, MRI devices are widely available in hospitals. Figure 3.4a depicts an experimental setup installed inside a 1.5 T Siemens Magnetom Vision MRI bore. In this example, the goal was to use the system to provide the driving force in three dimensions to a ferromagnetic core that could be embedded on a specialized microdevice [43].

The use of a clinical MRI scanner to direct the motion of magnetic devices is well developed at millimeter scale, since low-level multiplexed controllers and observers have been developed and *in-vivo* experiments have since been performed on living animals. In [44], automatic control of an untethered millimeter sized bead was achieved in the carotid artery of a live swine. Figure 3.4b depicts the *in vivo* navigation of a 1.5 mm ferromagnetic bead inside the carotid artery of the living swine. The trajectories were superimposed over an x-ray angiography, with the line of dots over the artery showing actual displacement of the bead, and the arrow showing the direction of the displacement. However, it is interesting to note that, in this experience, the blood flow has been stopped using a balloon catheter.

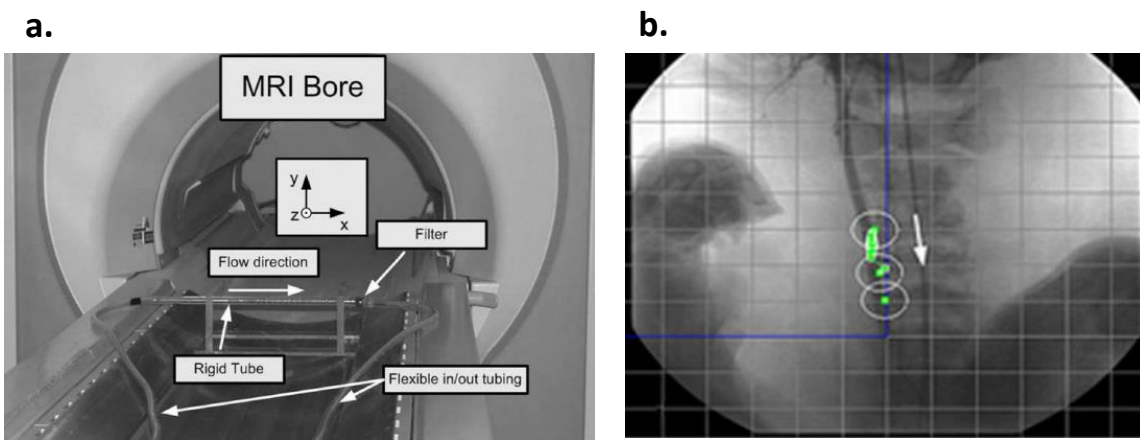

Figure 3.4 a) *Preliminary experimental setup installed inside a 1.5T Siemens Magnetom Vision MRI bore* [43]*;* ***b)*** *In vivo automatic navigation of a 1.5-mm ferromagnetic bead inside the carotid artery of a living swine. The trajectories are superimposed over an X-ray angiography* [44].

The main drawback of this approach results from the limitations on the magnetic gradient amplitude in available MRI systems. The most severe technical challenges are encountered when working with particles with diameters smaller than a few dozens of micrometers. At this scale, the magnetic gradients have to be higher than those generated by clinical MRIs to efficiently propel the particles against the drag force. Currently, research groups investigate approaches for increasing the magnetic forces acting on the magnetic particles. To overcome these problems, one of the approaches is the use of additional coils to achieve higher gradients. MRI systems upgraded with these additional gradient steering coils in order to increase the standard gradient amplitudes to values in the range of 100-500 mT/m is currently being investigated [45, 46]. One different approach to overcome the limitations of the clinical MRI is based on the aggregation properties of the magnetic particles, leading to an increase in the magnetic volume, which in turn gives rise to larger ratio of magnetic forces over drag forces [47]. An alternative to this method is to encapsulate drug molecules and magnetic nanoparticles into larger biodegradable polymer microcarries. This approach is followed in [48] where the MRI scanner (with additional steering coils) steers the polymer microcarriers in the blood vessels near the tumor and embolizes the surrounding capillaries. The embolized polymer carriers biodegrade and release the encapsulated therapeutic agents, which are then directed into the tumor. It is expected that the maximum targeting efficacy will be achieved with a combination of these different approaches.

Other important limitation of this approach is the spatial resolution of the current clinical MRIs, especially within real-time constraints [49]. In [44] it was demonstrated that these systems are compatible with real-time control loops for larger millimeter-scaled robots, with a tracking routine within 20 ms. However, controlling particles at smaller scales is a challenging issue with real-time imaging limitations. As already mentioned, the use of an MRI system makes endovascular navigation possible through the integration of propulsion and tracking events. The main drawback of MRI localization is that the choice of material for the magnetic device is limited. Ferromagnetic objects create imaging artifacts that can be larger than the object itself. Depending on size and object of the device, these artifacts can be accounted for in software, requiring software modifications or additions to the commercially available MRI systems [50]. Also, MRI systems are designed for periodic imaging and they cannot provide large duty cycles with high magnetic field gradients. The resultant significant heat dissipation of the gradient coils is a major practical constraint. Thus, for continuous microrobot propulsion, the system must be operated below its maximum achievable gradient field.

3.4.1.2 Custom built apparatus

An alternative to the use of an MRI systems is the use of custom-built apparatus capable of controlling magnetic microdevices. In 1996, Ishiyama *et al.* at Tohoku University developed a magnetic propulsion system for controlling millimeter-sized devices in the human body [15]. The proposed millidevice consisted of a spiral structure containing a permanent magnet. By applying an external rotational magnetic field produced by three pairs of Helmholtz coils, the millidevice rotated around its main axis and it was able to penetrate the tissues. This group published numerous papers showing the application of these screw-type structures in muscle tissue or inside the gastrointestinal tract [51]–[53]. However, due to their main focus on the gastrointestinal tract, no further miniaturization was attempted.

Only in 2007, following the previous example and the primary studies using magnetic gradients from an MRI to propel a microdevice in the blood vessels, a group from ETH Zurich successfully demonstrated the first microscale custom-built prototype. The magnetic propulsion and steering of microparticles has been employed by Nelson *et al.* in [27] where the magnetic torque and force acting on a microdevice were induced independently by Maxwell and Helmholtz coils respectively (Figure 3.5a). Thus, the orientation and direction of motion of

the microrobot were commanded on a 2-dimensional plane. However, this approach used optical tracking so, without modifications, it can only be considered for a few medical interventions where line of sight is possible. This group also proposed a microrobot that mimicked the propulsion mechanism of *E.coli* bacteria [54]. The spiral type microrobot was rotated by an external rotational magnetic flux, and the rotation generated the propulsion force. However, this produced force was very small and could not overcome the force of the blood flow.

Since the custom- built prototype from Nelson *et al.* has been proposed, several groups have been studying the feasibility of these types of apparatus, with different designs being presented [55-56]. In [57], the authors proposed a platform which they called electromagnetic actuation system (EMA; this term is adopted throughout this dissertation). This device is based on a pair of stationary Helmholtz-Maxwell coils and a pair of rotational Helmholtz-Maxwell coils for manipulation of a microrobot in a 3-dimensional space (Figure 3.5b). As in [27], the uniform magnetic flux density was provided by the Helmholtz coils and the gradients were provided by the Maxwell coils. The advantage of these types of approaches is that the torque acting on the microrobot is not constrained to a single direction, as it happens with an MRI-based actuation system with one fixed Helmholtz coil. This can be an advantage when using shape-anisotropic microrobots, but it is not significant for spherical devices. The EMA system has several advantages that may prove to be suitable for specific types of interventions especially in larger blood vessels.

Another promising project is the OctoMag system with eight electromagnets, which enables a microrobot to perform a 5-DOF motion [58]. This system achieves a high level of wireless control with the use of non-uniform magnetic fields, by exploiting linear representations of coupled field distributions of various soft-magnetic-core electromagnets. This system can be scaled up for human intervention and can produce high magnetic gradients for microparticle control.

The strongest reported electromagnetic field gradient for magnetic drug targeting applications was developed by Alexiou *et al.* in [59], which reached a maximum of 100T/m in a volume of 20mm^3. An important challenge in this research seems to be the difficulty in generating high magnetic field gradients over a large volume.

All the mentioned custom built apparatus have two main disadvantages when compared to an MRI-bases platform, namely, they produce much lower static magnetic fields at the center of the workspace which may result in a relatively low induced magnetic force.

Also, the MR-imaging during the interventions would have to be replaced by other medical imaging modalities without enhanced tissue contrast.

In Figure 3.5 several approaches for magnetic actuation of microrobots are showed, namely the 2-dimensional actuation system proposed by Yesin *et al.* (figure 3.4a), the 3-dimensional actuation system proposed by Jeong *et al.* (figure 3.4b), and the Octomag (figure 3.4c).

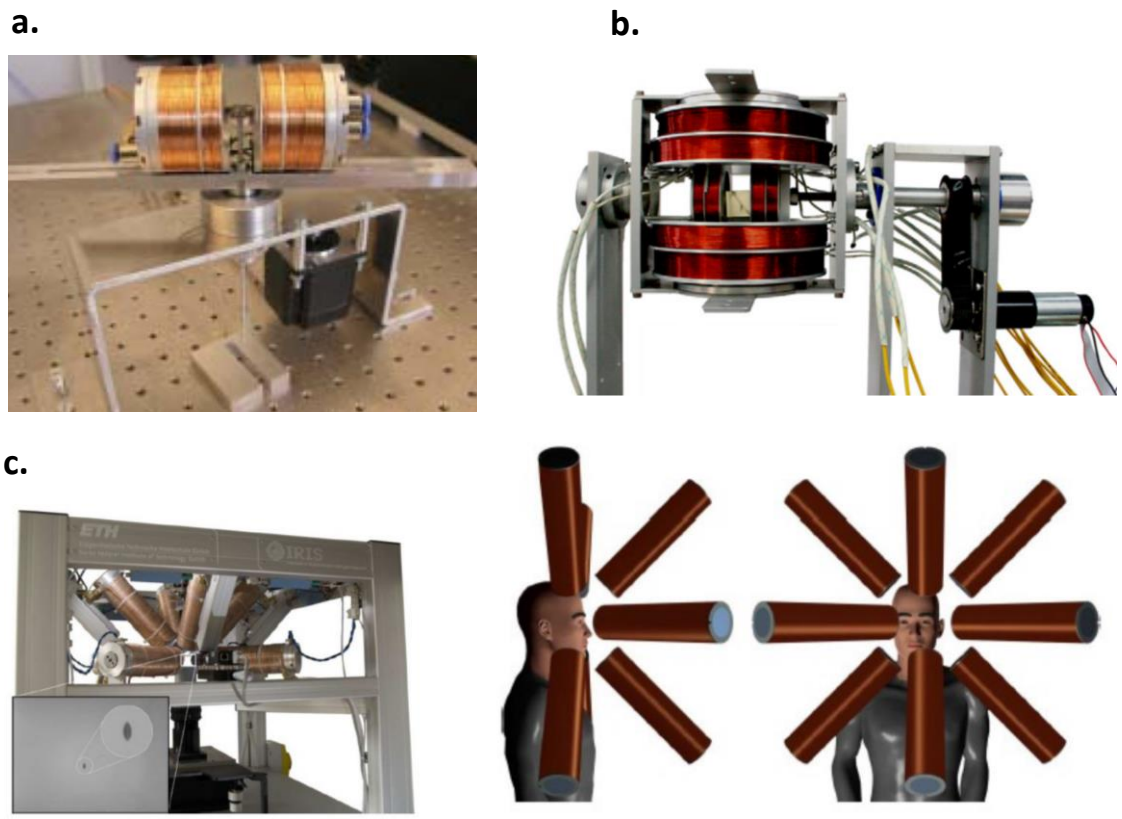

Figure 3.5 a) *Electromagnetic actuation system proposed by Jeong et al.* [57]*,* ***b)*** *2-dimensional actuation system proposed by Yesin et al.* [27] ***c)*** *Real image and concept image of OctoMag electromagnetic system for the control of intraocular microrobots* [58].

3.4.1.3 Modeling and Computational Tools

Modeling untethered microrobots and their complex interactions with the blood flow and vessel walls is an important but also challenging topic. Magnetic drug delivery is not only a multiphysics process involving various physical domains (for example, magnetic fields and fluid dynamics), but it is also a multiscale process, ranging from the millimetric-size of some blood

vessels to the nano- or microsize depending on the considered particles. Due to this complexity, there is not a complete modeling framework for simulating the entire process, since this would require the integration of multiparticle simulation, molecular simulation, continuum-based models, stochastic methods and nanomechanics [60]. A number of deterministic dynamic modeling approaches for magnetic targeting have been developed [61]–[64]. However, the critical physical parameters of endovascular navigation can be determined in simplified models where the magnetic particle is subjected to the forces described in Section 3.4.2.

It is possible to simulate molecular and atomic scales using molecular dynamics tools, while sizes greater than 500 nm are modeled using finite element modeling (FEM) or using computational fluid dynamics (CFD) simulations. These approaches are suitable when accurate modeling is a primary concern. However, there are no systematic simulation environments for studying, for example, the dynamics of dispersed particles in a fluid.

A macroscale approach has been followed in [65] where 3-dimensional computational simulations were performed of blood flow and magnetic particle motion in a left coronary artery and carotid artery, using the properties of presently available magnetic carriers and strong superconducting magnets. Other approach has been adopted in [62] where a 2-dimensional simulation platform for magnetic targeting of microparticles has been designed and developed. The simulation platform was based on discrete element modeling techniques and predicts the size and geometry of resulting aggregations, and their response, during magnetic propulsion using an MRI system.

In the future, planning a reliable and feasible path against the blood flow and vessel networks will be an important issue to be addressed for innovative microrobotics for biomedical applications. This will require better modeling tools and specific algorithms will have to be developed.

3.4.2 Forces acting on a microdevice

The purpose of this section is to present a simplified model of a homogeneous spherical ferromagnetic device with a high saturation magnetization in a blood vessel. The preponderant forces acting on the device are the magnetic force provided by the magnetic system ($\overrightarrow{F_m}$), the drag force applied by the blood flow ($\overrightarrow{F_d}$) and the apparent weight ($\overrightarrow{W_a}$) [66]. These different forces acting on the magnetic device can be seen in the diagram from Figure 3.6. Contact forces between particles were neglected in the following theoretical analysis, however, this parameter has been studied in detail by Panagiotis Vartholomeos in [62].

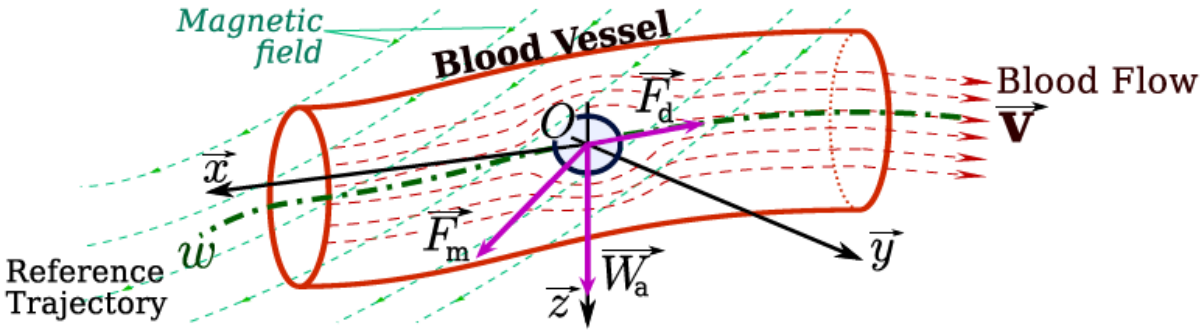

Figure 3.6. *Forces applied on the microdevice navigating in a blood vessel* [67].

3.4.2.1 Magnetic Force and Torque*

A general formula for the force on a magnetic dipole due to a varying magnetic field is given by equation 3.1.

$$\vec{F}_m = \mu_0(\vec{m} \cdot \nabla)\vec{H} \qquad 3.1$$

where μ is the permeability of the medium, m is the dipole moment (A.m^2) and $\vec{H}$ is the applied magnetic field intensity (A/m). It is also possible to express the applied magnetic field as an applied magnetic flux density $\vec{B}$ with units Tesla (T) to obtain equation 3.2.

$$\vec{F}_m = (\vec{m} \cdot \nabla)\vec{B} \qquad 3.2$$

*This chapter follows the book *Electromechanics of Particles* from Thomas B. Jones [68]

If the particle is in free space, $\vec{m} = V\vec{M}$ and equations 3.1 and 3.2 give rise to the usual form (equation 3.3 and equation 3.4) for the magnetic force.

$$\vec{F}_m = \mu_0 \mathrm{V}(\vec{M} \cdot \nabla)\vec{H} \quad 3.3$$

$$\vec{F}_m = \mathrm{V}(\vec{M} \cdot \nabla)\vec{B} \quad 3.4$$

where V is the magnetic volume of the object (m^3) and $\vec{M}$ is the magnetization of the microrobot (A/m^2).

3.4.2.1.1 Magnetic dipole moment

First, a homogeneous sphere with radius R and net magnetic polarization $\overrightarrow{M_1}$ suspended in a magnetically linear fluid of magnetic permeability μ_2 and subjected to an externally magnetic field intensity vector $\overrightarrow{H_0}$ will be considered. In chapter 2.2 the relationship between the flux density $\vec{B}$, the volume magnetization $\vec{M}$, and the magnetic intensity $\vec{H}$, were reviewed and it is important to consider in the present analysis.

$$\vec{B} = \mu_0(\vec{H} + \vec{M}) \quad 3.5$$

Equation 3.5 is general thus it allows consideration of any type of magnetic material (paramagnetic, diamagnetic or ferromagnetic). In this analysis it is assumed that $\overrightarrow{M_1} || \overrightarrow{H_0}$ and that there is no electric current flow. Thus, the equation 2.5 from chapter 2 is considered to be valid (magnetostatics problem) and can be solved using a scalar potential φ, defined by $\vec{H} = -\nabla\varphi$. The assumed solutions for the potential outside $\varphi_1$and inside $\varphi_2$the sphere take the form of equations 3.6 and 3.7, respectively.

$$\varphi_1(r,\theta) = -H_0 r\cos\theta + \frac{A\cos\theta}{r^2}, \quad r > R \quad 3.6$$

$$\varphi_2(r,\theta) = -Br\cos\theta\,, \quad r < R \quad 3.7$$

where A and B are unknown coefficients to be determined using boundary conditions. This conditions are applied at r=R, the surface of the particle. First, the magnetostatic potential must be continuous across the particle-fluid boundary:

$$\varphi_1(r = R,\theta) = \varphi_2(r = R,\theta) \quad 3.8$$

Second, the magnetic flux density must be continuous across the boundary.

$$\mu_2 H_{r2} = \mu_0(H_{r1} + M_{r1}), \quad r = R \quad 3.9$$

Where $H_{r1} = -\partial\varphi_1/\partial r$ is the normal magnetic field intensity in the sphere and $H_{r2} = -\partial\varphi_2/\partial r$ is the normal magnetic field intensity in the fluid. Combining the equations from the potential 3.6 and 3.7, and the boundary equations 3.8 and 3.9, the coefficients A and B can be determined.

$$A = \frac{\mu_0 - \mu_2}{\mu_0 - 2\mu_2} R^3 H_0 + \frac{\mu_0 R^3 M_1}{\mu_0 + 2\mu_2} \quad 3.10$$

$$B = \frac{3\mu_1}{\mu_0 + 2\mu_2} H_0 - \frac{\mu_0}{\mu_0 + 2\mu_2} M_1 \quad 3.11$$

By comparing the dipole term in the assumed solution Equation 3.6 to equation 3.12, it is possible to determine the effective magnetic dipole moment.

$$\varphi_{dipole} = \frac{m_{eff} \cos\theta}{4\pi r} \quad 3.12$$

This results in equation 3.13.

$$\vec{m}_{eff} = 4\pi A = 4\pi R^3 \left[\frac{\mu_0 - \mu_2}{\mu_0 - 2\mu_2} \vec{H}_0 + \frac{\mu_0}{\mu_0 + 2\mu_2} \vec{M}_1 \right] \quad 3.13$$

where the first term of the equation is the contribution to the net moment of the fluid displaced by the particle, and the second term is due to any magnetization of the particle itself.

3.4.2.1.2 Magnetically linear particle

Considering a magnetically linear particle of radius R and permeability μ_2, the net magnetic polarization is given by equation 3.14.

$$\overrightarrow{M_1} = \chi_1 \overrightarrow{H_1} \quad 3.14$$

where $\chi_1 = \mu_1/\mu_0 - 1$ is the susceptibility of the particle. In this special case the effective dipole moment $\vec{m}_{eff}$ is expressed through equation 3.15.

$$\vec{m}_{eff} = 4\pi R^3 K(\mu_2, \mu_1) \vec{H} \quad 3.15$$

Where the Clausius-Mossotti factor K is defined in terms of permeability by equation 3.16.

$$K(\mu_2, \mu_1) = \frac{\mu_1 - \mu_2}{\mu_1 - 2\mu_2} \quad 3.16$$

It is possible to model the magnetic force using the effective dipole moment approach wherein the magnetized particle is replaced by an “equivalent” point dipole. The magnetic force on the dipole is given by equation 3.1.

Thus, it is possible to obtain the magnetophoretic force for a magnetizable spherical particle in a magnetic field gradient by combining equation 3.1 with the one for the effective moment giving rise to equation 3.17.

$$\vec{F}_m = (\mu_0 4\pi R^3 K(\mu_2, \mu_1) \overrightarrow{H_0} \cdot \nabla) \overrightarrow{H_0} \quad 3.17$$

Taking into account that $(\overrightarrow{H_0} \cdot \nabla) \overrightarrow{H_0} = {}^1/_2 \nabla {H_0}^2$ the equation can be rearranged, giving rise to equation 3.18.

$$\vec{F}_m = \mu_0 2\pi R^3 V K(\mu_2, \mu_1) \nabla {H_0}^2 \quad 3.18$$

Some important conclusions about the magnetic force $\vec{F}_m$ can be achieved analyzing equation 3.18, namely:

- It is proportional to particle volume
- It is proportional to the permeability of the suspension medium
- It is directed along the gradient of the magnetic field intensity $\nabla \mathrm{H_0}^2$
- It depends upon the magnitude and sign of the Clausius-Mossotti function (equation 3.16)

Thus, depending of the relative magnitudes of the magnetic permeability of the particle and the medium, it is possible to attract or repel a magnetizable particle. If $\mu_1 > \mu_2$ (K > 0), particles are attracted to magnetic field intensity maxima and repelled from minima. On the contrary, if $\mu_1 < \mu_2$ (K < 0), particles are attracted to magnetic field intensity minima and repelled from maxima.

By common convention, the magnetic force on a particle is often described in terms of the magnetic induction $\vec{B}$ rather than $\vec{H}$:

$$\vec{F}_m = {}^1\!/_2 VK(\mu_2, \mu_1)\nabla {B_0}^2 \quad 3.19$$

$$\vec{F}_m = {}^1\!/_2 \frac{VX}{\mu_0}\nabla {B_0}^2 \quad 3.20$$

3.4.2.1.3 Nonlinear magnetic media

In chapter 2 it was discussed that ferromagnetic materials can be grouped in two classifications, namely, soft and hard materials. The principal manifestation of nonlinearity in magnetically soft materials is saturation, which limits the magnitude of the magnetization vector. Hysteresis phenomenon can be important in the mechanics of magnetic particles since it creates a phase lag between the imposed magnetic field $\overrightarrow{H_0}$and the effective magnetic moment $\vec{m}_{eff}$. This phase lag is important in particle rotation.

In this section, a spherical ferromagnetic particle immersed in a linear magnetizable fluid of permeability μ_2 will be considered. Also, it will be assumed that the particle magnetization is some nonlinear function of the field, so that $\overrightarrow{M_1}(\overrightarrow{H_1})||\overrightarrow{H_0}$, where $\overrightarrow{H_1}$ is the uniform field within the particle. Taking this into account, it is possible to obtain the magnetophoretic force.

$$\vec{F}_m = 2\pi\mu_2 R^3 \left[\frac{\mu_0-\mu_2}{\mu_0-2\mu_2}\nabla \mathrm{H_0}^2 + \frac{2\mu_0}{\mu_0+2\mu_2}\overrightarrow{M_1}(\overrightarrow{H_1})\cdot\nabla\overrightarrow{H_0}\right] \quad 3.21$$

To use equation 3.22, $\overrightarrow{H_1}$ has to be obtained in terms of $\overrightarrow{H_0}$. If the particle is magnetically soft and the magnetic field is strong, the particle will saturate and $M_1 \to M_{sat}$.

Nonlinear magnetic properties have no significant qualitative effect on the nature of magnetopheresis. Saturation only influences the magnitude of the magnetic force by limiting the effective moment, and particles will still be attracted to regions of higher or lower magnetic field depending on whether they are more or less magnetizable than the medium. In the case of hysteresis, this nonlinear magnetic property creates a phase difference between the magnetic field and the induced moment and has more influence on the particle rotation (this will be discussed in the next section).

3.4.2.1.4 Magnetic Torque

A microrobot in a uniform magnetic field does not experience any force, only a torque, until $\vec{M}$ is collinear with $\vec{B}$. The torque, in newton meters, acting on a magnetic object exposed to an externally applied magnetic field $\vec{H}$ with a flux density $\vec{B} = \mu_0 \vec{H}$ is described by equation 3.22.

$$\vec{\tau}_m = V_m \vec{M} \times \vec{B} \qquad 3.22$$

where $\vec{M}$ is the magnetization of the object of a certain magnetic volume V_m. The torque tends to align the magnetization vector with the applied field. At this point, the torque $\vec{\tau}_m$ becomes zero and the microrobot remains immobile.

A permanent magnet obeys a predefined magnetization axis. However, when a soft-magnetic object is exposed to an externally applied magnetic field, the body is magnetized to a certain magnetization $\vec{M}$ that increases with $\vec{H}$, as long as the saturation magnetization is not yet reached.

3.4.2.2 Hydrodynamic drag force

The hydrodynamic drag force acting on a spherical body in an infinite extent of fluid is expressed by equation 3.23:

$$\overrightarrow{F_d} = -\frac{1}{2}\rho_f (\overrightarrow{v_p} - \overrightarrow{v_f})^2_\infty A C_d \qquad 3.23$$

where ρ_f is the density of the fluid, $v_p - \overrightarrow{v_f}$ is the relative velocity between the immersed body and the fluid, A is the frontal area of the immersed device and C_d is the drag coefficient,

which is a function of the Reynolds number. For a spherical body, this drag coefficient is expressed as [69]:

$$C_d \approx \frac{24}{Re} + \frac{6}{1+\sqrt{Re}} + 0.4 \tag{3.24}$$

and

$$Re = \frac{\rho_f \|\overrightarrow{v_p} - \overrightarrow{v_f}\|_\infty d}{\mu_f} \tag{3.25}$$

is the capsule's Reynolds number, a dimensionless positive number characterizing the flow regime as laminar or turbulent, where d is the capsule's diameter and μ_f is the fluid's viscosity.

As can be seen in equation 3.26, according to the Stokes law of resistance, for low Reynolds number ($Re < 1$), the drag force is no longer a function of the fluid's density and it is linearly proportional to the velocity, viscosity and diameter of the device [66]. These conditions can be encountered in smaller diameter blood vessels, such as capillaries and small arterioles or venules.

$$\overrightarrow{F_d} = 3\pi \overrightarrow{v_p} \mu_f d \tag{3.26}$$
$$0 \leq Re \leq 1$$

When a microdevice navigating in a blood vessel is considered the non-newtonian behaviour of the blood should be taken into account. By doing so, the fluid's viscosity μ_f becomes a function of vessel diameter and haematocrit rate according to the following empirical relations [70]:

$$\mu_f = \frac{\mu_{plasma} d^2}{(d-1.1)^2} \left[1 + \frac{(\mu_{0.45}-1)d^2}{(d-1.1)^2} \frac{(1-h_d)^c - 1}{(1-0.45)^c - 1}\right] \tag{3.27}$$

where μ_{plasma} is the plasma viscosity and $\mu_{0.45}$ is the relative apparent blood viscosity for a fixed discharge haematocrit of 0.45 which is given by:

$$\mu_{0.45} = 6e^{-0.085d} + 3.2 - 2.44e^{-0.06d^{0.645}} \tag{3.28}$$

and c describes the shape of the viscosity dependence on haematocrit:

$$c = \frac{10^{11}}{d^{12}} - (0.8 + e^{-0.075d}) \left(\frac{d^{12}}{d^{12}+10^{11}}\right) \tag{3.29}$$

Also, the influence of the vessel walls on the velocity of the device has to be taken into account for endovascular applications. Typically, the wall effect is represented in terms of ratio between the terminal relative velocity of the device and its velocity in an infinite extent of fluid (wall factor) [71]:

$$\frac{|\overrightarrow{v_p} - \overrightarrow{v_f}|_t}{|\overrightarrow{v_p} - \overrightarrow{v_f}|_\infty} = \frac{1-\lambda^{\alpha_0}}{1+\left(\frac{\lambda}{\lambda_0}\right)^{\alpha_0}} \tag{3.30}$$

where $\lambda = 2r/d_v$, d_v is the vessel diameter (m), α_0= 1.5 and λ_0 =0.29 [69]. Thus, it is possible can insert equation 3.30 into equation 3.23 and obtain a corrected equation for the drag force, taking into account wall effects. Wall effects on the fluid in a vessel typically result in a parabolic profile of the blood flow in a cylinder.

Also, the pulsatile blood's velocity should be modeled by an affine combination of time-varying periodic flow with a parabolic shape. To fully take into account the pulsatile flow in arteries caused by the cardiac pumping, one must consider a periodic 10% deformation of the vessel's diameter synchronized with the pulsatile blood's velocity [72]. This phenomena will not be considered in this work, however it is important to note that this is a relevant problem for practical applications and should be compensated for.

3.4.2.3 Apparent weight

In addition to the magnetic and drag forces, apparent weight (combined action of weight and buoyancy) is acting on the spherical device:

$$\overrightarrow{W_a} = V_m(\rho_t - \rho_f)\vec{g} \qquad 3.31$$

where $\rho_t = \tau_m \rho_m + (1 - \tau_m)\rho_{poly}$, with $\tau_m = {V_m}/{V}$, and ρ_m and ρ_{poly} the magnetic material's and polymer's densities. The weight and buoyance of the microdevice can be neglected in small blood vessels because these parameters are smaller when compared to the drag force by several orders of magnitude. This doesn't remain true for larger devices because the effects of buoyance and weight become comparable to that of the drag force.

3.5 Microrobots localization

For the motion control of medical microrobots, one of the main challenges, especially with the use of custom-built apparatus, is to localize and track the devices inside the human body. Nearly all current techniques for microrobot control rely on vision-based localization using conventional machine vision-automated tracking algorithms. However, this can only be useful for eye surgery wherein imaging and localization of intraocular microrobots is possible through simple components such as microscopes and cameras. For confined spaces such as inside the human body (for example, GI tract and circulatory system) alternative techniques

must be developed. For this purpose, several methods have been proposed, including electromagnetic tracking, magnetic resonance imaging, computer tomography and ultrasound.

Electromagnetic tracking is possible using a paired magnetic field generator and sensor. The generator emits a low-frequency electromagnetic field which induces a voltage. Since voltage is a function of distance and orientation, on the pick-up coils of the sensor, localization is possible. The accuracy of these systems depends on the presence of other magnetic objects in the environment. Many factors need to be considered, such as the material properties, shape, size and position of these objects relative to the field generator or sensor. It is also possible than the sensor is embedded in the device to be tracked. Therefore, magnetic tracking is an alternative methodology for wireless medical microrobots. A magnet is encapsulated in the device to be tracked, and an array of external magnetoresistive sensors are used to measure the magnet's field. However, this is only promising for line-of-sight problems since the human body is transparent to static and low-frequency magnetic field.

X-ray computer tomography is technology that uses computer-processed x-rays to produce tomographic images of specific areas of the scanned part of the body. CT scans offer very good low-contrast resolution and are capable of reconstructing the final image in 3-dimensions. However, CT scans are not well suited for imaging region of soft tissue surrounded by large volumes of high-density material such as bone. The images produced with this technique typically have resolutions of 1-2 mm. Fluoroscopy also used an X-ray source and a fluorescent receiver. High-resolution 2-dimensional radiographic images can reach approximately 100 um pixel size. Both CT and fluoroscopy are suitable for in vivo applications, however, the potential radiation dosage that a potential patient receives should be taken into consideration. This could limit its use in healthcare or other biological applications [17].

Ultrasound imaging is a low-risk alternative to x-rays for medical applications. This technique works by transmitting a sound wave of several MHz and detecting the echoes to form an image. For localization in soft tissue, only ultrasound combines good resolution, minimal adverse health effects, safety, high speed, adequate frame rates and low cost. These systems usually provide accuracies better than 1 mm, however, higher frequency operations yields better spatial resolution with less tissue penetration ability. The major drawbacks of ultrasound are related to low signal-to-noise ratio and the presence of strong wave reflectors such as bones, which may produce artifacts in the images. It could be possible to localize a wireless medical microrobot using a device that acts as an emitter by carrying an ultrasound transducer onboard. For example, it is possible to use a cantilever vibrating at its resonant

frequency. The emitted signal could be measured by receivers on the surface of a patient's body [30].

It could also be possible to use infrared (IR) radiation to track a microbot. However, for this the microrobot would have to have a higher temperature than the surrounding body tissue, which is difficult to achieve because of the device's small volume. An interesting idea is to have a microrobot capable of maintaining a higher temperature, for example, by breaking down glucose or by carrying a hot radioactive source.

Positron emission tomography (PET) is a nuclear medicine, functional imaging technique that produces a 3-dimensional image of functional processes in the body. It detects a pair of gamma rays emitted indirectly by a positron-emitting radionuclide, which is introduced in the body on a metabolically active molecule. Primarily, this technique is used for tumor localization. It is possible that the same radioactive isotopes could be incorporated into a wireless microrobot. This approach could be interesting especially if the goal is to use the microbot for brachytherapy [30].

As it was discussed in chapter 3.4.1, clinical MRI machines are naturally suited to track the 3-dimensional position of microrobots. With this systems it is possible to track and navigate ferromagnetic objects or magnetotactic bacteria under real-time MRI. Some advantages and disadvantages in the use of MRI machine were already discussed. In general, these systems represents a useful tool for microrobot actuation and tracking studies and could be a potential infrastructure for future microrobot healthcare applications. However, several limitations should be taken into account.

"Science may be described as the art of systematic oversimplification."

-Karl Popper

Chapter 4

Modeling

In chapter 3 it was explained that a magnetic device in a uniform magnetic field experiences a torque and that in order to generate a continuous actuation of the device the magnetic field has to go through a spatial change (or temporal change). In general, magnetic fields created with electromagnets have the disadvantage of non-linearity. However, in chapter 2, it was explained that static magnetic fields and constant magnetic field gradients can be generated with special coil configurations. In a Helmholtz configuration, the identical coils are placed on the same axis at a distance equal to the radius of the coils. Applying currents in the same direction to the coils generates a uniform magnetic field in the center. In a Maxwell configuration, identical coils are separated with a distance equal to $\sqrt{3}$ times the radius of the coils. Applying currents in opposite direction to the coils generates a uniform magnetic gradient.

In this chapter, the first goal was to, through numerical simulations using MATLAB, define the general requirements in order to control magnetic devices in blood vessels, for smaller (1 μm - 100 μm) and bigger ($>$ 100 μm) devices at the micrometer scale. Taking into account these requirements, the next step was to achieve, through finite element analysis (FEA) using the software COMSOL, different coil configurations that would allow this control. Through the Particle Tracing Module the efficiency of these proposed systems was tested.

4.1 Problem description

The main goal of this project was to design a magnetic actuation systems capable of producing sufficiently high static magnetic fields and high magnetic field gradients in order to overcome the drag force acting on microdevices in blood vessels. For this, it was important to study in some detail the forces acting on these particles and its significance.

Given the forces described in chapter 3, the motion of a magnetic device particle can be predicted using Newton's law (equation 4.1).

$$m_p \frac{d\overrightarrow{v_p}}{dt} = \vec{F} \tag{4.1}$$

Where m_p and $\overrightarrow{v_p}$ are the mass and velocity of the particle and $\vec{F}$ is the total force acting on the particle. Although there are several forces acting on particles moving in blood vessels, including buoyancy, gravity, hydrodynamic drag, inertia and particle-particle interactions, these are several orders of magnitude weaker than the magnetophoretic force and hydrodynamic drag. Thus, the total force acting on a particle can be considered to be the sum of the magnetic and drag forces (equation 4.2).

$$\vec{F} = \overrightarrow{F_m} + \overrightarrow{F_d} \tag{4.2}$$

Where F_m is the magnetic force, and F_d is the drag force.

The magnetic force acting on a magnetized particle in a nonmagnetic fluid (one with approximately zero magnetic susceptibility) is given by equation 3.4. For the purpose of this preliminary numerical analysis, a simplified 1-dimensional model is employed. Assuming that the magnetic field gradients exist only along the $\vec{x}$-axis and that the magnetization of the particle is also in the direction of the $\vec{x}$-axis, the magnetic force F_m is given by equation 4.3.

$$\overrightarrow{F_m} = V M_s \frac{dB_x}{dx} \tag{4.3}$$

where V is the volume of the particle (or agglomeration), M_s is the saturation magnetization and $\frac{dB_x}{dx}$ is the magnetic gradient.

The fluidic force is obtained using Stokes' law for the drag on a sphere (equation 3.24). Making and approximation for Reynolds numbers $0.01 < R_e < 1000$, which is a condition often encountered in small arteries, arterioles and capillaries, it is possible obtain equation 4.4.

$$\overrightarrow{F_d} = 6\pi\rho_f A(\overrightarrow{v_p} - \overrightarrow{v_f})_\infty^2 \tag{4.4}$$

where ρ_f is the density of the fluid, A is the area of the immersed body, $\overrightarrow{v_p} - \overrightarrow{v_f}$ is the relative velocity between the immersed body and the fluid in a vessel of infinite diameter which it is related to the velocity in a vessel of finite diameter.

Taking into account the forces acting on the magnetic device it is possible to define a non-dimensional number C_{MD} describing the ratio of magnetic forces over drag forces exerted on a particle and given by equation 4.5 (In paper [73] this is called the Magnetic-Richardson Number).

$$C_{MD} = \frac{F_m}{F_d} \tag{4.5}$$

For a successful control of the devices against the blood flow, $C_{MD} > 1$ (at least). As this number increases to a value greater than unit, the magnetic forces experienced by the device are much higher that the drag forces created by the blood flow in the blood vessels. As the number decreases below unity, the drag forces dominate.

Ideally, therapeutic devices will be able to access any remote part of the human vasculature. Table 4.1 classifies different types of vessels and lists their size and average blood flow velocity (minimum to maximum). Since the control of these devices requires them to resist the drag, these parameters have to be taken into account.

Type of blood vessel	Vessels's radius (mm)	Average flow's velocity (min to max) (mm s^{-1})
Aorta	12.5	400 (−200 to 1, 200)
Artery	5	100–400 (−50 to 500)
Large arteriole	0.5	1–100
Small arteriole	0.05	<50
Capillary	0.003	<1
Small veinule	0.01	<2
Large veinule	0.5	<3
Vein	2.5	3–50
Vena cava	15	50–200

Table 4.1 *Human blood vessel's characteristics from aorta to vena cava. Negative values of the flow stand for the backflow values in arterial vessels* [72].

With the software MATLAB, a numerical computing environment, and taking into account equations 4.1 to 4.5, the parameter C_{MD} was plotted against the ratio of the device/particle to vessel diameter λ for four different types of blood vessels (artery, small artery or large arteriole, arterioles and capillaries). A family of curves (Figure 4.1) was produced where each single curve represents a different value of applied magnetic field

gradient. The chosen values of magnetic gradients are based on the ones that are currently used in clinical MRIs and preclinical systems.

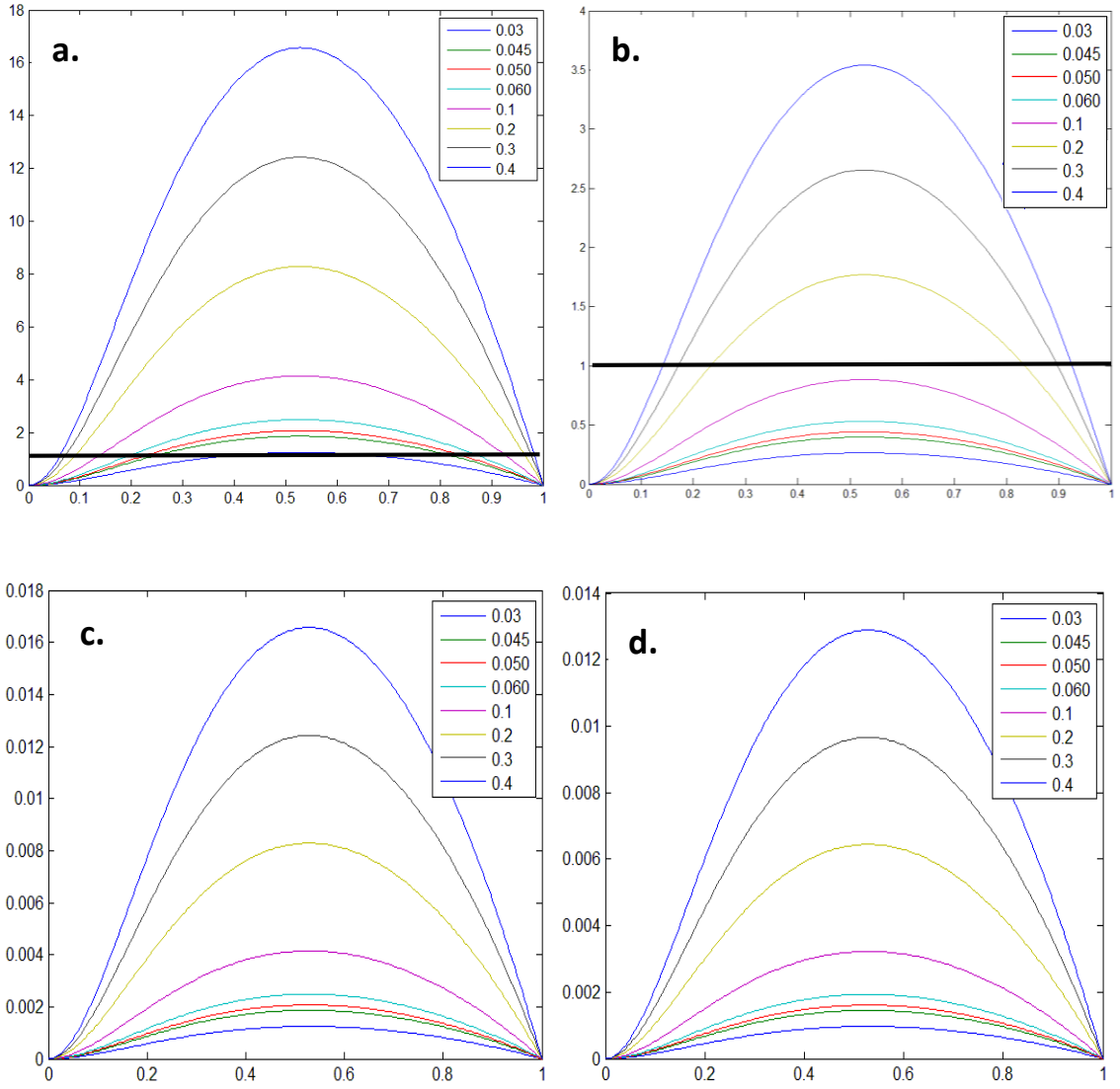

Figure 4.1 *Ratio of magnetic forces over drag forces (C_{MD}) versus the ratio of particle to vessel diameter λ for each type of vessel* ***a)*** *artery (v=$1 \times 10^{-1} m/s$, r=$1 \times 10^{-3} m$);* ***b)*** *small artery/large arteriole (v=$1 \times 10^{-2} m/s$, r=$5 \times 10^{-4} m$);* ***c)*** *small arterioles (v=$1 \times 10^{-2} m/s$, r=$3 \times 10^{-5} m$);* ***d)*** *capillaries (v=$1 \times 10^{-4} m/s$, r=$7 \times 10^{-6} m$). Each colored curve depicts a different magnetic gradient in T/m. The black line represents $C_{MD} = 1$.*

From the graphs in Figure 4.1 it is possible to conclude that one fundamental rule seems to be to navigate a magnetic device within an acceptable vessel diameter relative to the diameter of the device itself. For a given blood vessel, there is an optimum value λ to efficiently propel each device, which seems to be between 0.4 and 0.6. Particles or

agglomerations can only be steered efficiently if their λ is close to the optimum value. Thus, taking into account the range of vessel diameters in the vascular network it is possible to conclude that an effective navigation will require some type of regulation of the size of the navigated particles (or agglomerations).

From Figure 4.1 it is also possible to conclude that, depending on the size of the devices, the magnitude of the magnetic fields gradients necessary to propel them against the blood flow varies greatly. From Figures 4.1a) and 4.1b) it is possible to conclude that fields greater than 200 mT/m are required to propel particles of tens of microns against the flow in small and regular arteries. Also, taking into account Figures 4.1c) and 4.1d) it is possible to conclude that no clinical, or preclinical magnetic gradients can propel particles with less than approximately 20 μm against the blood flow even in the case of arterioles and capillaries where the blood velocity is low and using materials with high saturation magnetization (10^6 A/m). This was also observed by Cherry et al. in [74] where he and his team concluded that there is a difficulty in controlling particles smaller than 20 μm in diameter since the magnetic force acting on them cannot overcome the blood flow drag in vessels, making it nearly impossible to use the existing magnetic actuation systems to deliver magnetic nanoparticles to a specific part of the body such as a tumor. This is because magnetic forces scale down proportional to the particle volume, while drag forces scales down with the surface area of the particle. Thus, when approaching the micrometric scale, the viscous drag force becomes predominant compared to the volumetric forces. It is possible to conclude that to reach the same magnetophoretic velocity, a smaller microdevice must be subjected to a larger magnetic gradient than would a large device. The overall sizes of these microdevices are also constrained by physiological parameters such as the diameter of the blood vessels used to reach the target and the characteristics of the devices used for a specific application.

Since the control of magnetic devices in blood vessels is very dependent on the scale of the problem, in the next sections, two special cases are going to be explored. Finite element simulations will be done for an electromagnetic actuation system with the purpose of controlling devices permanently magnetized and bigger than 100 μm and for an electromagnetic actuation system with the purpose of controlling particles (or agglomerations) with diameters ranging from 1 μm to 100 μm and taking into account different values of saturation magnetization.

4.1.1 Magnetic actuation of a permanently magnetized microdevice

Figure 4.2 shows the parameter C_{MD} plotted against a range of applied magnetic field gradients. Considering a magnetic device with a diameter of approximately 100 μm and with a saturation magnetization in the order of 10^5 A/m (for example, iron oxide as can be seen in Table 4.2) it is possible to conclude from Figure 4.2a that a magnetic gradient of at least 420 mT/m is needed to propel it against the blood flow in an artery. If the magnetic device has a saturation magnetization in the order of 10^6 A/m (for example, steel or permendur) it is possible to conclude that a magnetic field gradient of at least 150 mT/m is needed.

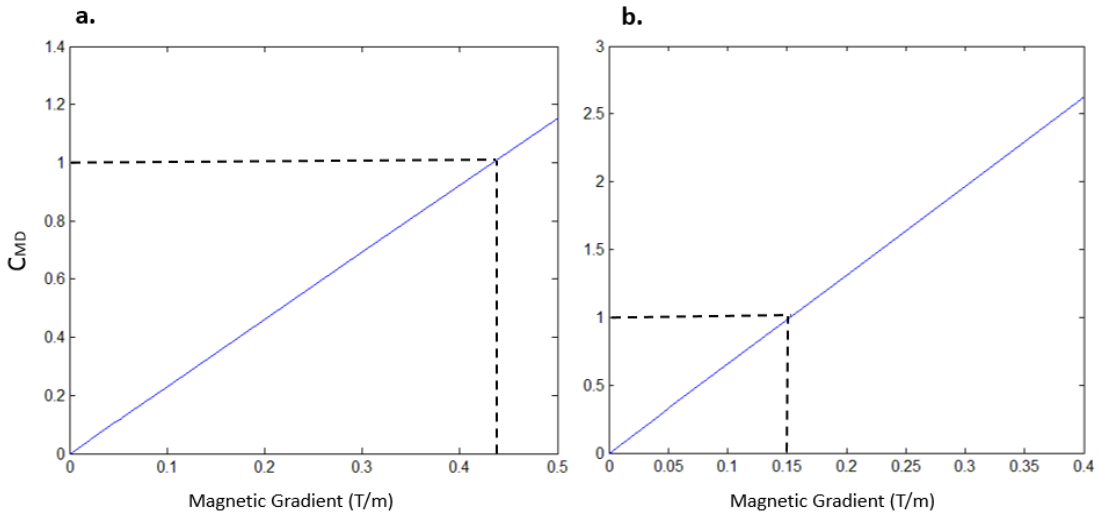

Figure 4.2 *Ratio of magnetic forces over drag forces (C_{MD}) versus the magnetic field gradient for a magnetic device 100 µm in an artery with 0.1m/s blood flow, for two different values of saturation magnetization:* ***a)*** 10^5 *A/m (Iron oxide);* ***b)*** 10^6 *A/m (NdFeB).*

Material	Magnetization at saturation (A m^{-1})	Density (kg m^{-3})
Permendur	1.95 10^6	8,200
Carbon steel 1,010/1,020	1.72 10^6	7,874
97Fe-3Si	1.60 10^6	7,700
NdFeB-35	1.23 10^6	7,500
Alfenol	0.63 10^6	6,500
Supermalloy	0.79 10^6	8,800
$Fe_3 O_4$	0.35 10^6	5,200

Table 4.2*. Properties of ferromagnetic materials* [72].

With this first study the goal was to design a magnetic actuation system to be fabricated from the ground up, taking into account cost constraints.

For a two-dimensional control of microdevices, two different approaches were proposed. These two possibilities are illustrated in Figure 4.3.

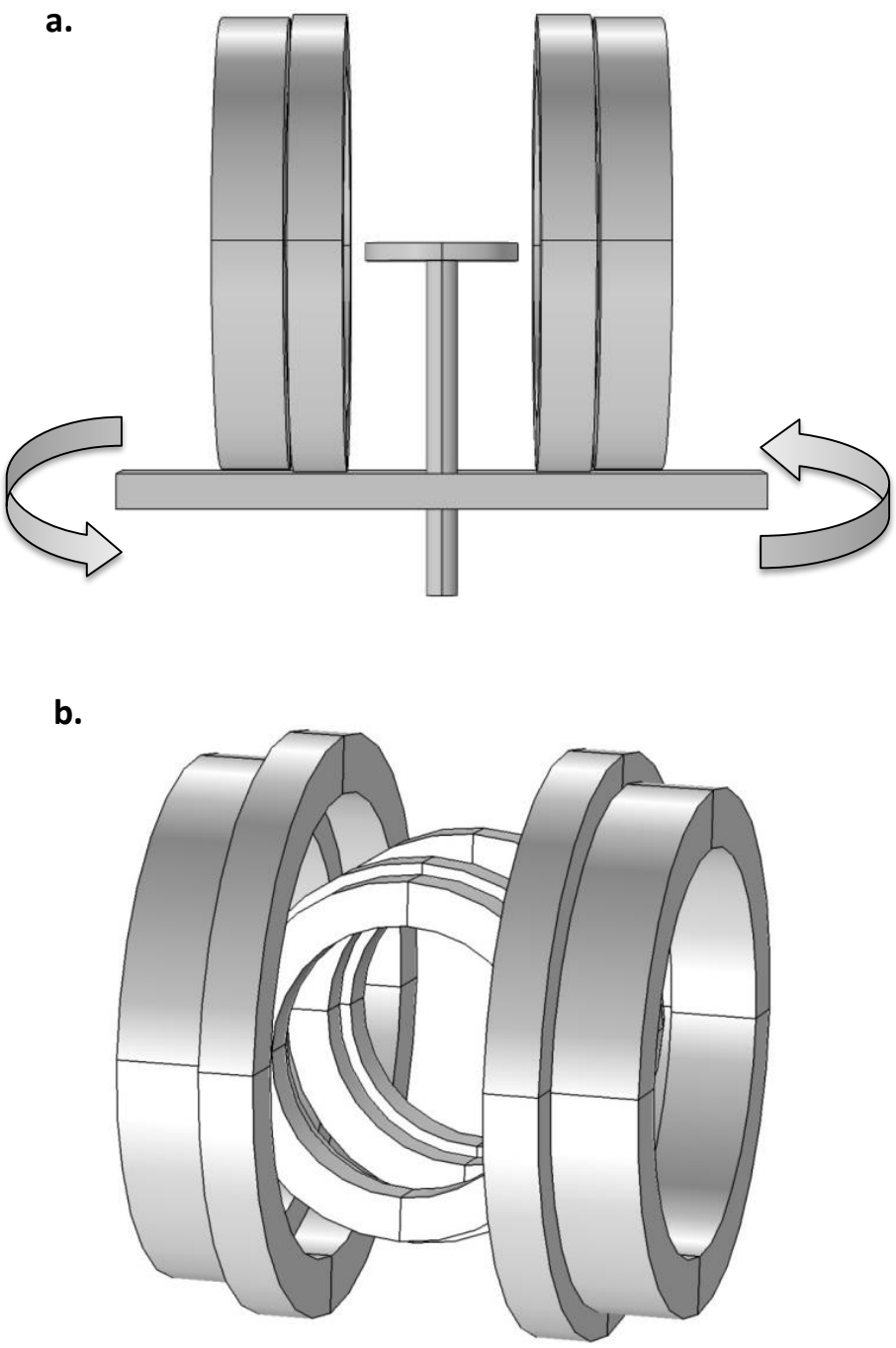

Figure 4.3 *Finite element model using COMSOL Multiphysics for two different configurations of electromagnetic actuation systems:* ***a)*** *one pair of rotational Helmholtz Coils and one pair of rotational Maxwell coils disposed in the same axis;* ***b)*** *two pairs of Helmholtz and Maxwell coils, fixed perpendicularly.*

As discussed in chapter 3, in general, the static magnetic fields and magnetic field gradients generated with electromagnets and permanent magnets have the disadvantage of non-linearity. One approach to reduce the effects of non-linearity is to use special configurations of coils to create uniform magnetic fields and gradients. In chapter 2, it was explained that a Helmholtz configuration generates a uniform magnetic fields in the center of the coils and a Maxwell configuration generates a uniform magnetic field gradient in the center of the coils. Thus, it is possible to combine both configurations to simultaneously produce magnetic forces and torques in the desired direction. In Figure 4.3, two different three-dimensional models of two possible magnetic actuation system based on these special coil configurations are presented.

The 100 μm sized device is considered to be made of NdFeB (alloy of neodymium, iron, and boron). Thus, the device is considered to be permanently magnetized and there is no need to generate a high static magnetic field that otherwise would be needed to magnetize it. This would be hard to achieve without an MRI (or with severe cost constraints).

The first proposed design, illustrated in Figure 4.3a, consists of one pair of rotational Helmholtz Coils and one pair of rotational Maxwell coils disposed in the same axis. The Helmholtz coils can align the microrobot in the axial direction and the Maxwell coils can propel the microrobot in the aligned axial direction. Thus, by rotating the coils, the microrobot can move in any direction in a 2-dimensional plane. This electromagnetic actuation system design is based on the concept developed by Yesin *et al* in [27].

The other proposed system, illustrated in Figure 4.3b, consists of two pairs of Helmholtz and Maxwell coils, which are fixed perpendicularly. When two pairs of Helmholtz coils are arranged perpendicularly, the vector sum of the magnetic fluxes is considered to be the final magnetic flux generated by the two pairs. Therefore, with this system it is possible to generate a uniform magnetic flux along a desired direction in a 2-dimensional plane and, consequently, to align the permanently magnetized microrobot in that direction (Figure 4.4a). Similarly, the two pairs of Maxwell coils arranged perpendicularly are able to generate a gradient of the magnetic flux density along the axis and, consequently, it is possible to produce a propulsion force at the microrobot in the desired direction (Figure 4.4b).

First, for the simulation of the magnetic actuation system, the possible sizes and the arrangements for the Helmholtz and Maxwell coils were considered. As it is possible to see from equation 2.24 that, at any point, the magnetic field generated by the coils is inversely proportional to the square distance between the point and the coils. Thus, it is possible to conclude that a compact coil system design is more effective and should be considered in the

design of the actuation system. Also, this results in a cheaper system and it is easier to fabricate.

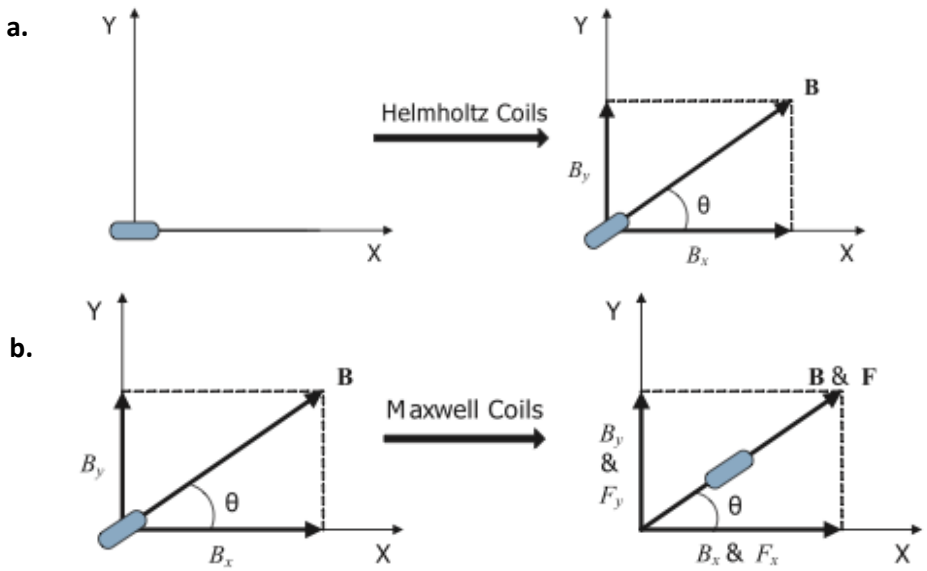

Figure 4.4 *Electromagnetic actuation mechanism of a microrobots using a system illustrated in Figure 4.3b. a) Rotation of the microrobot by Helmholtz coils. b) Propulsion of the microrobot by Maxwell coils* [75].

Firstly, the range of ROI (region of interest) was decided, where ROI can be defined as the workspace of the device. A 40-mm diameter sphere as the ROI for the device control in the center of the actuation system was chosen. This would allow enough room to make experiments with a millimetric sized device while still maintaining a relatively compact system. For future experiments, the coil set must have an opening large enough to put an animal or human subject.

Based on the specific range of ROI, the diameter of the Helmholtz and Maxwell coils were defined. For conventional Helmholtz and Maxwell coils, the cross section parameters (width and height) are much less than the radius, however, these are not suitable to be used in magnetic navigation systems since they don't generate enough magnetic force. The magnetic field gradient (thus, the magnetic force) can be increased by increasing the currents of the coils, however, the cross-sectional area of the wires limits the current of the coils. Wires with a larger cross-sectional area should be used to increase the current in the coils, however, this makes them bigger and heavier. Alternatively, it is possible to increase the number of turns in the coils, which will also result in an increase in size and weight. An equilibrium between the applied current and the number of turns in the coils should be achieved. For this application, multi-turn thick coils were considered. In the simulations, the current in the coil is assumed to be equal to the maximum possible current that could be achieved with the available voltage

source. The chosen diameter of the copper wire (1.4 mm) was relatively high in order to avoid overheating of the wire. The dimensions of the coils were chosen to have a good compromise between the width and the thickness of the coils and taking into account equation 4.6.

$$\boldsymbol{Turns} = \left|\frac{\boldsymbol{w}}{\boldsymbol{D_c}}\right| \times \left|\frac{\boldsymbol{h}}{\boldsymbol{D_c}}\right| \qquad 4.6$$

Where *w* is the width, h is the height and D_c is the diameter of the copper wire. In section 4.2.1, the final dimensions of the system are presented. The coils of the system in figure 4.3a are the same as the smaller coils in figure 4.3b.

4.1.2 Magnetic actuation of small microparticles

The design of an electromagnetic actuation system becomes more complex when the size of the particles is decreased to a smaller scale. From equation 4.3 it is possible to conclude that the magnetic force is proportional to the cube of the particle radius and that the drag force is linearly proportional to the surface area of the particle. Therefore, a greater magnetic force is needed to overcome the fluid drag force for moving, for example, magnetic nanoparticles when comparing to magnetic microparticles. In Figure 4.5, it is possible to see that if a magnetic particle with 10 μm size and a saturation magnetization in the order of 10^5 A/m, a magnetic gradient of at least 3100 mT/m is needed to propel it against the blood flow. This value is much higher than any magnetic gradient encountered in preclinical systems. However, if the particle has a saturation magnetization in the order of 10^6 A/m a magnetic gradient of approximately 750 mT/m is needed. This value is easily achievable.

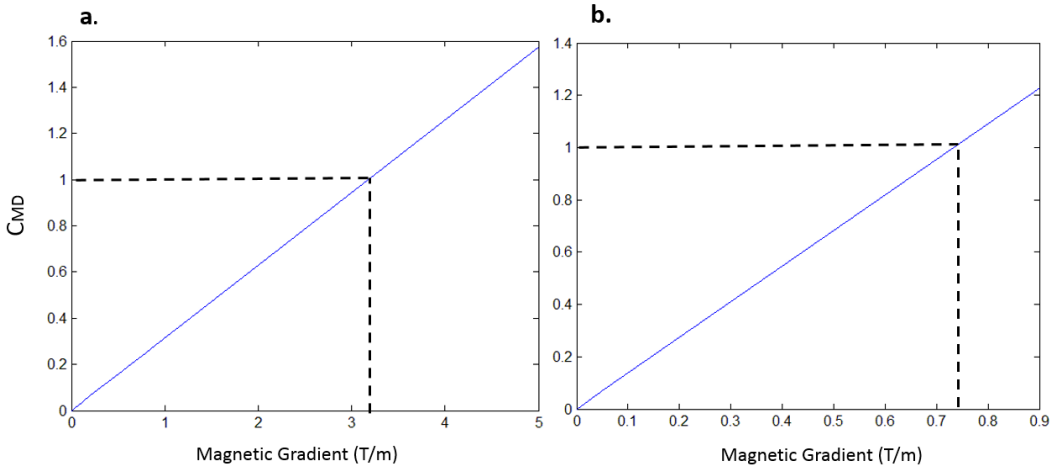

Figure 4.5 *Ratio of magnetic forces over drag forces (C_{MD}) versus the magnetic field gradient for a magnetic device 10 µm in a small artery with blood flow 1 mm/s and two different values of saturation magnetization:* ***a)*** 10^5 *A/m (iron oxide);* ***b)*** 10^6 *A/m (permendur).*

A major challenge for magnetic actuation is to create sufficiently high magnetic force to control particles of a reasonably small size. Small microparticles cannot be propelled against the blood flow and are dragged away by the systemic circulation without ever reaching the target [76]. Some solutions can be considered to overcome this problem. For example, it could be addressed by taking advantage of the natural tendency of magnetic particles to form aggregations, an approach first proposed in [7]. This idea is based on the observation that an aggregation has a large magnetic volume and thus one can induce relatively large magnetic forces compared to physically isolated microparticles. One possible problem with this approach is that a relatively large aggregation could form clots in the small arteries which obviously is not a desirable effect. The study of magnetic particle aggregation will not be carried out in the present work, however, it is interesting to consider that when, for example, a microparticle is being simulated it can be considered as an approximation for an aggregation of nanoparticles.

Another option would be not to try to propel the devices against the blood flow. Instead, a strategy could be to use the blood flow to propel the particles and use the magnetic gradients only for steering, by altering the radial position of the particles moving in the blood vessels to direct them to the desired exit at the next bifurcation. If the particles are positioned in the appropriate region of the vessel before arriving at a bifurcation, they will enter the correct branch. Figure 4.6 illustrates a simple model of this approach.

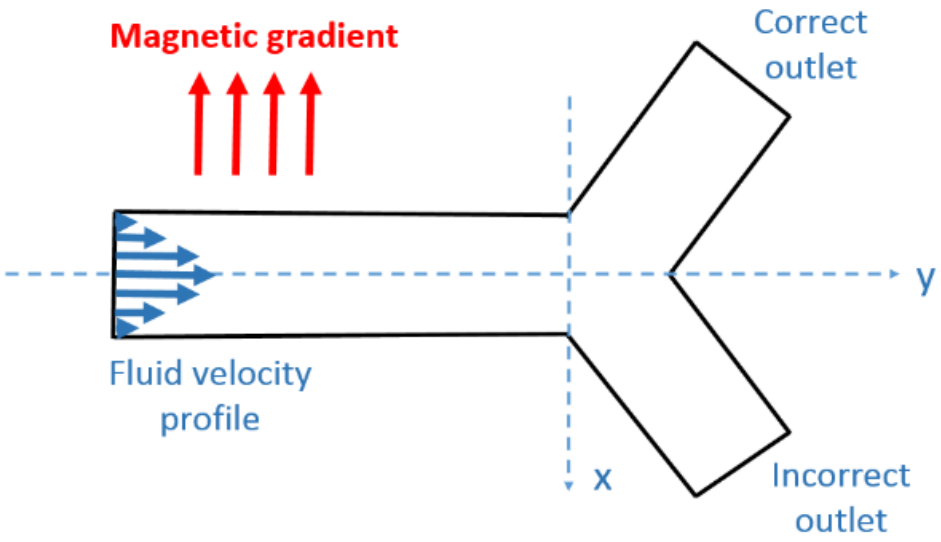

Figure 4.6 *Blood vessel bifurcation. The magnetic field gradient is applied perpendicularly to the blood flow. With this approach the goal is to steer the particles navigating in the blood vessel to make them enter in the correct branch.*

This approach is possible due to the very light weight of the smaller microparticles. They can be carried by the blood flow in the vascular network and the magnetic force produced by the electromagnetic actuation is simply used to move the particles in a direction that is perpendicular to the blood flow in the vessel. The drag force exerted on a particle moving perpendicularly to the blood flow is less than the drag force in the direction of the blood flow. Thus, the magnetic force needed to overcome the drag force for steering is less that the force needed for propulsion. This technique could be used to control smaller microparticles.

The material properties and magnetic field should be chosen to maximize the steering efficiency. This parameter can be defined as the ratio of the particles entering the correct branch of the channel over the total number of simulated particles. Therefore, the higher this parameter, the better the method is. In section 4.2.2, the steering efficiency was investigated with COMSOL. Trajectories of several particles released at the inlet of the channel with a bifurcation, similar to the one in figure 4.6, were investigated to examine the performance of the magnetic guiding system.

For one-dimensional control (steering) of microparticles in a blood vessel, two different coil arrangements are proposed. The system in Figure 4.7a is similar to the one illustrated in Figure 4.3a with a difference in the dimensions in order to produce higher static magnetic fields and higher magnetic field gradients. The system in Figure 4.7b is based on a concept proposed by Tehrani *et al.* in [77] which they called differential current coil approach. This system doesn't use the conventional coil configurations, instead, it is based on the fact that the magnetic particles are always moving toward the points of higher magnetic field intensity. Thus, the system generates a magnetic gradient field by increasing the current density in one coil, while decreasing it the other, attracting the particles towards the coil with higher current density. The finite element analysis for this system is presented in Appendix B.

As discussed before, the magnetic force depends, not only on the gradient of the magnetic field, but also on the magnetization of the particles. Since the magnetic force exerted on a small microparticle (or nanoparticle) is lower, the magnetization of the particle should be increased in order to overcome the drag force. The magnetization of the magnetic material is a function of the magnetic field (and not the magnetic gradient), reaching a maximum value or saturation magnetization when the magnetic field is sufficiently high, which is usually the case when placed in the bore of a conventional clinical MRI system with a static magnetic field of at least 1.5T.

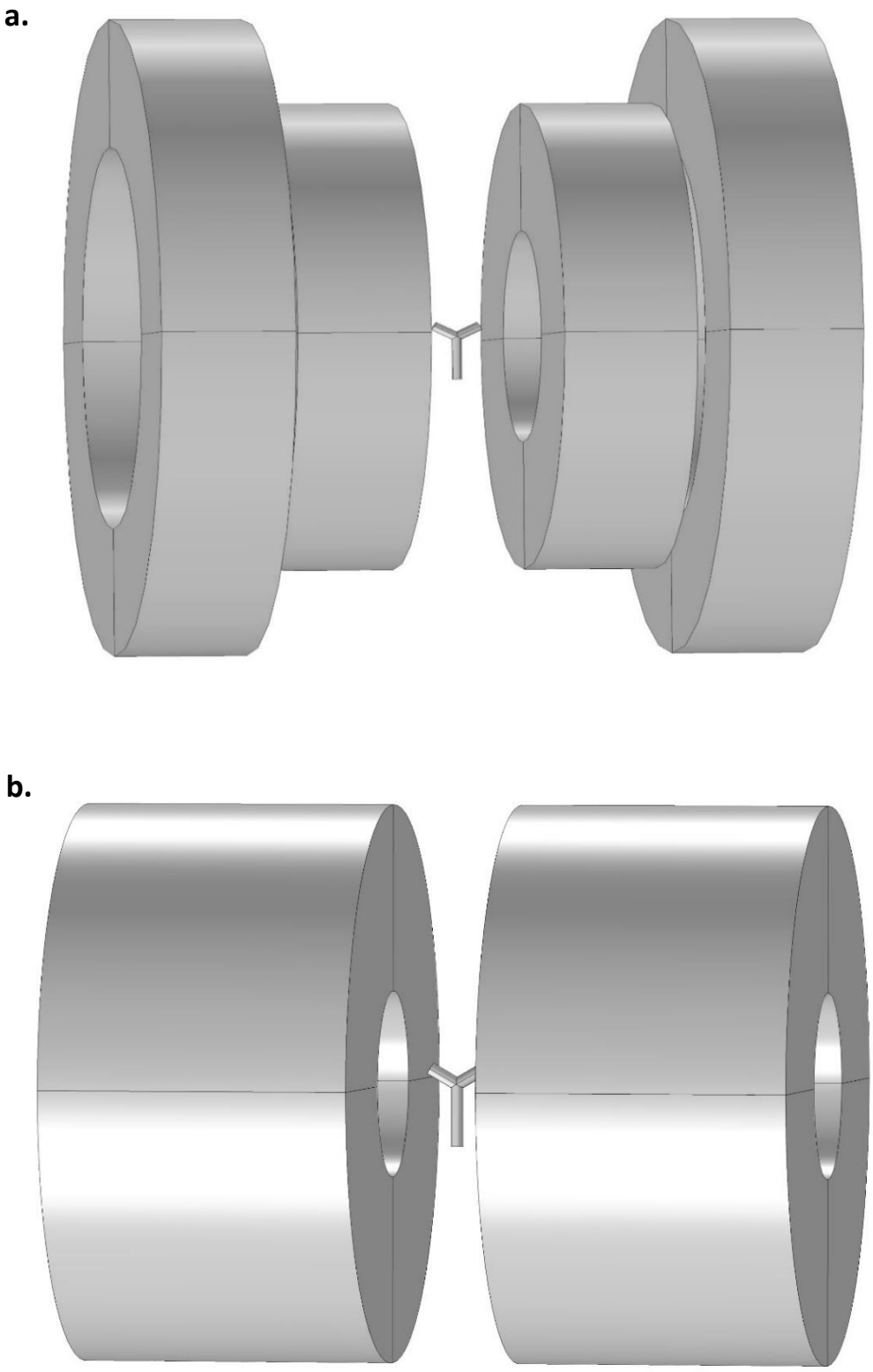

Figure 4.7 *Finite element model in COMSOL Multiphysics of two different configurations of electromagnetic actuation systems for nanoparticle/ small microparticles* ***a)*** *Helmholtz and Maxwell coil system;* ***b)*** *differential current coil approach.*

Figure 4.8 shows the magnetization plot of magnetite, which is a material commonly used in magnetic nanoparticles. In this case, a magnetic intensity of about H_{sat}=1300KA/m (1.63T) is needed to saturate the magnetite (M_{sat}=5.70× 10^5A/m). However, with a magnetic field of H=100kA/m (0.126T) corresponding to 8% of the H_{sat} the magnetite is magnetized to M=421kA/m (74% of M_{sat}). Therefore, it is possible to conclude that an electromagnetic actuation system applying a medium range of the magnetic field can be efficient. This was taken into considerations in the design of a system.

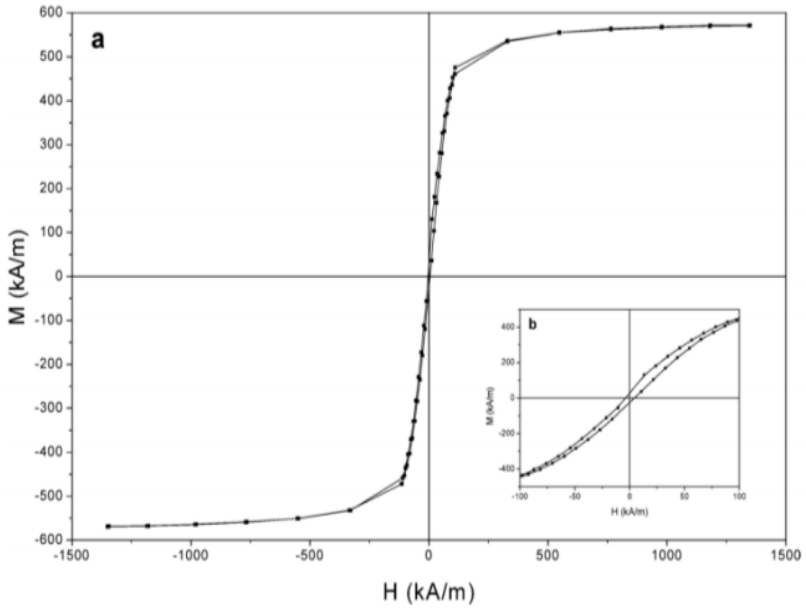

Figure 4.8 *Hysteresis cycle of the magnetization of magnetite powder at room temperature (298+-0.2K)* [77].

Other materials with higher saturation magnetization can also be used, resulting in a higher magnetic force. For example, the material permendur with the highest saturation magnetization (M_{sat}=1.95× 10^6A/m) could be of particular interest in this type of applications since it could provide the highest magnetic force/unit of volume.

On option in order to amplify the static magnetic field to the extent required to magnetize the smaller microparticle or nanoparticles could be to add soft iron cores to the Helmholtz coils. The previous described designs are linear systems. The soft iron cores were not considered in the present study since its use results in a non-linear magnetic field. However, in the future this possibility could be explored.

4.2 COMSOL Modeling

Using COMSOL Multiphysics v4.4, a finite element modeling (FEM) software package, computer models for the different magnetic actuation systems were created (using the 3D modeling mode). This simulation software can be used for various physics and engineering applications, especially coupled phenomena (multiphysics), thus, it was ideal for this project.

FEM is a numerical method for finding approximate solutions to boundary value problems for partial differential equations. The basic concept is the subdivision of the model into disjoint (non-overlapping) components of simple geometry, called finite elements, and the use of calculus of variations to solve the problem by minimizing an associated error function. Thus, a typical use of the method involves first dividing the domain of the problem into a collection of subdomains, with each subdomain represented by a set of element equations to the original problem, followed by systematically recombining all sets of element equations into a global system of equations for the final equations. The global system of equations has known solution techniques, and can be calculated from the initial values of the original problem to obtain a numerical answer. COMSOL Multiphysics is an environment which may be used to define the geometry, specify the physics of the model, mesh generation, solve and post-processing results. The basic program structure of a study is depicted in figure 4.9.

The FEM study made with this software allowed to do calculations on the magnetic fields and was used to check their uniformity, magnitude and direction.

.

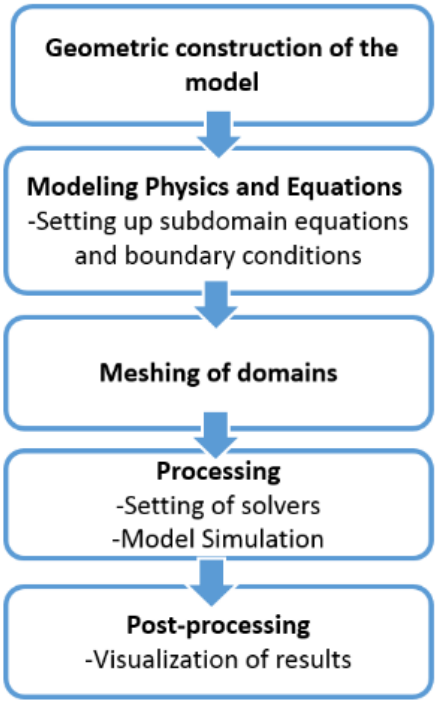

Figure 4.9 *Basic Program Structure of Numerical Simulation in COMSOL Multiphysics.*

4.2.1 Magnetic actuation of microdevices

4.2.1.1 Geometry

The first step was the geometric construction of the model. To make the coil geometry, a 2-dimensional work plane (xy-plane) was selected and 4 rectangles, one for each coil, were defined. The revolve tool was selected to revolve the planar objects into 3D structures. The final geometry is depicted in Figure 4.10a. For the option of a 2-dimensional magnetic control without rotation as illustrated in Figure 4.3b, the process was repeated with the definition of another 2-dimensional work plane (xy-plane) and the definition of 4 rectangles, but this time with a different direction vector for the revolution axis. The final geometry of the 8 coils system is depicted in Figure 4.10b. In the absence of any test object, this model is fully axisymmetric and could be implemented as a 2D axisymmetric model, which would be much less computationally demanding. However, a full 3D model has the advantage that, with it, it is possible to include a non-axisymmetric test object in the analysis as a slight modification of the model.

For the definition of a Helmholtz coil pair, the goal is to obtain circular coils separated by a distance of one radius. For the definition of a Maxwell coil pair, the goal is to obtain circular coils separated by a distance of $\sqrt{3}\ \times$ radius. With a chosen space between the coils of 5 cm that means that the radius of the Helmholtz coils had to be 5 cm. Next, in order to determine the radius of the Maxwell coils it was necessary to define the width of the Helmholtz coils. Taking into account the estimated number of turns and the diameter of the copper wire, and also taking into account that the larger the width of the Helmholtz coils, the bigger the Maxwell coils would have to be, resulting in more expenses and technical problems, a series of iterative simulations were made considering equation 4.6. The final measurements can be seen in Figure 4.11.

An area of air surrounding the system was defined which was necessary for calculating and displaying the magnetic field generated by the coils using the Magnetic Fields mode. For this model, the air was arbitrarily given a dimension of a sphere with radius 20 cm.

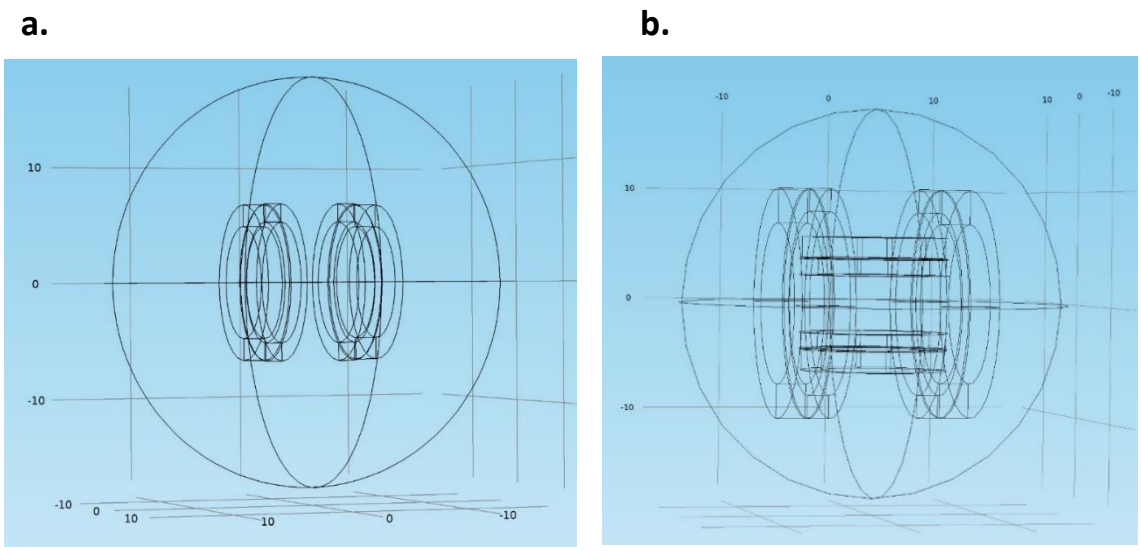

Figure 4.10 *Model Geometry* ***a)*** *Two coil pair system;* ***b)*** *Four coil pair system.*

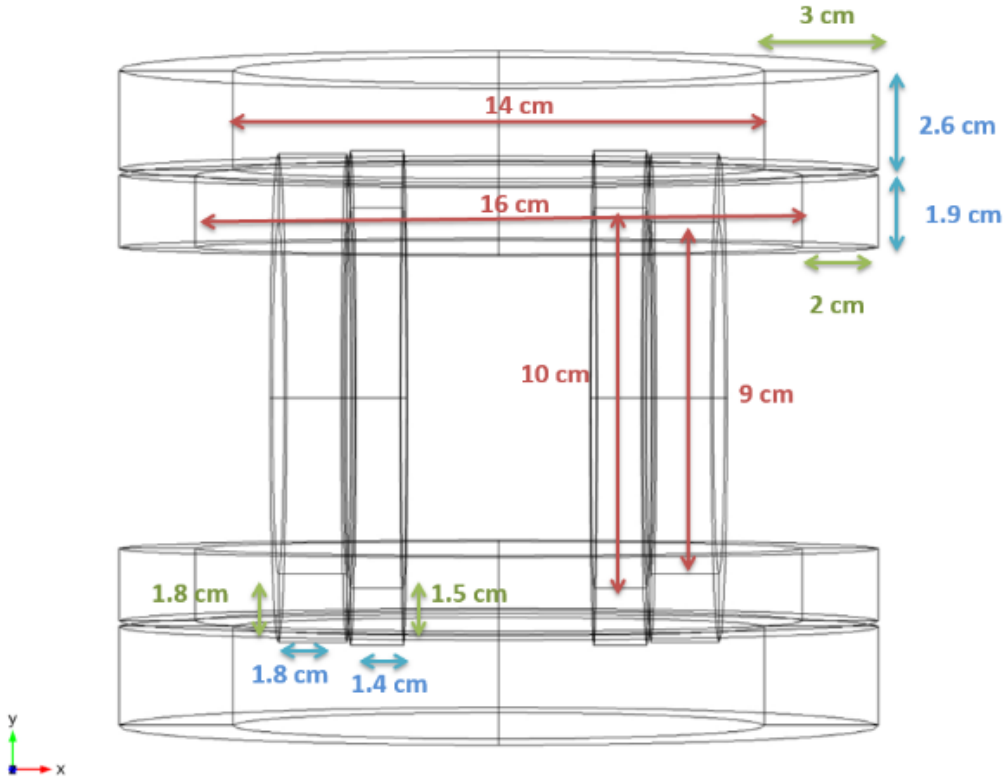

Figure 4.11 *Model Geometry of the four coil pair system with defined measurements.*

4.2.1.2 Magnetic Fields Mode

The Magnetic Fields interface, found under the AC/DC branch when adding a physics interface, is used to compute magnetic fields and induced current distributions in and around coils, conductors and magnets.

Assuming static currents and fields, the magnetic vector potential $\vec{A}$ must satisfy equation 4.7.

$$\nabla \times \left(\mu^{-1} \nabla \times \vec{A}\right) = \overrightarrow{J^e} \quad 4.7$$

Where μ is the permeability, and $\overrightarrow{J^e}$ denotes the externally applied current density. The magnetic flux density, $\vec{B}$, the magnetic field, $\vec{H}$, and the magnetic vector potential can be related via the magnetic permeability using equations 4.8 and 4.9.

$$\vec{B} = \nabla \times \vec{A} \quad 4.8$$

$$\vec{H} = \mu^{-1} \vec{B} \quad 4.9$$

The Multi-Turn Coil option is a model for a bundle of wires tightly wound together but separated by and electrical insulator. In this scenario, the current flows only in the direction of the wires and is negligible in other directions. The option circular coil was chosen so that the wires are considered to be wounded in circles around the same axis. In order to specify the direction of the wires in the circular coil, the reference Edge subfeature was added and a group of edges was selected, forming a circle. The path of the wires was automatically computed from the geometry of the selected edges.

In the case of the $\vec{x}$-axis Helmholtz coils, the external current density was computed using a homogenized model for the coils, each one made with 100 wire turns and excited by a current of 4 A where the current flowed through both the coils in the same direction. The currents were specified to be parallel for the two coils. In the case of the $\vec{x}$-axis Maxwell coils, each one was chosen to have 150 wire turns and excited by a current of 4 A but in opposite directions.

In the case of the $\vec{y}$-axis Helmholtz coils, each one was made with 130 wire turns and the $\vec{y}$-axis Maxwell coils were chosen to have 400 wire turns. These coils were excited with currents with the same magnitude as the $\vec{x}$-axis coils. The goal was to obtain static magnetic fields and magnetic field gradients with the same magnitude in both directions, when a current with equal magnitude is applied to the different coils.

The only boundary condition specified was for the exterior boundary, that is, the spherical surface, where a condition corresponding to zero magnetic flux was applied:

$$\vec{n} \times \vec{A} = 0 \quad 4.10$$

where $\vec{n}$ is the unit normal vector.

4.2.1.3 Coefficient Form PDE

When computing the magnetic fields induced by currents as well as tridimensional electromagnetic wave problems, COMSOL Multiphysics uses vector elements (or curl). In these cases, the vector element computes the magnetic vector potential, $\vec{A}$. However, the vector element can only compute the first derivative of the field.

In the previous section it was shown that the magnetic flux density, $\vec{B}$, the magnetic field $\vec{H}$, and the magnetic vector potential can be related via the magnetic permeability using equation 4.7 and equation 4.8. These equations show that the magnetic flux density and the magnetic field are functions of the first derivative of the magnetic vector potential. Since the second derivative is not defined on vector (curl) elements, the spatial gradients of $\vec{B}$ and $\vec{H}$ cannot be computed.

In this work, a technique was used so that each component of the magnetic field $\vec{H} = [H_x, H_y, H_z]$ could be mapped to a separate variable by adding an extra equation with three unknown variables. The new variables used the Lagrange element. Since both first and second order spatial derivatives are defined on Lagrange elements, it was possible to obtain the spatial gradients of $\vec{B}$ and $\vec{H}$ fields.

The first step was to map the results from the magnetic field on Lagrange elements. For that, the Coefficient Form, PDE interface with three dependent variables (one per component) was used, which used the Lagrange element by default. The right units for the dependent variables were also chosen. The second step was to correctly set up the coefficients on the PDE, in order to get the right expression for mapping the results, as can be seen in figure 4.12. The goal was to obtain an equation in the form: $a\vec{u} = \vec{f}$ where a=1, $\vec{u}$ is the vector field, and $\vec{f}$ represents the components of the magnetic field. Hence it was possible to directly relate these new variables to the components of the magnetic field vector, that is:

campo1=mf.Bx

campo2=mf.By

campo3=mf.Bz

where campo1 is the $\vec{x}$-component of the magnetic field, campo2 is the $\vec{y}$-component of the magnetic field and campo 3 is the $\vec{z}$-component of the magnetic field.

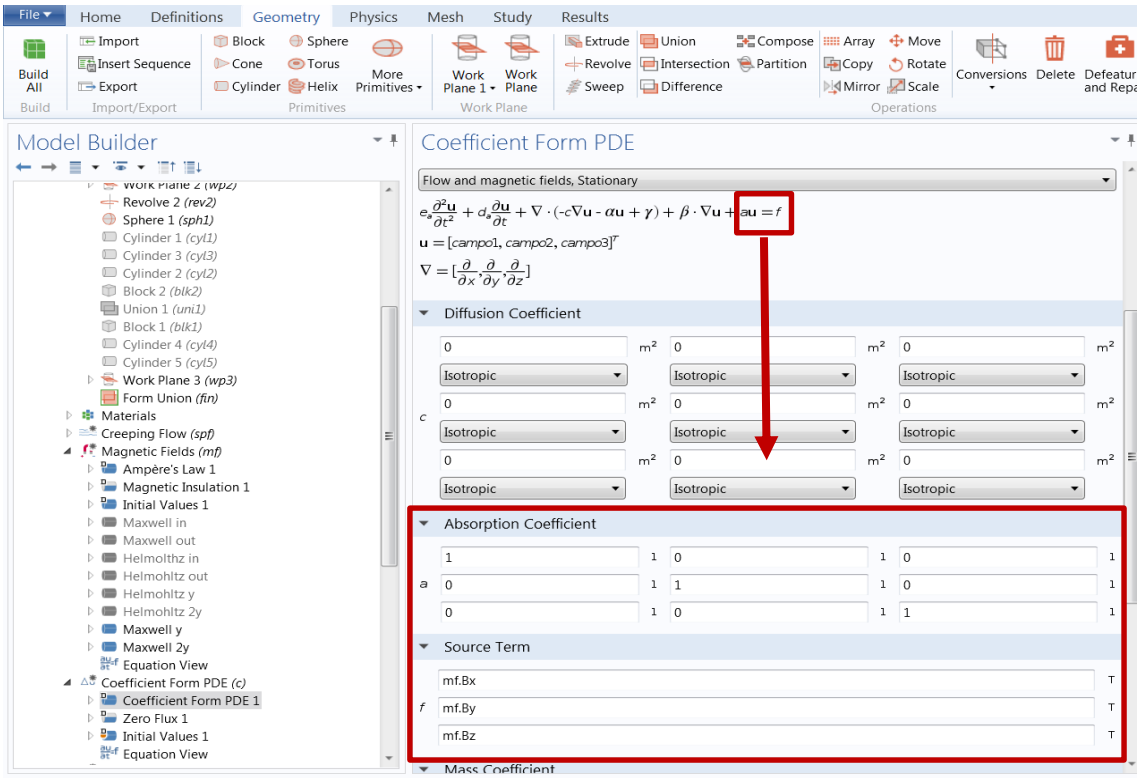

Figure 4.12 *Process of setting up the coefficients on the PDE in order to get the right expression for mapping the results.*

4.2.1.4 The Mesh and study

When using the finite element method, the accuracy of the solution is linked to the mesh size. Tetrahedral elements (default element type for most physics) were chosen. For the coils domains, the predefined mode “finer”, with a maximum element size of 1.87 cm and minimum element size of 0.136 was chosen. For the air domain, the predefined mode “coarse” with a maximum element size of 5.1 cm and minimum element size of 0.95 cm was chosen. The final tetrahedral mesh had approximately 23318 elements and around 300898 degrees of freedom. Figure 4.13 depicts the resulting mesh for the 8 coils.

Concerning the study setup, the Magnetic fields problem in Study 1 was first computed, and in the second study the variables campo1, campo2 and campo 3 were computed. In order to take the values from the electromagnetic solution, the feature “Values of variable not solved for” was activated.

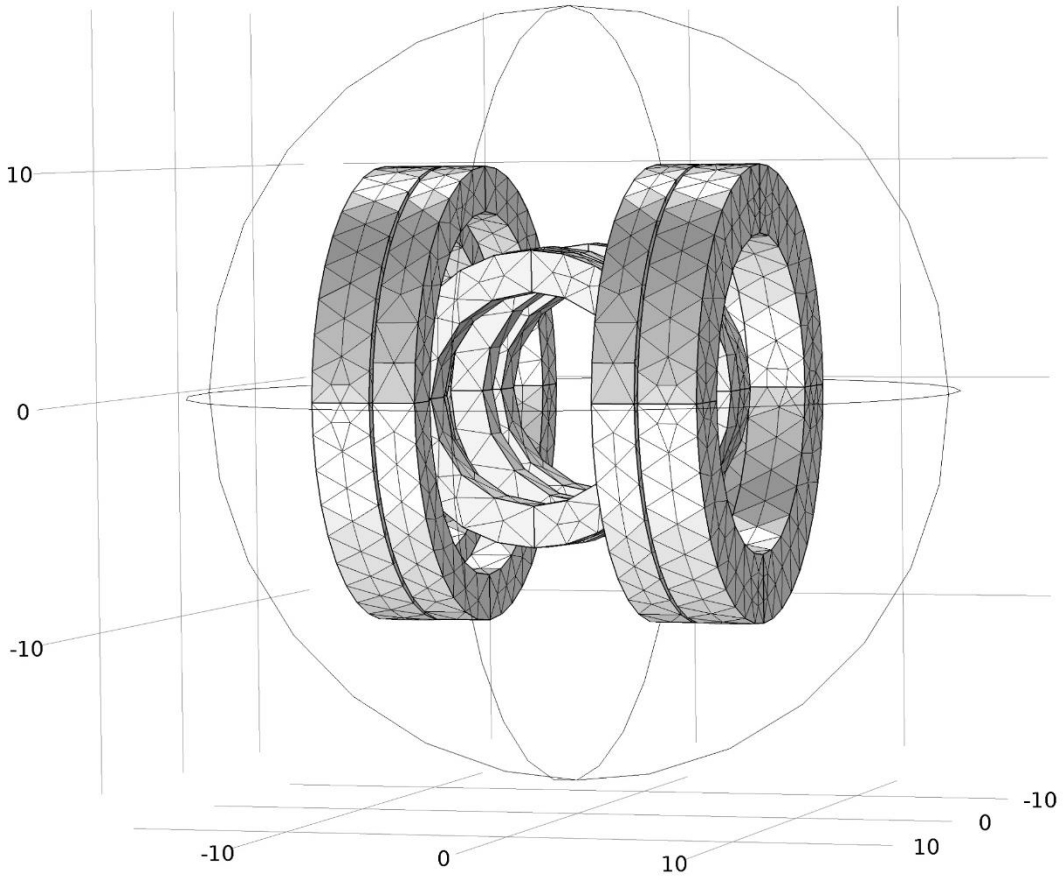

Figure 4.13 *Three dimensional Mesh Model of the coils (the mesh for the air domain was omitted).*

4.2.1.5 Results

The finite element models developed with COMSOL Multiphysics allowed calculations on the magnetic fields produced by the coil configurations and therefore they were used to study its uniformity, magnitude and direction. In this section, these results will be presented and discussed. The different coil configurations were analyzed separately and then simultaneously. The first step was to model and study the $\vec{x}$-axis Helmholtz and Maxwell configurations individually and then they were activated simultaneously. Next, the same process was repeated for the $\vec{y}$-axis Helmholtz and Maxwell coils. Finally, both $\vec{x}$-axis and $\vec{y}$-axis coils were simulated simultaneously to study the resultant magnetic field. With this simulations it was then possible to study the impact of the produced magnetic fields on a magnetic device, using the particle tracing module.

4.2.1.5.1 $\vec{x}$-axis Helmholtz coils

Figure 4.14 shows the magnetic flux density on the x-z plane (y=0) produced by the $\vec{x}$-axis Helmholtz coils. In this figure, the color scale indicates the magnitude of the magnetic flux density (also represented in Figure 4.15a.) and the arrows indicate the magnitude and direction of the magnetic field (also represented in Figure 4.15b.). The magnetic flux density norm along the axis direction of the coil pair is shown in Figure 4.16.

From the results of the COMSOL simulations it was possible to conclude that the flux strength distribution presents a high degree of uniformity within the central region between the two coils. This homogeneity of the magnetic field is well illustrated in Figure 4.15a). In Figure 4.16 it is possible to see that with this coil configuration, and applying a current of 4 A, the magnetic flux density along a line in the $\vec{x}$-axis is approximately 4.8 mT (3800 A/m) with a difference of $\pm\ 0.02\ \mathrm{mT}\ (16\ \mathrm{A/m})$ within the central region between the two coils. The field drop off outside these areas is quite drastic, with 0.6 mT (477 A/m) being lost upon crossing the threshold of one of the coils. Once completely outside the coil assembly, the flux drop off is immediate. From 4.16 b) it is possible to see the directionality of the magnetic field within the simulated Helmholtz coils. This coil configuration seems to produce a magnetic field with a uniform direction within the central region between the coils. As was described in equation 3.23, a magnetic device placed between the two coils would align with this field.

It is possible to control the magnitude of the produced static magnetic field by changing the currents in the Helmholtz coils, as depicted in figure 4.17. Also, changing the direction of the current in both coils changes the direction of the magnetic field.

The overall flux strength distribution correlates very closely with what was anticipated and, as discussed before, all simulations show a very uniform field in the core region of the Helmholtz coil construction. This uniformity is the main property and often the sought feature of a Helmholtz coil pair. As expected, since the magnetic fields are homogenous between the coils, the magnetic gradient is zero which can be confirmed in images 4.18a and 4.18b. This is important since, when these coils are activated, the goal is to control the orientation (torque) of the microdevice and not to influence the propulsion direction.

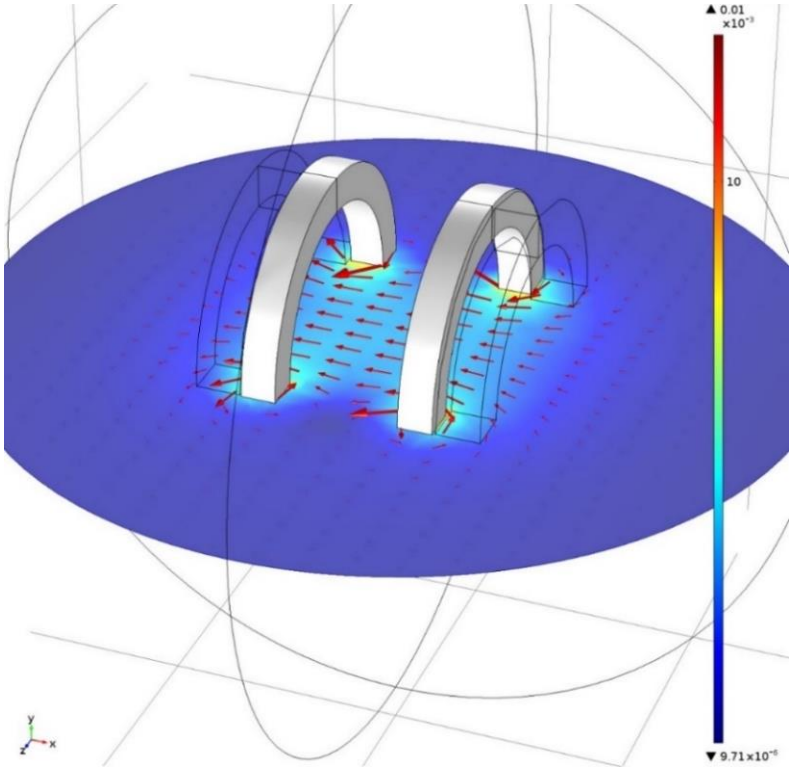

Figure 4.14 *The slice plot shows the magnetic flux density norm (T) produced by the Helmholtz coils (In the color bar the minimum value is 9.71× $10^{-5}T$ and the maximum is 1.00× $10^{-2}T$). The arrows indicate the magnetic field strength (A/m) and direction.*

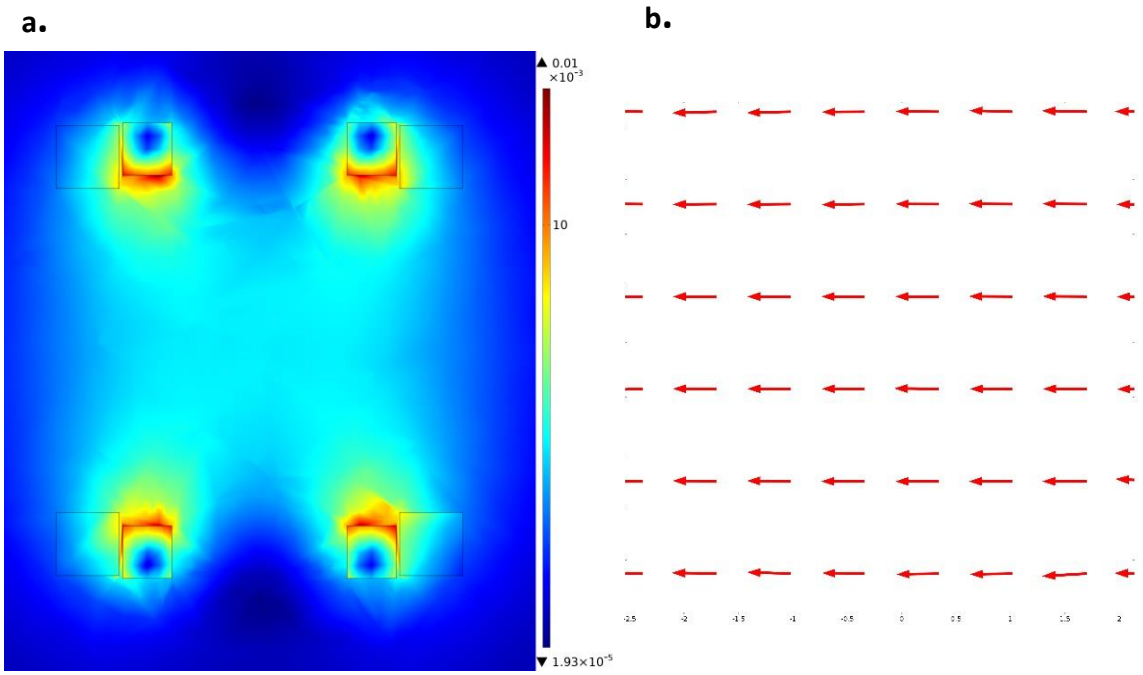

Figure 4.15 a) *The slice plot shows the magnetic flux density norm (T) produced by the Helmholtz coils (In the color bar the minimum value is 9.71× $10^{-6}T$ and the maximum is 1.00× $10^{-2}T$).**b)*** *The arrows indicate the magnetic field strength and direction in the ROI.*

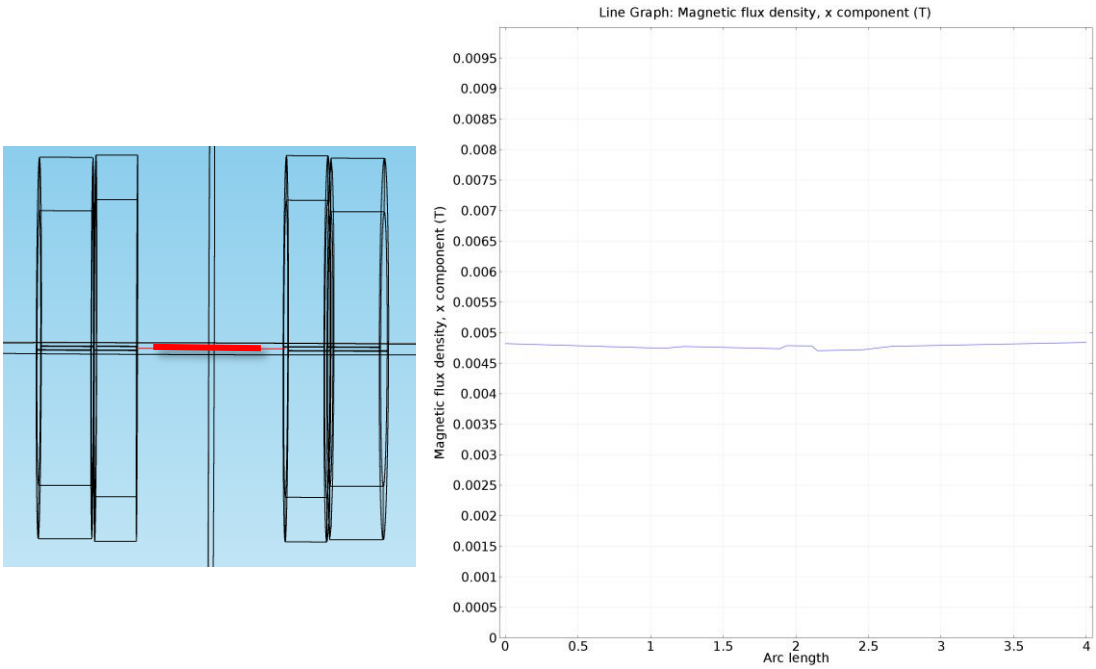

Figure 4.16 *The magnetic flux density norm (T) profile generated by the Helmholtz coils. The plot shows the profile taken along a line in the x-axis (this line is represented in red on the left).*

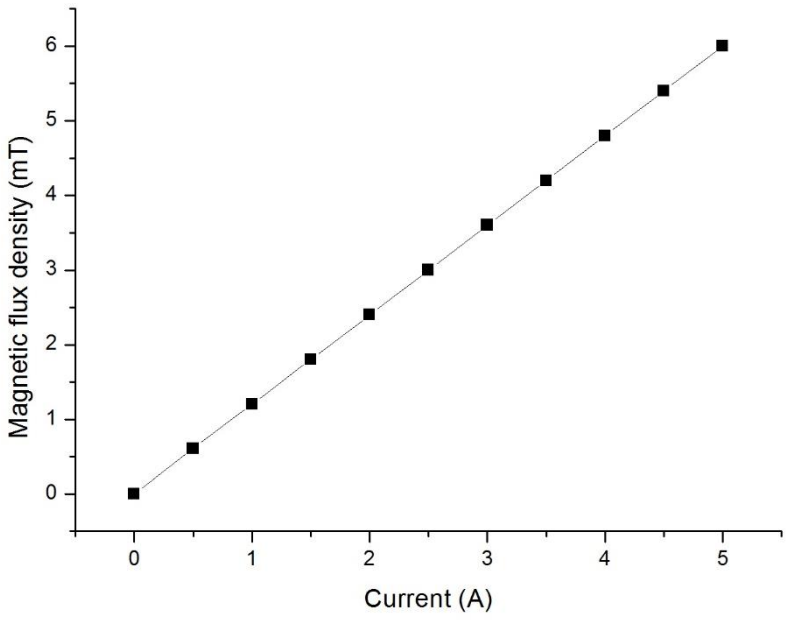

Figure 4.17 *The magnetic flux density norm (mT) vs applied current (A) in the x-axis Helmholtz coils.*

a. **b.**

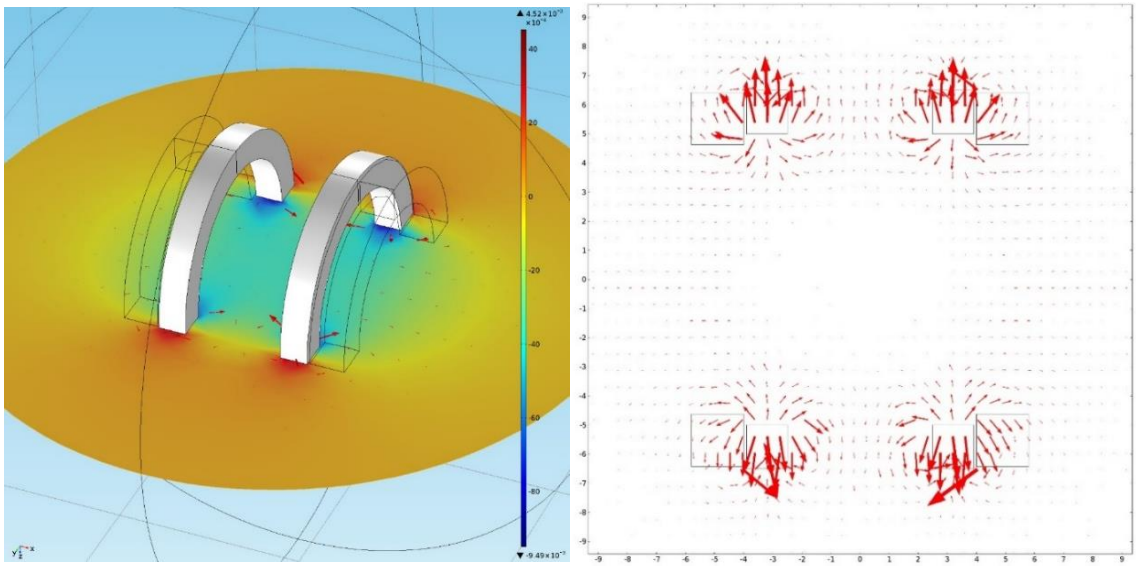

Figure 4.18 a) *The slice plot shows the x-component of magnetic flux density norm (T) produces by the Helmholtz coils (In the color bar the minimum value is -9.49×* $10^{-3}T$ *and the maximum value 4.52×* $10^{-3}T$ ***b)*** *The arrows indicate the magnetic gradient strength and direction in the ROI.*

4.2.1.5.2 $\vec{x}$-axis Maxwell coils

Regarding the $\vec{x}$-axis Maxwell configuration, Figure 4.19 illustrates the magnetic flux density on the x-z plane (y=0) between the coils. In this figure, the color scale indicates the magnitude of the magnetic flux density (also represented in Figure 4.19a) and the arrows indicate the magnitude and direction of the magnetic field (also represented in Figure 4.19b). The distribution of magnetic flux density of the Maxwell coil pair along the axial direction is illustrated in Figure 4.21.

The simulated flux strength distribution, unlike the results from the Helmholtz configuration, is non-uniform within the central region between the two coils. The maximum values of magnitude for the magnetic flux densities are achieved in regions closer to the coils and these values drop to zero at the center of the coils. From the plot in Figure 4.5, it is possible to conclude that the magnitude of magnetic flux density varies linearly between the two coils. Applying a current of magnitude 4 A, the magnetic flux density presents a maximum value in a point close to one of the coils (+3mT or +2387 A/m), achieves zero at the center and has a minimum value closer to the other coil (-3mT or -2387 A/m).

In this simulation, with the chosen parameters and applying a current of magnitude 4 A in opposite directions in the two coils, a magnetic gradient of approximately 125mT/m (99272 $\mathrm{A/m^2}$) is obtained. Also, as expected from a Maxwell coil configuration, the simulation results showed that the magnetic flux density increases in proportion to the input current density as depicted in figure 4.23. Thus, different magnetic forces can be obtained by adjusting the input current in the Maxwell coils to generate different magnetic field gradients. For example, by increasing the magnitude of the applied current from 4A to 5A, the gradient of the magnetic flux density in the working area is approximately 155 mT/m, which from the preliminary numerical simulation seems to be sufficient to control a 100 μm magnetic device with saturation magnetization 10^6 A/m moving in blood in a desired trajectory. Also, by controlling, the direction of the current, it is possible to control the direction of the magnetic field gradient, as shown in figures 4.24a and 4.24b, which in turns makes it possible to control the propulsion direction of a magnetic device.

The most important feature in a Maxwell coil pair is the uniformity and strength of the magnetic field gradient. This proposed configuration originates a constant magnetic gradient with a magnitude sufficiently high to control a microdevice bigger than 100 μm against the blood flow.

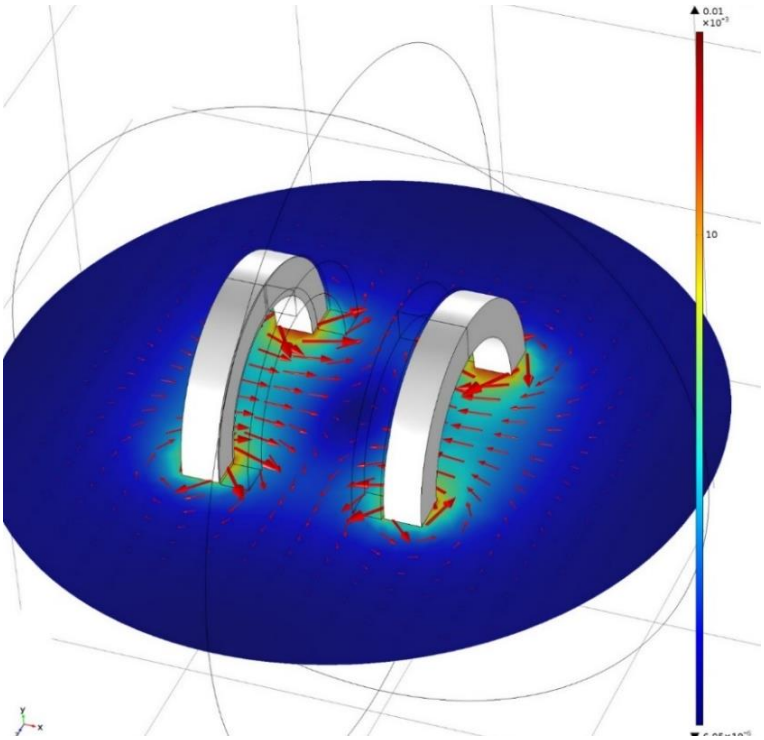

Figure 4.19 *The slice plot shows the magnetic flux density norm (T) produced by the Maxwell coils (In the color bar the minimum value is 6.05× $10^{-6}T$ and the maximum is 1.00× $10^{-2}T$). The arrows indicate the magnetic field strength (A/m) and direction.*

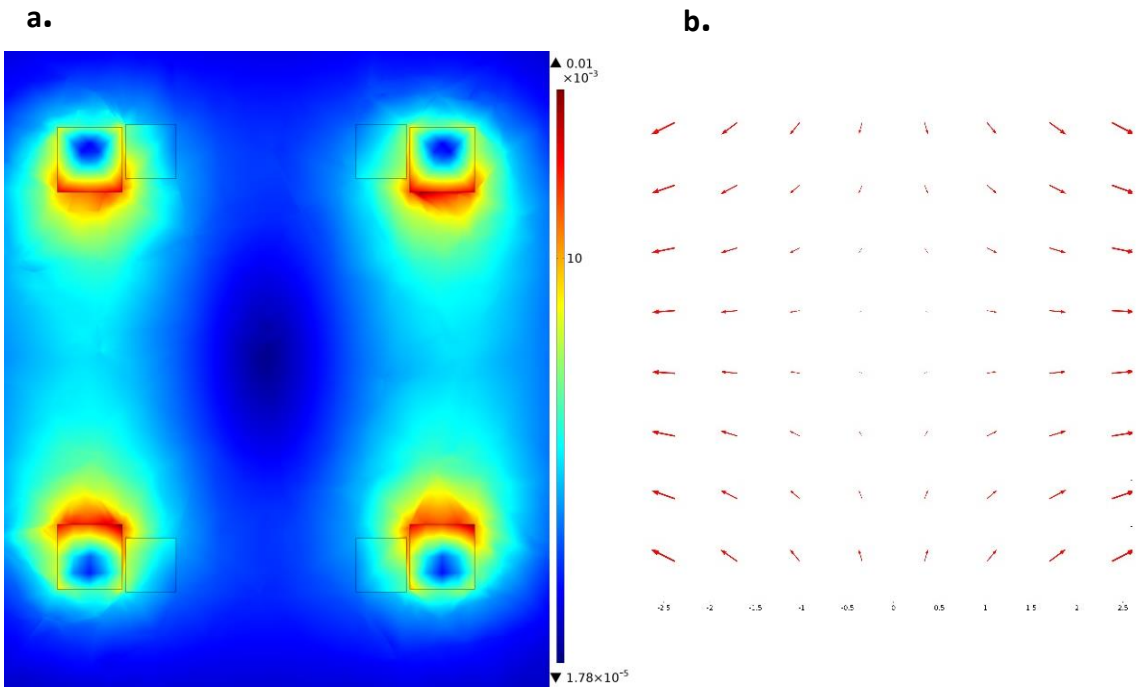

Figure 4.15 a) *The slice plot shows the magnetic flux density norm (T) produced by the Maxwell coils (In the color bar the minimum value is 1.78× $10^{-5}T$ and the maximum is 1.00× $10^{-2}T$).* ***b)*** *The arrows indicate the magnetic field strength and direction in the ROI.*

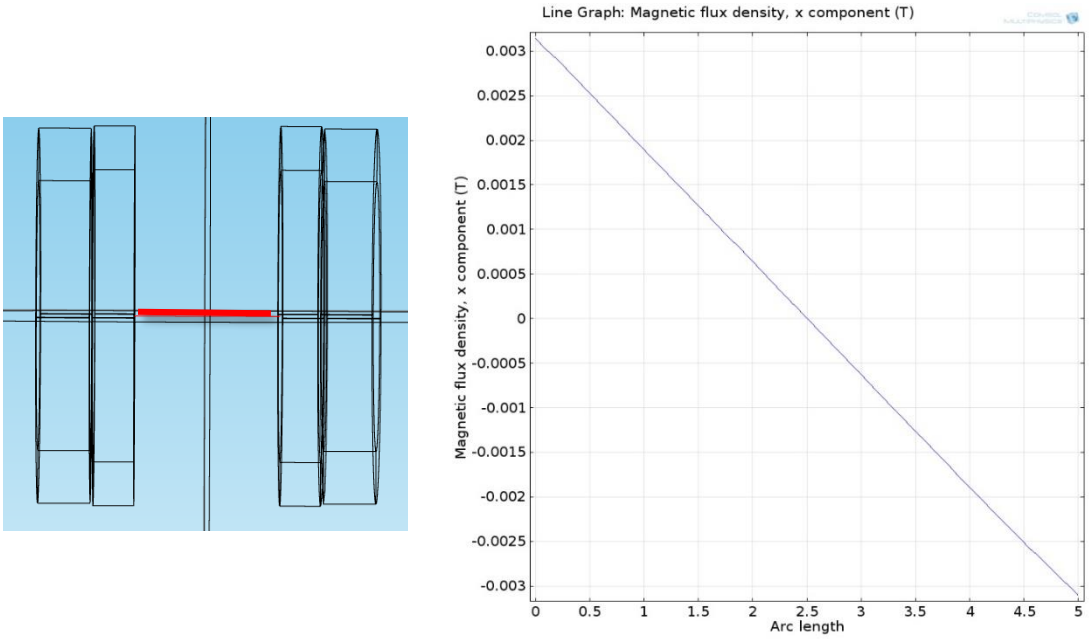

Figure 4.21 *The magnetic flux density norm (T) profile generated by the Maxwell coils. The plot shows the profile taken along a line in the x-axis (this line is represented in red on the left).*

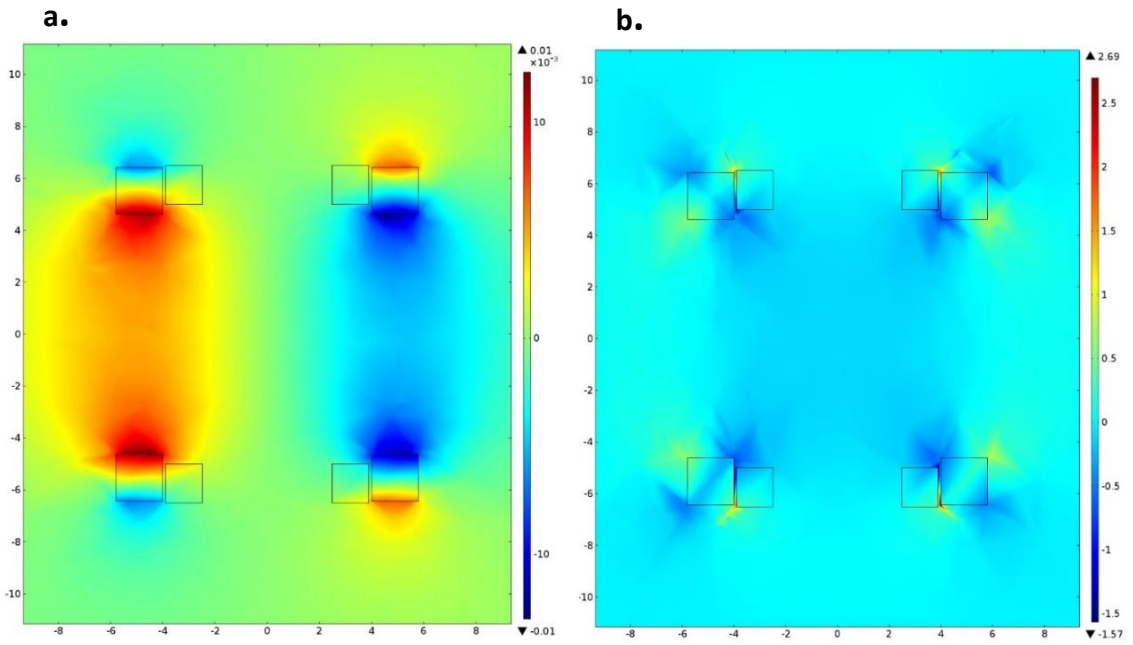

Figure 4.22 a) *The slice plot shows the x-component of the magnetic flux density (T) (In the color bar the minimum value is -1.00× $10^{-2}T$ and the maximum is 1.00× $10^{-2}T$). b) The slice plot shows the magnetic field gradient produced by the Maxwell coils (In the color bar the minimum value is -1.57 T/m and the maximum value is 2.69 T/m).*

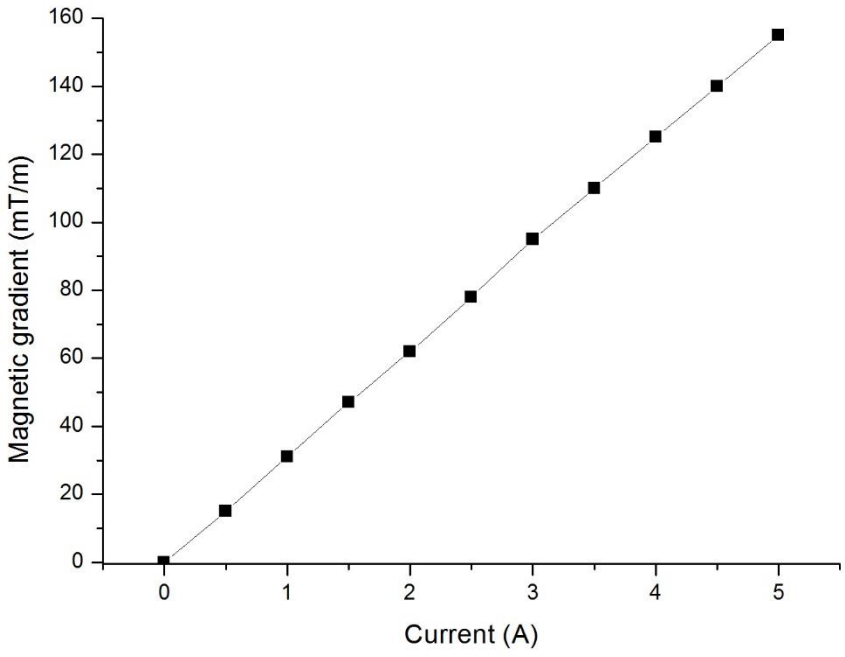

Figure 4.23 *The magnetic flux gradient norm (mT/m) vs applied current (A) in the x-axis Maxwell coils.*

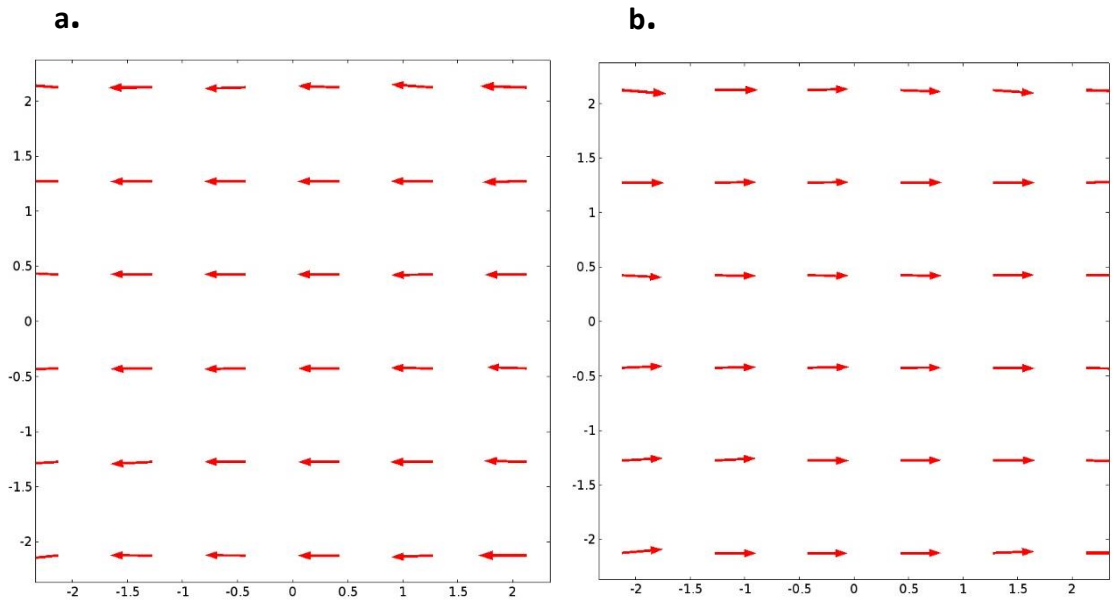

Figure 4.24 *The arrows indicate the magnetic field gradient strength (A/m²) and direction for applied currents with opposite directions: a) direction θ =180º; b) direction θ =0º, where θ is the angle represented in Figure 4.4.*

4.2.1.5.3 $\vec{x}$-axis Helmholtz and Maxwell coils

From the previous simulations it was possible to conclude that in a limited range, the Helmholtz coils generate a uniform magnetic field, while the Maxwell coils generate a smooth gradient field. Both pairs of Helmholtz and Maxwell coils have to work simultaneously to align and propel the magnetic device in a desired direction. Applying both sets of coils, their magnetic fields are superimposed. Figure 4.25 shows the magnetic flux density on the x-z plane (y=0) produced by the $\vec{x}$-axis Helmholtz and Maxwell coils. In this figure, the color scale indicates the magnitude of the magnetic flux density and the arrows indicate the magnitude and direction of the magnetic field.

In this case where the Helmholtz and Maxwell coil pairs from the electromagnetic actuation system are used simultaneously, the simulation results show that an electromagnetic interference can occur from the superposition of the electromagnetic fields produced by both coil configurations. It seems that the electromagnetic fields produced by the Helmholtz coils can interfere with those produced by the Maxwell coils and vice versa. Also, this interference seems to be closely dependent on the position of the microrobot in the ROI inside the electromagnetic coils system.

In Figure 4.26a, it is possible to see that the flux is relatively uniform between the coils, however, an interference is evident closer to the edges of the coils (compare Figure 4.26a with Figure 4.15b). This means that a magnetic device placed at the edge of the ROI will not rotate with the desired angle. Also, from Figure 2.28.b it is possible to see, although not so evident, an interference in the direction of the magnetic gradient mainly at the edges of the ROI (compare figure 4.26b with Figure 4.24b). From this observation, it is possible to conclude that the alignment direction and propulsion force of the microrobot can be distorted according to the position of the microrobot. This problem was previously reported by Choi *et al* in [78] where they proposed a compensation algorithm for the electromagnetic field interference using the position information of the microrobot to correct the magnetic field interferences.

In the context of this work, this problem will not be fully explored. However, it is important to consider the existence of these electromagnetic interferences among the coils, and in future simulations, when precision is required, this phenomenon should be better analyzed and compensated for precise manipulation of a microrobot.

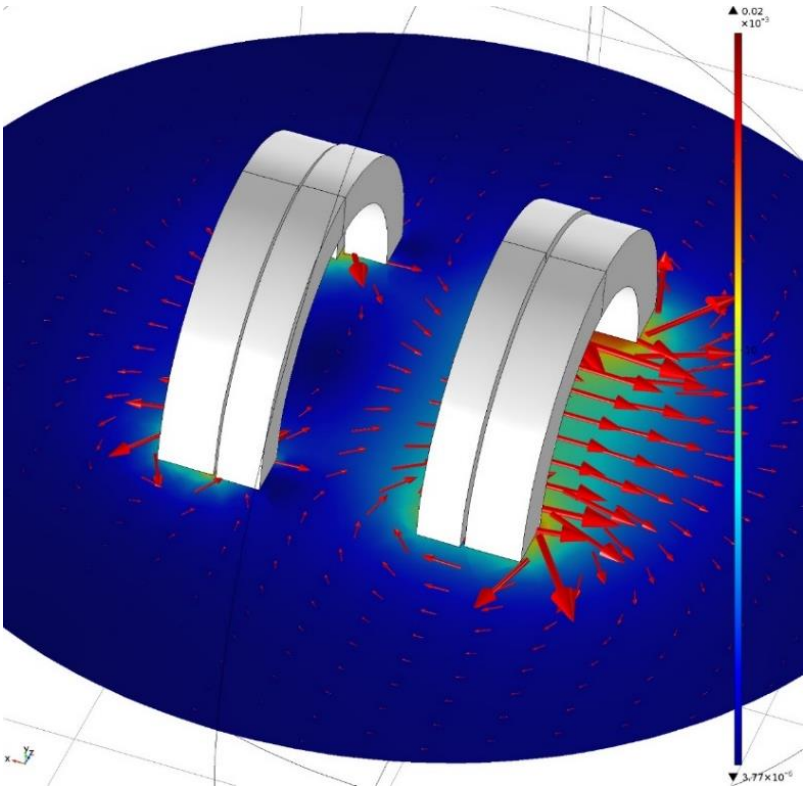

Figure 4.25 *The slice plot shows the magnetic flux density norm (T) produced by the combination of Maxwell and Helmholtz coils (In the color bar the minimum value is 3.77× $10^{-6}T$ and the maximum is 2.00× $10^{-2}T$). The arrows indicate the magnetic field strength (A/m) and direction.*

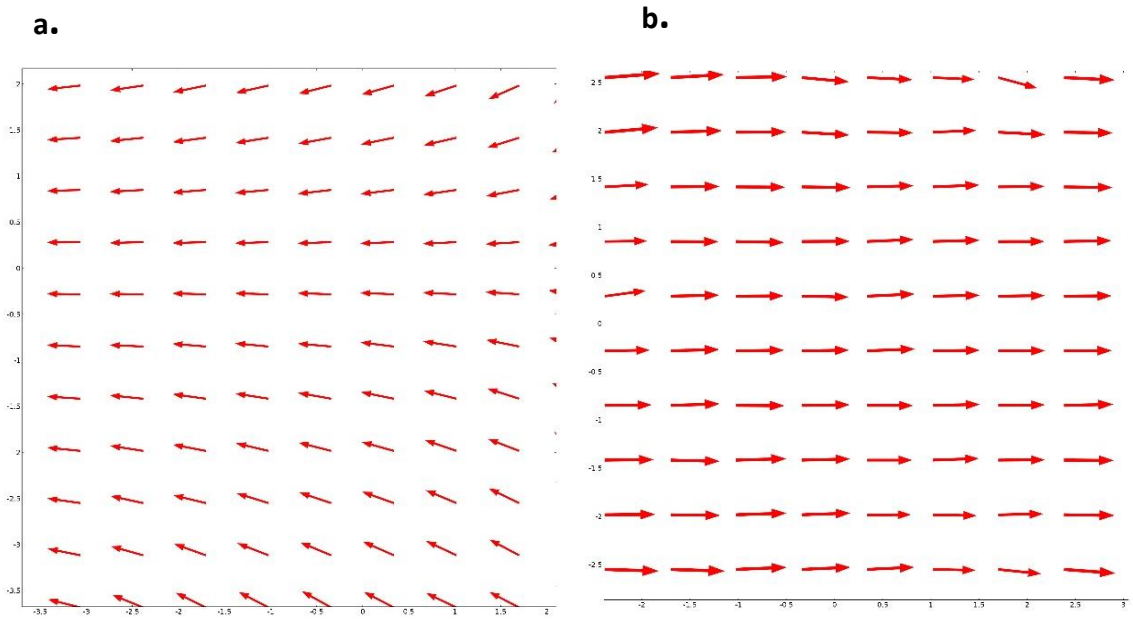

Figure 4.26 *Combination of the $\vec{x}$-axis Helmholtz and Maxwell coils* ***a)*** *The arrow indicates the magnetic field strength and direction.* ***b)*** *The arrows indicate the magnetic field gradient direction (the arrow length is normalized to easily see the directions).*

4.2.1.5.4 $\vec{y}$-axis Helmholtz and Maxwell coils

In this work, the proposed Helmholtz coils were designed in a way that both the $\vec{y}$-axis and $\vec{x}$-axis generate the same magnitude of magnetic flux with the same applied current and both $\vec{y}$-axis and $\vec{x}$-axis Maxwell coils generate the same magnetic gradients with the same applied current.

The extensive analysis made for $\vec{x}$-axis coils regarding the uniformity and magnitude of the magnetic fields was repeated for the $\vec{y}$-axis coils. The main results are depicted in figures 4.27 and 4.28. From the results of the COMSOL simulations it was possible to conclude that the flux strength distribution produced by the $\vec{y}$-axis Helmholtz configuration presents a high degree of uniformity within the central region between the two coils and, with an applied current of 3A, the magnetic flux density along a line in the y-axis is approximately 4.8 mT (or 3800 A/m) with a difference of only $\pm\, 0.02$ mT $(16\ \mathrm{A/m})$ within the central region between the two coils.

The $\vec{y}$-axis Maxwell coils were able to generate a magnetic gradient of 129 mT/m with an applied current of magnitude 4A. By changing the direction of the current in these coils it was possible to change the direction of the magnetic gradient which could be in the direction

$\boldsymbol{\theta} = 90º$ (figure 4.29a) or $\boldsymbol{\theta} = 270º$ (figure 4.29b). The angle θ is measured with the initial side on the positive x-axis and the terminal side moving counterclockwise around the origin and it is depicted in figure 4.4.

a. **b.**

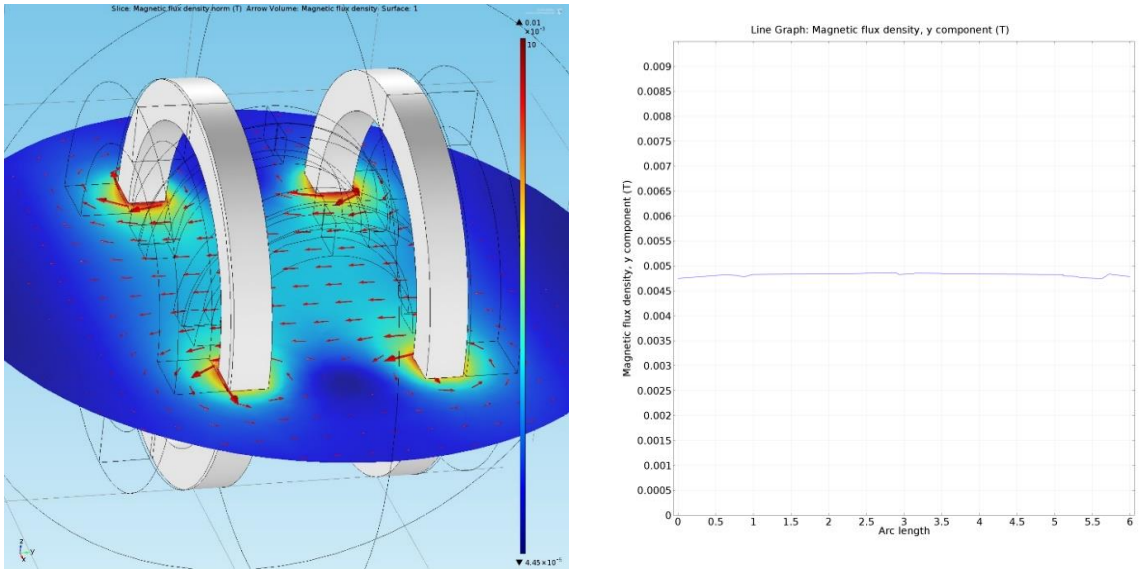

Figure 4.27 *a) The slice plot shows the magnetic flux density norm (T) (In the color bar the minimum value is 4.45× $10^{-5}T$ and the maximum is 1.00× $10^{-2}T$). The arrows indicate the magnetic field (H) strength and direction; b) The plot shows the magnetic flux density (T) profile taken along a line in the y-axis.*

a. **b.**

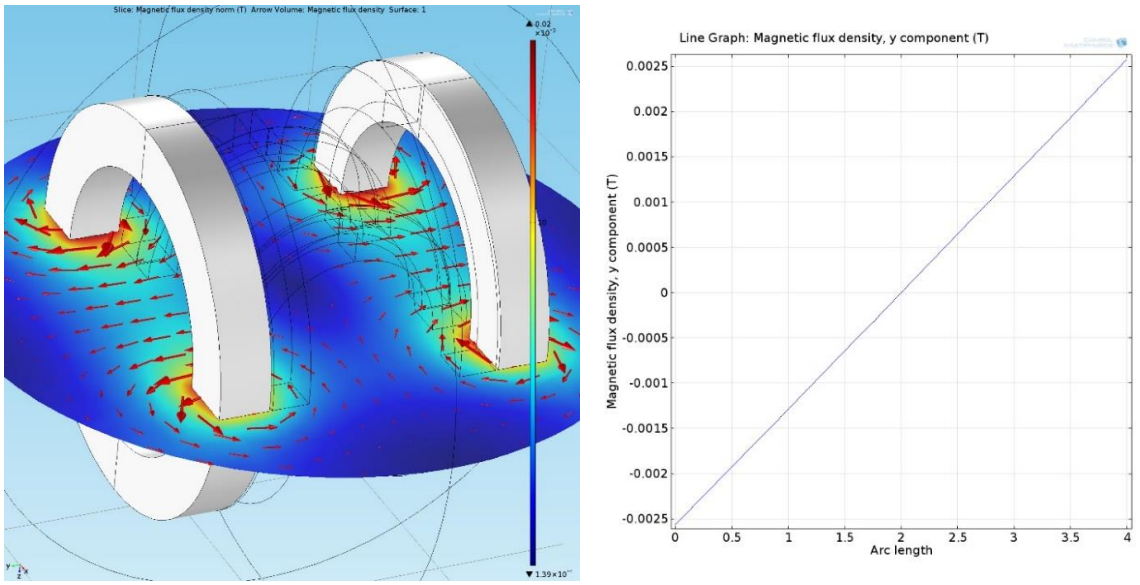

Figure 4.28 *The slice plot shows the magnetic flux density norm (T) (In the color bar the minimum value is 1.39× $10^{-4}T$ and the maximum is 2.00× $10^{-2}T$). The arrows indicate the magnetic field (H) strength and direction, b) The plot shows the profile taken along a line in the y-axis.*

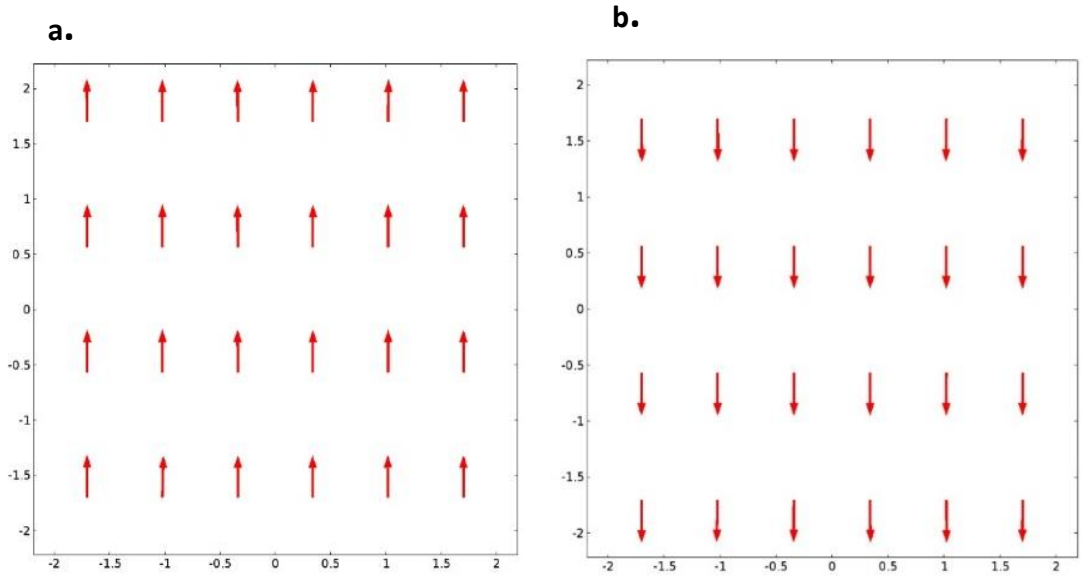

Figure 4.29 *The arrows indicate the magnetic field gradient strength (A/m²) and direction for applied currents with opposite directions: a) direction θ =90º; b) direction θ =270º, where θ is the angle represented in Figure 4.4.*

4.2.1.5.5 $\vec{x}$-axis and $\vec{y}$-axis Helmholtz and Maxwell coils

In the previous simulations, it was possible to confirm that one Helmholtz coil pair can generate a uniform magnetic field and one Maxwell coil pair can generate a uniform magnetic gradient field, at the region of interest, in one direction.

With the two proposed Helmholtz coil pairs, positioned perpendicularly, it was possible generate a vector sum of the uniform magnetic flux in the desired direction in a 2D plane. The ratio of the coil currents of the two perpendicular Helmholtz coil pairs determines the desired rotation of the microrobot, according to $\frac{B_x}{B_y} = \tan\theta$.

Also, with the two proposed Maxwell coil pairs, positioned perpendicularly, it was possible to generate a vector sum of the magnetic gradient field, in the desired direction. As depicted in figure 4.30, the FEM simulations confirmed that the proposed electromagnetic actuation system can generate uniform magnetic fluxes allowing the control of a microbot in the desired directions, in a 2D plane (in this case 45º, 130º, 225º and 315º).

Thus, it was confirmed that the permanent magnetic microrobot can be aligned and moved by the proposed electromagnetic actuation system in a 2D plane. With three

orthogonal arranged Helmholtz and Maxwell coil pairs it would be possible to generate a uniform magnetic field at the region of interest in any direction in space (in a 3D space).

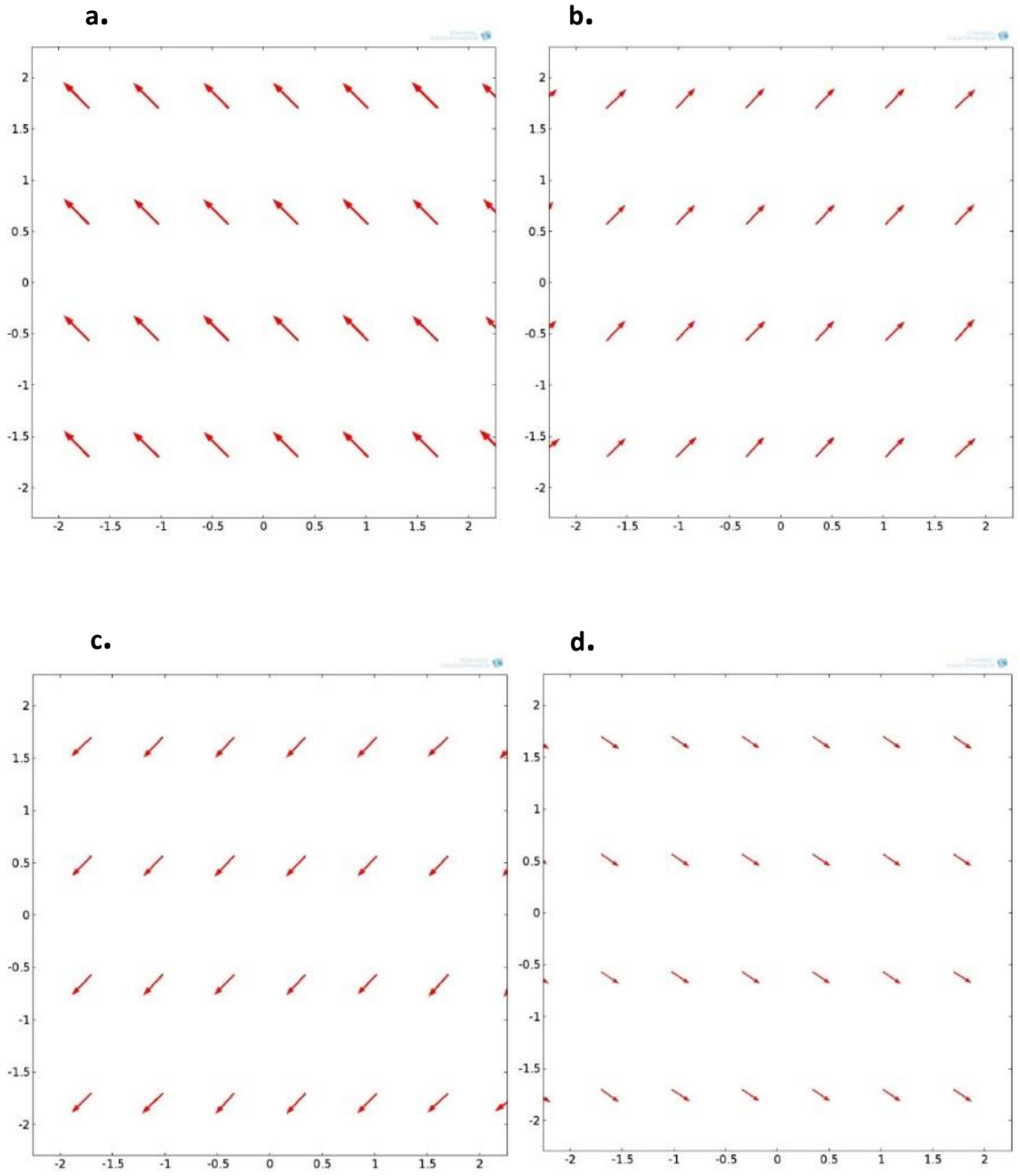

Figure 4.30 *The arrows indicate the magnetic field gradient strength (A/m^2) and directions: a) θ =45º; b) θ =135º; c) θ =225º; d) θ =315º.*

4.2.1.6 Particle Tracing

In this section, the goal was to test the performance of the proposed electromagnetic actuation system in propelling a magnetic device with the characteristics described in section 4.1.1. To relate the magnetic field distribution and the trajectory of the particles, the particle tracing interface was used.

The Particle Tracing For Fluid Flow interface, found under the Fluid Flow branch when adding a physics interface, is used to compute the motion of particles in a background fluid. It provides a Lagrangian description of a problem by solving ordinary differential equations using Newton's law of motion described in equation 4.1, which requires specification of the particle mass, and all forces acting on the particle. The forces acting on particles can be divided into two categories, those due to external fields and due to interactions between particles. Forces due to external fields are typically computed from a finite element model, using the physics interfaces available in COMSOL. In this project, the external field was computed with the Magnetic fields interface and was described in the previous sections. The forces due to interactions between particles will not be considered. For each particle, an ordinary differential equation is solved for each component of the position vector. At each time step, the forces acting on each particle are queried from the external fields at the current particle position.

A cylinder with radius 1.5 cm and height 1 cm was modeled at the center of the setup as a water container as can be seen in figure 4.31. Several analysis were performed to investigate the controllability of the particle trajectory by changing the current in the two pairs of Maxwell coils. Some of the tested currents and resultant magnetic field gradients are depicted in table 4.3. Figures 4.32 and 4.33 show the resultant particle trajectories applying the magnetic field gradients from table 4.3, for 2 seconds. In figure 4.33, the different images correspond to different directions of the applied magnetic gradient, namely 45º, 130º, 225º and 315º, which were depicted in figure 4.30. In all cases, the magnetic gradient had magnitude 124 T/m in x-axis and y-axis. With this parameters a maximum velocity of 120 mm/s was achieved. Other excitation types, with different magnetic gradients between the two coil pairs are depicted in Figure 4.33. The results confirmed that it is possible to align the particle trajectory to all desired directions simply by changing the current in the coils. For all these excitation types it was assumed that the magnetic field intensity at each particle position was high enough to saturate the particle (or that they are permanently magnetized).

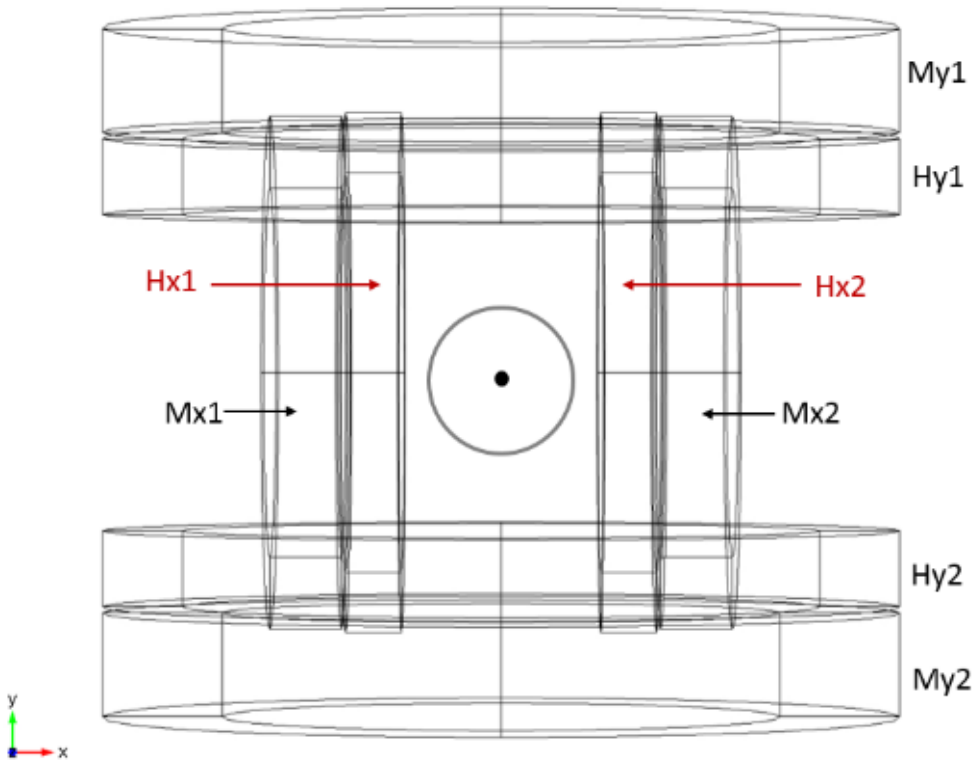

Figure 4.31 *Model Geometry of the four coil pair system with a cylinder at the center.*

	I_{Mx1}	I_{Mx2}	I_{My1}	I_{My2}	Gradx	Grady
a	4A	-4A	-4A	4A	-125mT/m	125mT/m
b	-4A	4A	-4A	4A	125mT/m	125mT/m
c	-4A	4A	-4A	4A	125mT/m	125mT/m
d	-4A	4A	-4A	4A	125mT/m	125mT/m
e	4A	-4A	0	0	-125mT/m	0
f	4A	-4A	2A	-2A	-125mT/m	-62mT/m
g	-2A	2A	-4A	4A	62mT/m	125mT/m
h	1A	-1A	-4A	4A	-31mT/m	125mT/m
i	2.5A	-2.5A	-4A	4A	-78mT/m	125mT/m
j	0	0	4A	-4A	0	-125mT/m

Table 4.3*. Different currents assigned to x-axis and y-axis Maxwell coils and resultant magnetic gradients in the x-axis and y-axis*

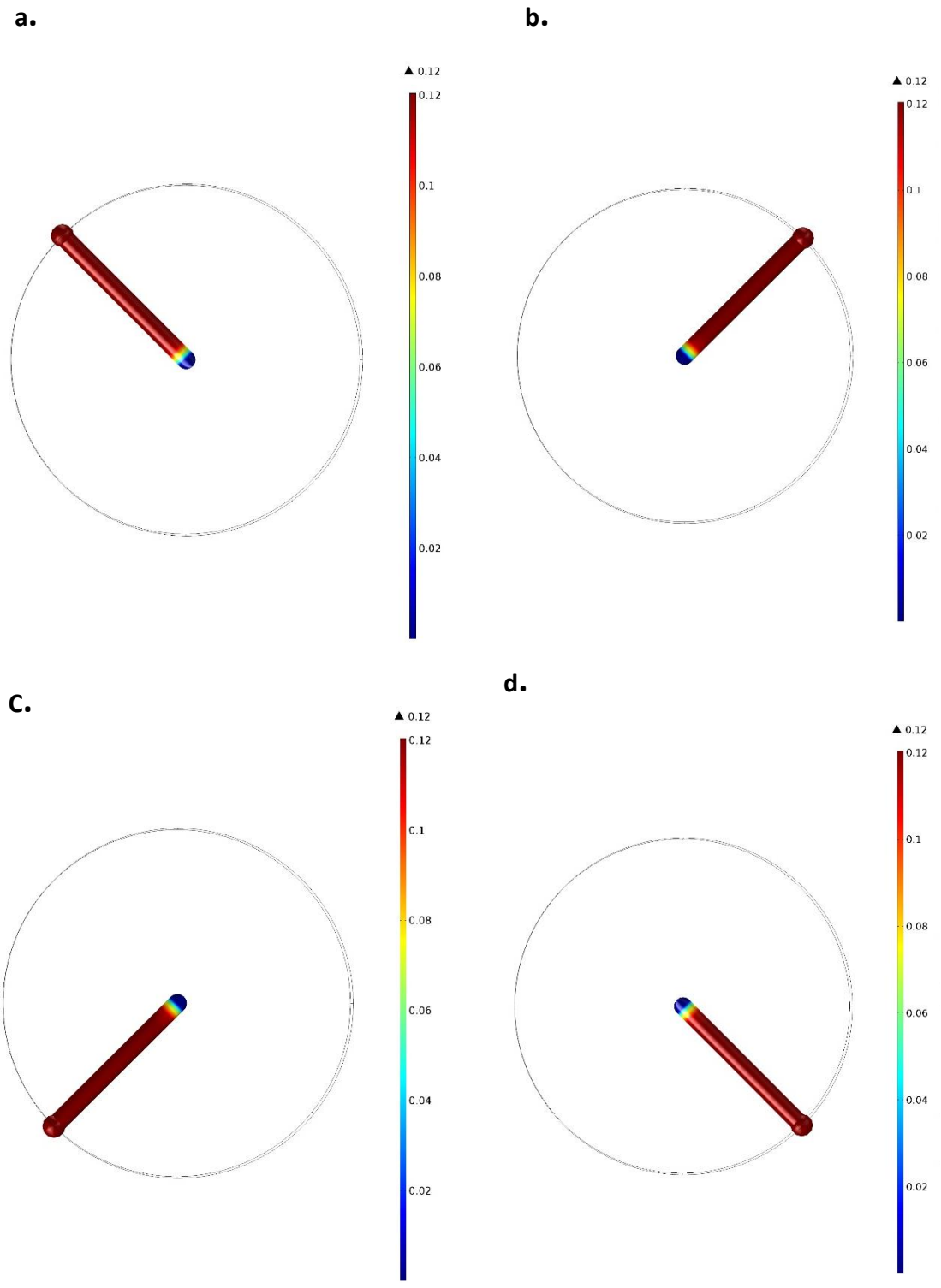

Figure 4.32 *Particle trajectories with a magnetic field gradient applied in different directions. The color bar depicts the velocity of the particle in m/s. The different excitation types are depicted in table 4.3.*

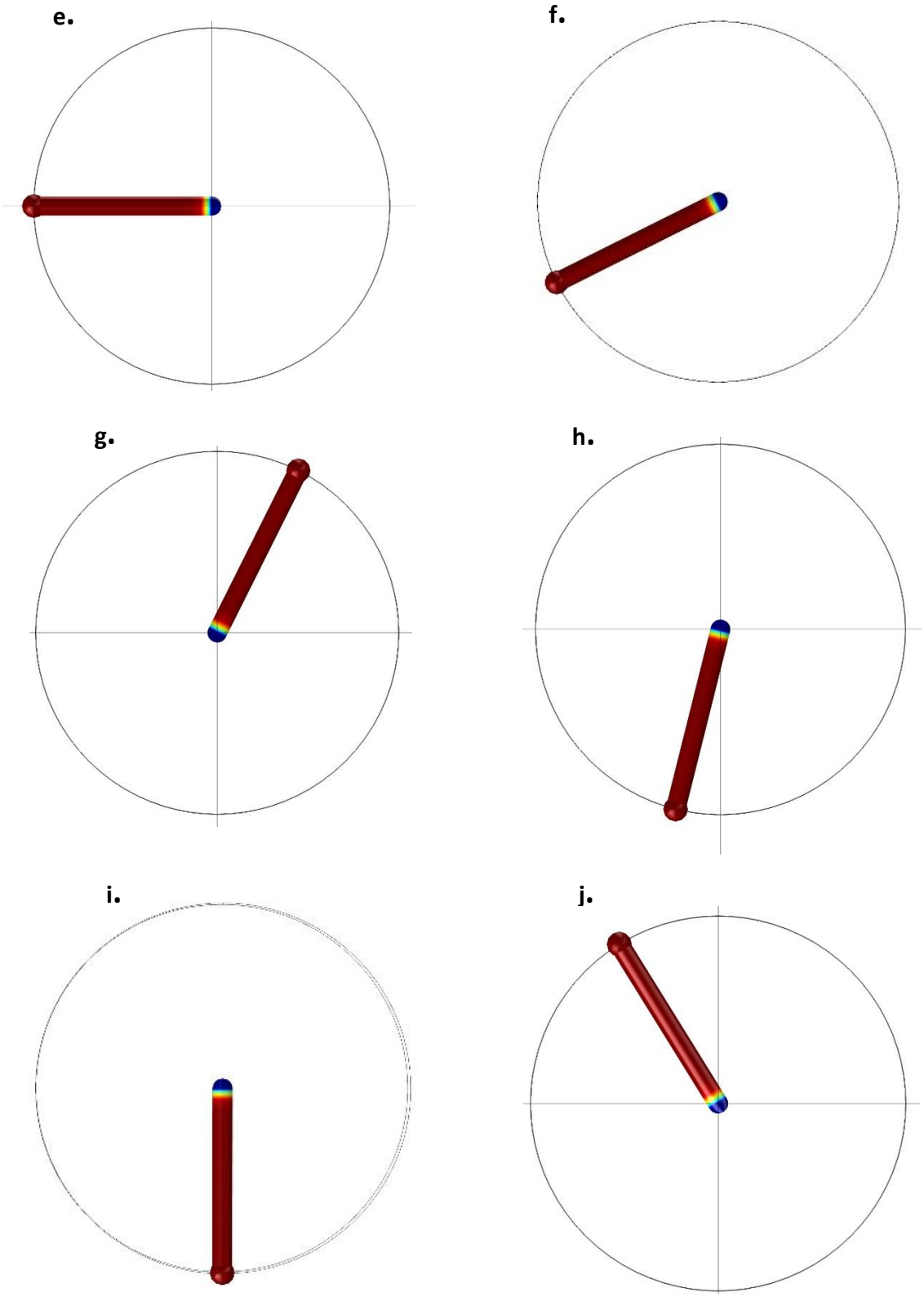

Figure 4.33 *Particle trajectories with a magnetic field gradient applied in different directions. The different excitation types are depicted in table 4.3.*

Another analysis was performed to investigate the feasibility of using the proposed system to control a magnetic device against the blood flow. In the preliminary numerical analysis from section 4.1.1, it was shown that a magnetic field gradient with a magnitude of at least 150 mT/m is needed to propel a 100 μm device in a small artery (Figure 4.2a). To test this with finite element analysis, a cylinder with 1 cm radius and 3 cm height, mimicking a small artery, was modeled at the center of the setup. The cylinder was supposed to be full of liquid with the viscosity of blood and with a velocity 0.1 m/s in the direction of the x-axis. The magnetic force was applied in the opposite direction. This experience is illustrated in the diagram from figure 4.34. A 100 μm particle with 10^6 A/m was released at the origin and its moving path due to calculated magnetic field and drag force was tracked using the Particle-Tracing module of Comsol.

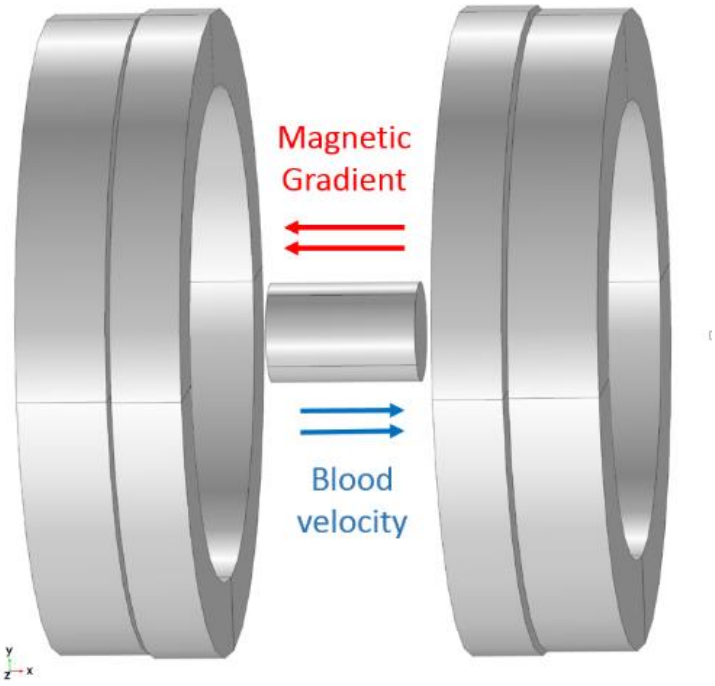

Figure 4.34 *Model Geometry of the two smaller coil pairs with a cylinder at the center. The applied magnetic gradient is in opposite direction to the blood velocity.*

In Figure 4.35a it is depicted the trajectory of the particle with no applied magnetic force. It is possible to see that the particle moves with the blood flow with a velocity of 0.1 m/s. The Maxwell pair creates a region of nearly spatially uniform magnetic field between the coils in the opposite direction of the blood flow. The simulation tracks the motion of the particle over time by solving equation 4.1, calculating the forces (magnetic and drag) based on the particle's current position and velocity.

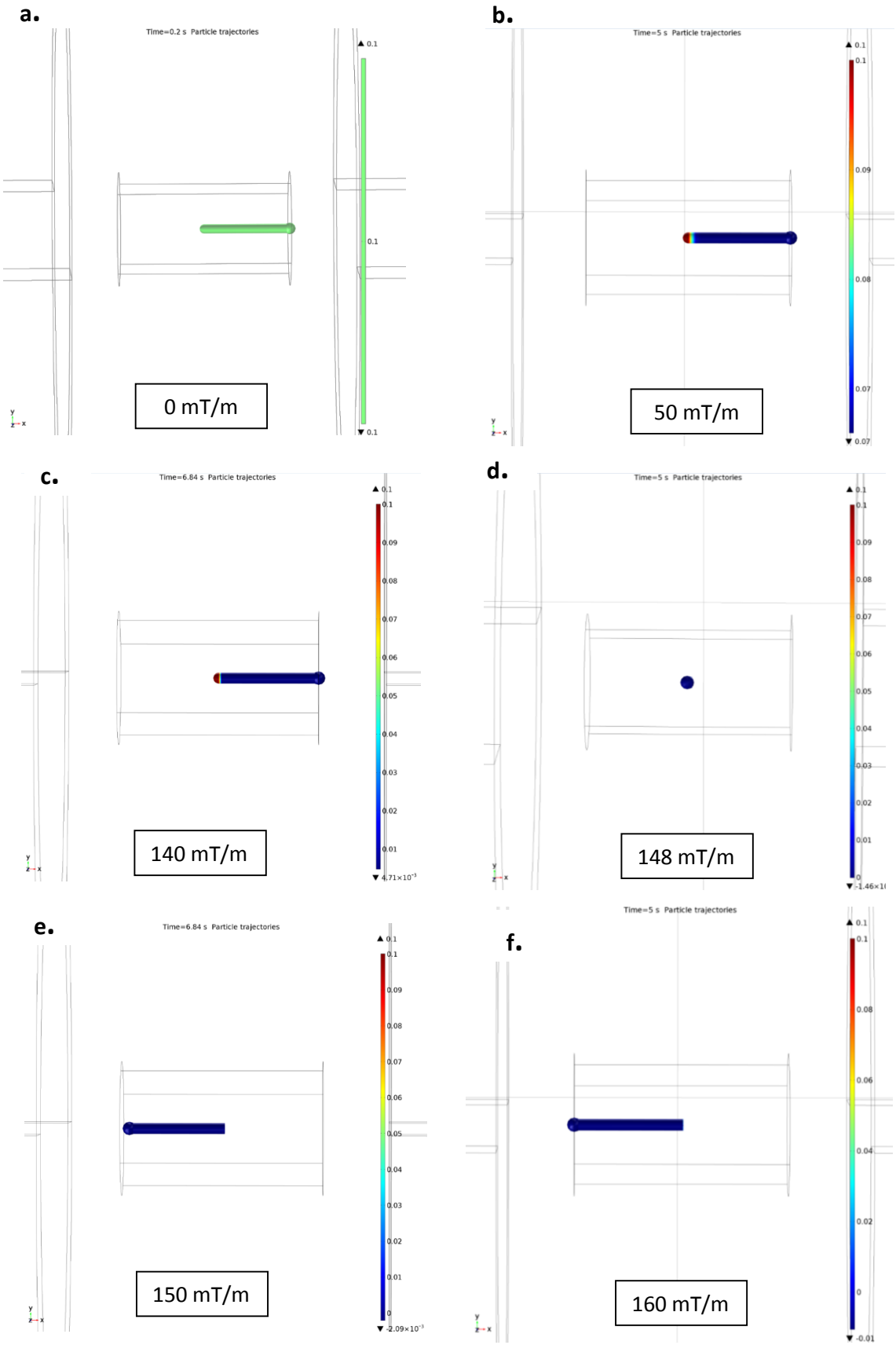

Figure 4.35 *Particle trajectories with applied magnetic field gradients of different magnitudes: a) 0mT/m,b) 50 mT/m, c) 140mT/m, d) 148mT/m, e) 150mT/m, f) 160mT/m. The color bar depicts the particle velocity.*

By energizing the coils, a nearly constant force in the direction opposite to the flow acts on the magnetized particles in the region of the constant gradient. If the magnetic force equals the drag force, the particles reach a state of equilibrium, stopping between the coils, as can be seen in figure 4.36b. In Figure 4.36a it is possible to see how the magnetic force increases with the magnetic gradient. With higher values of magnetic gradient, the velocity in the direction of x-axis is progressively lower, until it reaches the equilibrium point between the magnetic force and the drag force, where the velocity is zero. From this point, the higher the magnetic force acting on the particle, the higher the velocity achieved (in the opposite direction of the x-axis).

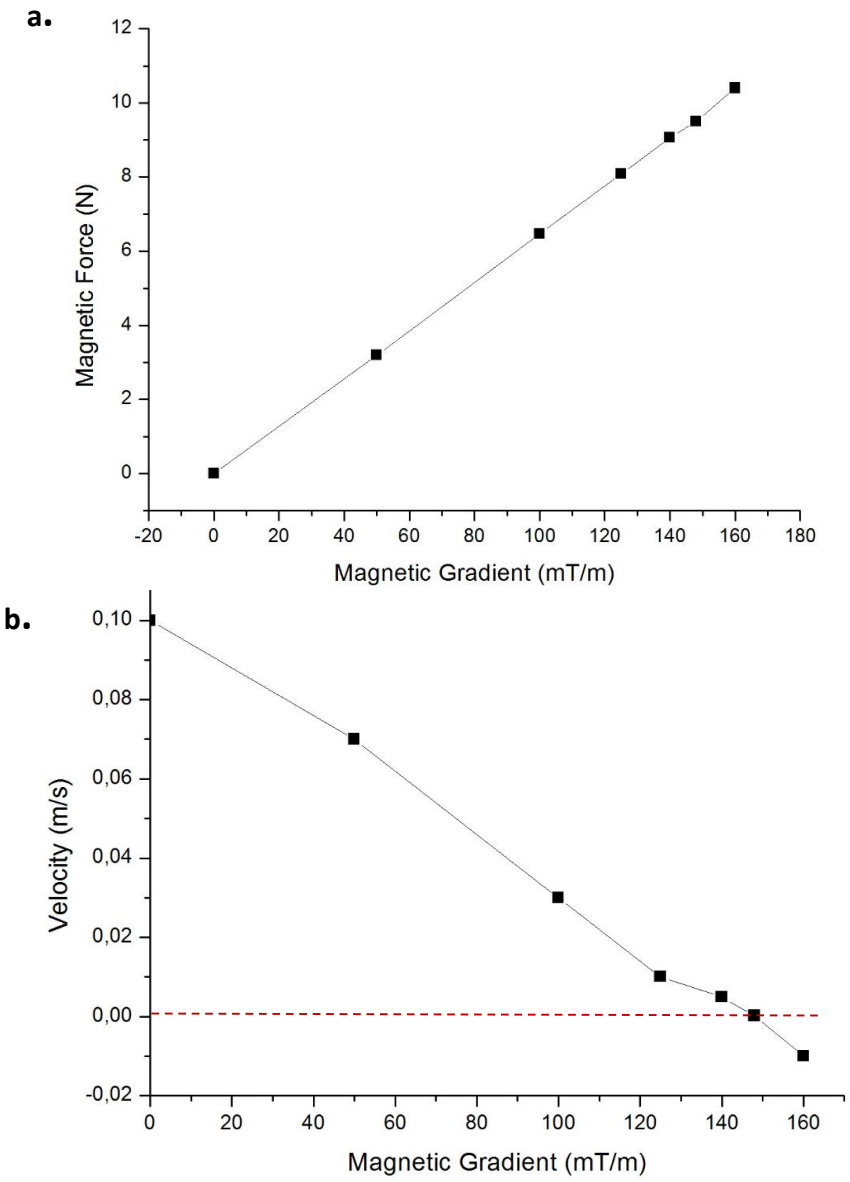

Figure 4.36*.a) Magnetic Force (N) vs the applied magnetic field gradient. b) Particle's velocity (m/s) vs the applied magnetic field gradient (mT/m). The red line represents the zero velocity.*

4.2.2 Magnetic actuation of small microparticles

4.2.2.1 Geometry

To create the model geometry the same technique from section 4.2.1.1 was used. This time, since higher static magnetic fields and higher magnetic field gradients were needed to control smaller particles, the overall dimensions of the coils had to be bigger. Iterative testing was done in order to obtain a compact system while respecting the Maxwell and Helmholtz coil configurations, and taking into account equation 4.5. The final measurements can be seen in Figure 4.37. Also, in this model a Y-Shaped vessel was added at the center of the coils. It should be mentioned that in the figures depicted in this section the scale of the channel is different from the one used in the particle tracing simulations.

In the case of Helmholtz coils, the external current density was computed using a homogenized model for the coils, each one made with 3000 wire turns and excited by a current of 7.5 A where the current flowed through both the coils in the same direction. The currents were specified to be parallel for the two coils. In the case of the Maxwell coils, each one was chosen to have 3000 wire turns and excited by a current of magnitude 7.5 A but in opposite directions. The final tetrahedral mesh had approximately 47857 elements and around 300898 degrees of freedom. Figure 4.38 depicts the resulting mesh for the 4 coils.

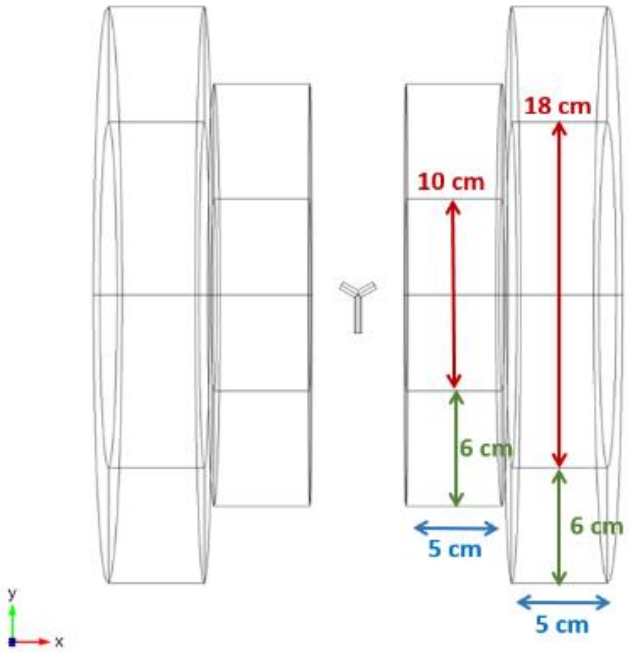

Figure 4.37 *Model Geometry of the two coil pair system with defined measurements.*

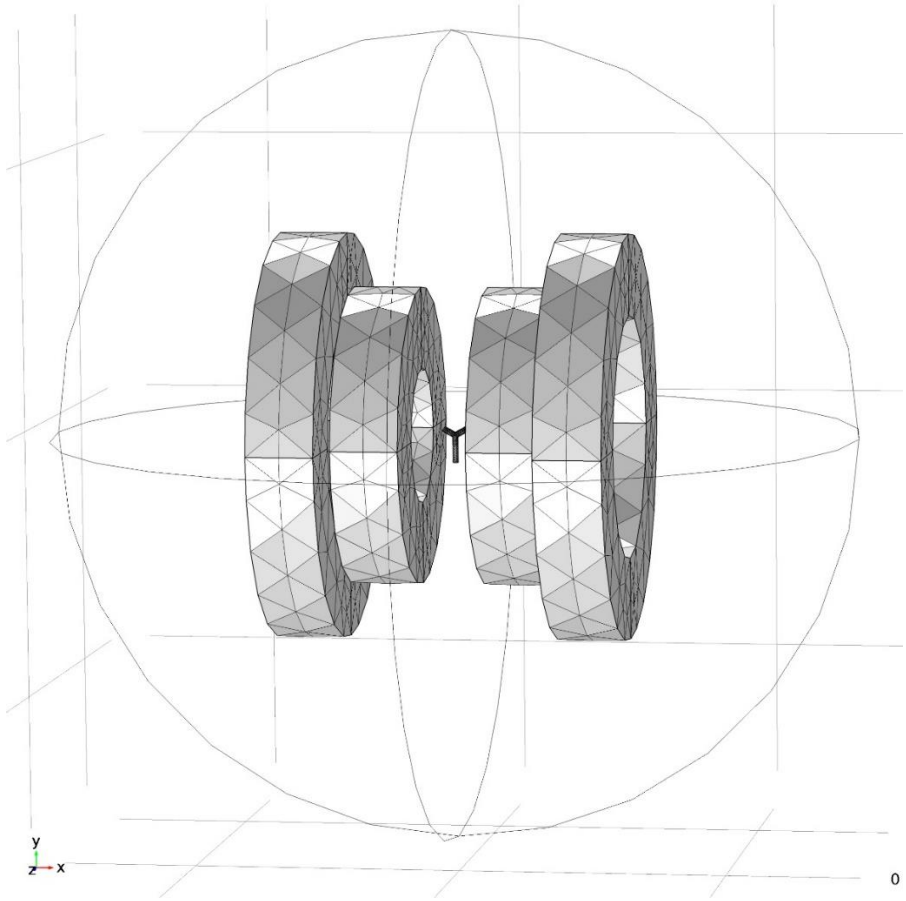

Figure 4.38 *Three dimensional Mesh Model of the two pair coils (the mesh for the air domain was omitted).*

4.2.2.2 Helmholtz coils

From Figures 4.39 to 4.41 it is possible to see that the proposed Helmholtz coil configuration is capable of generating a uniform magnetic field at the ROI. In this example, a current of 7.5 A in the same direction was applied to the two coils. Figure 4.40 shows the homogeneity of the field at the center of the coil pair and its defined direction. In Figure 4.41 it is possible to see that, with this coil configuration and applying a current of 7.5A, the magnetic flux density along a line in the $\vec{x}$-axis is approximately 130 $\pm$ 2 mT. This magnetic field intensity is not sufficient to make most materials used in these applications reach their saturation magnetization. However, as it was already discussed, for the case of magnetite, when applying an external magnetic field of H=100kA/mm (0.126T) which correspond to only 8 % of H_{sat}, the magnetite will be magnetized to M=421kA/m which corresponds to 74% of the magnetization saturation. It could be possible to increase the intensity of the magnetic field by adding soft iron cores to the coils. This possibility will be discussed in chapter 6.

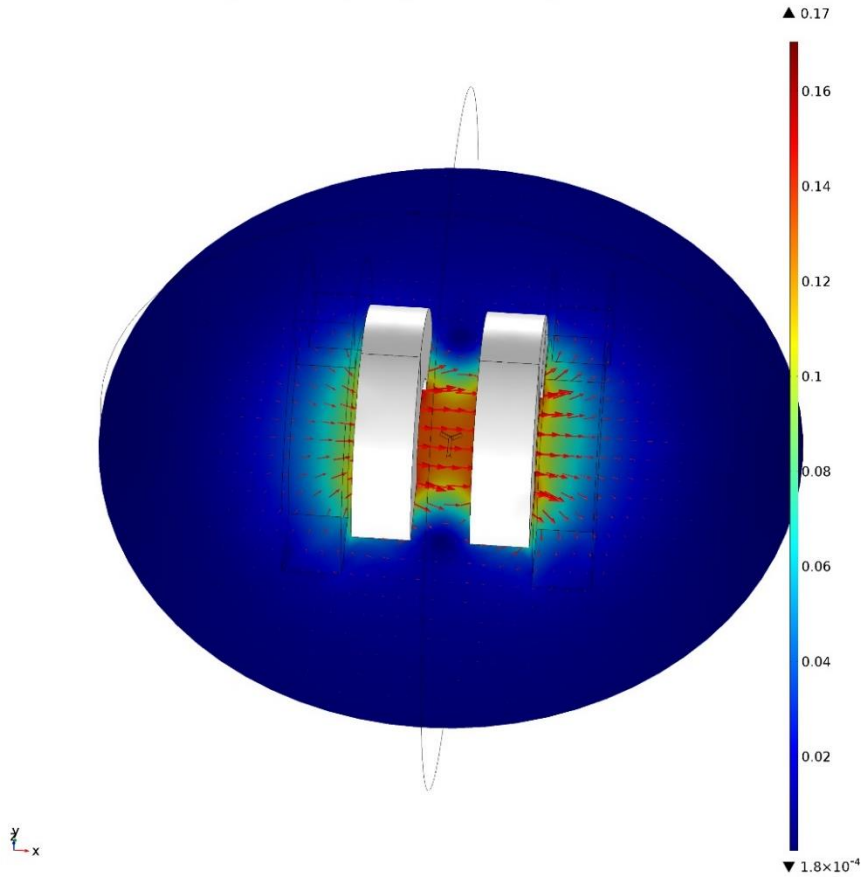

Figure 4.39 *The slice plot shows the magnetic flux density norm (T) produced by the Helmholtz coils. The arrows indicate the magnetic field strength (A/m) and direction.*

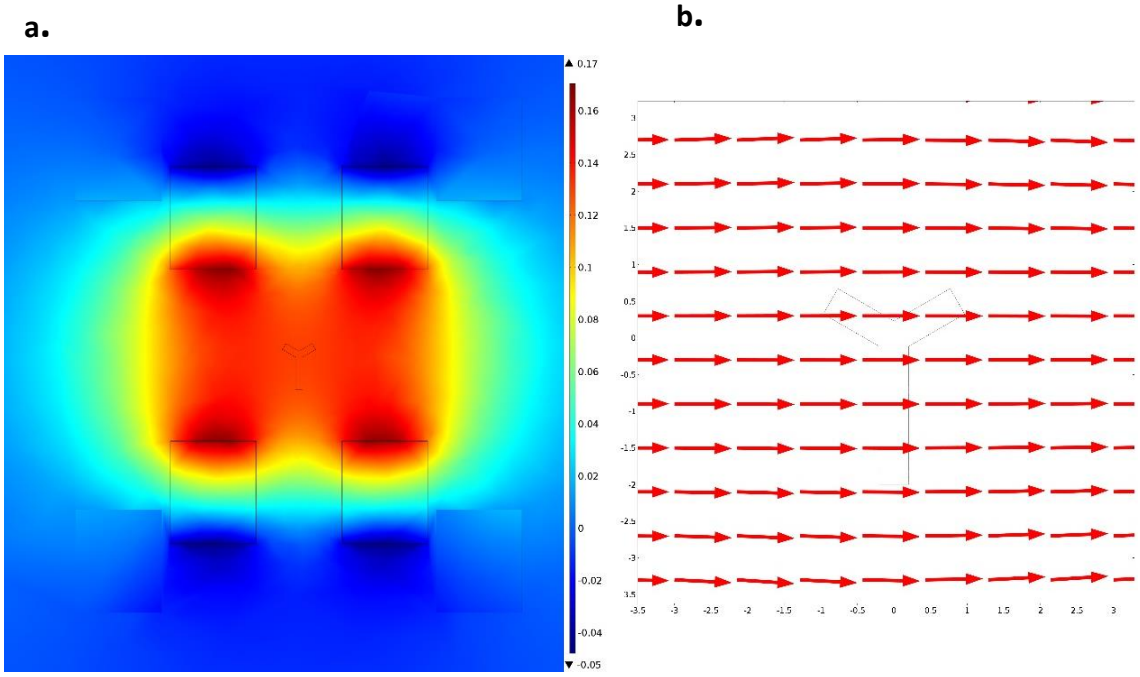

Figure 4.40 a) *The slice plot shows the magnetic flux density norm (T).* ***b)*** *The arrows indicate the magnetic field (H) direction (the arrow length is normalized to easily see the directions) in the ROI.*

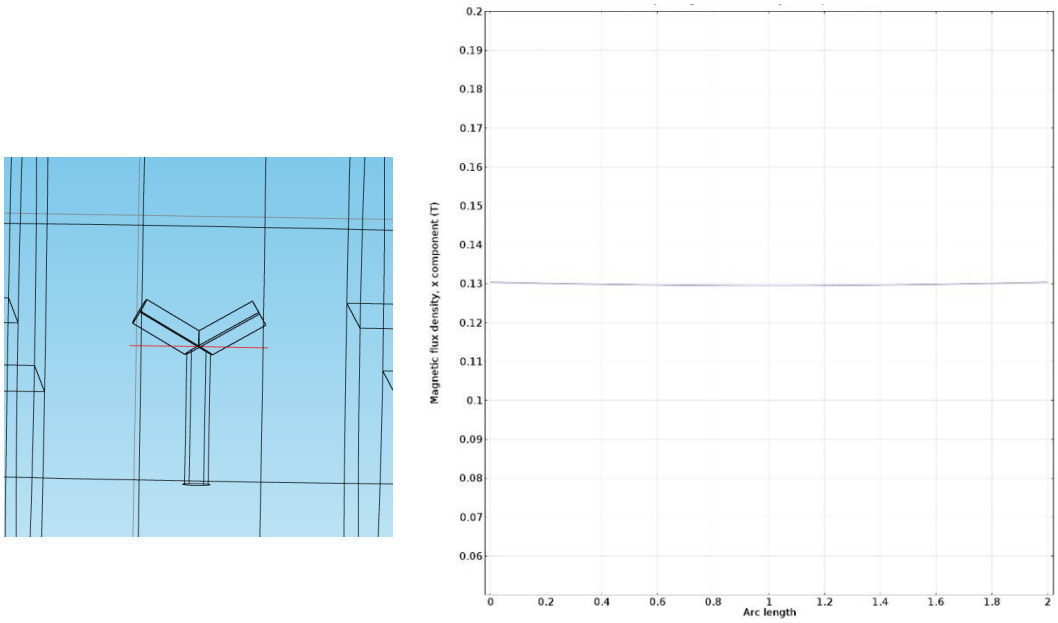

Figure 4.41 *The magnetic flux density norm (T) profile. The plot shows the profile taken along a line in the x-axis (this line is represented in red at left). A high degree of uniformity is clearly shown.*

4.2.2.3 Maxwell coils

The Figures 4.42 to 4.45 depict the results from the simulations of the Maxwell coils when a current with magnitude 7.5 A is applied in opposite directions in each coil. From the plot in Figure 4.43 it is possible to conclude that, with this configuration, the magnetic flux density varies linearly inside the two coils. At the center of the coils this value is zero which means that if only a Maxwell coil configuration is used (without combining it with the Helmholtz configuration), a material will not become magnetized, thus, it would not be possible to control it. It is possible to conclude that with this specific configuration and applying a current of magnitude 7.5A in different directions to the coils, a constant magnetic gradient of approximately 900 mT/m would be generated. This is a high value when compared to most pre-clinical devices and, from the preliminary simulations in section 4.1.2, it seems to be sufficient to propel a 10 μm particle against the drag force (Figure 4.5), depending on its saturation magnetization. In Figure 4.44 it is possible to see the linearity of the magnetic field gradient produced by this coil pair. Also, as it was shown for the previous coil design, the magnetic flux density increases in proportion to the input current density. Different magnetic force can be obtained by adjusting the input current of Maxwell coils to generate different gradient magnetic fields. By changing the direction of the currents in the coils, the gradient direction is changed (Figure 4.45). This is important to control the direction of the particles and it will be demonstrated in section 4.2.2.5.

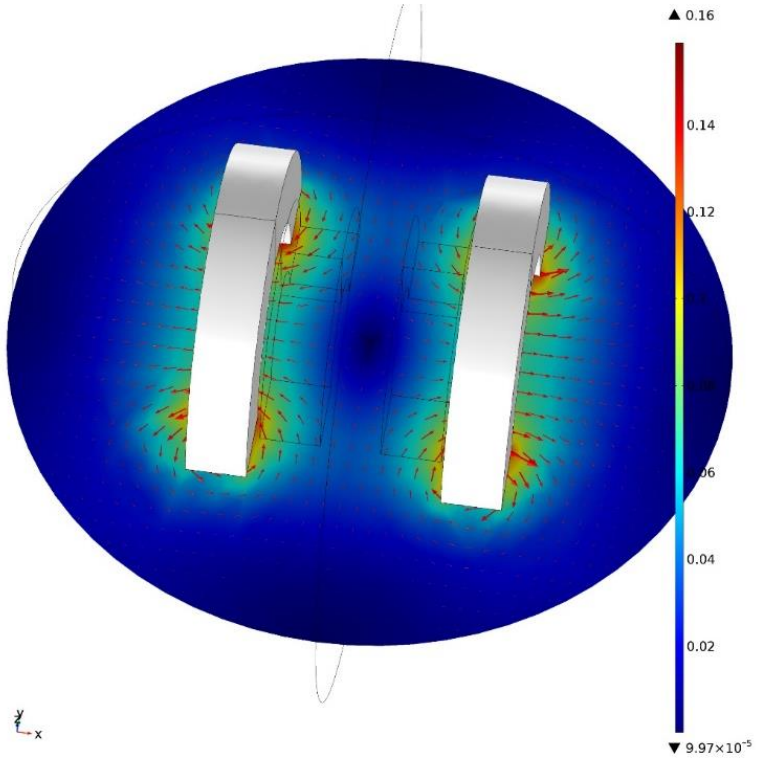

Figure 4.42 *The slice plot shows the magnetic flux density norm (T). The arrows indicate the magnetic field (H) strength and direction*

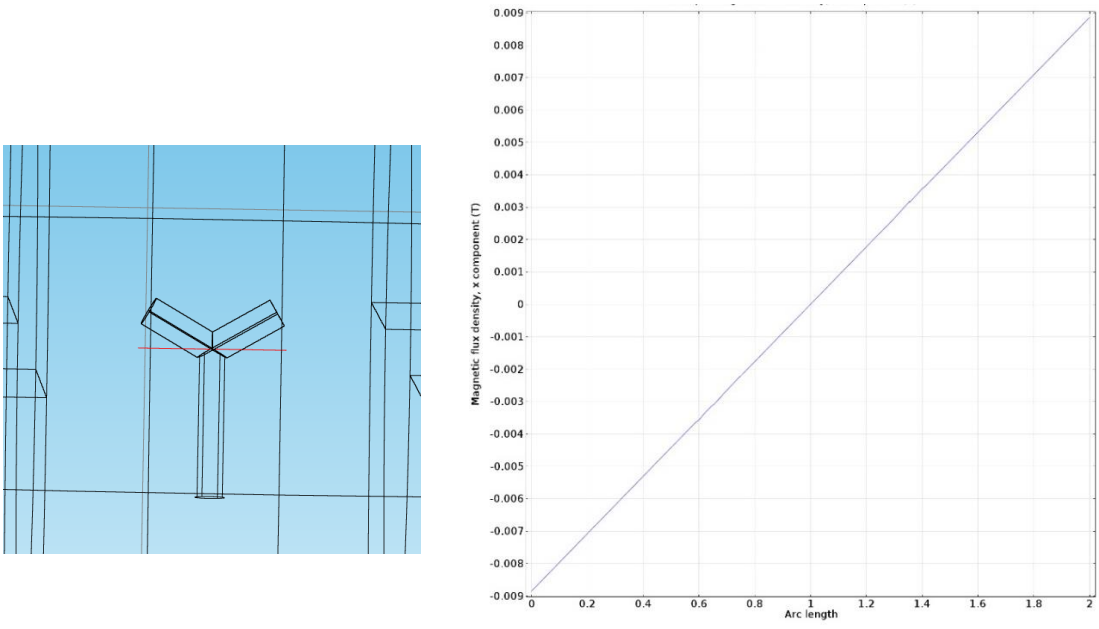

Figure 4.43 *The slice plot shows the magnetic flux density norm (T). The arrows indicate the magnetic field (H) strength and direction.*

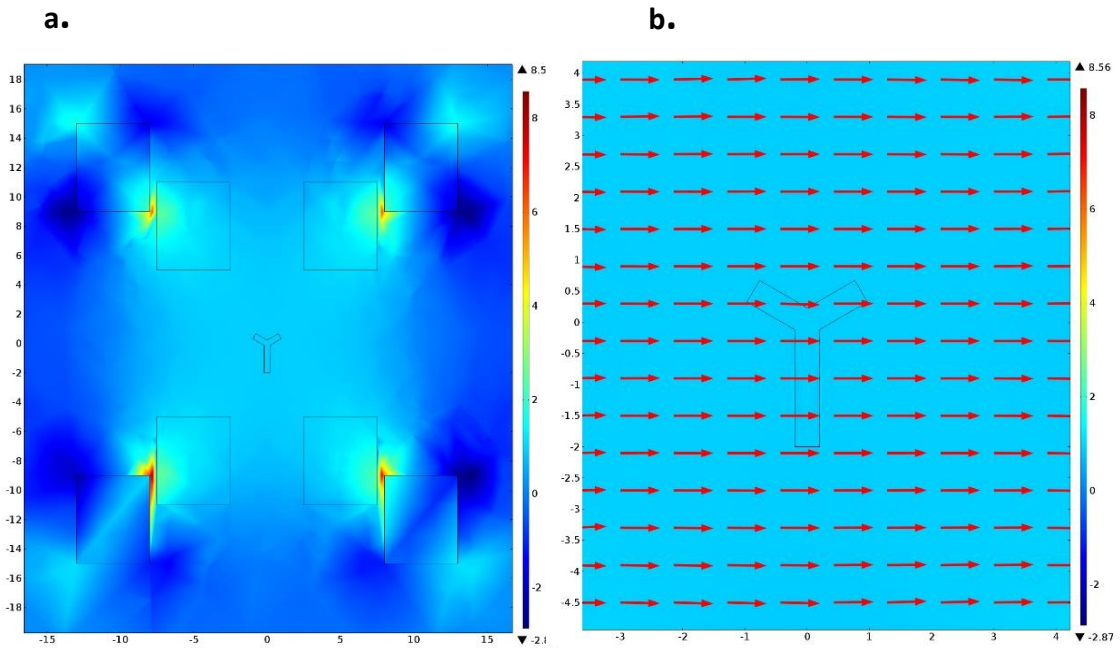

Figure 4.44 a) *The slice plot shows the magnetic field gradient in T/m.* ***b)*** *The arrows indicate the gradient field (H) direction (the arrow length is normalized to easily more see the directions) in the ROI.*

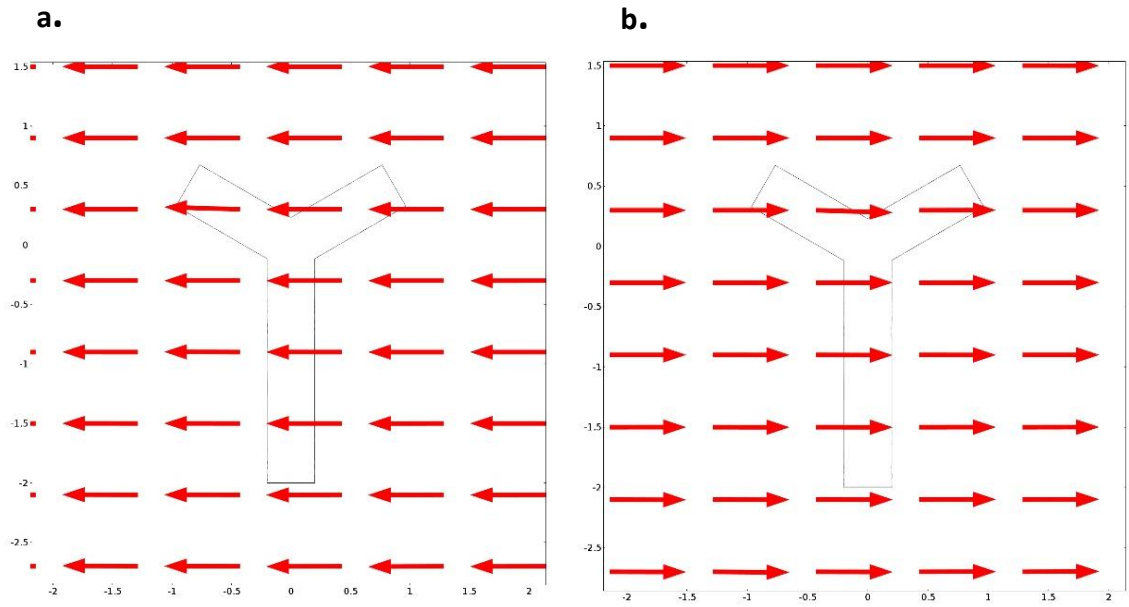

Figure 4.45 *The arrows indicate the magnetic field gradient direction for applied currents with opposite directions: a) direction θ =180º; b) direction θ =0º, where θ is the angle represented in Figure 4.4.*

4.2.2.4 Helmholtz and Maxwell coils

Both pairs of Helmholtz and Maxwell coils have to work to simultaneously magnetize and propel the magnetic device in a desired direction. Applying both sets of coils, their magnetic fields are superimposed. Figure 4.46 shows the magnetic flux density on the x-z plane (y=0) produced by the $\vec{x}$-axis Helmholtz and Maxwell coils. In this figure, the color scale indicates the magnitude of the magnetic flux density (also represented in Figure 4.47a) and the arrows indicate the magnitude and direction of the magnetic field (also represented in Figure 4.47b). Similarly to what was observed and explained in section 4.2.1.5.3, with this configuration, it is also possible to detect an interference caused by the superposition of the electromagnetic fields produced by both coil configurations. This is possible to see in Figure 4.47 and in Figure 4.48 where it is particularly problematic: the flux is relatively uniform between the coils, however an interference is evident closer to the edges of the coils (compare Figure 4.47b with Figure 4.40b). Thus, the alignment direction and propulsion force of the microrobot can be distorted according to the position of the microrobot.

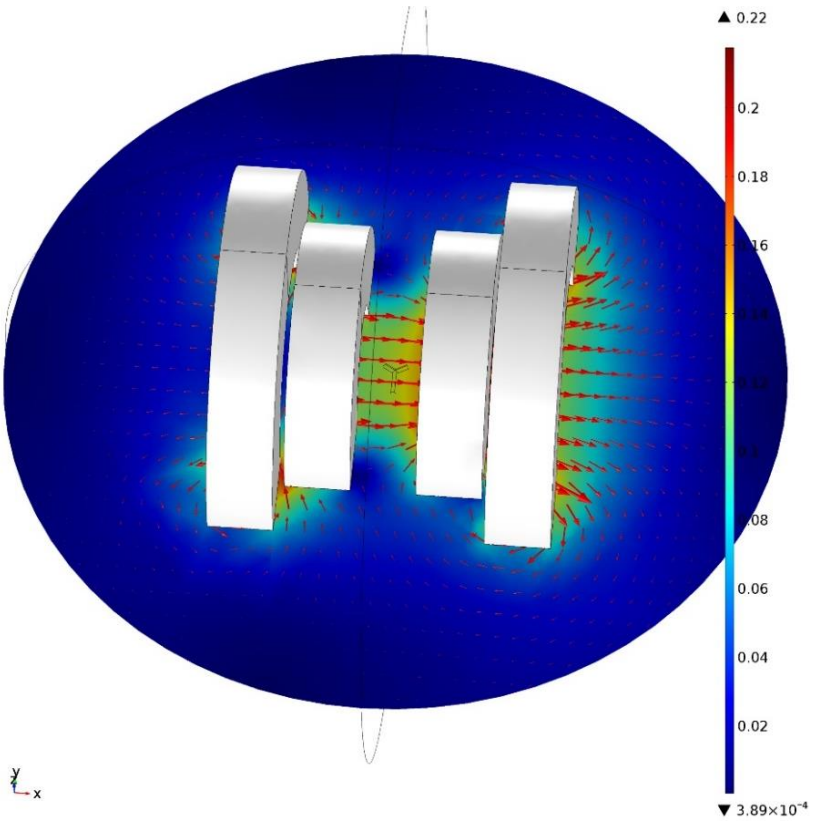

Figure 4.46 *The slice plot shows the magnetic flux density norm (T). The arrows indicate the magnetic field (H) strength and direction.*

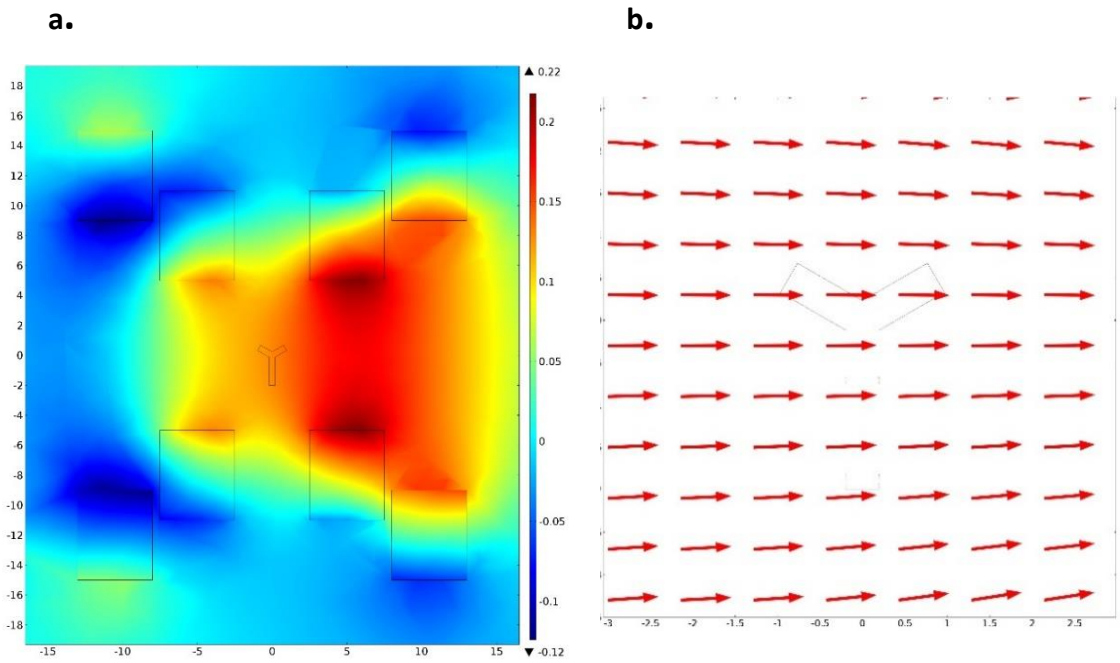

Figure 4.47 a) *The slice plot shows the x-component of the magnetic flux density (T).**b)** The arrows indicate the magnetic field (H) direction (the arrow length is normalized to easily see the directions).*

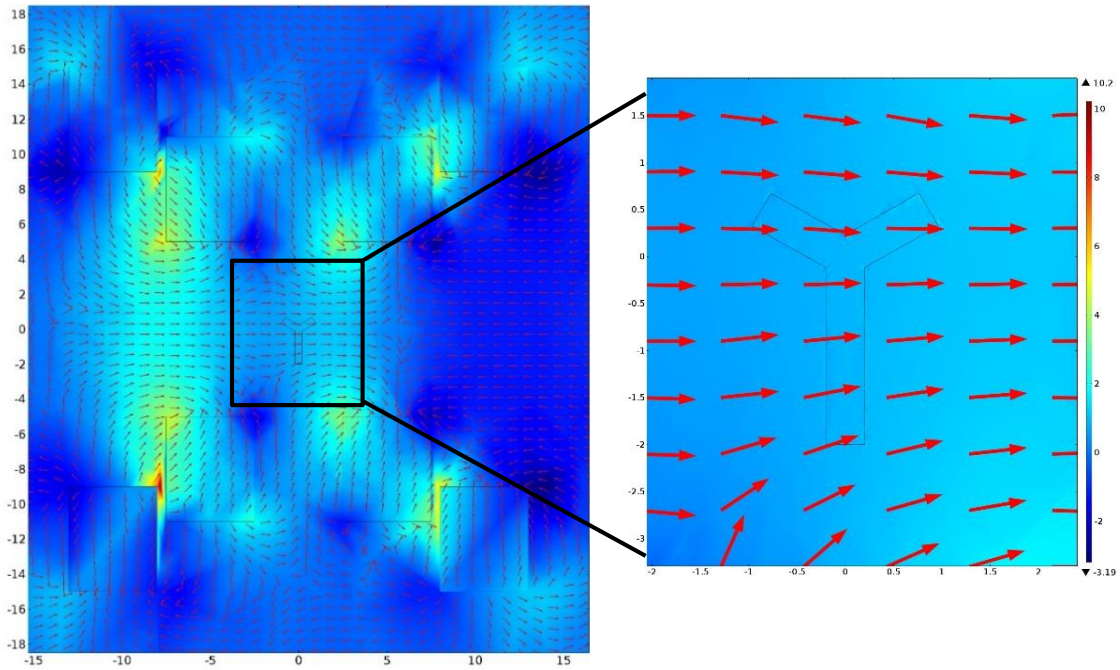

Figure 4.48 a) *The slice plot shows the magnetic field gradient (T/m). The arrows indicate the magnetic field gradient direction.*

4.2.2.5 Particle Tracing

To simulate the path of magnetic particles in blood vessels due to magnetophoretic and drag forces, the creeping flow interface as well as the particle tracking module of COMSOL were used. The goal was to evaluate the performance of the proposed setup and steering approach.

The geometry chosen for this study was a bifurcation vessel (Y-shaped) with one inlet and two outlet channels, as shown in figure 4.49a. The radius of the vessel was considered to have a constant value of 0.5 mm (large arteriole) and the length of the inlet was considered to be 2 mm. The model was created in 3D and meshed automatically using an extra fine mesh. The mesh needed to be extra fine to ensure that the particle motion was accurate through the modeling domain. The result can be seen in Figure 4.49b.

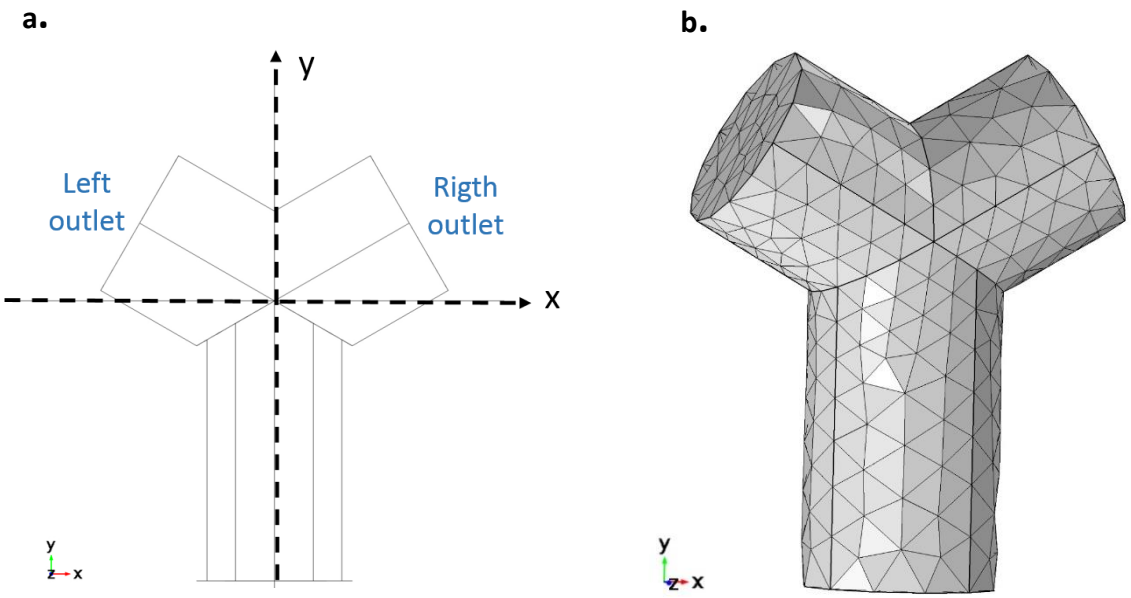

Figure 4.49 *Bifurcation vessel (Y-shaped) a) Schematic, b) Three dimensional Mesh Model.*

The blood flow was considered to be steady creeping flow, which was supposed to flow into the channel from the inlet and to exit the channel in the outlets. Thus, in the creeping flow interface, a uniform velocity was applied for the inlet section and a fixed pressure for the outlets. This interface, found under the Single-Phase Flow branch when adding a physics interface, solves the Stokes equations for conservation of momentum and the continuity equation for conservation of mass. It is used for simulating fluid flows for low Reynolds numbers for which the inertial term in the Navier-Stokes equations can be neglected. In this

interface, a no-slip condition for all vessel walls was assumed. In fluid dynamics, the no-slip condition is a common assumption for liquids flowing close to a solid, non-moving wall and it is due to the inner friction of the liquid. It states that layers close to the wall move at the velocity of the wall itself, which means that the fluid will have zero velocity relative to the boundary.

Fluid modeling parameters were selected to be similar to blood behavior and the surrounding environment was assumed to be air. Although blood flow is a suspension of particles and should be treated as a non-Newtonian flow, it is generally accepted that in behaves as a Newtonian fluid in arteries with diameters $\geq$ 1 mm (which is the case). The flow velocity was kept at 1 mm/s (minimum velocity value for a large arteriole). The different parameters used in these simulations are shown in Table 4.4. The resultant fluid velocity profile inside the channel is illustrated in figure 4.50.

Parameter	Value	Unit
Vessel Radius	0.5	mm
Blood Velocity	1	mm/s
Blood Viscosity	0.004	Pa.s
Blood relative permeability	1	–

Table 4.4 *Different model parameters used in the simulations.*

The Particle Tracing for Fluid Flow module was used to compute the motion of particles in the background fluid. In this study, two types of spherical particles were considered, namely, iron oxide particles with magnetization saturation in the order of 10^5 A/m and permendur particles with saturation magnetization in the order of 10^6 A/m. Also, different simulations were made for particles with different dimensions, namely, 10 μm and 1 μm.

The maximum value of the magnetic field gradient was chosen based on the maximum values that the proposed actuation system can generate. The magnetic field gradient direction was designed to be perpendicular to the channel in such a way that particles are attracted to one of the two outlet depending on the direction of the current in the Maxwell coils.

For simplicity, the channel toward which the particles were guided is defined here as the correct outlet and the other outlet is defined as the incorrect outlet (see Figure 4.6). The particles that don't reach either outlet are assumed to remain inside the channel.

Some simplifications were made. For example, particle-to-particle interactions were neglected. The mathematical complexity of these interactions requires models that are beyond the scope of the present study. Also, there are commercial magnetic particles that are currently available without aggregations. In all the simulations it was considered that particles are at the value of saturation magnetization. For realistic results, the B-H curves for the particle's material should be applied. The different parameters used to simulate the particles are presented in Table 4.5 and Table 4.6 for magnetite and permendur, respectively.

Parameter	Value	Unit
Particle Radius	1×10^{-5} 1×10^{-6}	m
Particle Magnetization	3.5×10^{5}	A/m
Particle density	5200	Kg/m^3

Table 4.5 *Different model parameters used in the simulations for magnetite (iron oxide).*

Parameter	Value	Unit
Particle Radius	1×10^{-6}	m
Particle Magnetization	1×10^{6}	A/m
Particle density	6500	Kg/m^3

Table 4.6 *Different model parameters used in the simulations for permendur.*

To check the performance of the proposed method, the particle trajectories inside the channel were investigated. In the first simulation, to test the response of a magnetic particle to the direction of the magnetic gradient, one particle with 10 μm and characteristics from table 4.5, was released at the center of the inlet and directed to the desired outlet by controlling the direction of the current. The particle moving path due to the calculated magnetic field and drag force in blood flow was tracked for 2 seconds using the Particle-Tracking module of COMSOL. The particle and its paths towards the different outlets are shown in Figure 4.51 and 4.52, for gradients in opposite directions.

In the next simulation, the trajectory of 30 particles with the same characteristics released at random positions from the inlet surface was studied. By controlling the current in the coils it was possible to control the magnitude of the magnetic field gradient. Several magnetic field gradients were considered with intensities in the range of 0 up to 1000mT/m (0 to 8×10^5 A/m^2), to deliver 10 μm particles with to a specific region which, in this case, was the left outlet. The resultant particle trajectories are depicted in Figures 4.53 to 4.57. Figure 4.53 shows the trajectory of the particles with no applied magnetic force. The numbers of particles entering into each outlet channel and the number of particles remaining in the inlet channel were counted for each sample. With this information, different plots were created.

Finally, in a different set of simulations, the trajectories of 30 particles released at random position of the inlet surface were studied but this time the particles had 1 μm size. Magnetic field gradients with the same intensity range (0 up to 1000mT/m) were applied. First, the control was attempted with particles made of magnetite and next with particles made of permendur with characteristics described in table 4.6.

4.2.2.5.1 Results

Figure 4.50 illustrates the computed blood flow velocity profile inside the channel. The slice plot shows the low velocity near the walls and higher velocity in the center of the channel.

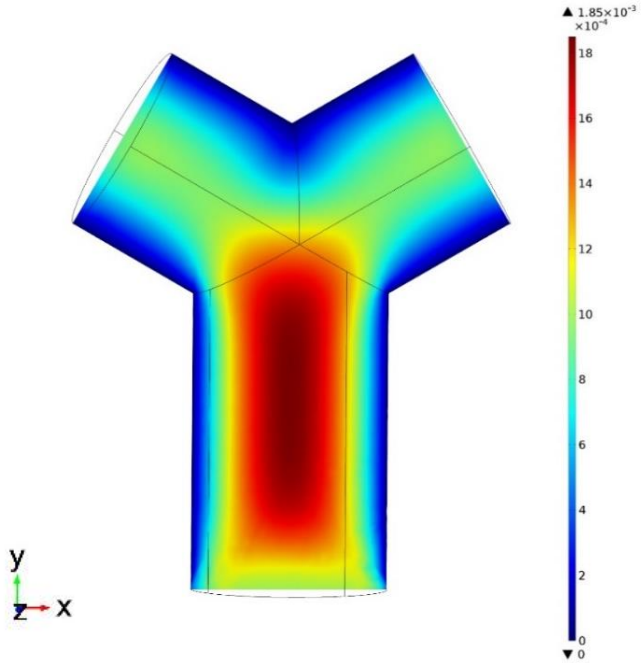

Figure 4.50 *The slice plot shows the velocity magnitude (m/s) inside the channel.*

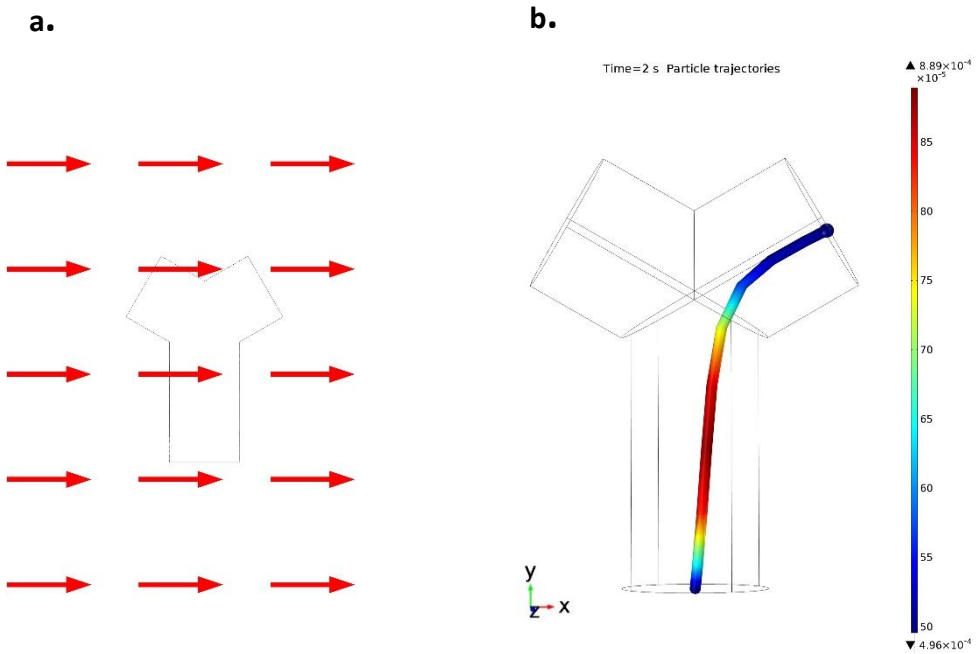

***Figure 4.51**: **a)** Direction of the applied magnetic field gradient **b)** Trajectory of one particle with 10 µm size and magnetization saturation 3.5×10^5A/m, with an magnetic gradient of 125 T/m (1×10^5 A/m^2).*

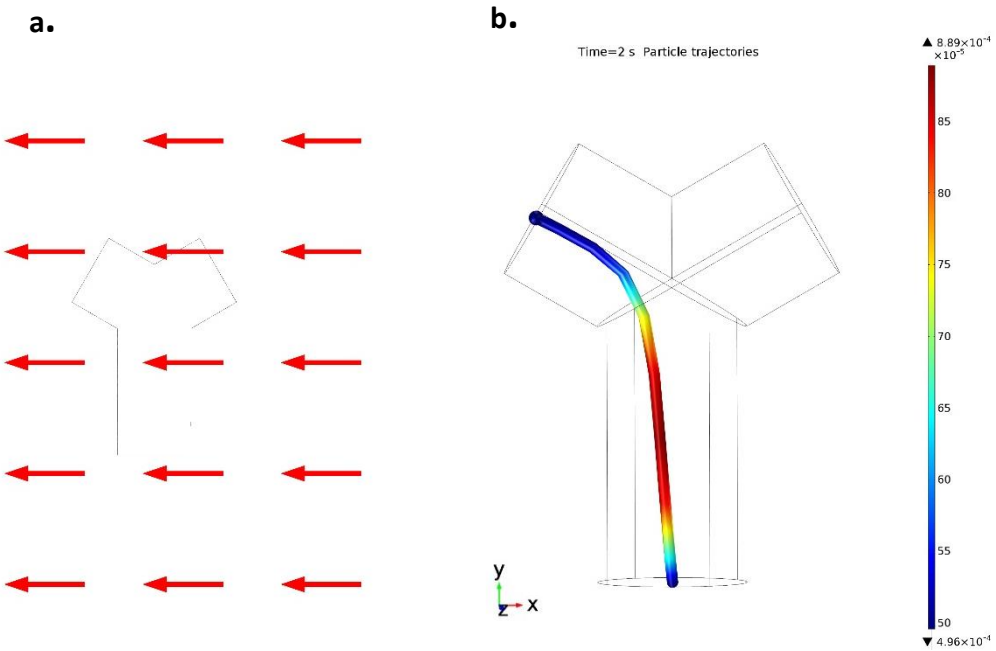

***Figure 4.52 a)** Direction of the applied magnetic field gradient **b)** Trajectory of one particle with 10 µm size and magnetization saturation 3.5×10^5A/m, with an magnetic gradient -125 T/m (-1×10^5 A/m^2).*

Figure 4.51 and figure 4.52 show that is possible to steer a 10 μm particle navigating in the center of a blood vessel. By controlling the direction of the magnetic gradient it is possible to choose the outlet where this particle ends.

To investigate the performance of the method it was important to study the trajectory of several particles with different starting points since, as it is possible to see in figure 4.50 the velocity in the blood vessel is different in different points. Several magnetic field gradients were applied and the steering rate parameter was estimated.

With this chosen geometry (a Y-shaped vessel), the particles can only be directed to two outlets. Thus, the steering ratio without an applied magnetic force should be approximately 0.5. In other words, it was expected that the flow would direct an equal number of particles to the left outlet and right outlet branches of the channel. By applying a magnetic force in a perpendicular direction to the blood flow, it was expected that a progressively higher number of particles would reach the desired outlet and that, consequently, the steering rate would rise. In the results depicted from figure 4.53 to figure 4.57, 30 particles were simulated and a progressively higher magnetic field gradient (0 up to 1000mT/m or 0 up to 8.0×10^5 A/m^2) was applied in a direction opposite to x-axis. The goal was to maximize the percentage of magnetic particles that flow through the left branch.

The numbers of particles entering each outlet and the steering ratios are in showed in Table 4.7 and are plotted in figures 4.58 and 4.59.

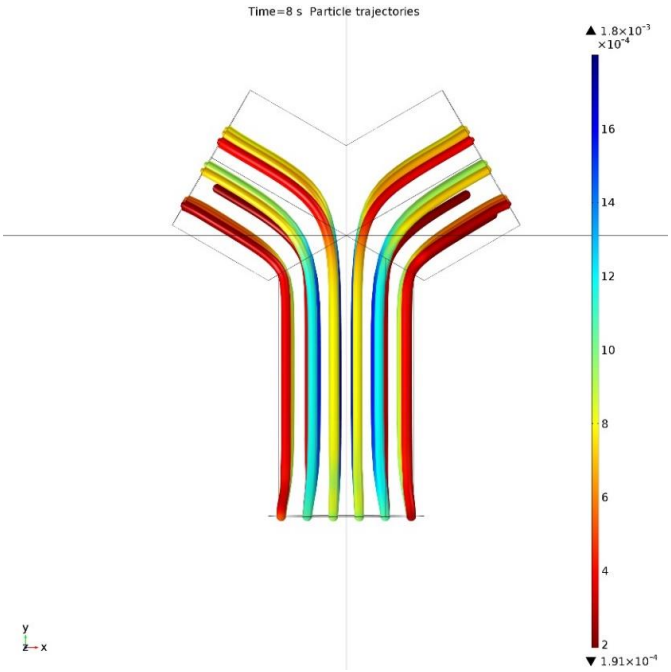

***Figure 4.53**: Trajectory of 30 particles with 10 µm size with no applied magnetic field gradient and U_0=0.5×10^{-3}m/s.*

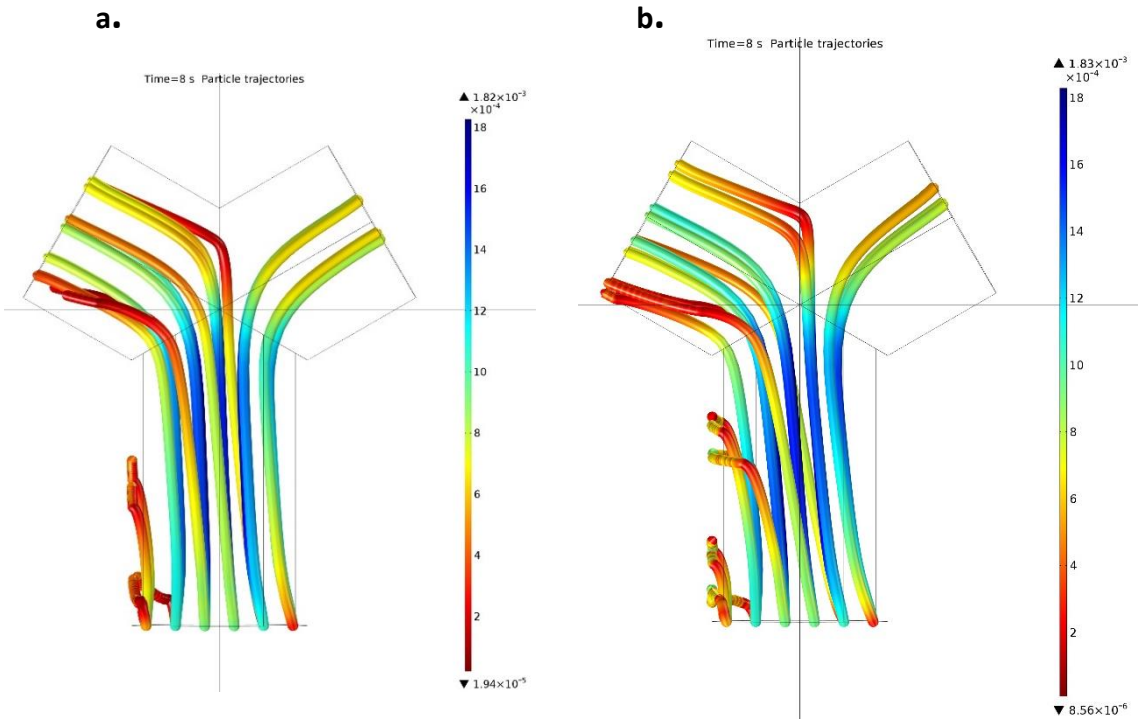

***Figure 4.54**: Trajectory of one particle with 10 µm size and magnetization saturation 3.5×10^{5}A/m, with an applied magnetic gradient of **a)** -125mT/m (-1×10^5 A/m^2); **b)** -250 mT/m (-2×10^5 A/m^2).*

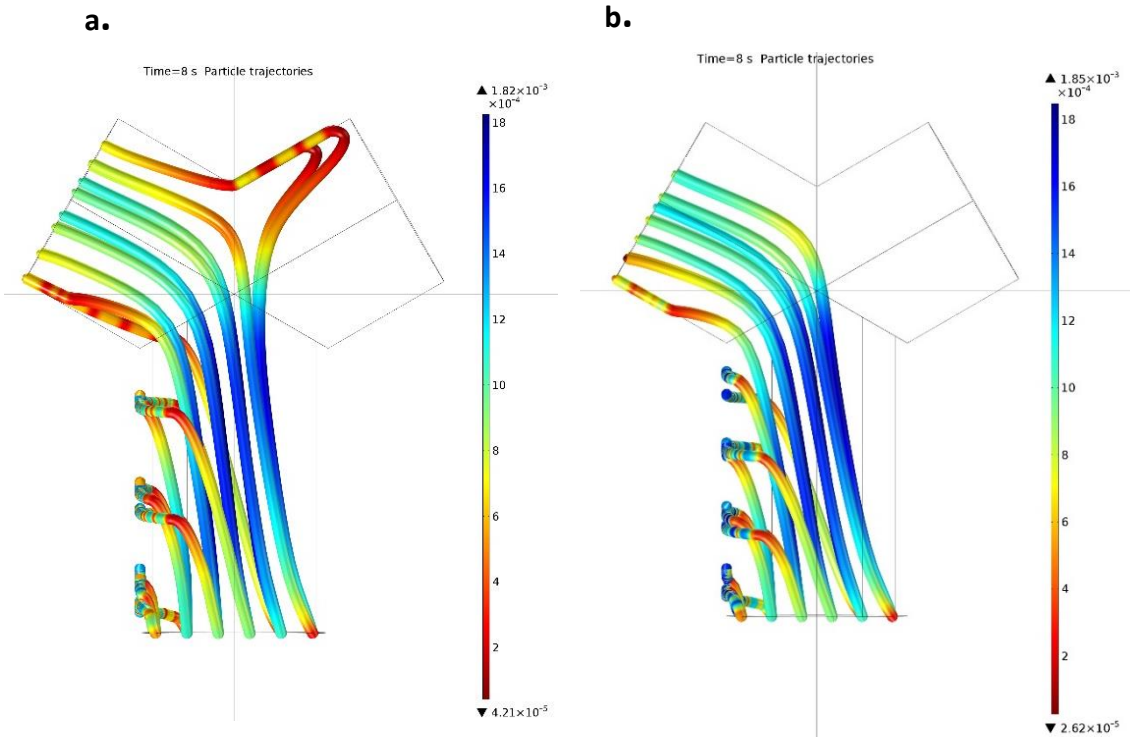

***Figure 4.55** Trajectory of one particle with 10 µm size and magnetization saturation 3.5×10^{5}A/m, with an applied magnetic gradient of **a)** -380mT/m (-3×10^5 A/m^2); **b)** -500 mT/m (-4×10^5 A/m^2).*

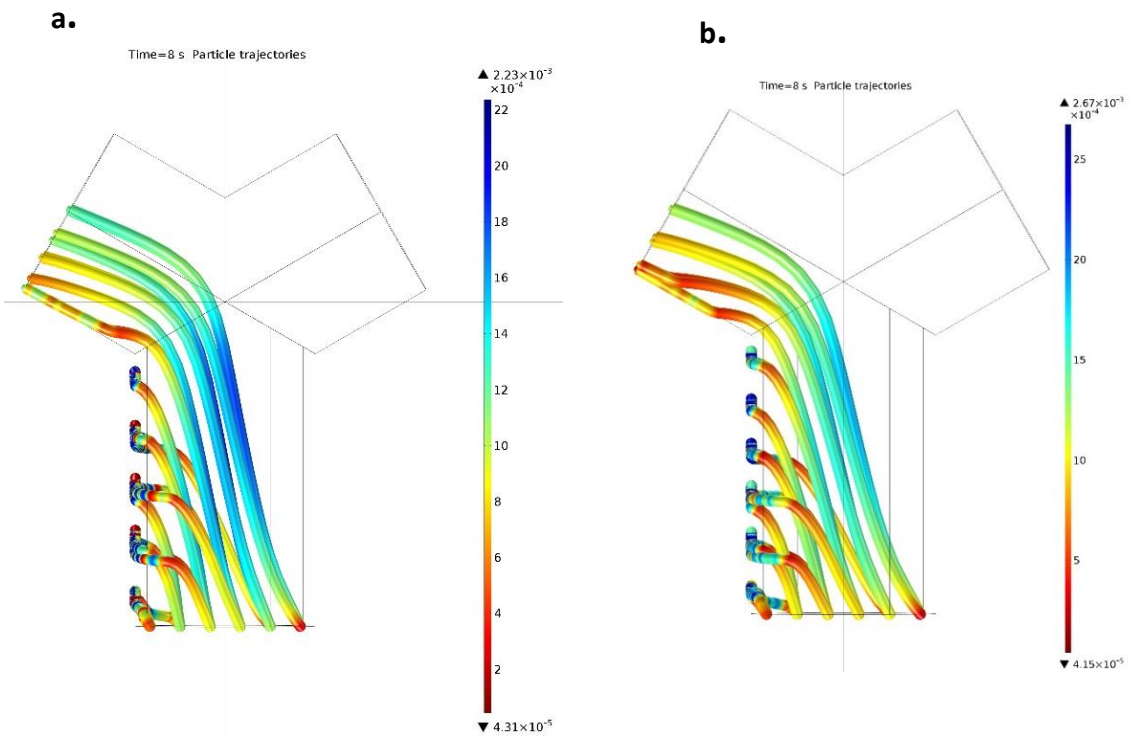

Figure 4.56 *Trajectory of one particle with 10 µm size and magnetization saturation 3.5×10^{5}A/m, with an applied magnetic gradient of* ***a)*** *-630 mT/m (-5×10^5 A/m^2);* ***b)*** *-750 mT/m (-6×10^5 A/m^2).*

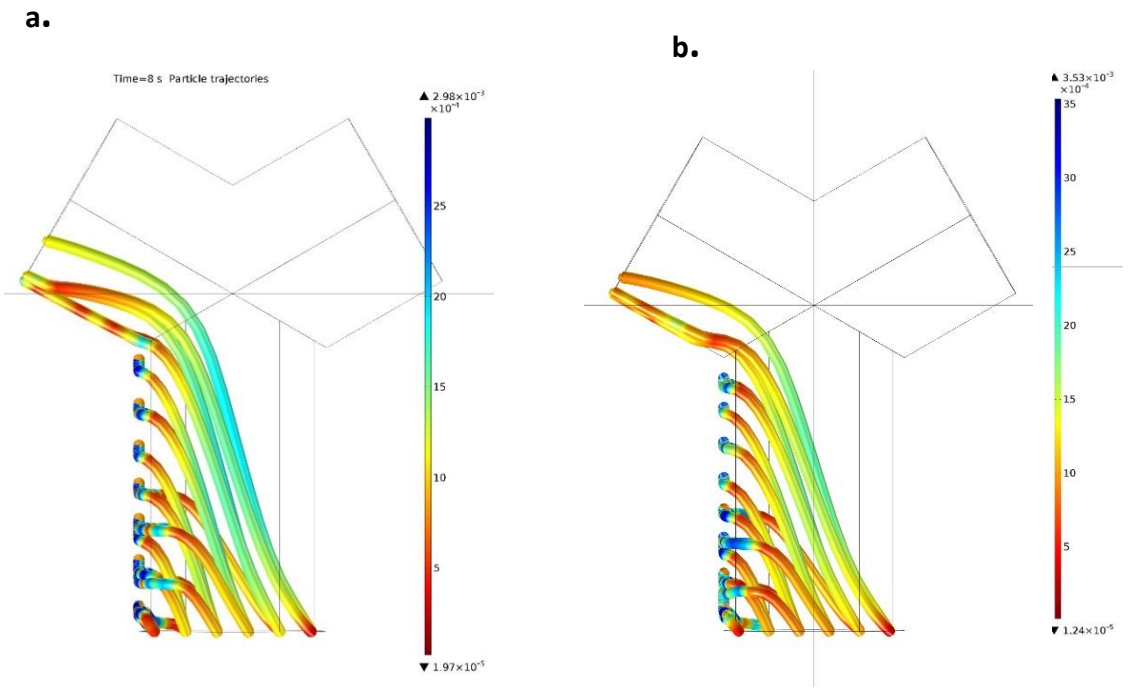

Figure 4.57 *Trajectory of one particle with 10 µm size and magnetization saturation 3.5×10^{5}A/m, with an applied magnetic gradient of* ***a)*** *-880mT/m (-7×10^5 A/m^2);* ***b)*** *-1000 mT/m (-8×10^5 A/m^2).*

Magnetic gradient (A/m²)	Magnetic Force (N)	Correct Outlet	Remaining	Steering efficiency
0	0	15	0	0.50
$\mathbf{2.5 \times 10^4}$	6.6×10^{-12}	12	3	0.40
$\mathbf{5.0 \times 10^4}$	1.3×10^{-11}	13	4	0.43
$\mathbf{7.5 \times 10^4}$	2.0×10^{-11}	16	5	0.53
$\mathbf{1.0 \times 10^5}$	2.6×10^{-11}	17	5	0.57
$\mathbf{2.0 \times 10^5}$	5.3×10^{-11}	17	9	0.57
$\mathbf{3.0 \times 10^5}$	7.9×10^{-11}	17	13	0.57
$\mathbf{4.0 \times 10^5}$	1.1×10^{-10}	14	16	0.47
$\mathbf{5.0 \times 10^5}$	1.3×10^{-10}	12	18	0.40
$\mathbf{6.0 \times 10^5}$	1.6×10^{-10}	10	20	0.33
$\mathbf{7.0 \times 10^5}$	1.8×10^{-10}	8	22	0.27
$\mathbf{8.0 \times 10^5}$	2.1×10^{-10}	6	24	0.20

Table 4.7 *Results from the simulations. Trajectory of 30 particles with 10 µm size and magnetization saturation 3.5×10⁵A/m, with a range of applied magnetic gradient, in A/m².*

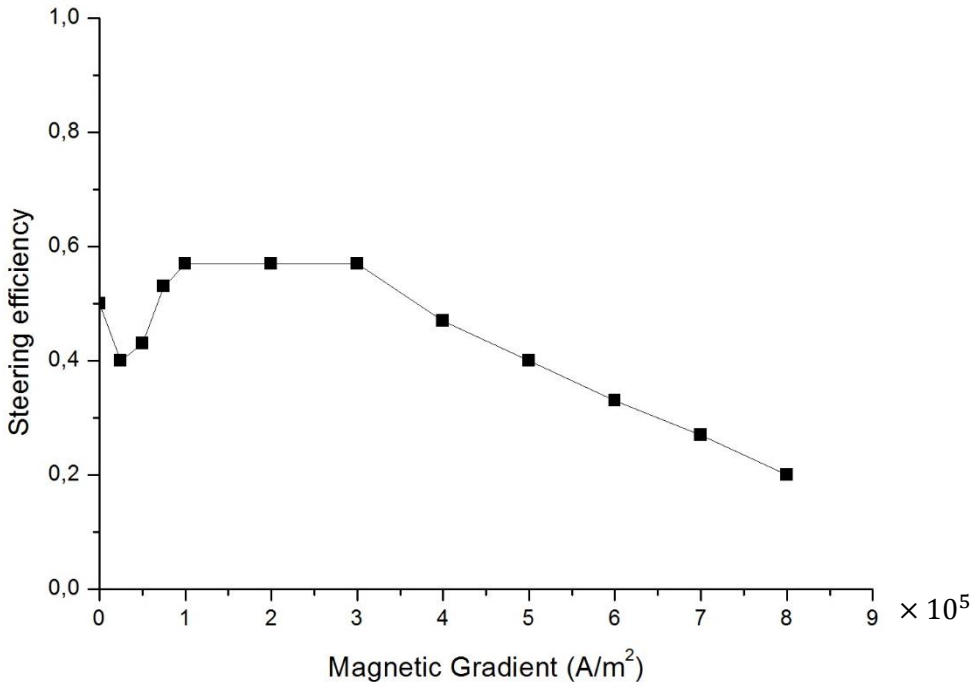

Figure 4.58 *Steering efficiency for different applied magnetic gradient, for one particle with 10 µm size and magnetization saturation 3.5×10⁵A/m.*

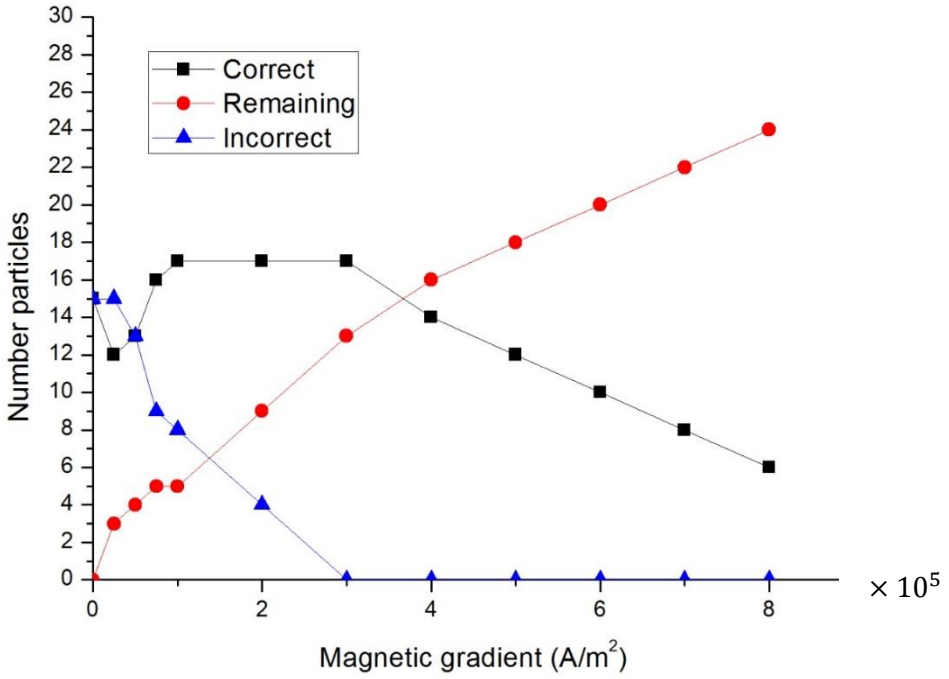

Figure 4.59 *Number of particles entering into each outlet channel (correct and incorrect) and the number of particles remaining in the channel, for different applied magnetic gradient, for one particle with 10 µm size and magnetization saturation 3.5×10^{5}A/m.*

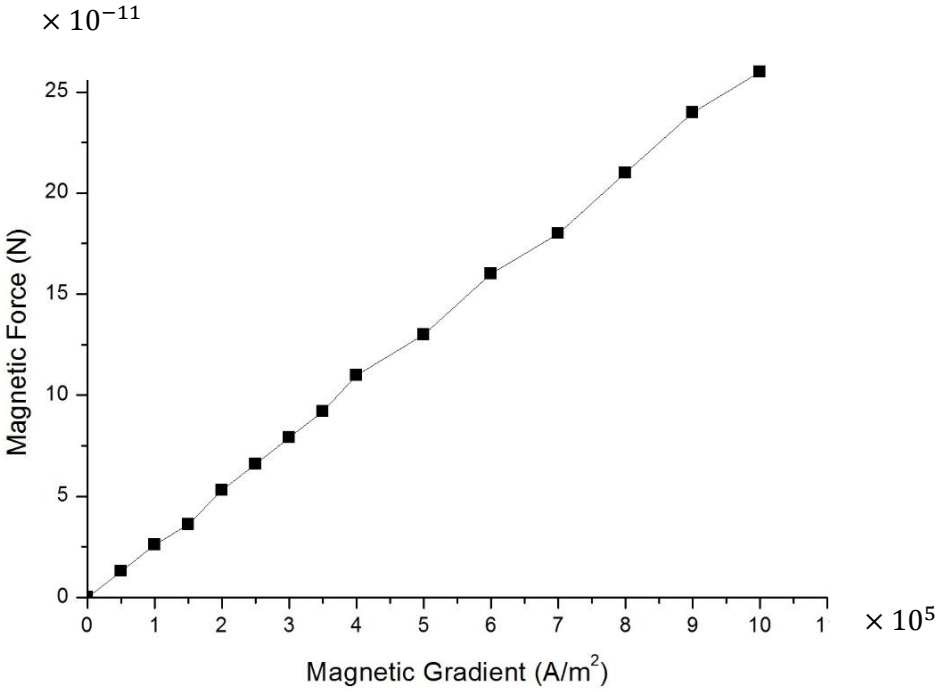

Figure 4.60 *Magnetic force (N) for different applied magnetic gradients, for one particle with 10 µm size and magnetization saturation 3.5×10^{5}A/m.*

The steering efficiencies for the different applied magnetic field gradients are depicted in Table 4.7 and plotted in Figure 4.58 (using particles with the parameters described in Table 4.5). It is possible to see that, with this parameters, the steering efficiency is maximized for a range of magnetic gradients between 125mT/m (1.0×10^4 A/m^2) and 380 mT/m (3.0×10^4 A/m^2) with the highest value of 57% being achieved. Smaller gradients produce weaker forces unable to steer the particles, resulting in an efficiency lower than 50%. However, contrary to what could be expected, from gradients larger than 380 mT/m (3.0×10^5 A/m^2) the steering efficiency started to decrease reaching approximately 20% with the maximum magnetic gradient that the proposed system can produce. This happened not because the particles ended up in the wrong outlet but because they adhered to the wall and remained inside the channel. Particles inside the channels were attracted to regions near the walls by the magnetic field gradients that were created to guide the particles to the correct outlet of the channel and. The steering force made the particles collide and "stick" to the vessel wall before reaching the bifurcation. As it was shown in figure 4.50, the velocity of the blood flow close to the vessel walls are lower that other positions inside the vessels. Thus, these particles get trapped to the wall due to the zero flow boundary condition and consequently the steering efficiency it's significantly reduced.

This phenomena is obviously not desired since it results in a low efficiency of magnetic particle guiding inside a blood vessel. Thus, it should be taken into consideration and solutions should be proposed. If the particles could be returned to the central region of the vessel, the number of the particles remaining in the vessel would decrease and, as a result, the number of particles reaching the correct outlet would increase. After some investigation it became clear that this is a new are of research. And although not many, some research groups have investigated particle behavior and possible issues during the guiding phase inside the blood vessels. In [79] the sticking and concentration of particles near a Y-shaped channel was reported. Also, in [80] and [81], the adherence of particles to vessels with a constant magnetic field was examined experimentally and through simulation, respectively. In [81] the authors claimed that the best steering strategy was to generate aggregations. This may result in clogging of the branches, which is clearly not desirable in drug delivery. To date, sticking of magnetic micro/nanoparticles in blood vessels and the effects on steering have not been fully investigated.

The same experiments were made with 1 μm magnetite particles. First, one particle with characteristics from table 4.5, was released at the center of the inlet and directed to the desired outlet by controlling the direction of the current. The results are depicted in figures 4.61a and b.

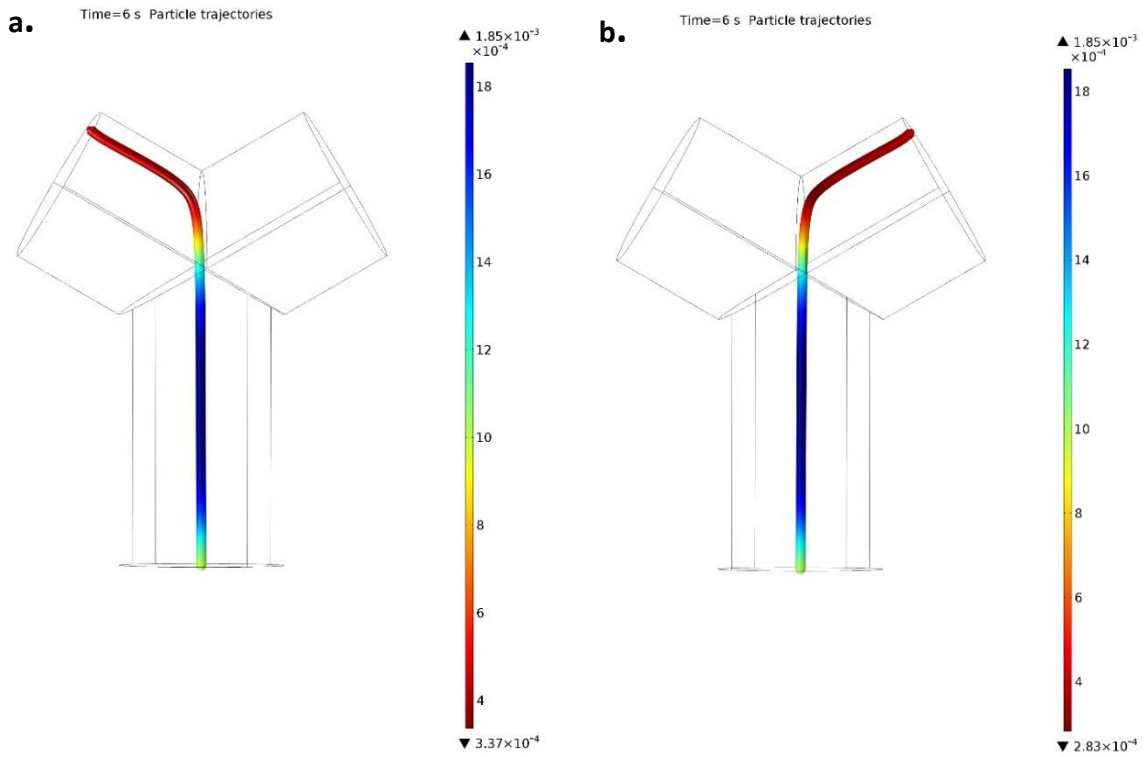

Figure 4.61 *Trajectory of one particle with 1 µm size and magnetization saturation 3.5×10^{5}A/m, with an applied magnetic gradient of* ***a)*** *-380mT/m (-3×10^5 A/m)^2;* ***b)*** *380 mT/m (3×10^5 A/m^2).*

Even though the size of the particle was reduced by an order of magnitude, the proposed magnetic system seems to be efficient in steering a 1 μm magnetite particle travelling in the centerline of a vessel. By controlling the direction of the magnetic gradient it was possible to decide the outlet where the particle ended up. It was possible to determine that the minimum magnetic field gradient required to steer the device is 350 mT/m (2.8×10^5 A/m^2). However, by simulating 30 particles, it was possible to conclude that this efficient steering is only possible for particles positioned at the center of a vessel where the velocity is lower. In figure 4.62, the trajectories of 30 magnetite particles (with 1 μm) are presented. In this case, the maximum magnetic field gradient was applied. It is possible to conclude that even by applying this high value it is not possible to steer particles that are not in the center of the blood vessel. This results were not surprising since the magnetic forces acting on the

particles are directly related to their volume, as can be seen in equation 4.3. One possible solution could be to increase the saturation magnetization of the particles.

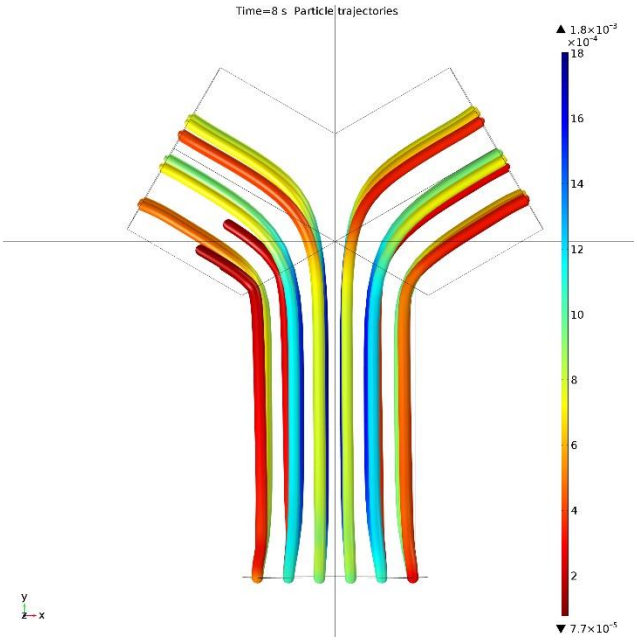

Figure 4.62 *Trajectory of 30 particles with 1 μm size and magnetization saturation 3.5×10^5A/m, with an applied magnetic gradient of 1000mT/m (-8×10^5 A/m^2).*

The same experiments were made with another 1 μm particle, this time considered to be made of permendur, which corresponds to an increase in one order of magnitude in the saturation magnetization. First, one particle was released from the center of the inlet. As expected, a smaller magnetic field gradient was required to steer particles with a higher saturation magnetization: it is possible to control them with a minimum magnetic gradient of 110 mT/m (9×10^4 A/m^2). Next, 30 particles were released at different points from the inlet. It was possible to conclude that even with an increase in one order of magnitude in the saturation magnetization, it is not possible to steer particles that are not in the center of the blood vessel with the magnetic actuation system proposed in this chapter. To steer particles with $\leq$1 μm, their saturation magnetization will have to be even higher or the magnetic actuation system will have producing higher magnetic field gradients.

"In theory, theory and practice are the same. In practice, they are not."

-Albert Einstein

Chapter 5

Experimental Work

The goal of this project was the simulation, design and fabrication of an electromagnetic actuation system to study the two dimensional locomotion of magnetic devices. In the previous chapter, different coil configurations that would allow the control of these devices at different size scales were simulated, using finite element analysis. Based on the simulation results, a prototype of a magnetic actuation system was designed and built from the ground up, taking into account cost constraints. The final system comprised one pair of rotational Helmholtz coils and one pair of rotational Maxwell coils placed along the same axis. Furthermore, additional components had to be designed or selected to fulfil the requirements of the system and to work together in an efficient manner.

In this section, the different components of the system are first described in detail, taking into account its characteristics, functionality and constraints. The functionality of the fabricated system was tested by performing experiments. The magnetic field was measured to investigate the linearity and magnitude of the magnetic fields produced by both coil configurations. In this chapter, this results are compared to the ones from the FE model. A millimeter sized permanent magnet was controlled in a 2-dimensional space using the fabricated electromagnetic actuation system. In the end of this chapter, the results of this control experiment are presented and discussed.

5.1 Problem Description

In chapter 4, two different coil configurations that would allow the control of magnetic devices with more than 100 μm were proposed. One of the designs consisted of one pair of Helmholtz coils and one pair of Maxwell coils which could be rotated by a motor. It was already discussed that the Helmholtz coil generate a uniform magnetic field and, by being rotated, can produce a torque on the magnetic device. Therefore, it was possible to conclude that a rotating Helmholtz coil pair could be used to align the device in the desired direction. Next, the Maxwell coils could be activated to generate a uniform gradient magnetic flux, moving the magnetic device in a straight line. However, this design with the rotational coils has one major disadvantage since the rotational movement of the coils reduces the time response to realign the field, which may be a constraint on achieving the required real-time performance. In general, coil movement during a magnetic navigation intervention could be a serious limitation for clinical applications. Also, there is a need for a motor with a high torque which can be expensive.

The second configuration described in chapter 4 consisted of four pairs of stationary Helmholtz and Maxwell coils, which were fixed perpendicularly. A fixed structure is advantageous for real-time performance. The major disadvantage of this configuration is that it can be considerable bulkier and heavier. In general, the separation of the second set of coils equals the diameter of the coils in the first set and, in the case of the control in a 3-dimensional space, this is even more problematic since the third set will have to be even larger. Thus, this increases the amount of space occupied by the system, and it requires a greater amount of electrical power to generate an effective magnetic field. Also, to fabricate 4 more (bigger) coils would have meant that much more copper wire would be needed, which is costly. Furthermore, with this approach, since the direction and velocity of the magnetic device are controlled by controlling the currents in the coils' power supplies with high potency, the power supply would also needed to be controlled by a computer interface. This was the decisive factor in the choice of the ideal approach for fabrication. Since power supplies controlled by a computer interface were not available, the rotational coils approach was chosen. The front and top views of the chosen electromagnetic actuation system are depicted in Figure 5.1a and 5.1b, respectively.

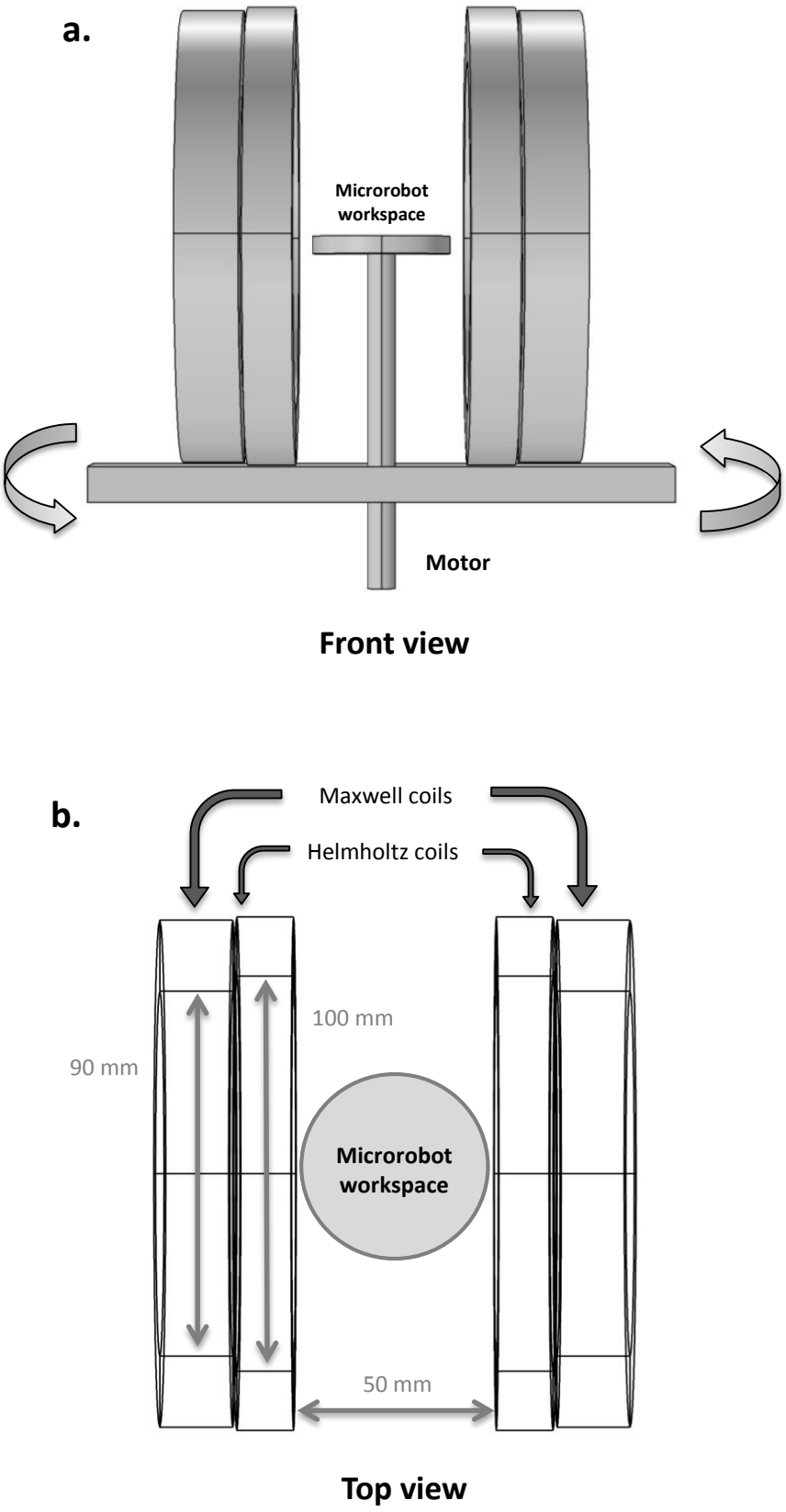

Figure 5.1 Final design of the coil system **a)** Frontal View, **b)** Top view.

5.2 Setup Overview

Figure 5.2 shows the overall view of the experimental setup.

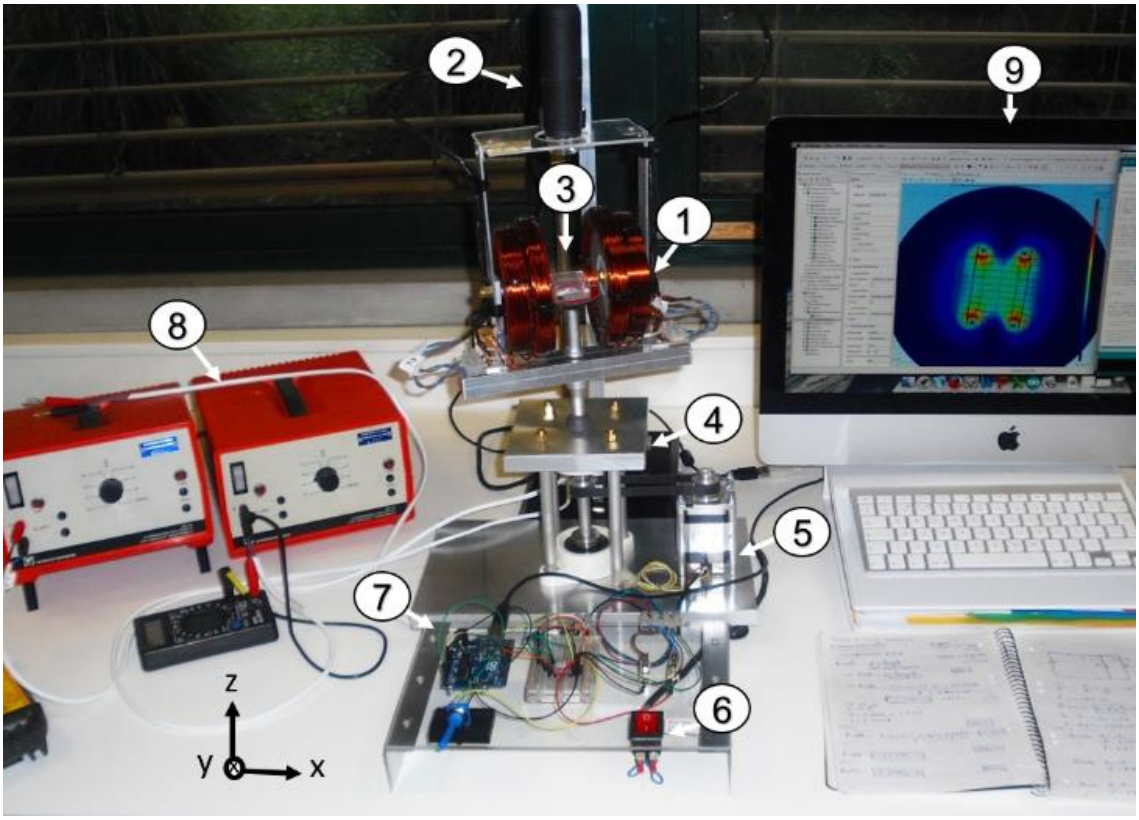

Figure 5.2 Overall view of the system and working desk: (1) The two coil pairs (Helmholtz and Maxwell), (2) Microscope (with respective support), (3) Sample holder, (4) Coil support, (5) Stepper motor, (6) Current inverter (Switch), (7) electronic controlling circuit, (8) Power sources, (9) Computer.

The overall electromagnetic actuation system is composed by different functional parts, namely:

1. Two coil pairs (Helmholtz and Maxwell)
2. Digital microscope (Veho-VMS-001- 200X USB Microscope) and respective support
3. Sample holder (ROI)
4. Coil support
5. Stepper motor (NEMA 23-size hybrid)
6. Current inverter (switch)
7. Electronic circuit for motor control
8. Power suppliers
9. Computer interface

5.2.1 Coils

The construction of the coils was a very challenging process. A coil winder was designed and fabricated from the ground up and it included a counter to measure the number of turns in the coils. The frame was made from 19 mm thick plywood and the overall dimensions can be seen in the schematic from Figure 5.3. As can be seen from this schematic, two 16 mm diameter holes were pierced, one at each end of lateral planks to insert the bearings, at 220 mm from the base. Next, through the bearings, an iron screwed pole was inserted and a reel was placed to proceed with the winding of the 2 coil pairs. This reel was built in plywood with 10 mm thickness and it included sideways openings as can be seen in figures 5.3b and 5.4b. The goal of these openings was to facilitate the deposit of a special varnish (Dolphs-Synthite ER-41) between the different interlayers of the coils. This is a red polyurethane insulating enamel that dries rapidly at ambient temperatures forming a tough, flexible film and it had the important function of improving the consistency between the turns in the coils, keeping them cohesive. The reel had to be strong enough to resist the pressure of all the windings, otherwise, it could result in a coil deformation. The reel core was also made in plywood with the predefined measurements of 90 mm high* and 18 mm width for the Maxwell coils and 100 mm high and 14 mm width for the Helmholtz coils.

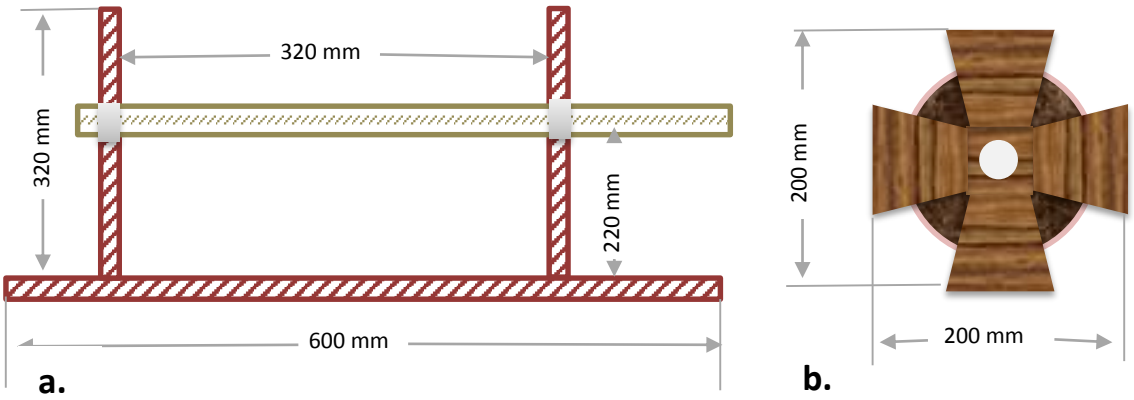

Figure 5.3 Design of the coil winder **a)** Overall measures: length of the plywood structure was 600 mm and the overall height of the plywood structure was 320 mm. The overall thickness (not represented in the picture) of the structure was approximately 300 mm. **b)** Design of the plywood reel with dimensions 200 mm×200 mm and sideway cuts.

*Actually, an error was commited in the fabrication of the reel core for the Maxwell coils and they ended up with a diameter of approximatly 80 mm instead of the 90 mm obtained from the simulations. This error was taken into consideration in the next sections.

To count the number of turns in each coil (which were determined through simulations), a mechanical counter (Hand Tally Counter-Type H102-4) was placed on the sideways panels. This is important when the goal is to wind more than a few tens of turns in an efficient way, making the process more reliable, avoiding errors in the number of turns. This is especially important when constructing a Helmholtz coil pair since with this configuration the goal is to obtain a homogenous static magnetic field. The counter was activated by pressing a button located above the screen. This causes the first ring to advance one number. To press the button on the counter with each coil turn, a wooden wheel with a small eccentric was placed on the iron pole as can be seen in figure 5.4a. A piece of metal was used as a winding handle. Thus, every time the handle rotated around, the piece of wood incremented the counter.

All the coils were made with 1.40 mm diameter copper wire, insulated by varnish coating. The copper wire was wounded up around the wood core by rotating the handle, at a controlled pace. Also, when winding the coil it was important to control the pressure asserted on the thread. The final fabricated coils, aligned with a mechanical support, satisfying the measurements and separation obtained from the finite element simulations can be seen in figure 5.5.

a. **b.**

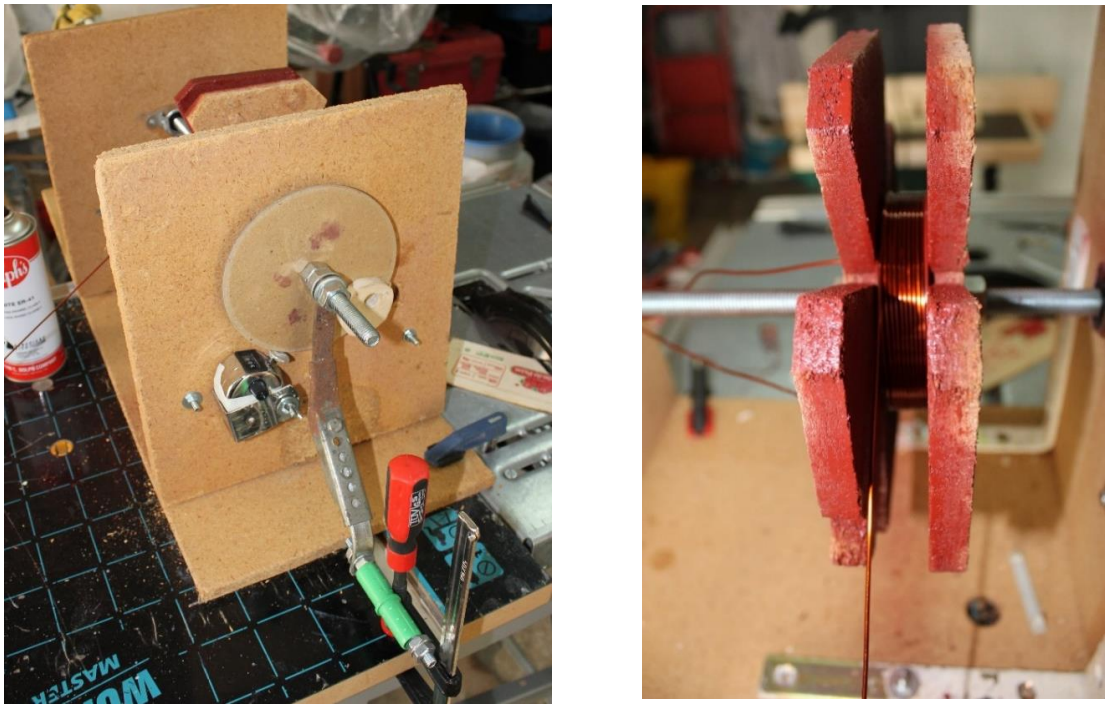

Figure 5.4 Fabrication of the coil system **a)** Coil winder fabricated from the ground up, made of wood, and including a counter, **b)** close up on the winding of a coil.

Figure 5.5 Final coil system.

The measured characteristics of the fabricated Helmholtz and Maxwell coil pairs are summarized in tables 5.1a and 5.2b, respectively.

a.

	Helmholtz coil 1	Helmholtz coil 2
Diameter of copper wire (mm)	1,4	1,4
Radius (mm)	50	50
Coil turns	103	101
weight (g)	540	506
Resistance (ohm)	0,3	0,3

b.

	Maxwell coil 1	Maxwell coil 2
Diameter of copper wire (mm)	1,4	1,4
Radius (mm)	40	40
Coil turns	151	151
weight (g)	634	632
Resistance (ohm)	0,55	0,51

Table 5.1 Final characteristics of the fabricated coil pairs: **a)** Helmholtz coil pair, **b)** Maxwell coil pair.

Table 5.1 includes the measured resistances of each coil. The resistances of the two coils in the same pair are nearly identical, which ensures that the currents passing through the two coils in the same coil pair are also nearly identical when the same voltage is applied. This consideration is especially important in the Helmholtz coil configuration since non identical currents could influence the homogeneity of the magnetic field generated by the coil pair and create unexpected magnetic gradients.

Taking into account Ohm's Law, V=RI, and applying the measured resistances, it is possible to conclude that the Maxwell coils require approximately 1.5 V and the Helmholtz coils require approximately 1 V when operated at 3 A. Since the available power supplies are only capable of delivering a maximum current of 6 A and there is the need to control both coil configurations separately, it was decided that each coil configuration pair was connected to a different power supply. Because two coils are connected in parallel to each power supply, a voltage of 3 V is needed for the Maxwell configuration and 2 V for the Helmholtz configuration.

In the Maxwell configuration, the coils were connected in a way that the current passes in opposite directions as depicted in the diagram from figure 5.6.

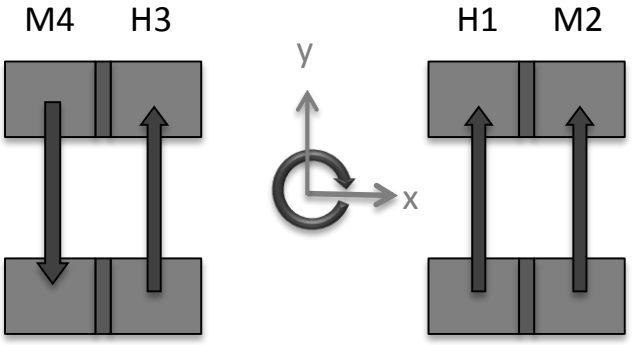

Figure 5.6 Schematic of the direction of the currents in the coil system. H1 and H3 depict the Helmholtz coil pair and M2 and M4 depict the Maxwell coil pair.

Since magnetic field gradients with high amplitudes must be generated for particle actuation, the gradient efficiency is an important parameter to optimize. In this context, power dissipation can be a limiting factor. Large power dissipation leads to significant heating of the coil wires potentially leading to coil failure. This happens because the resistance of the coils increases with the temperature, making the intensity of the magnetic field lower. Depending on the power consumption and duty cycles, cooling may be necessary. To check if a cooling system was required some calculations on power of the coils were made. The power dissipated by each Helmholtz coil and each Maxwell coil are:

$$P = RI^2 = 0.5 \times 3^2 = 5\ W$$

$$P = RI^2 = 0.3 \times 3^2 = 2.7\ W$$

The power dissipated by each Helmholtz coil is approximately 5.0W and the power dissipated by each Maxwell coil is approximately 2.7W. These values of power dissipation are one order of magnitude lower that most similar systems mainly due to the low coil resistance (due to the large diameter of the copper wire). Also, during the time required for the experiments a decrease in the intensity of the magnetic fields was not detected. Thus, a cooling system was not considered for this project.

For the characterization of the coil system, the magnitude of the magnetic fields produced by the Helmholtz and Maxwell coil pairs were theoretically calculated and experimentally measured. The theoretical fields were calculated using COMSOL (chapter 4) and the real magnetic values were measured with a Gaussmeter (Model 908A of Magnetic Instrumentation) with an accuracy of $\pm\ 1\%$, supplied with a transverse Hall probe as can be seen in Figure 5.7b. To explore the spatial dependence of the field magnitude, the probe was moved slowly along the $\vec{x}$-axis (Figure 5.7a). The magnetic field was measured at coordinates [-2 -1 0 1 2] cm along the $\vec{x}$-axis, and the average results for each coordinate are given in table 5.4a and 5.4b for the Helmholtz and Maxwell coils, respectively.

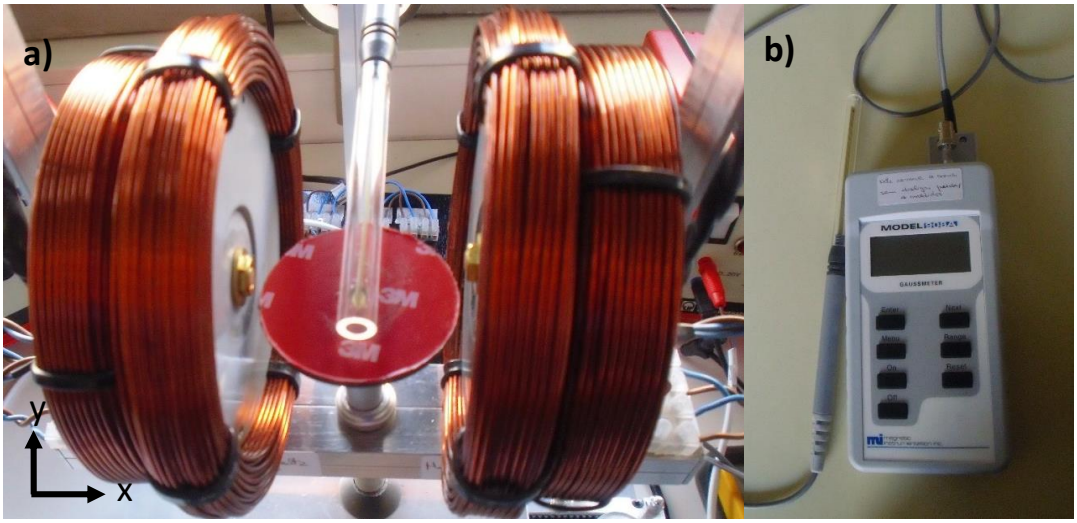

Figure 5.7 Measurement of the magnetic field with a gaussmeter a) placement of the probe, b) Gaussmeter used to measure the magnetic fields (Model 908A of Magnetic Instrumentation).

a.

x (cm)	Magnetic flux (mT)
-2,00	3,70
-1,00	3,60
0,00	3,60
1,00	3,60
2,00	3,70

b.

x (cm)	Magnetic flux (mT)
-2,00	-1,50
-1,00	-1,00
0,00	-0,00
1,00	0,90
2,00	1,50

Table 5.2 Average result of the experimentally measured magnetic fields with a gaussmeter with accuracy $\pm 1\%$ **a)** Helmholtz coil pair, **b)** Maxwell coil pair.

The measured values of magnetic field generated by the Helmholtz coil pair presented an average deviation of 0.01 mT. The measured values of magnetic field generated by the Maxwell coil pair presented an average deviation of 0.02 mT. In general, this measurement method was not very accurate due to the difficulty in positioning the probe, however, it still allowed a qualitative understanding of the magnetic field behavior. The measured magnetic field was compared to the simulated magnetic field under the same conditions. Although the large diameter coil wire can support 4A, due to material constraints, the maximum current used was 3A. The FE model was supplied with the same input as the experimental setup, and the same data points were extracted from the model. Figures 5.8 a and b show the comparison results between the theoretical values and the measurement values for the Helmholtz and Maxwell configurations, respectively.

As expected, it was possible to see that the Helmholtz coils generate an approximately uniform magnetic field and the Maxwell coils generate an approximately uniform magnetic flux gradient, and, in general, the experimentally measured magnetic values were coincided with the theoretically ones. Regarding the Helmholtz coil pair, it can be seen from Figure 5.8a that it was possible to achieve a uniform static magnetic field with magnitude 3.5 ± 0.1 mT in the ROI, when a 3 A current is applied. This value is very similar to the FE simulations with a maximum deviation from the theoretical results of 2.7%. Regarding the Maxwell coil pair, it is possible to see from Figure 5.8b that it was possible to obtain a constant magnetic field gradient of approximately 75±5 mT/m in the center of the coils, however, this value decreases to 50±5 mT/m in the regions close to the coils. Even if the constant value at the center is considered, this is significantly lower than the 100 mT/m achieved in the simulations (deviation of 25%).

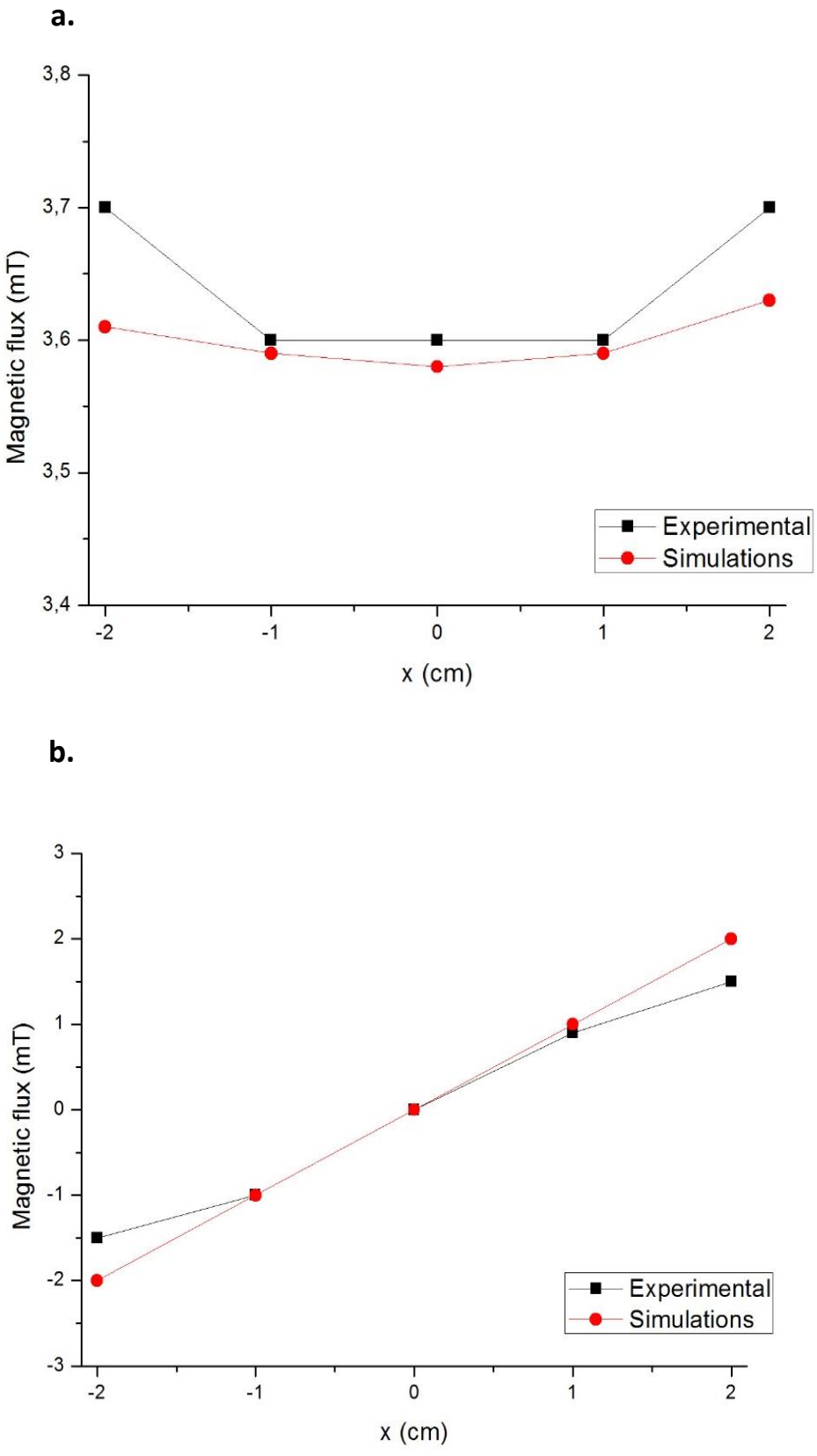

Figure 5.8 Comparison between the experimentally measured magnetic fields with a gaussmeter and the data from the simulation for **a)** Helmholtz coil pair, **b)** Maxwell coil pair.

A discrepancy in magnitude between the simulation model and the practical implementation was expected. These can be due to imperfections on the coils fabrication and a possible misalignment between the pairs of coils. Also, the position and orientation of the probe of the magnetometer was set by hand which affects the actual coordinates at which the magnetic field is measured.

5.2.2. Coil support

The mechanical support for the coils was made from the ground up. The main goal was to design and fabricate a structure that would allow a controlled rotation of the electromagnetic actuation system and also to have the coils correctly aligned and separated. A schematic of the coil support is depicted in figure 5.9.

First, a support base made with plywood and tinfoil was built. Above this base, a small sub-structure was placed to give stability to the structure and allow the placing of two bearings. Between these two bearings a 12 mm hollow aluminum pipe was placed and fixed with screws. Inside the hollow pipe, a solid 8 mm pipe was placed and fixed to the support base. The torque transmission (rotation) to the rotary axis was ensured by two pulleys and a bipolar stepper motor with 200 steps connected by a transmission belt. Next, a rectangular aluminum pipe with 150 mm length, 35 mm width and 19 mm height was fixed to the upper part of the rotating axis. The 4 coils were fixed to the aluminum structure and centered with a steady plastic base. This way, when the axis rotates due to the torque produced by the stepper motor, the horizontal arm that holds the coils also rotated. On the top of the steady axis, a plastic platform with radius 45 mm was placed at the center of the Helmholtz coils. This platform was designed to hold the container where the magnetic device was controlled. Finally, an acrylic plaque was placed above the coils to allow the insertion of a microscope, avoiding the chance of having the wires falling into the working area.

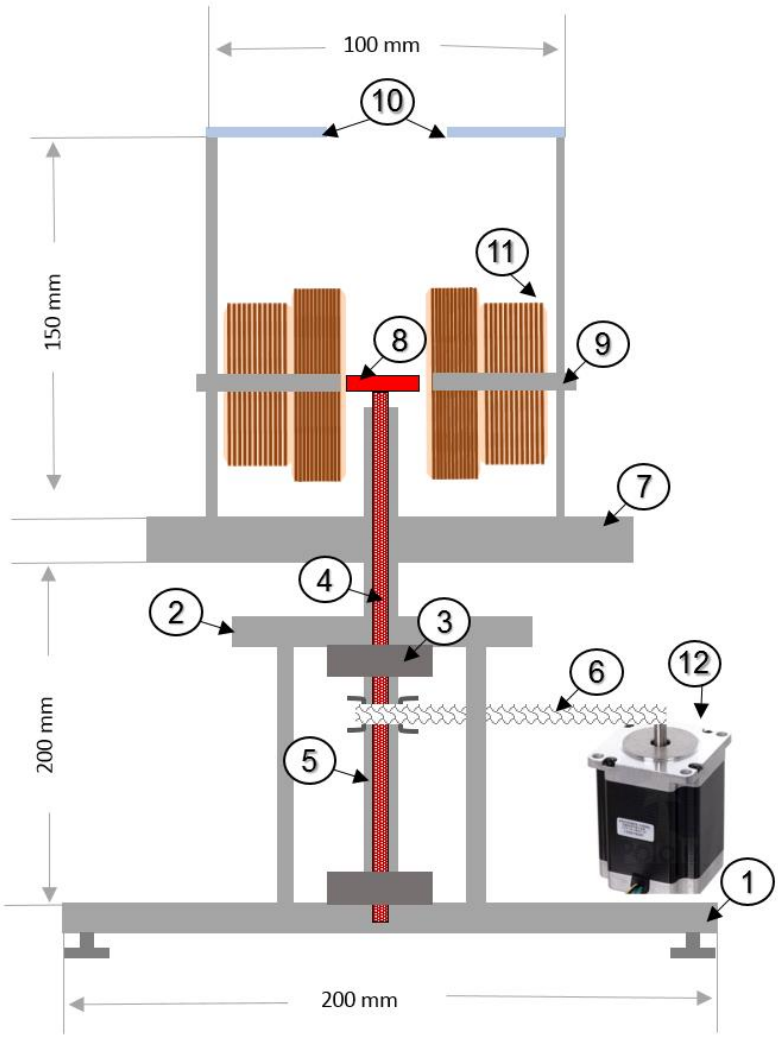

Figure 5.9 Schematic of the coil support (frontal view) with the following components: **1)** support base, **2)** secondary platform, **3)** bearings, **4)** aluminum hollow pipe (rotating axis), **5)** solid pipe (fixed axis), **6)** transmission belt, **7)** rectangular aluminum pipe, **8)** plastic circular platform, **9)** aluminum pipe fixed to the rotating axis, **10)** Acrylic plaque with opening for the microscope, **11)** Coils, **12)** Bipolar stepper motor.

While developing this structure, it was always taken into consideration the need to exclude the use of ferromagnetic materials like iron to avoid any interference of these materials with the produced magnetic fields. Brass screws and washers were used, as well as aluminum and various woods. An exception was made to the bearings that support the axis where the coils are placed, for lack of better solutions in the market. However, it did not seem to significantly disturb the study.

5.2.3. Wiring and microscope support

In the fabricated electromagnetic actuation setup, a digital microscope (Veho-VMS-001- 200X USB Microscope) was used to provide a visual feedback of the ROI. Thus, it was necessary to design and fabricate, from the ground up, a support for the microscope to place it in an ideal point, between the Helmholtz coils without disturbing the study. Besides holding the microscope in a fixed point, the microscope support was also designed in order to organize the 8 coil wires (2 for each coil: in and out) with section 0.75 mm^2.

First, a support plywood base with 200 mm length and 19 mm width was built. Next, the eight wires were introduced in an aluminum hollow tube with a rectangular profile and 20 thickness which was fixed to the base. On the top of this tube, a smaller identical tube was inserted through which the wires were passed and were connected to terminal blocks in the rotating aluminum platform. The wires at the base were fixed to terminal blocks where the connections to the respective power supplies were made.

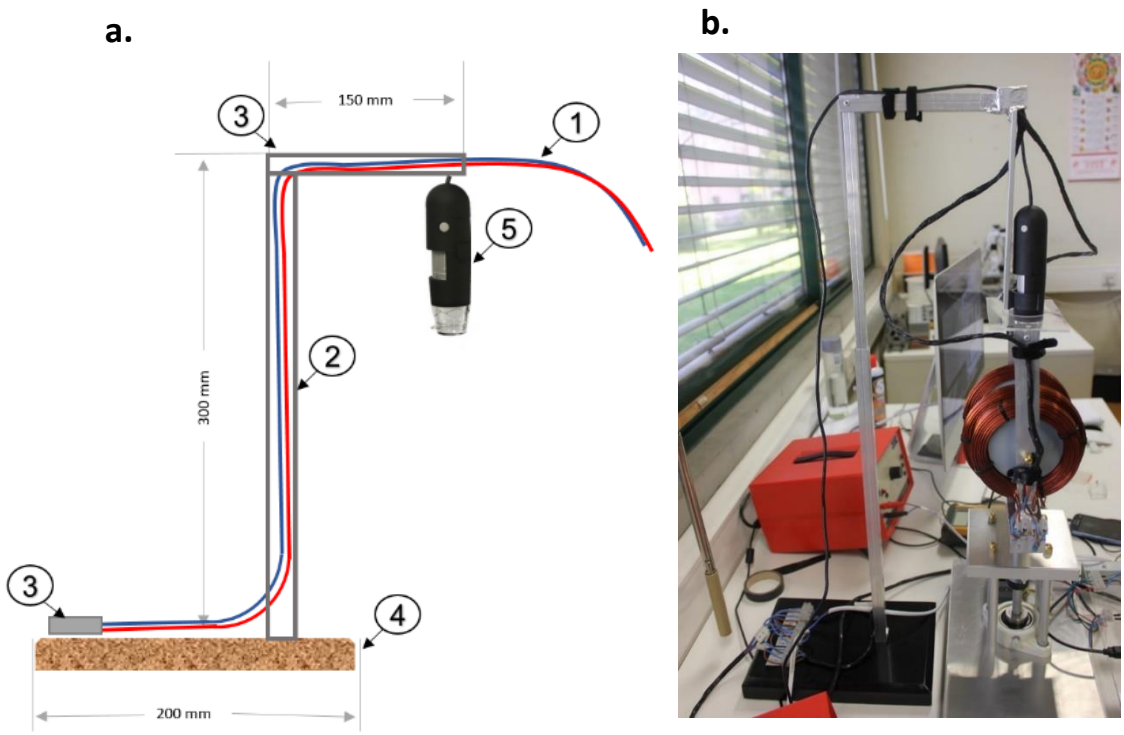

Figure 5.10 Wiring and microscope support (Lateral view) **a)** schematic with the following components: 1) 8 wire, 2) aluminum pipe fixed to the rotating axis 3) rectangular aluminum pipe, 4) plywood support base, 5) microscope, 6) transmission belt. **b)** Final fabricated system.

5.2.4 Electronic system

With the chosen coil configuration, the control of the magnetic device in a pre-defined path is achieved by rotating the coil pairs in a controlled way. To achieve this control, an electronic circuit was designed and mounted. The global view of the circuit is depicted in figure 5.11. It is composed by different parts, namely:

1. Arduino Uno
2. Capacitor (1mF)
3. Driver (Aleggro A4988)
4. Fuses
5. Potentiometer
6. Stepper motor
7. Current inverter (switch)

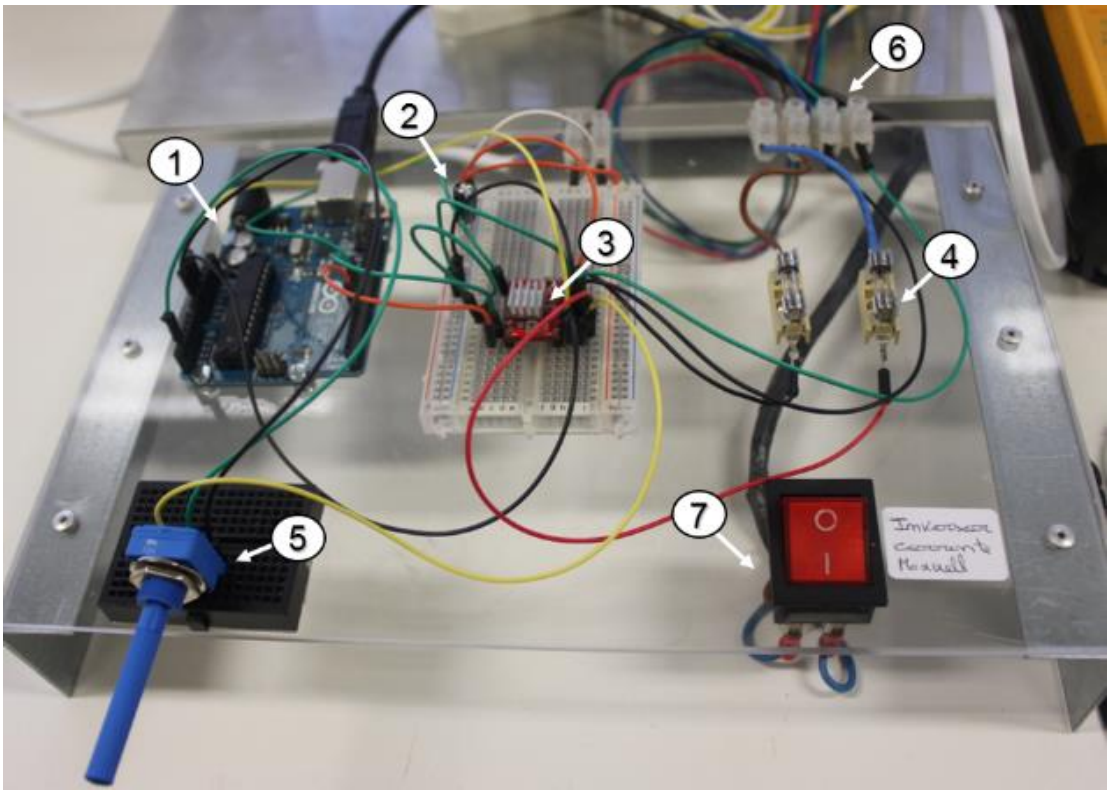

Figure 5.11 Electronic circuit that controls the rotation of the coils: (1) Arduino Uno, (2) Capacitor, (3) Driver (Aleggro A4988), (4) Fuses, (5) Potentiometer, (6) Current inverter.

5.2.4.1 Stepper motor

The rotational coil system was driven by a stepping motor. Steppers are motors capable of rotating a specific number of degrees in response to control pulses. They are usually constructed with permanent magnets as their rotors and electromagnetic drive coils with their surrounding stator to generate motion (torque). When the coils are energized in the proper order, the rotor moves to align itself along with the stator and, this way, the stepper can be made to move in discrete incremental steps. Each time an incoming pulse is applied to the motor, the shaft turns a specific angular distance. The number of degrees in each step is motor-dependent, ranging from one or two degrees per step up to 30 degrees or more. Also, the shaft can be driven in either direction and operated at low or very high stepping rates. Therefore, the stepper motor has the capability of controlling the velocity, distance, and direction of a mechanical load. It also produces a holding torque at standstill to prevent unwanted motion or disturbance.

For this project, a NEMA 23-size hybrid stepping motor was chosen which can be seen in Figure 5.12.

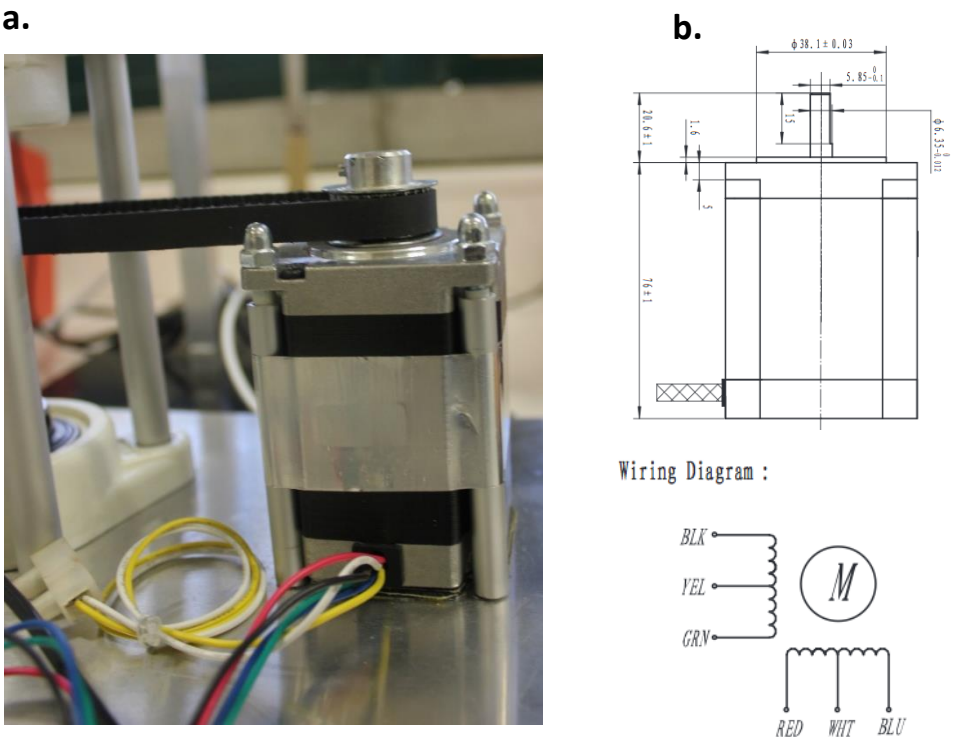

Figure 5.12 Stepping motor (Nema 23-size hybrid stepping motor) **a)** photo of the motor used in the system, including the pulley and the transmission belt, **b)** Measurements of the stepper motor and wiring diagram.

There are two basic types of stepper motors, namely, unipolar and bipolar. They have the same in their physical construction, but differ in the way that their coils are wired. Bipolar motors provide independent access to both ends of the drive coils, whereas unipolar steppers have one end of each coil tied to one (or more) common connection(s).

The stepper motor used in this project model can be used in unipolar or bipolar configurations and has a 1.8° step angle (200 steps/revolution). Each phase draws 1 A at 8.6 V, allowing for a holding torque of approximately 14 kg.cm. This motor was chosen due to this high holding torque since the coils are heavy (2.5Kg total) with a 5 cm separation (5cm×2.5kg=12.5Kg.cm).

The bipolar stepper motor usually has four wires coming out of it. Unlike unipolar steppers, bipolar steppers have no common center connection, instead, they have two independent sets of coils. As can be seen from figure 5.12, this motor has six color-coded wires terminated with bare leads that allow it to be controlled by both unipolar and bipolar stepper motor drivers. When used with a unipolar stepper motor driver, all six leads are used. When used with a bipolar stepper motor driver, the center-tap yellow and white wires can be left disconnected (the red-blue pair gives access to one coil and the black-green pair gives access to the other coil as can be seen in Figure 5.12b). In this project, because a bipolar driver was used, the motor was used as a bipolar stepper motor.

By energizing the coils in the right order using an arduino, a driver and a potentiometer as can be seen in the electronic circuit depicted in figure 5.13, the motor was driven in a controlled manner.

5.2.4.2 Arduino and driver

Arduino, depicted in figure 5.14a, is an open-source physical computing platform based on a simple microcontroller board, and a development environment for writing software for the board.

In this project, the model Arduino Uno was used because it was already available. This particular model is a microcontroller board based on the ATmega328. It has 14 digital input/output pins, 6 analog inputs, a 16 MHz ceramic resonator, a USB connection, a power jack, an ICSP header, and a reset button. Arduino boards offer several advantages since they are relatively inexpensive compared to other microcontroller platforms and the software is published as open source tools.

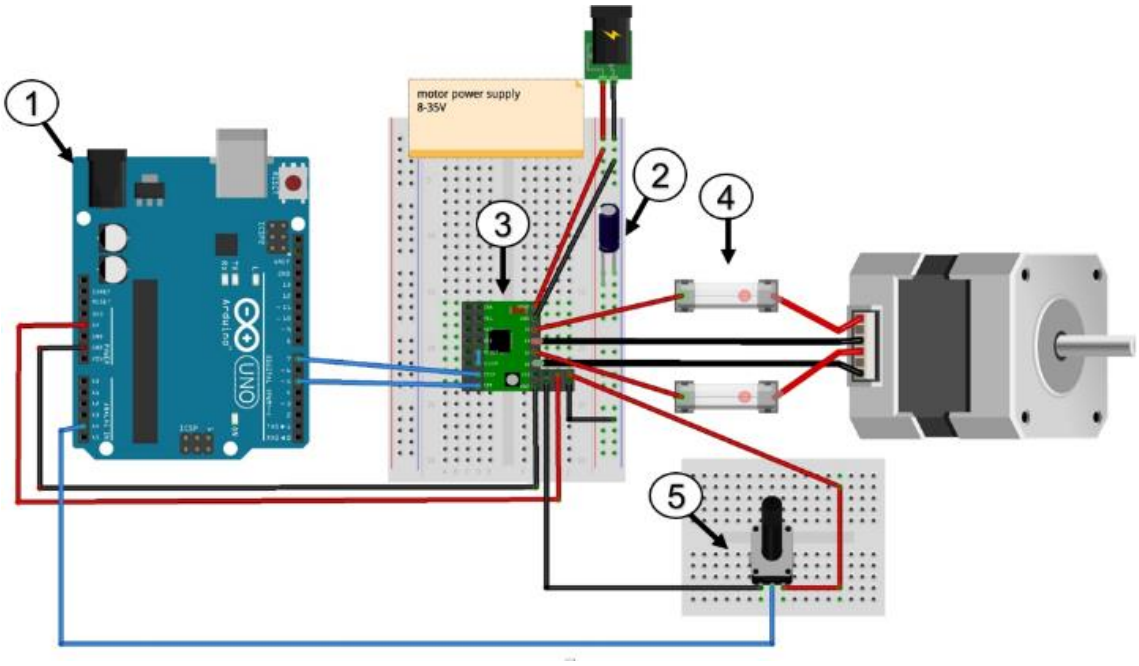

Figure 5.13 Electronic circuit that controls the rotation of the coils: (1) Arduino Uno, (2) Capacitor, (3) Driver (Aleggro A4988), (4) Fuses, (5) Potentiometer, (6) Current inverter.

An electric motor can be powered and controlled directly from the Arduino board, or using the same Arduino board with an additional shield or driver. The first option, using the power source from the Arduino board, is not always the right method and has several limitations since it is only possible to connect directly to the Arduino board small stepper motors that require a small amount of current for spinning. This power limitation comes from the powered source of the board, which can be a USB port or the DC jack on the board connected to a 5V power adapter.

In this project, the used stepper motors required more power than can be supplied by the Arduino. Thus, a motor driver (A4988) was used.

The model A4988, depicted in figure 5.14b, is a microstepping motor driver with built-in translator for easy operation. It is designed to operate bipolar stepper motors in full-, half-, quarter-, eighth-, and sixteenth-step modes, with an output drive capacity of up to 35 V and ±2A.

The Arduino was powered by a USB cable connected to the computer. The driver required a motor supply voltage (10 V) to be connected across VMOT and GND and logic supply voltage (5 V) to be connected across the VDD and GND pins (it was connected to the

pins 5V and GND in arduino). These supplies should have appropriate decoupling capacitors close to the board, and they should be capable of delivering the expected currents (peaks up to 4 A for the motor supply). To protect the A4988 drives from possible destructive LC voltage spikes, a large electrolytic capacitor with 100 µF was placed across the motor power (VMOT) and the ground (GND), as depicted in figure 5.13.

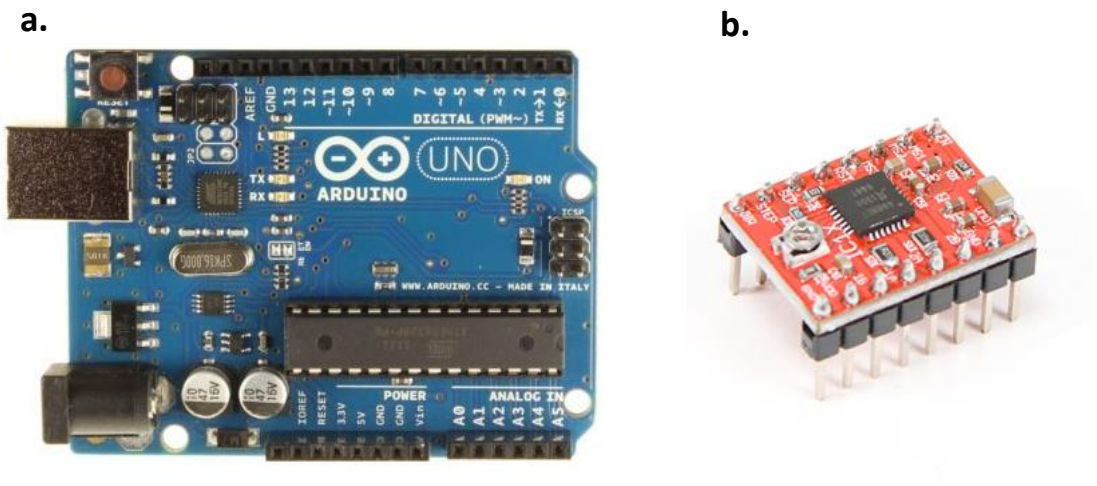

Figure 5.14. a) Arduino Uno (microcontroller board based on the ATmega328, 14 digital input/output pins and 6 analog inputs) **b)** Motor Driver (model A4988).

As can be seen in figure 5.13, one of the coils from the stepper motor was connected to the pins 1 A and 1B and the other coil to the pins 2A and 2B in the driver. The pin DIR (determines the direction of the motor) and the pin STEP (A low-to-high transition on this input advances the motor one increment) were connected to the arduino uno pins 7 and 5, respectively. The pin EN (turns on or off all the outputs) was connected to pin 8 in the arduino and the pin reset (all step inputs are ignores until the reset input is set to high) was connected to sleep (to minimize power consumption when the motor is not in use, a logic low in this pin puts the A4988 in sleep mode) which results in the driver being always turned on.

The circuit also included two fuses to protect the stepper motor from high current and a potentiometer which was connected to the pins A4, GND and 5V in the arduino. The potentiometer produces an analog voltage output the can be controlled with its rotation. The program code can read this analog value using the analogRead () command and use this value to control the rotation of the motor. The final program can be consulted in the appendix D.

After the program sketch was loaded on to the Arduino board, it was possible to revolve the motor clockwise and counter-clockwise using the potentiometer.

5.2.4.3 Switch for current inversion

To allow an inversion of the current direction in the Maxwell coils, resulting in a control of the magnetic force direction and thus, the propulsion direction of the magnetic device the circuit depicted in figure 5.15 was created, using a switch. This electrical component can be used to break an electrical circuit, interrupting the current or diverting it from on conductor to another. The coils were connected to the switch in a way that, depending on its state, the currents passed in one direction or the opposite (but always in different directions in the two coils).

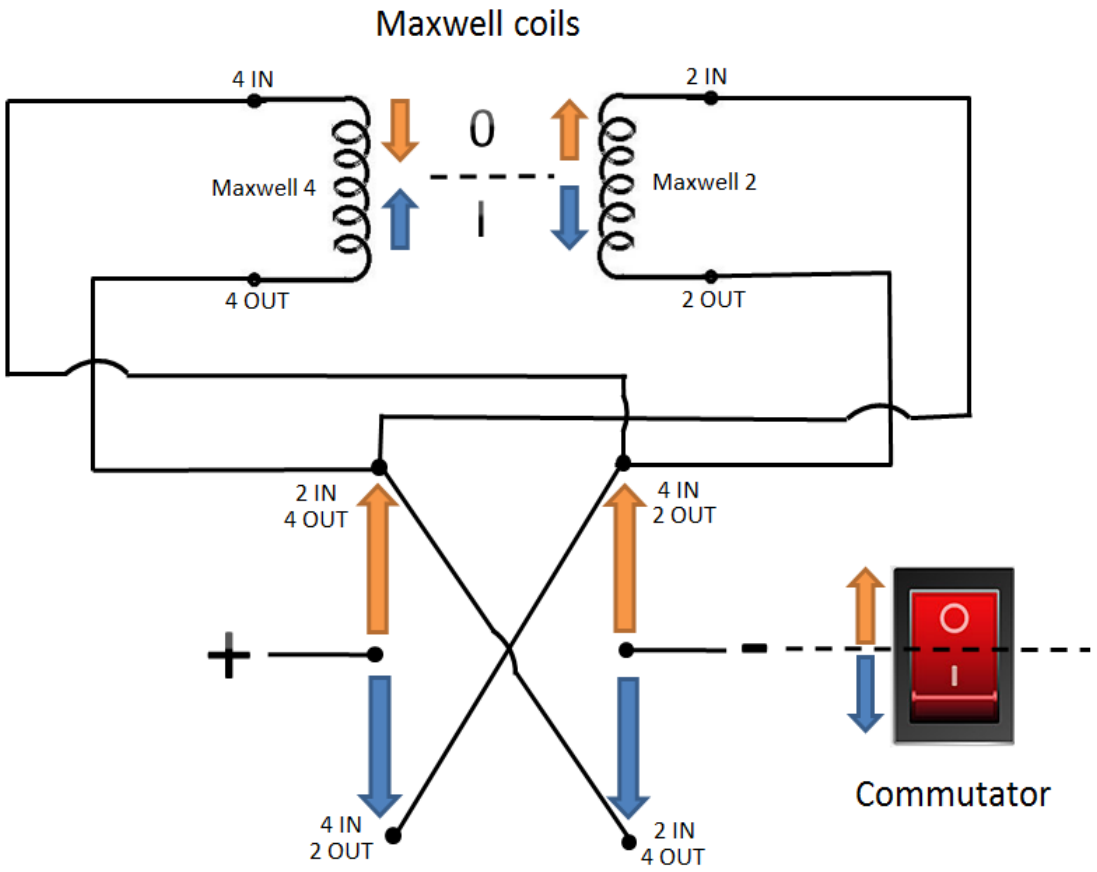

Figure 5.15 Diagram of the circuit for the current inversion in the Maxwell coils

5.3 Experiments

For the evaluation of the fabricated electromagnetic actuation system and proposed methods described in the previous sections, preliminary tests were carried out. Different magnetic devices were controlled in a 2-dimensional plane and the results of this control experiment are discussed.

5.3.1 Experimental setup

For the actuation of the magnetic devices, the fabricated electromagnetic actuation coil system described in the previous sections was used. A cylindrical (3 mm diameter, 6 mm height) neodymium magnet and a spherical (3 mm diameter) neodymium magnet, both with an axial magnetization and depicted in figure 5.16, were introduced in these experiments. More information about these devices can be consulted in the Appendix C. To study the rotation, half of the cylindrical magnet was painted red.

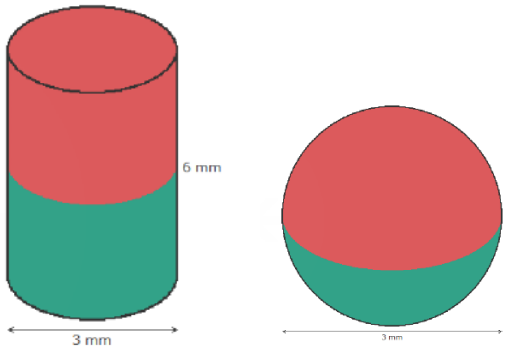

Figure 5.16 Material used in the experience, namely, the two permanent magnets used as microrobots placed in the acrylic test cube.

The tracking performance of the magnetic devices along selected directions was tested in an acrylic test cube ($30\times15\times30mm^3$) and in a maze-like structure cut into a plastic substrate, both filled with water and placed at the center of the rotating coils. These different test cubes and the permanent magnets can be seen in the photo from figure 5.17. For the observation of the microrobot the cap of the test bed was made of transparent acrylic.

To observe the movement of the magnetic device, a microscope camera system (Veho VMS 001 200X USB Microscope) was used for visual feedback. Movies and still images of the locomotion of the magnetic devices were obtained and can be seen in section 5.3.2.

The coil currents were supplied from two power supplies (one for each coil configuration). Furthermore, to change the direction of the coil current, an extra circuit based on switch components was applied (figure 5.16).

The orientation of the coils and propulsion of the robot were manually controlled by rotating the potentiometer and through a computer interface. For evaluation of the fabricated system, five representative rotation angles were selected in the x-y plane (θ=0º, 45º, 90º, 135º and 180º) and six propulsion angles (θ=0º, 45º, 90º, 135º, 180º, 270º). The switch was used when necessary and all cases were repeated ten times. For these experiments, the same currents values of Helmholtz coil pairs and Maxwell coil pairs as in the previous numerical analysis were applied. The currents applied to the Helmholtz coils were adjusted to align the microrobot in the desired direction. The Maxwell coils have the same current of 3 A but in opposite directions. Finally, the movements of the magnetic device along a predefined path were tested.

.

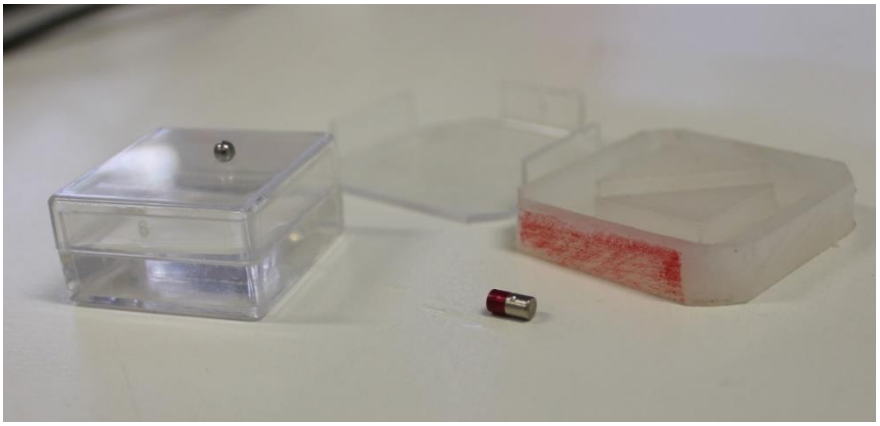

Figure 5.17 Material used in the experience, namely, the two permanent magnets used as microrobots and the acrylic test cubes.

5.3.2 Experimental Results and Discussion

The actuation performance of the magnetic device, using the proposed system, was validated by experiments. As expected, the two Helmholtz coils were capable of generating a uniform magnetic flux in the desired direction. Through these experiments, it was validated that the magnetic device could be aligned in the desired directions (θ=0º, 45º, 90º, 135º and 180º) by the proposed electromagnetic actuation system. The results are depicted in figures 5.18 to 5.22, for different angles, where the image on the left shows the orientation of the coils and the image on the right shows the influence of this orientation on the magnetic device.

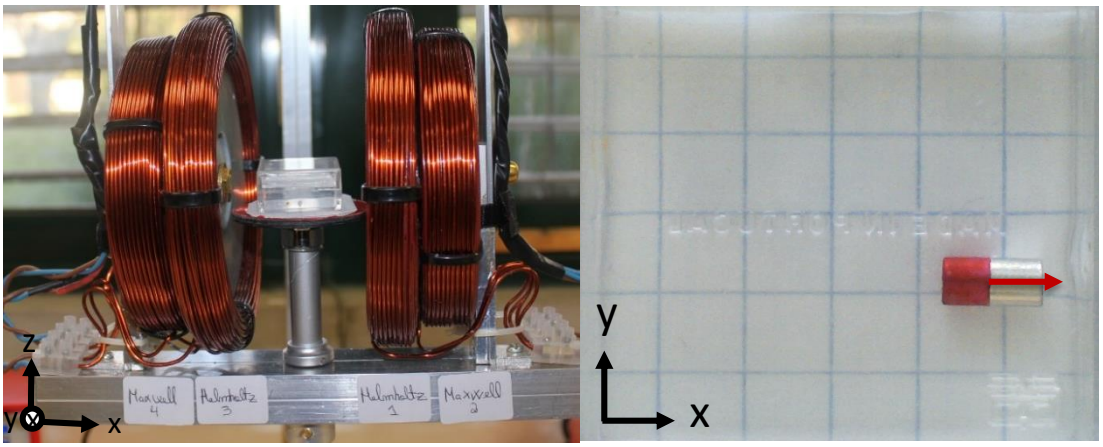

Figure 5.18 Rotation of the magnetic device by Helmholtz coils: Angle of rotation θ=0º.

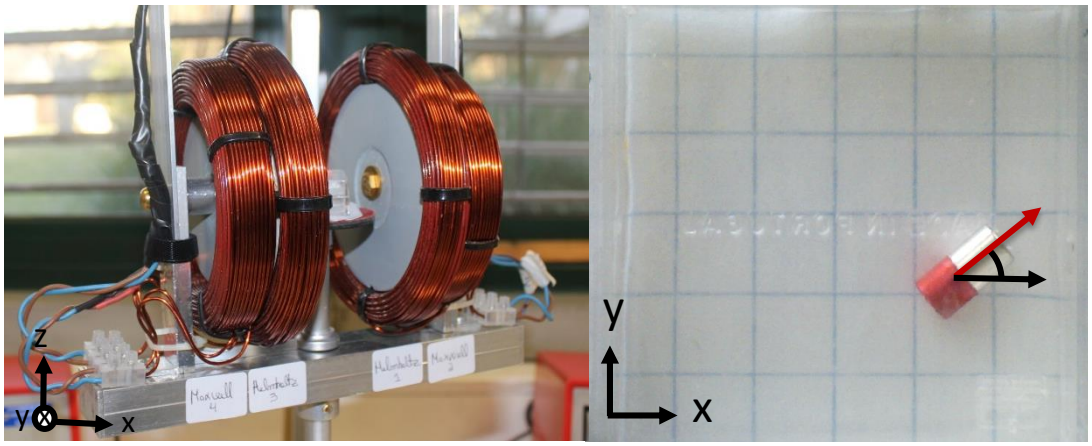

Figure 5.19 Rotation of the magnetic device by Helmholtz coils: Angle of rotation θ=45º.

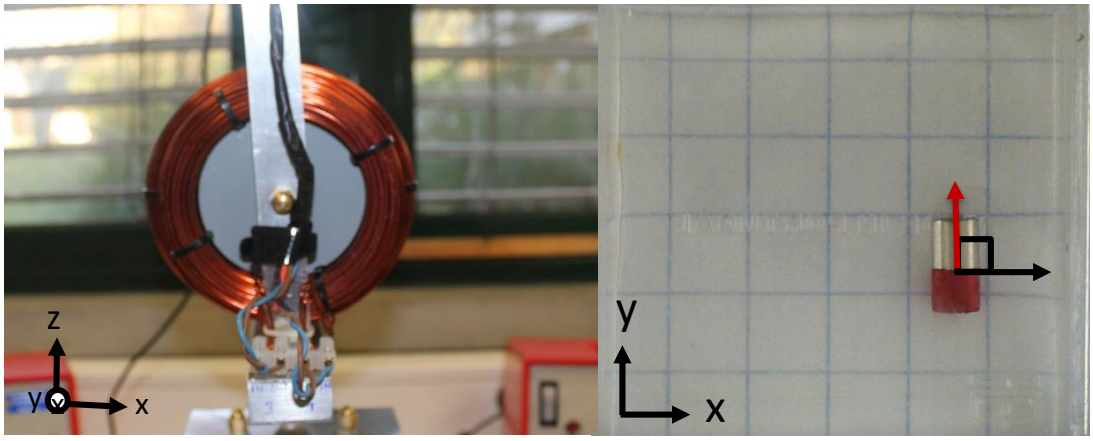

Figure 5.20 Rotation of the magnetic device by Helmholtz coils: Angle of rotation θ=90º.

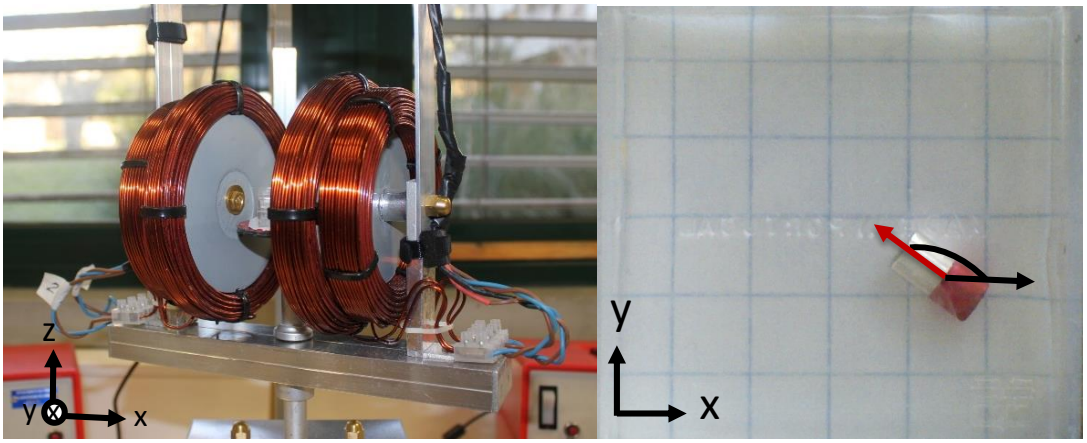

Figure 5.21 Rotation of the magnetic device by Helmholtz coils: Angle of rotation θ=135º.

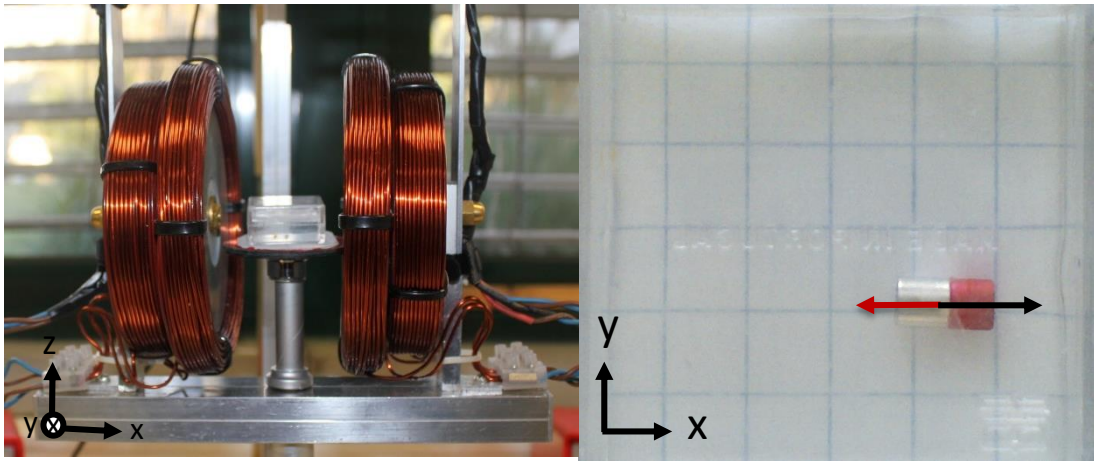

Figure 5.22 Rotation of the magnetic device by Helmholtz coils: Angle of rotation θ=180º.

The rotating Maxwell coil pair provided a uniform gradient magnetic field and, combined with the Helmholtz coils, generated the propulsion force acting on the magnetic device in the aligned direction. The starting point of the magnetic device was approximately (x,y)=(4.5, 0)mm. When the two Maxwell coil pairs were energized, the magnetic device moved along a linear path in the desired direction. The results are depicted in figures 5.23 to 5.27, for different chosen angles (θ=0º, 45º, 90º, 135º and 180º). The red line in the images indicates the path followed by the device. It was possible to demonstrate that the microrobot can move in various desired directions on a 2D plane.

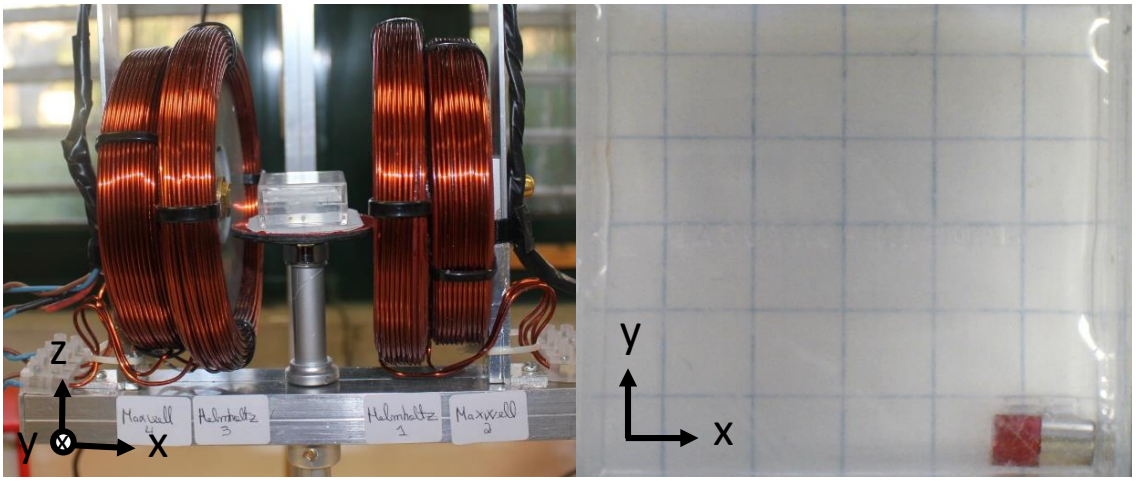

Figure 5.23 Locomotion of the magnetic device by the combination of Helmholtz and Maxwell coils: Initial position (x,y)=(4.5, 0)mm.

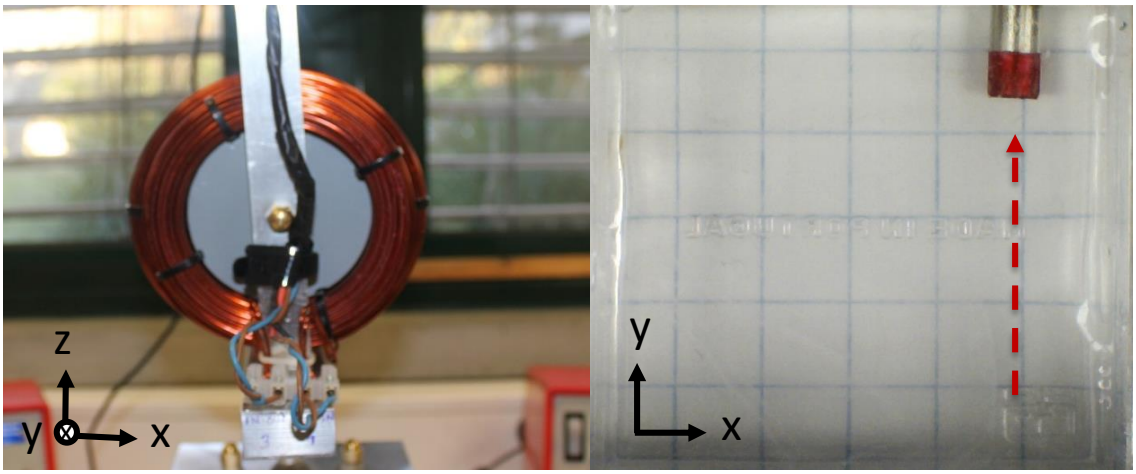

Figure 5.24 Locomotion of the magnetic device by the combination of Helmholtz and Maxwell coils: angle θ=90º.

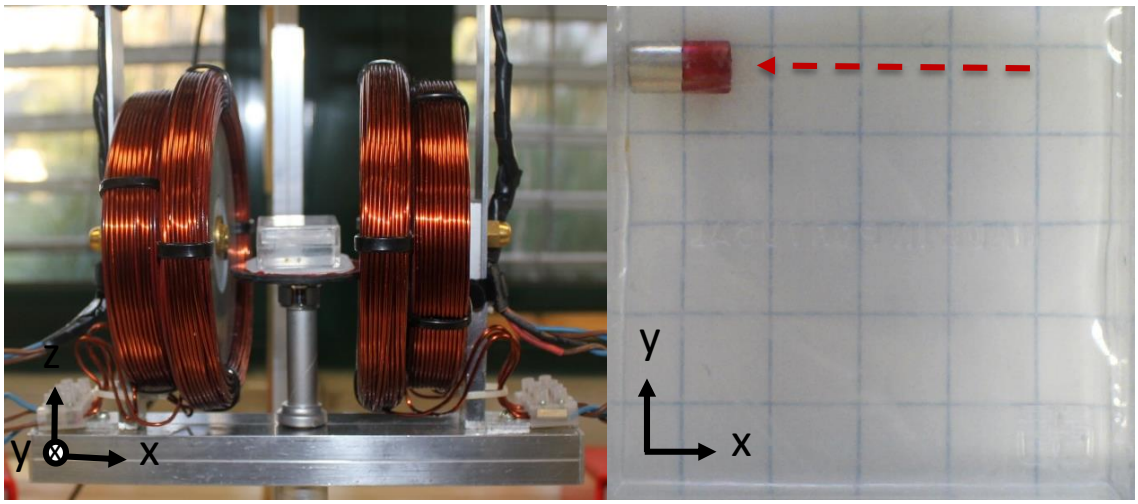

Figure 5.25 Locomotion of the magnetic device by the combination of Helmholtz and Maxwell coils: angle θ=180º.

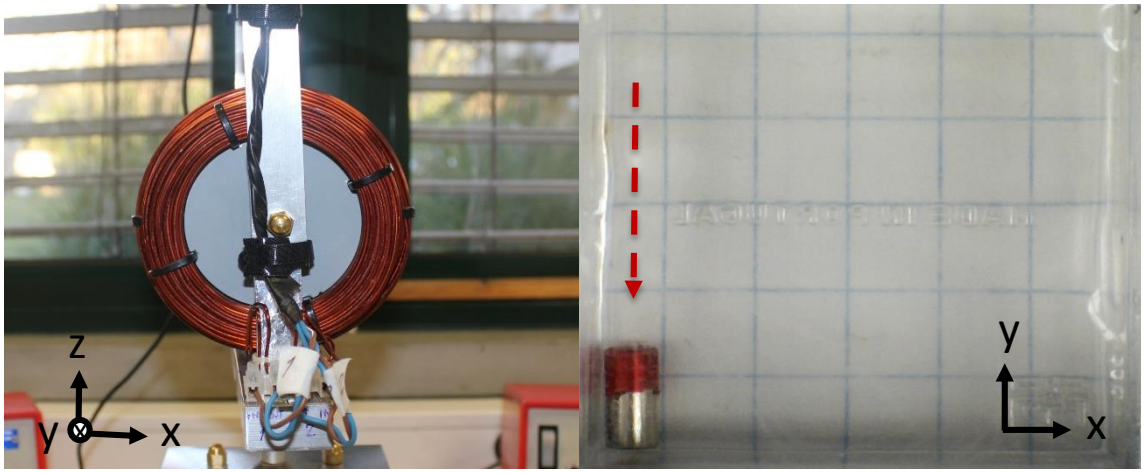

Figure 5.26 Locomotion of the magnetic device by the combination of Helmholtz and Maxwell coils: angle θ=270º.

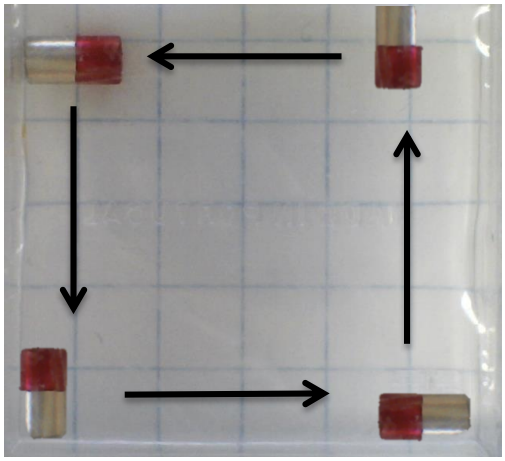

Figure 5.27 Final path of the magnetic device using a combination of the Helmholtz and Maxwell coils.

For the direction switch of the magnetic device, the current direction of the Maxwell coils had to be changed. This was possible with the circuit depicted in figure 5.15. Thus, by changing the direction of the input current in the Maxwell coils, the wireless capsule microrobot could move "backwards". In figures 5.28 and 5.29 it is possible to see two examples of the use of this switch. In 5.28, with a coil angle of θ=135º, in a first instance the device was being attracted to direction of the Maxwell coil 4 (inferior right corner in the ROI), however, by changing the direction of the current in the coils, the device was attracted in the opposite direction (left superior corner in the ROI). In figure 5.29, with a coil angle of θ=0º, the device was being attracted in the direction of the Maxwell coil 4 (opposite to the x-axis direction in the ROI). By using the switch, the device was powered towards the opposite direction (in the x-axis direction).

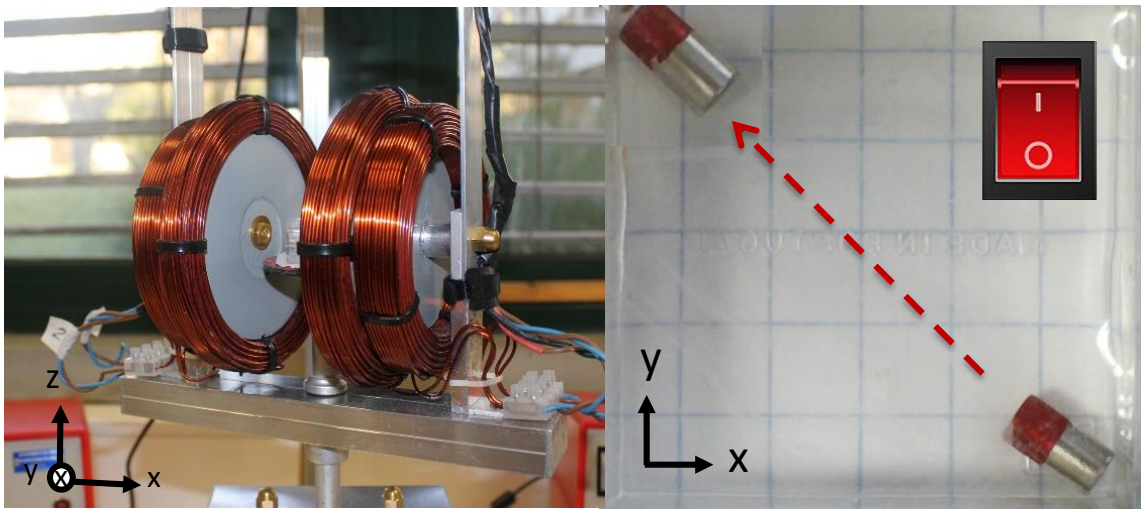

Figure 5.28 Change in the direction of the Maxwell coil current by using the switch (coil angle θ=135º).

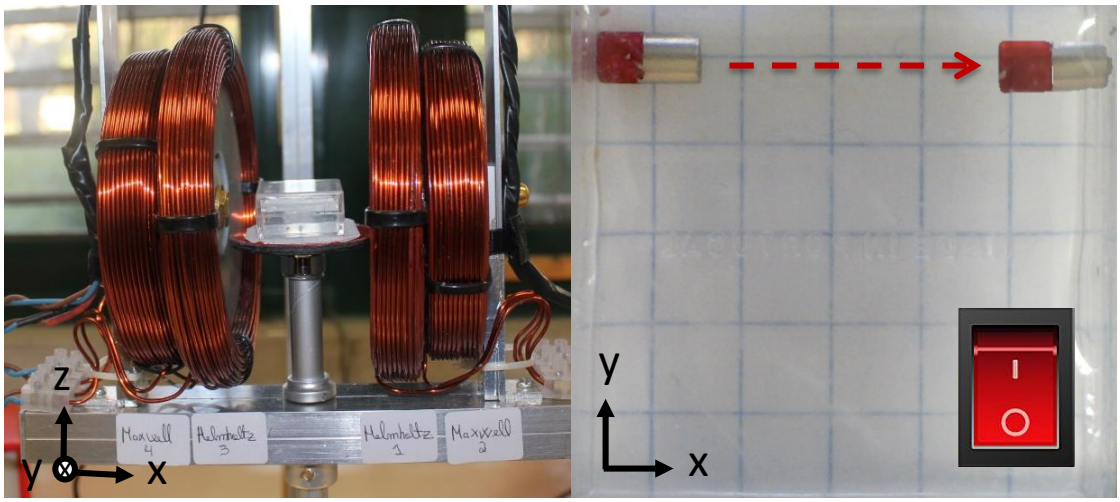

Figure 5.29 Change in the direction of the Maxwell coil current by using the switch (coil angle θ=0º).

Finally, a simple arduino program was developed in order to automatically control the magnetic device in a predefined path, without the need of the potentiometer, by rotating the coils counterclockwise.

Since with the available power supplies it was not possible to automatically control the direction of the currents, it was not possible to control the magnetic device along predefined diagonal paths (without using the switch). Thus, a rectangular shape was selected and tested, and the experiments were performed in a maze-like structure cut into a plastic substrate.

The results of these preliminary tests are depicted in figure 3.30. It was validated that the microrobot could move along the predefined paths.

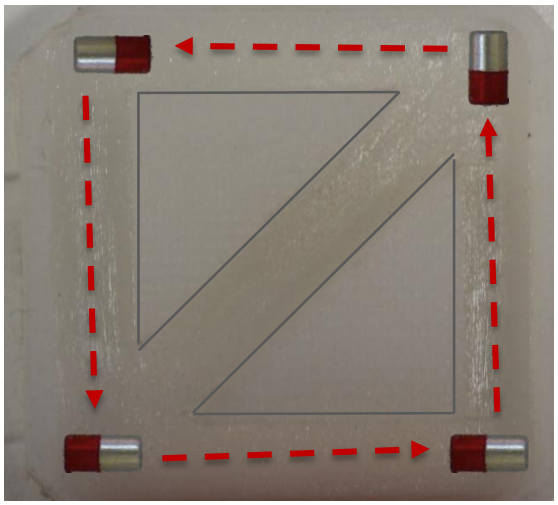

Figure 5.30 Locomotion of microrobot along a predefined path.

With the fabricated system, the magnetic device was easily controlled and moved to a defined position. The rotation of the electromagnetic actuation system was achieved with a manual potentiometer (functioning like a joystick) which allowed the position of the microrobot to be manually adjusted, taking into account the visual feedback from the digital microscope. When the rotation mechanism rotated, the microrobot followed. The rotation angle of the device approximately equals the angle of the rotating platform. This is consistent with equations 3.22 from chapter 3. The torque was implemented on the microrobot with the Helmholtz coils and the Maxwell coils were used to drive the microrobot along a line. This was possible due to the magnetic gradient produced by these coils and it was consistent with equation 3.4. However, since the device was manually adjusted, the coils rotation angles were measured by eye. Thus, there is a difficulty in evaluating the positioning accuracy of the system.

All the same experiences were repeated using the spherical magnet and the same results were obtained.

To sum it up, the motion of a millimetric device in a 2-dimensional plane was tested. Through various experiments, it was verified that the microrobot actuated by the fabricated electromagnetic actuation system could move along a desired direction and path. Thus, the feasibility of these systems was validated. In the next chapter, improvements for the system will be proposed.

"Somewhere, something incredible is waiting to be known"

-Carl Sagan

Chapter 6

Conclusion and Future Work

This chapter will present a discussion of the presented work. Improvements to the current systems and potential applications in the future will be discussed.

6.1 Conclusion

In this dissertation a variety of questions related to the magnetic actuation of microdevices were studied and the feasibility of various types of magnetic actuation systems to control them in blood vessels, at different scales, was evaluated. This work can be divided in three major parts. In the first part, the bibliography related to magnetic actuation was studied in some detail. In the second part, numerical and finite element simulations were performed to define the general requirements to control magnetic devices in blood vessels and test different coil configurations as actuation systems. The third part was the experimental work. A magnetic actuation system was fabricated and the different components of the system were described in detail, taking into account its characteristics, functionality and constraints.

The first step was crucial to understand the physics of the problem, namely, the behavior of the magnetic fields produced by the different coil configurations, the main forces acting on a magnetic device navigating in the blood vessels and the main physiological constraints that should be considered with these applications. Also, this thesis reviewed state-of-the-art magnetic actuation methods to guide magnetic particles. This allowed proper hypotheses and extrapolations to be made. The most important conclusions from this first part are summarized below:

- At the present time, due to the challenges in the miniaturization of actuators and power sources, the most realistic approach to control microdevices in the blood vessels is through the use of magnetic fields;
- For this control, it is possible to use a combination of Helmholtz and Maxwell coils. A Helmholtz configuration generates uniform magnetic fields in the center of the coils and a Maxwell configuration generates uniform magnetic field gradients;
- The two major forces acting on a magnetic microrobot navigating in the blood vessels are the magnetic force and the drag force. The magnetic force is proportional to the magnitude of the applied magnetic gradient, to the magnetic volume of the device and to the magnitude of its magnetization. The drag force is proportional to the surface area of the magnetic device, to the density of the fluid, to the drag coefficient and to the relative velocity between the microdevice and the fluid;
- Several research groups have proposed ways of manipulating magnetic devices in the human body, however a complete actuation system has yet to emerge that addresses the integration of many inter-disciplinary components within real-time, physiological and technological constraints and that could be readily used by the medical community.

With the knowledge obtained from the literature it was possible to perform numerical and finite element simulations to understand the needed magnetic field gradients and to test different proposed systems. The most important conclusions from the numerical simulations are summarized below:

- For a given blood vessel, there is an optimum value λ (ratio of the device to vessel diameter) for efficiently propelling each device which seems to be between 0.4 and 0.6. Particles or agglomerations can only be steered efficiently if their λ is close to the optimum value;
- Depending on the size of the magnetic device, the magnitude of the magnetic fields gradients necessary to propel it against the blood flow varies greatly since the magnetic force is proportional to the volume of the particle and the drag is proportional to the area.
- No clinical or preclinical magnetic gradients can propel particles with less than 20 μm against the blood flow.

- A magnetic field gradient of at least 150 mT/m is needed to propel a magnetic device with 100 μm and 10^6 A/m saturation magnetization, against the blood flow in an artery;
- A magnetic field gradient of at least 750 mT/m is needed to propel a device with 10 μm with 10^6 A/m saturation magnetization against the blood flow. If the device is made of a commonly used material such as magnetite (with 10^5 A/m saturation magnetization) a magnetic field of at least 3100 mT/m is needed.

Since the control of magnetic devices in blood vessels is very dependent on the scale of the problem, two special cases were explored in the finite element simulations. In one case, an electromagnetic actuation system with the purpose of controlling devices permanently magnetized and bigger than 100 μm was considered and, in the other case, an electromagnetic actuation system with the purpose of controlling particles with diameters ranging from 1 μm to 100 μm and taking into account different values of saturation magnetization was studied. From these simulations it was possible to conclude that:

- It is possible to design simple coil systems capable of producing static magnetic fields and homogenous magnetic field gradients between the coils;
- When the Helmholtz and Maxwell coil pairs from the electromagnetic actuation system are used simultaneously, it is possible to obtain an electromagnetic interference which can occur from the superposition of the electromagnetic fields produced by both coil configurations. This interference seems to be closely dependent on the position of the ROI inside the electromagnetic coils system;
- With the finite element method it was confirmed that a magnetic field gradient with a magnitude of at least approximately 150 mT/m is needed to propel a 100 μm device in an artery. With a magnitude of approximately 148 mT/m an equilibrium state is achieved, and the device does not move in the vessel;
- With two pairs of Helmholtz and Maxwell coils it is possible to control a magnetic device in all directions in a 2-dimensional plane;
- Instead of propelling the magnetic devices against the blood flow it is possible to use the flow to propel them and apply the magnetic fields only for steering, moving the particles to the desired exit in a bifurcation on a blood vessel. This approach could be an interesting solution since the magnetic field gradients needed for steering are smaller than the ones needed to propel a particle against the blood flow;

- Contrary to what could be expected, beyond a certain value of applied magnetic gradient, the steering efficiency starts to decrease. This happens because the magnetic particles stick to the vessel walls. This phenomenon should be studied in more detail and solutions should be proposed;
- For a 10 μm size magnetite particle, the steering ratio is optimized with a magnetic gradient between 1×10^4 A/m^2 and 3×10^4 A/m^2 with the highest value of 57% being achieved (once more, this small value is due to the sticking);
- For 1 μm particles, the applied magnetic gradients produced with the proposed system cannot steer it to the desired outlet unless the particle is at the center of the vessel.

In general, it has been proved that CO<MSOL can be successfully used to study the design of magnetic actuation systems and the effect of the produced magnetic field gradients on magnetic devices with different sizes and different magnetization saturations in a blood vessel. These models have taken into consideration the dominant magnetic and fluidic forces that govern the particle motion, using the magnetic fields and the particle tracing module. In the next section, some improvements in the simulations will be proposed. It is possible to conclude that this type of simulations should be considered in the development of novel magnetophoretic systems for medical applications, providing important information for experimental research.

In the third part, a magnetic actuation system based on a concept from Yesin *et al.* was designed, constructed and tested. A *do-it-yourself* (DIY) approach which consists in building something without the aid of experts or professionals, was employed in the fabrication of the system. The system was composed of one pair of Helmholtz coils for the generation of the static magnetic field and one pair of Maxwell coils for the generation of the constant magnetic gradient. It also included a rotational system with a stepper motor and an arduino for the control through the use of a *joystick*, a microscope and a complex structure to support the coils, the microscope and the wires. The orientation of the static magnetic field and orientation of the magnetic field gradient could be manually controlled in all directions using the fabricated mechanism.

Due to the cost restrictions and the *DIY* approach the fabricated system had its limitations. The fabricated magnetic system was capable of generating an almost uniform magnetic field in the workspace with a maximum magnitude of 3.5 ± 0.1 mT and maximum magnetic field gradient of 75±5 mT/m in the center of the coils. However, this value fell short from the one obtained with the FEM simulations (100 mT/m) and was less homogenous.

Also, unfortunately, these magnetic fields and gradients were only tested to control millimetric devices, since a micrometer device was not available. Also, to test smaller devices a better microscope would be needed. Measurements of the velocities and forces were not made since it required a video analysis software which was not yet developed at this time. However, this should be addressed in the future.

The major goal of this part of the project was to gain knowledge and tools which hopefully could be applied to fabricate a more precise system to control magnetic devices at smaller scales.

In general, it was possible to conclude from this work that magnetic actuation seems to provide a suitable means of energy transfer for future biomedical microdevices. However, several problems have to be addressed and much work has to be completed before a clinical solution fully emerges.

6.2 Future Work

There are innumerous ways in which the current work can be extended. In this chapter, some ideas for future research based on the models developed in this dissertation and on the results obtained from the experimental work are presented.

For example, a simulation of the particle trajectory inside realistic blood vessels could be achieved. To obtain more realistic results, the finite element simulations could be applied to more complex arterial geometries, with flexible walls and pulsatile flows. It is possible to use COMSOL to simulate these complex geometries and physics. The flowing blood applies pressure to the artery's internal surfaces and its branches, thereby deforming the tissue. To simulate the flexible walls, the analysis would consist of two distinct but coupled procedures: first, a fluid-dynamics analysis including a calculation of the velocity field and pressure distribution in the blood (variable in time and in space) would have to be made. The second step would consist on a mechanical analysis of the deformation of the tissue and artery. In COMSOL it is possible to simulate this coupling using the ALE (arbitrary Lagrangian-Eulerian) method. In Figure 6.1, it is depicted a model of a portion of the vascular system, in particular the upper part of the aorta. This is an example of a simple geometry but it is more realistic than the Y-shaped one used in the simulations.

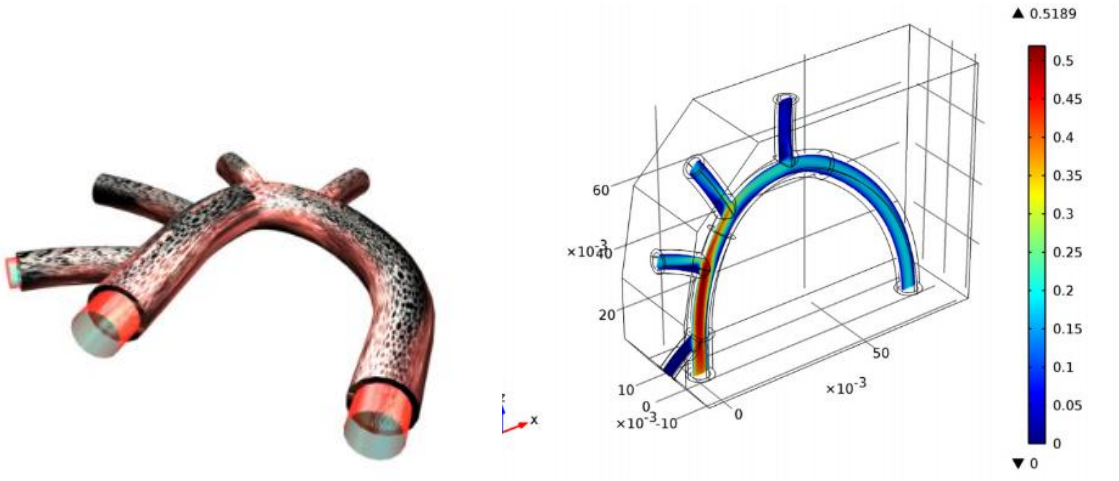

Figure 6.1 *Aorta and its ramifications (branching vessels)* ***a)*** *A view of a 3-dimensional model* ***b)*** *velocity profile inside the vessel* [82].

An interesting approach could be to extract the vessel geometry using MRI images and, based on the extracted information, create a model of the vessels with CAD software. Then, it would be possible to import this model to COMSOL for particle trajectory simulations. In the future, for realistic magnetic microparticle guidance in *in vivo* experiments, the 3-dimensional blood vessel map of each subject should be extracted with an imaging modality such as a MRI. Subsequently, multiparticle guidance schemes at different bifurcations of blood vessels should be considered further and investigated.

Other physical properties and parameters could be considered in future simulations. For example, it would be interesting to include all nontrivial forces acting of the particles, such as inter-particle magnetic forces, dispersion due to collisions between the particles and blood cells and complex viscous forces applied by non-Newtonian blood. Also, in all the simulations it was considered that the particles were at its value of saturation magnetization. For realistic results, the B-H curves for the particle's material should be applied. In general, the simulation environment should be expanded so that more realistic scenarios are studied.

Still related to the FEM simulations, other different coils with various sizes, shapes, arrangements, and materials (for example, including or not soft magnetic cores could be simulated) for generating sufficiently high static magnetic field and magnetic field gradient for controlling smaller microparticles could be explored. The resulting optimal designs could be used for an apparatus construction. The simulation model should be validated with experimental data for the particle control.

In this work, an apparatus was successfully designed and built for guiding large magnetic microdevices by manually controlling the applied static magnetic fields and magnetic field gradients. In the future, it would be interesting to design and fabricate a new system while improving and experimenting with the present one.

Improvements to the present system could include adding a third pair of coils to have control in the three spatial dimensions. The third coil would have to be considerably stronger in order to propel the particle against the force of gravity. Other interesting improvements could be the implementation of video analysis in order to measure forces, velocities and displacements of the microdevices and compare this data with the FEM simulations. Also, a software application could be developed in which it would be possible to define the end target site and, for the particle position and fluid flow velocities, define and apply the suitable magnetic field gradient pulses using a proper algorithm. For example, the microscope images could be acquired and processed using MATLAB for identifying the particles' position and then the proper magnetic field scheme could be programmed into computer-controlled power sources. This approach would enable a real-time control of the magnetic device which would be important for future medical applications. With this feedback control system it would be possible to adjust the applied external magnetic field gradient to steer the magnetic devices towards the correct arterial path.

Additionally, improved mechanics (framework and motors) and electronics control could be developed for a more suitable integration of the system with the microscope setup.

The design of a new system should focus on the control of smaller magnetic microdevices. For this, higher static magnetic fields and higher magnetic gradients are required. One option could be the use of special core materials in order to generate magnetic fields with higher magnitude at lower electrical currents. It would also be important to include computer-controlled power sources to power the coils such that automatic and seamless guiding of the particle would be achieved.

In future studies, different particles with different dimensions and saturation magnetizations, as well as different fluid flow velocities, and magnetic field pulse schemes should be tested using vascular phantoms. One of the simplest phantoms to be tested could be the Y-shaped millimeter/micrometer-sized channels like the one used in the finite element simulations. It would also be interesting to increase the complexity of the phantoms which, as it was explained before, could be first designed and modeled in COMSOL. The fluid flow in the phantom could be achieved by using computer-controlled pumps in order to better simulate the blood flow.

The efficiency of microparticle guiding could be evaluated qualitatively via visual inspection and also quantitatively through the use of atomic absorption spectroscopy (AAS). A suspension containing the magnetic particles could be collected in vials at both outlets of a Y-shaped channel and the iron content of each vial could be measured with AAS. If particles are guided to one the outlets of the Y-shaped channel (correct outlet) it would be expected that a high iron content would be measured in that collection vial, whereas in the other collection vial it would be expected that the iron content would be negligible. If the particles are made of iron oxide with stoichiometric proportions Fe_3O_4, the iron content of the particles gathered in each vial is a direct measurement of their mass. This mass information could be used to calculate the steering ratio. These steering ratios could be compared to the ones obtained from the FEM simulations.

In general, future research should focus on medical implementation. Ways of modifying this magnetic actuation setup to make it suitable for clinical use should be evaluated. For example, the microscopic system should be replaced with a system capable of visualizing the microrobot in the circulatory system without disturbing its position. In chapter 3, some possible solutions were presented. If in the future the control of nanoparticles is made possible, magnetic particle imaging will be a promising technique, however, it must be made faster and proven to work on moving devices. The problem of visualization is an important consideration when developing a final functional actuation system.

Also, to control the microrobots in the human body, a larger magnetic workspace will be needed. At any point, the magnetic field generated by the coils is inversely proportional to the square distance between the point and the coils. Thus, much larger coils with a higher number of turns and higher currents will have to be used which could be problematic. This problem should be evaluated.

The future work in this field will have to involve a multidisciplinary approach. One important issue to assess is the safety of this method. There is a possibility that the magnetic devices could cause damage to vessels and tissues. Until now these possible negative effects were not studied by any research group. The interactions between the particles and the tissue environment and its possible consequences should be investigated in the future. Also, it must be shown that exposure to strong magnetic field gradients (much stronger than the ones used in clinical MRIs) will not harm the patients.

To conclude, medical microrobots navigating in the vascular network is a new field of research that starts to show potential in target interventions such as in cancer therapies. Hopefully, this technology will contribute to enhanced therapeutic efficacy while reducing severe secondary toxicity for the patients.

The broader goal of this dissertation project was to provide basis for future developments allowing the implementation of magnetic actuation systems in clinical practice. Much progress still has to be made towards understanding and optimizing these types of systems. Before magnetic actuation systems can be used on patients, further research must be completed in several areas, some of them unrelated to this work. The future work will have to involve a multi-disciplinary approach from engineers, biologists, doctors and other researchers. Also, all the process will have to be approved by the FDA (Food and Drug Administration) and by the EMA (European Medicines Agency) which will involve extensive testing in animals and humans. Hopefully, within a few years, this technique will be in clinical trials, opening new possibilities to humanity.

References

[1] M. C. Carrozza, P. Dario, and L. P. S. Jay, “Micromechatronics in surgery,” *Trans. Inst. Meas. Control*, vol. 25, no. 4, pp. 309–327, 2003.

[2] M. J. Mack, “Minimally Invasive and Robotic Surgery,” *JAMA*, vol. 285, no. 5, p. 568, Feb. 2001.

[3] S. Martel, O. Felfoul, J.-B. Mathieu, A. Chanu, S. Tamaz, M. Mohammadi, M. Mankiewicz, and N. Tabatabaei, “MRI-based Medical Nanorobotic Platform for the Control of Magnetic Nanoparticles and Flagellated Bacteria for Target Interventions in Human Capillaries.,” *Int. J. Rob. Res.*, vol. 28, no. 9, pp. 1169–1182, Sep. 2009.

[4] J. Coey, *Magnetism and magnetic materials*, 1st ed. Cambridge uniiversity press, 2010.

[5] M. Getzlaff, *Fundamentals of Magnetism*, 1st ed. Springer Verlag, 2007.

[6] H. E. Knoepfel, *Magnetic Fields: A comprehensive Theoretical Treatise for Pratical Use*, 1st ed. Wiley-Interscience, 2000.

[7] B.D.Cullity and C.Graham, *Introduction to Magnetic Materials*, 2nd ed. Wiley-IEEE Press, 2008.

[8] H. W. F. Sung and C. Rudowicz, “A closer look at the hysteresis loop for ferromagnets - A survey of misconceptions and misinterpretations in textbooks,” no. 1985, pp. 1–24, 1999.

[9] E. Furlani, *Permanent Magnet and Electromechanical Devices: Materials, Analysis, and Applications*, 1st ed. Academic Press, 2001.

[10] D. Jiles, *Introduction to Magnetism and Magnetic Materials*, 2nd ed. CRC Press, 1991.

[11] J. Jin, *Electromagnetic Analysis and Design in Magnetic Resonance Imaging*. CRC Press, 1998.

[12] S. Martel, “Magnetic resonance propulsion, control and tracking at 24 Hz of an untethered device in the carotid artery of a living animal: an important step in the development of medical micro- and nanorobots.,” *Conf. Proc. IEEE Eng. Med. Biol. Soc.*, vol. 2007, pp. 1475–8, Jan. 2007.

[13] N. Chaillet and S. Régnier, *Microrobotics for Micromanipulation*, 1st ed. Wiley-ISTE, 2010.

[14] R. P. Feynman, “There’s plenty of room at the bottom,” *Engineering and science*, vol. 23. pp. 22–36, 1960.

[15] K.Ishiyama, “Micro Swimming Mechanisms Propelled by External Magnetic Fields,” *IEEE Transactions on magnetics*, 1996.

[16] I. Kassim, L. Phee, W. S. Ng, P. Dario, and C. A. Mosse, “Locomotion techniques for robotic colonoscopy,” *IEEE Eng. Med. Biol. Mag.*, vol. 25, no. 3, pp. 49–56, May 2006.

[17] B. J. Nelson, I. K. Kaliakatsos, and J. J. Abbott, “Microrobots for minimally invasive medicine.,” *Annu. Rev. Biomed. Eng.*, vol. 12, no. April, pp. 55–85, 2010.

[18] N. T. Series, F. Leonard, M. Diallo, J. Duncan, N. Savage, W. Ahmed, R. Leach, V. Lindroos, M. Hull, Y. Sun, V. Zhirnov, R. K. Cavin, and J. Ramsden, *Microbiorobotics*. .

[19] S. A. Berger, W. Goldsmith, and E. R. Lewis, *Introduction to bioengineering*, 1st ed. Oxford University Press, 1996.

[20] P. D. Purdy, T. Fujimoto, R. E. Replogle, B. P. Giles, H. Fujimoto, and S. L. Miller, “Percutaneous intraspinal navigation for access to the subarachnoid space: use of another natural conduit for neurosurgical procedures.,” *Neurosurg. Focus*, vol. 19, no. 1, p. E11, Jul. 2005.

[21] M. S. Grady, “Preliminary experimental investigation of in vivo magnetic manipulation: Results and potential application in hyperthermia,” *Med. Phys.*, vol. 16, no. 2, p. 263, Mar. 1989.

[22] G. Kosa, M. Shoham, and M. Zaaroor, “Propulsion Method for Swimming Microrobots,” *IEEE Trans. Robot.*, vol. 23, no. 1, pp. 137–150, Feb. 2007.

[23] S. Roy, L. A. Ferrara, A. J. Fleischman, and E. C. Benzel, *BioMEMS and Biomedical Nanotechnology*. Boston, MA: Springer US, 2007.

[24] “Human Anatomy Reference.” [Online]. Available: http://www.livelancaster.org/brain-ventricle/.

[25] J. Edd, S. Payen, B. Rubinsky, M. L. Stoller, and M. Sitti, “Biomimetic propulsion for a swimming surgical micro-robot,” *Proc. 2003 IEEE/RSJ Int. Conf. Intell. Robot. Syst. (IROS 2003) (Cat. No.03CH37453)*, vol. 3, 2003.

[26] B. Kristo, J. C. Liao, H. P. Neves, B. M. Churchill, C. D. Montemagno, and P. G. Schulam, “Microelectromechanical systems in urology,” *Urology*, vol. 61, no. 5, pp. 883–887, May 2003.

[27] K. B. Yesin, “Modeling and Control of Untethered Biomicrorobots in a Fluidic Environment Using Electromagnetic Fields,” *Int. J. Rob. Res.*, vol. 25, no. 5–6, pp. 527–536, May 2006.

[28] G. Dogangil, O. Ergeneman, J. J. Abbott, S. Pané, H. Hall, S. Muntwyler, and B. J. Nelson, “Toward targeted retinal drug delivery with wireless magnetic microrobots,” *2008 IEEE/RSJ Int. Conf. Intell. Robot. Syst. IROS*, pp. 1921–1926, 2008.

[29] D. L. Holligan, G. T. Gillies, and J. P. Dailey, “Magnetic guidance of ferrofluidic nanoparticles in an in vitro model of intraocular retinal repair,” *Nanotechnology*, vol. 14, no. 6, pp. 661–666, Jun. 2003.

[30] E. Diller, “Micro-Scale Mobile Robotics,” *Found. Trends Robot.*, vol. 2, no. 3, pp. 143–259, 2011.

[31] K. A. Cook-Chennault, N. Thambi, and A. M. Sastry, “Powering MEMS portable devices—a review of non-regenerative and regenerative power supply systems with special emphasis on piezoelectric energy harvesting systems,” *Smart Materials and Structures*, vol. 17, no. 4. p. 043001, 2008.

[32] S. A. Jacobson and A. H. Epstein, “An informal survey of power MEMS,” *Int. Symp. MicroMechanical Eng.*, vol. 12, pp. 513–519, 2003.

[33] N. Mano, F. Mao, and A. Heller, “A miniature membrane-less biofuel cell operating at +0.60 V under physiological conditions,” *ChemBioChem*, vol. 5, no. 12, pp. 1703–1705, 2004.

[34] J. F. Alksne, a G. Fingerhut, and R. W. Rand, “Magnetic probe for the stereotactic thrombosis of intracranial aneurysms.,” *J. Neurol. Neurosurg. Psychiatry*, vol. 30, no. 2, pp. 159–62, Apr. 1967.

[35] J. A. Molloy, R. C. Ritter, M. S. Grady, M. A. Howard, E. G. Quate, and G. T. Gillies, “Experimental determination of the force required for insertion of a thermoseed into deep brain tissues,” *Ann. Biomed. Eng.*, vol. 18, no. 3, pp. 299–313, May 1990.

[36] Z. Luo, K. Cai, Y. Hu, J. Li, X. Ding, B. Zhang, D. Xu, W. Yang, and P. Liu, “Redox-Responsive Molecular Nanoreservoirs for Controlled Intracellular Anticancer Drug Delivery Based on Magnetic Nanoparticles.,” *Adv. Mater.*, Dec. 2011.

[37] B. Chertok, A. E. David, and V. C. Yang, “Polyethyleneimine-modified iron oxide nanoparticles for brain tumor drug delivery using magnetic targeting and intra-carotid administration.,” *Biomaterials*, vol. 31, no. 24, pp. 6317–24, Aug. 2010.

[38] M. M. Yallapu, S. P. Foy, T. K. Jain, and V. Labhasetwar, “PEG-functionalized magnetic nanoparticles for drug delivery and magnetic resonance imaging applications.,” *Pharm. Res.*, vol. 27, no. 11, pp. 2283–95, Nov. 2010.

[39] A. D. Grief and G. Richardson, “Mathematical modelling of magnetically targeted drug delivery,” *J. Magn. Magn. Mater.*, vol. 293, no. 1, pp. 455–463, May 2005.

[40] G. Iacob, O. Rotariu, N. J. C. Strachan, and U. O. Häfeli, “Magnetizable needles and wires--modeling an efficient way to target magnetic microspheres in vivo.,” *Biorheology*, vol. 41, no. 5, pp. 599–612, Jan. 2004.

[41] Z. G. Forbes, B. B. Yellen, D. S. Halverson, G. Fridman, K. A. Barbee, and G. Friedman, “Validation of high gradient magnetic field based drug delivery to magnetizable implants under flow.,” *IEEE Trans. Biomed. Eng.*, vol. 55, no. 2 Pt 1, pp. 643–9, Feb. 2008.

[42] U. Häfeli, M. Zborowski, A. J. Rosengart, M. D. Kaminski, H. Chen, P. L. Caviness, A. D. Ebner, and J. A. Ritter, “Magnetizable implants and functionalized magnetic carriers: A novel approach for noninvasive yet targeted drug delivery,” *J. Magn. Magn. Mater.*, vol. 293, no. 1, pp. 633–638, 2005.

[43] J. B. Mathieu, S. Martel, L. Yahia, G. Soulez, and G. Beaudoin, “Preliminary investigation of the feasibility of magnetic propulsion for future microdevices in blood vessels.,” *Biomed. Mater. Eng.*, vol. 15, no. 5, pp. 367–74, Jan. 2005.

[44] S. Martel, J. B. Mathieu, O. Felfoul, A. Chanu, E. Aboussouan, S. Tamaz, P. Pouponneau, L. Yahia, G. Beaudoin, G. Soulez, and M. Mankiewicz, “Automatic navigation of an untethered device in the artery of a living animal using a conventional clinical magnetic resonance imaging system,” *Appl. Phys. Lett.*, vol. 90, no. 11, p. 114105, 2007.

[45] J. B. Mathieu and S. Martel, “Magnetic microparticle steering within the constraints of an MRI system: proof of concept of a novel targeting approach.,” *Biomed. Microdevices*, vol. 9, no. 6, pp. 801–8, Dec. 2007.

[46] J. B. Mathieu and S. Martel, “Steering of aggregating magnetic microparticles using propulsion gradients coils in an MRI Scanner.,” *Magn. Reson. Med.*, vol. 63, no. 5, pp. 1336–45, May 2010.

[47] J. Mathieu and S. Martel, “Aggregation of magnetic microparticles in the context of targeted therapies actuated by a magnetic resonance imaging system,” pp. 1–7, 2009.

[48] P. Pouponneau, J.-C. Leroux, and S. Martel, “Magnetic nanoparticles encapsulated into biodegradable microparticles steered with an upgraded magnetic resonance imaging system for tumor chemoembolization.,” *Biomaterials*, vol. 30, no. 31, pp. 6327–32, Oct. 2009.

[49] S. Zhang, “Real-Time Magnetic Resonance Imaging of Temporomandibular Joint Dynamics,” *Open Med. Imaging J.*, vol. 5, pp. 1–9, 2011.

[50] C. Sun, J. S. H. Lee, and M. Zhang, “Magnetic nanoparticles in MR imaging and drug delivery.,” *Adv. Drug Deliv. Rev.*, vol. 60, no. 11, pp. 1252–65, Aug. 2008.

[51] M. Sendoh, K. Ishiyama, and K.-I. Arai, “Fabrication of magnetic actuator for use in a capsule endoscope,” *IEEE Trans. Magn.*, vol. 39, no. 5, pp. 3232–3234, Sep. 2003.

[52] A. Yamazaki, M. Sendoh, K. Ishiyama, and K. I. Arai, “Effect of Machine Length on Swimming Properties of Spiral Magnetic Micro-Machine,” *J. Magn. Soc. Japan*, vol. 28, pp. 632–635, 2004.

[53] A. Chiba, M. Sendoh, K. Ishiyama, and I. Arai, “Magnetic actuator for capsule endoscope navigation system,” *INTERMAG Asia 2005. Dig. IEEE Int. Magn. Conf. 2005.*, vol. 12, no. 2, pp. 89–92, 2005.

[54] K. E. Peyer, E. C. Siringil, L. Zhang, M. Suter, and B. J. Nelson, “Bacteria-inspired magnetic polymer composite microrobots,” *Lect. Notes Comput. Sci. (including Subser. Lect. Notes Artif. Intell. Lect. Notes Bioinformatics)*, vol. 8064 LNAI, pp. 216–227, 2013.

[55] H. Choi, J. Choi, G. Jang, J. Park, and S. Park, “Two-dimensional actuation of a microrobot with a stationary two-pair coil system,” *Smart Mater. Struct.*, vol. 18, p. 055007, 2009.

[56] S. Jeon, G. Jang, H. Choi, and S. Park, “Magnetic navigation system with gradient and uniform saddle coils for the wireless manipulation of micro-robots in human blood vessels,” *IEEE Trans. Magn.*, vol. 46, no. 6, pp. 1943–1946, 2010.

[57] S. Jeong, H. Choi, J. Choi, C. Yu, J. O. Park, and S. Park, “Novel electromagnetic actuation (EMA) method for 3-dimensional locomotion of intravascular microrobot,” *Sensors Actuators, A Phys.*, vol. 157, pp. 118–125, 2010.

[58] M. P. Kummer, J. J. Abbott, B. E. Kratochvil, R. Borer, A. Sengul, and B. J. Nelson, “Octomag: An electromagnetic system for 5-DOF wireless micromanipulation,” *IEEE Trans. Robot.*, vol. 26, no. 6, pp. 1006–1017, 2010.

[59] C. Alexiou, D. Diehl, P. Henninger, H. Iro, R. Röckelein, W. Schmidt, and H. Weber, “A high field gradient magnet for magnetic drug targeting,” *IEEE Trans. Appl. Supercond.*, vol. 16, no. 2, pp. 1527–1530, 2006.

[60] P. Vartholomeos, M. Fruchard, A. Ferreira, and C. Mavroidis, “MRI-guided nanorobotic systems for therapeutic and diagnostic applications.,” *Annu. Rev. Biomed. Eng.*, vol. 13, pp. 157–184, 2011.

[61] J. J. Abbott, O. Ergeneman, M. P. Kummer, A. M. Hirt, and B. J. Nelson, “Modeling Magnetic Torque and Force for Controlled Manipulation of Soft-Magnetic Bodies,” *IEEE Trans. Robot.*, vol. 23, no. 6, pp. 1247–1252, Dec. 2007.

[62] P. Vartholomeos and C. Mavroidis, “Simulation platform for self-assembly structures in MRI-guided nanorobotic drug delivery systems,” *2010 IEEE Int. Conf. Robot. Autom.*, pp. 5594–5600, May 2010.

[63] P. Vartholomeos, C. Mavroidis, and N. Hata, “Magnetic targeting of aggregated nanoparticles for advanced lung therapies: A robotics approach,” in *2010 3rd IEEE RAS & EMBS International Conference on Biomedical Robotics and Biomechatronics*, 2010, pp. 861–868.

[64] P. A. Voltairas, D. I. Fotiadis, and L. K. Michalis, “Hydrodynamics of magnetic drug targeting,” *J. Biomech.*, vol. 35, no. 6, pp. 813–821, 2002.

[65] J. W. Haverkort, S. Kenjeres, and C. R. Kleijn, “Computational simulations of magnetic particle capture in arterial flows.,” *Ann. Biomed. Eng.*, vol. 37, no. 12, pp. 2436–48, Dec. 2009.

[66] J.-B. Mathieu, G. Beaudoin, and S. Martel, “Method of propulsion of a ferromagnetic core in the cardiovascular system through magnetic gradients generated by an MRI system.,” *IEEE Trans. Biomed. Eng.*, vol. 53, no. 2, pp. 292–9, Feb. 2006.

[67] K. Belharet and A. Ferreira, “3D Controlled Motion of a Microrobot using Magnetic Gradients,” vol. 8, pp. 1069–1083, 2011.

[68] T. B. Jones, *Electromechanics of Particles*. Cambridge: Cambridge University Press, 1995.

[69] L. Arcese, A. Cherry, M. Fruchard, and A. Ferreira, “High Gain Observer for backstepping control of a MRI-guided therapeutic microrobot in blood vessels,” *2010 3rd IEEE RAS EMBS Int. Conf. Biomed. Robot. Biomechatronics*, pp. 349–354, Sep. 2010.

[70] a R. Pries, T. W. Secomb, and P. Gaehtgens, “Biophysical aspects of blood flow in the microvasculature.,” *Cardiovasc. Res.*, vol. 32, no. 4, pp. 654–67, Oct. 1996.

[71] R. Lau, M. Hassan, W. Wong, and T. Chen, “Revisit of the wall effect on the settling of cylindrical particles in the inertial regime,” pp. 1–18.

[72] C. Mavroidis and A. Ferreira, *Nanorobotics: Current Approaches and Techniques*. Springer Science & Business Media, 2013.

[73] a. Nacev, C. Beni, O. Bruno, and B. Shapiro, “The behaviors of ferromagnetic nano-particles in and around blood vessels under applied magnetic fields,” *J. Magn. Magn. Mater.*, vol. 323, no. 6, pp. 651–668, 2011.

[74] E. M. Cherry, P. G. Maxim, and J. K. Eaton, “Particle size, magnetic field, and blood velocity effects on particle retention in magnetic drug targeting.,” *Med. Phys.*, vol. 37, no. 1, pp. 175–82, Jan. 2010.

[75] H. Choi, J. Choi, S. Jeong, C. Yu, J. Park, and S. Park, “Two-dimensional locomotion of a microrobot with a novel stationary electromagnetic actuation system,” *Smart Mater. Struct.*, vol. 18, p. 115017, 2009.

[76] J. W. Haverkort, S. Kenjereš, and C. R. Kleijn, “Computational simulations of magnetic particle capture in arterial flows,” *Ann. Biomed. Eng.*, vol. 37, pp. 2436–2448, 2009.

[77] M. D. Tehrani, M. O. Kim, and J. Yoon, “A Novel Electromagnetic Actuation System for Magnetic Nanoparticle Guidance in Blood Vessels,” *IEEE Trans. Magn.*, vol. 50, no. c, pp. 1–12, 2014.

[78] J. Choi, H. Choi, S. Jeong, B. J. Park, S. Y. Ko, J.-O. Park, and S. Park, “Position-based Compensation of Electromagnetic Fields Interference for Electromagnetic Locomotive Microrobot,” *Proc. Inst. Mech. Eng. Part C J. Mech. Eng. Sci.*, vol. 227, no. 9, pp. 1915–1926, 2012.

[79] M. M. Larimi, a. Ramiar, and a. a. Ranjbar, “Numerical simulation of magnetic nanoparticles targeting in a bifurcation vessel,” *J. Magn. Magn. Mater.*, vol. 362, pp. 58–71, 2014.

[80] B. Chertok, A. E. David, and V. C. Yang, “Brain tumor targeting of magnetic nanoparticles for potential drug delivery: Effect of administration route and magnetic field topography,” *J. Control. Release*, vol. 155, no. 3, pp. 393–399, Nov. 2011.

[81] P. Vartholomeos and C. Mavroidis, “In silico studies of magnetic microparticle aggregations in fluid environments for MRI-guided drug delivery.,” *IEEE Trans. Biomed. Eng.*, vol. 59, no. 11, pp. 3028–38, Nov. 2012.

[82] “COMSOL Multiphysics Model.” [Online]. Available: http://www.comsol.com/model/download/35115/blood_vessel_sbs.pdf.

Appendix A

MATLAB code

Through numerical simulations using MATLAB it was possible to define the general requirements in order to control magnetic microdevices in blood vessels. In this appendix the MATLAB code used to produce the family of curves in Figure 4.1 is presented.

```
%Magnetic gradients in T/m
Grad = [0.03 0.045 0.050 0.060 0.1 0.2 0.3 0.4];

%Vessel properties
N = 3*10^-3; %blood viscosity (Kg.m^-1.s^-1)
l= 3*10^-3; %Vessel diameter - artery (m)
U=1*10^-1; %Blood flow in artery (m/s)
l2=0.5*10^-3; %Vessel diameter-small artery (m)
U2=1.3*10^-2; %Blood flow in small artery (m/s)
l3=3*10^-5; %Vessel diameter-Arteriole (m)
U3=1*10^-2; %Blood flow in Arteriole (m/s)
l4=7*10^-6; %Vessel diameter-Capillary (m)
U4=7*10^-4; %Blood flow in capillary (m/s)

%Particle properties
Ms = 1*10^6; % Saturation magnetization of iron oxide(A/m)
r = linspace(1e-6, 1.2e-4);%radius of the particles
d=2.*r; %particle diameter
V = 4*pi*(r.^3)./3; %Volume of the MNP (or volume of the
agglomeration)

delta= d./l; %Ratio of particle to vessel diameter
deltazero=0.29; p=1.5; %Parameters for the wall-factor formula

Uinf=(U.*(1+(delta./deltazero).^p))./(1-(delta.^p)); %relative
terminal velocity

%Dominant forces exerted on a single NP: magnetic force and drag
force:
for i=1:8
Grad=Gradv(i);

Fm=V.*Ms.*Grad;  %Magnetic Force (N)

Fd=6*pi*N.*r.*Uinf; % Blood-flow drag force (N)

%Ratio of magnetic forces over drag forces exerted on the particle
Cmd=Fm./Fd;

plot(r, Cmd); xlim([1e-6, 1e-4])
legend('0.03','0.045','0.050','0.060','0.1','0.2','0.3','0.4')
hold all;end
```

Appendix B

Differential current coil approach

In this section, results obtained from the finite element simulation of a differential current coil system are presented. This system generates a magnetic gradient field by increasing the current density in one coil, while decreasing it in the other, attracting the particles towards the coil with higher current density. For this coil configuration, the external current density was computed using a homogenized model for the coils, each one made with 4000 wire turns. One of the coils was excited by a current of 20 A and the other was excited by a current of 10 A. The current flowed through both the coils in the same direction.

Figure B.1 depicts the resulting mesh for the system. Figure B.2 shows the resultant magnetic flux density norm and the direction of the magnetic field. In the Figure B.3, the resultant magnetic flux density and magnetic gradient along the x-axis in the ROI are presented. In Figure B.3, it is possible to see that, with this coil configuration, the magnetic flux density along the $\vec{x}$-axis is approximately 200 $\pm$ 25 mT. Also, it is possible to conclude that with this specific configuration, a magnetic gradient of approximately 1500$\pm$ 500 mT/m would be generated. Thus, a high magnetic field gradient is generated, however, it is not homogenous.

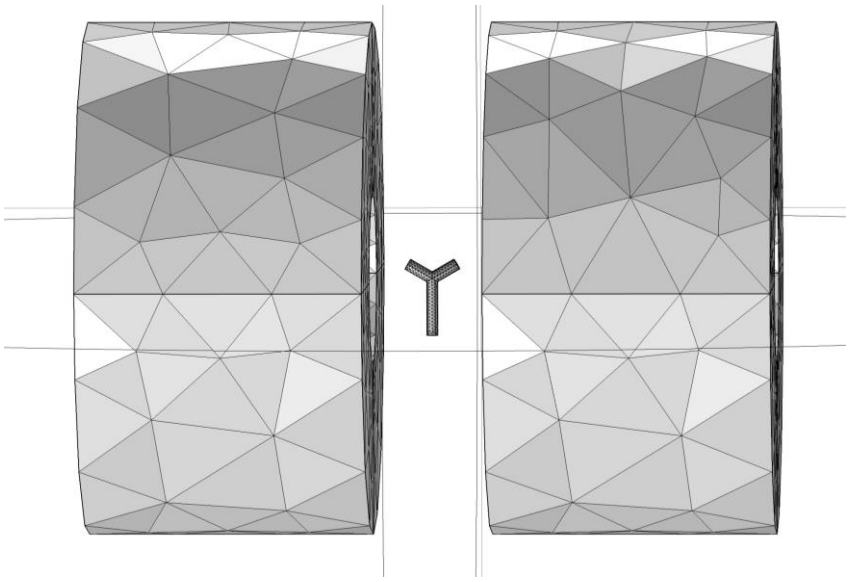

Figure B.1 *Three dimensional Mesh Model of the coil pair (the mesh for the air domain was omitted)*

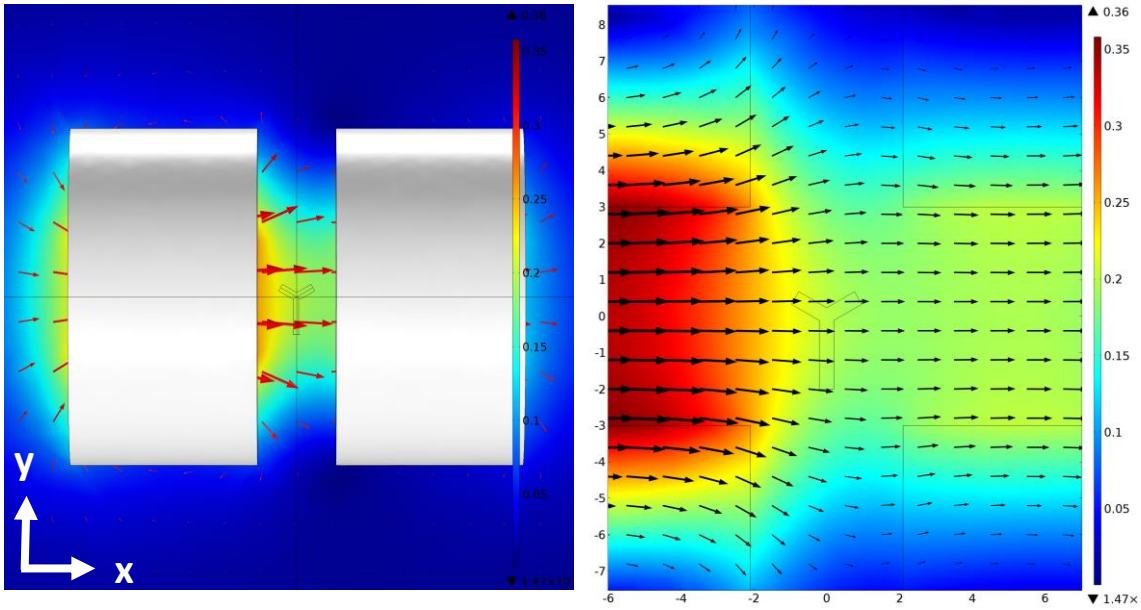

Figure B.2 *The slice plot shows the magnetic flux density norm (T) produced by this coil configuration. The arrows indicate the magnetic field strength (A/m) and direction.*

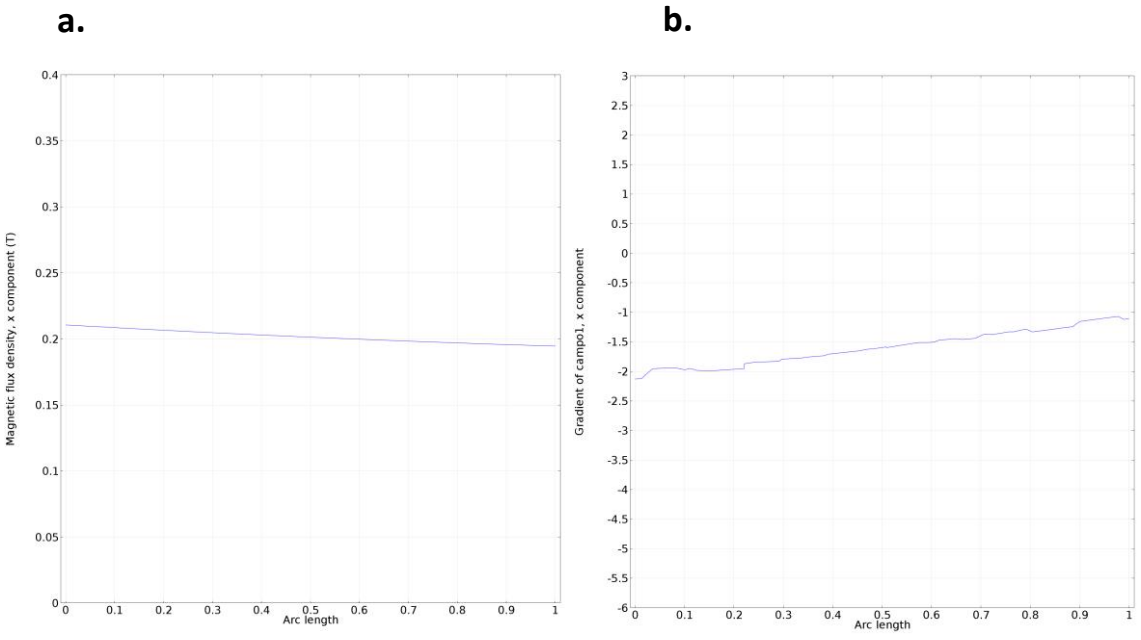

Figure B.3 a) *The magnetic flux density (T) profile along a line in the x-axis, b) Magnetic gradient (T/m) profile along the x-axis.*

Appendix C

Magnets

Characteristics of the permanent magnets used as microdevices in the experimental work:

Article	S-03-06-N	
Shape	Rod	
Diameter	3 mm	
Height	6 mm	
Tolerance in size	+/- 0,1 mm	
Direction of magnetisation	axial (parallel to height)	
Material	NdFeB (Neodymium Iron Boron)	
Type of coating	Nickel (Ni-Cu-Ni)	
Strength	approx. 350 g	approx. 3,43 N
Weight	0,3223 g	
Manufacturing method	sintered	
Magnetisation (Grade)	N48	
Max. working temperature	80°C	
Curie temperature	310 °C	
Residual magnetism Br	13700-14200 G	1.37-1.42 T
Coercive field strength bHc	10.8-12.5 kOe	860-995 kA/m
Coercive field strength iHc	≥12 kOe	≥955 kA/m
Energy product (BxH)max	45-48 MGOe	358-382 kJ/m^3

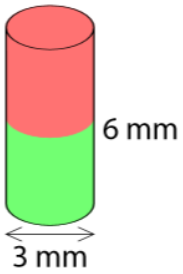

Article	K-03-C	
Shape	Sphere	
Diameter	3 mm	
Tolerance in size	+/- 0,1 mm	
Material	NdFeB (Neodymium Iron Boron)	
Type of coating	Chrome-plated nickel (Ni-Cu-Ni-Cr)	
Strength	approx. 130 g	approx. 1,26 N
Weight	0,1074 g	
Manufacturing method	sintered	
Magnetisation (Grade)	N42	
Max. working temperature	80°C	
Curie temperature	310 °C	
Residual magnetism Br	12900-13200 G	1.29-1.32 T
Coercive field strength bHc	10.8-12.0 kOe	860-955 kA/m
Coercive field strength iHc	≥12 kOe	≥955 kA/m
Energy product (BxH)max	40-42 MGOe	318-334 kJ/m^3

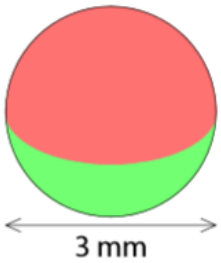

Pollutant-free according to RoHS Directive 2011/65/EU.
Exempt from registration according to REACH.

Appendix D

ARDUINO code

To control the rotation of the coils with a potentiometer, an arduino code was developed:

```
//The motor has a 1.8º step angle (200 steps/revolution)
// declare pins
int potPin= 4;
int stp = 7;
int dir = 5;
int enab = 8;
int TIMEOUT = 3000; //turns off after 3 sec of inactivity

//declare values
int prev = 0; //stepper position (0-200)->(0-360º)
int potval = 0; //value of the sensor
int val=0; //mapped value of the sensor
int lastpotval=0; //To implement a software Low-Pass-Filter
unsigned long stamp=0; //last move time stamped
//unsigned long variables are extended size variables for number storage
//and store 32bits (won't store negative numbers)

void setup ()
{
pinMode(potPin, INPUT);
  pinMode(stp, OUTPUT);
  pinMode(dir, OUTPUT);
  pinMode(enab, OUTPUT);
  digitalWrite(stp , LOW);
```

```
 digitalWrite(dir , LOW);
 digitalWrite(enab, HIGH);
 //Serial.begin (9600); //for debuging
}
void loop()
{
 // read the value from the potentiometer (range 0 - 1023)
 potval = analogRead(A4);
 // map it to the range of the motor
 val = map (potval, 0, 1023, 0, 200);
 //map(value, fromLow, fromHigh, toLow, toHigh)

 /*Pots can have small resistance oscillations that can cause the motor to keep
   making a positive step immediately followed by a negative step. Here this behavior
   is avoided by being sensitive only to variations greater than a threshold*/

 if(abs(val-prev)>4) //if diference is greater than 4 step
 {
  if((val-prev)>0)
  {
   digitalWrite(enab, LOW); //enable motor
   digitalWrite(dir, HIGH); //set direction
   digitalWrite(stp, HIGH);  //move a step to the right
   delay(20);
   digitalWrite(stp,LOW);
   delay(20);
   prev=prev+1;
  }
```

```
   if ((val-prev)<0)
   {
     digitalWrite(enab, LOW); //enable motor
     digitalWrite(dir, LOW); //other direction
     digitalWrite(stp, HIGH); //move a step to the left
     delay(20);
     digitalWrite(stp, LOW);
     delay(20);
     prev=prev-1;
   }
   stamp=millis(); //stamp actual time
  }
  else
  {
    if((millis()-stamp) > TIMEOUT)  //turn off to reduce motor heating
                                    //after TIMEOUT
    {
    digitalWrite(enab, HIGH);
    }
  }
}
```